



N° d'ordre NNT: 2019LYSEI066

# THÈSE DE DOCTORAT DE L'UNIVERSITÉ DE LYON

préparée au sein de  
l'Institut National des Sciences Appliquées de Lyon

École Doctorale 162  
Mécanique, Énergétique, Génie civil, Acoustique

Spécialité/discipline de doctorat  
**GÉNIE MÉCANIQUE**

Soutenue publiquement le 23 septembre 2019, par:

**Shaoyi Zhou**

---

## Advances in Passive and Active Vibration Damping Techniques

---

Devant le jury composé de:

Li Cheng	Professeur, Hong Kong Polytechnic University	Rapporteur
Christophe Collette	Professeur, Université Libre de Bruxelles	Rapporteur
Manuel Collet	Directeur de recherche CNRS, École Centrale de Lyon	Examineur
Guilhem Michon	Professeur, ISAE-SUPAERO	Examineur
Simon Chesné	Maître de conférences, INSA de Lyon	Directeur de thèse
Claire Jean-Mistral	Maître de conférences, INSA de Lyon	Co-Directrice de thèse

LaMCoS - CNRS UMR 5259 - INSA de Lyon  
20 Avenue Albert Einstein, 69621 Villeurbanne Cedex, France



**Département FEDORA – INSA Lyon - Ecoles Doctorales – Quinquennal 2016-2020**

<b>SIGLE</b>	<b>ECOLE DOCTORALE</b>	<b>NOM ET COORDONNEES DU RESPONSABLE</b>
<b>CHIMIE</b>	<b>CHIMIE DE LYON</b> <a href="http://www.edchimie-lyon.fr">http://www.edchimie-lyon.fr</a> Sec. : Renée EL MELHEM Bât. Blaise PASCAL, 3e étage <a href="mailto:secretariat@edchimie-lyon.fr">secretariat@edchimie-lyon.fr</a> INSA : R. GOURDON	<b>M. Stéphane DANIELE</b> Institut de recherches sur la catalyse et l'environnement de Lyon IRCELYON-UMR 5256 Équipe CDFA 2 Avenue Albert EINSTEIN 69 626 Villeurbanne CEDEX <a href="mailto:directeur@edchimie-lyon.fr">directeur@edchimie-lyon.fr</a>
<b>E.E.A.</b>	<b>ÉLECTRONIQUE, ÉLECTROTECHNIQUE, AUTOMATIQUE</b> <a href="http://edeea.ec-lyon.fr">http://edeea.ec-lyon.fr</a> Sec. : M.C. HAVGOUDOUKIAN <a href="mailto:ecole-doctorale.eea@ec-lyon.fr">ecole-doctorale.eea@ec-lyon.fr</a>	<b>M. Gérard SCORLETTI</b> École Centrale de Lyon 36 Avenue Guy DE COLLONGUE 69 134 Écully Tél : 04.72.18.60.97 Fax 04.78.43.37.17 <a href="mailto:gerard.scorletti@ec-lyon.fr">gerard.scorletti@ec-lyon.fr</a>
<b>E2M2</b>	<b>ÉVOLUTION, ÉCOSYSTÈME, MICROBIOLOGIE, MODÉLISATION</b> <a href="http://e2m2.universite-lyon.fr">http://e2m2.universite-lyon.fr</a> Sec. : Sylvie ROBERJOT Bât. Atrium, UCB Lyon 1 Tél : 04.72.44.83.62 INSA : H. CHARLES <a href="mailto:secretariat.e2m2@univ-lyon1.fr">secretariat.e2m2@univ-lyon1.fr</a>	<b>M. Philippe NORMAND</b> UMR 5557 Lab. d'Ecologie Microbienne Université Claude Bernard Lyon 1 Bâtiment Mendel 43, boulevard du 11 Novembre 1918 69 622 Villeurbanne CEDEX <a href="mailto:philippe.normand@univ-lyon1.fr">philippe.normand@univ-lyon1.fr</a>
<b>EDISS</b>	<b>INTERDISCIPLINAIRE SCIENCES-SANTÉ</b> <a href="http://www.ediss-lyon.fr">http://www.ediss-lyon.fr</a> Sec. : Sylvie ROBERJOT Bât. Atrium, UCB Lyon 1 Tél : 04.72.44.83.62 INSA : M. LAGARDE <a href="mailto:secretariat.ediss@univ-lyon1.fr">secretariat.ediss@univ-lyon1.fr</a>	<b>Mme Emmanuelle CANET-SOULAS</b> INSERM U1060, CarMeN lab, Univ. Lyon 1 Bâtiment IMBL 11 Avenue Jean CAPELLE INSA de Lyon 69 621 Villeurbanne Tél : 04.72.68.49.09 Fax : 04.72.68.49.16 <a href="mailto:emmanuelle.canet@univ-lyon1.fr">emmanuelle.canet@univ-lyon1.fr</a>
<b>INFOMATHS</b>	<b>INFORMATIQUE ET MATHÉMATIQUES</b> <a href="http://edinfomaths.universite-lyon.fr">http://edinfomaths.universite-lyon.fr</a> Sec. : Renée EL MELHEM Bât. Blaise PASCAL, 3e étage Tél : 04.72.43.80.46 Fax : 04.72.43.16.87 <a href="mailto:infomaths@univ-lyon1.fr">infomaths@univ-lyon1.fr</a>	<b>M. Luca ZAMBONI</b> Bât. Braconnier 43 Boulevard du 11 novembre 1918 69 622 Villeurbanne CEDEX Tél : 04.26.23.45.52 <a href="mailto:zamboni@maths.univ-lyon1.fr">zamboni@maths.univ-lyon1.fr</a>
<b>Matériaux</b>	<b>MATÉRIAUX DE LYON</b> <a href="http://ed34.universite-lyon.fr">http://ed34.universite-lyon.fr</a> Sec. : Marion COMBE Tél : 04.72.43.71.70 Fax : 04.72.43.87.12 Bât. Direction <a href="mailto:ed.materiaux@insa-lyon.fr">ed.materiaux@insa-lyon.fr</a>	<b>M. Jean-Yves BUFFIÈRE</b> INSA de Lyon MATEIS - Bât. Saint-Exupéry 7 Avenue Jean CAPELLE 69 621 Villeurbanne CEDEX Tél : 04.72.43.71.70 Fax : 04.72.43.85.28 <a href="mailto:jean-yves.buffiere@insa-lyon.fr">jean-yves.buffiere@insa-lyon.fr</a>
<b>MEGA</b>	<b>MÉCANIQUE, ÉNERGÉTIQUE, GÉNIE CIVIL, ACOUSTIQUE</b> <a href="http://edmega.universite-lyon.fr">http://edmega.universite-lyon.fr</a> Sec. : Marion COMBE Tél : 04.72.43.71.70 Fax : 04.72.43.87.12 Bât. Direction <a href="mailto:mega@insa-lyon.fr">mega@insa-lyon.fr</a>	<b>M. Jocelyn BONJOUR</b> INSA de Lyon Laboratoire CETHIL Bâtiment Sadi-Carnot 9, rue de la Physique 69 621 Villeurbanne CEDEX <a href="mailto:jocelyn.bonjour@insa-lyon.fr">jocelyn.bonjour@insa-lyon.fr</a>
<b>ScSo</b>	<b>ScSo*</b> <a href="http://ed483.univ-lyon2.fr">http://ed483.univ-lyon2.fr</a> Sec. : Viviane POLSINELLI Brigitte DUBOIS INSA : J.Y. TOUSSAINT Tél : 04.78.69.72.76 <a href="mailto:viviane.polsinelli@univ-lyon2.fr">viviane.polsinelli@univ-lyon2.fr</a>	<b>M. Christian MONTES</b> Université Lyon 2 86 Rue Pasteur 69 365 Lyon CEDEX 07 <a href="mailto:christian.montes@univ-lyon2.fr">christian.montes@univ-lyon2.fr</a>

\*ScSo : Histoire, Géographie, Aménagement, Urbanisme, Archéologie, Science politique, Sociologie, Anthropologie



# Abstract

Mechanical systems (e.g. flexible structures) are usually lightly damped so that they vibrate severely in response to dynamic loads. Therefore, vibration control strategies should be adopted in order to reduce the undesired vibration of mechanical systems. The objective of this thesis is to develop multiple vibration control techniques, which are either passive or active. All systems under investigation are in the mechanical and/or electrical domains, for which analytical optimization and theoretical analyses are performed.

The first part focuses on the application of inerter to enhance the vibration control performance of two existing control devices, the tuned mass damper (TMD) and the series double TMD (SDTMD). The inerter is employed to relate the tuned mass to the ground. In the case of TMD, a mechanical system under stiffness uncertainty is considered and the worst-case  $H_\infty$  optimization is addressed by means of an entirely algebraic approach. In the case of SDTMD, the vibration of a deterministic mechanical system is to be controlled and the  $H_\infty$  optimal design is carried out via an extended version of fixed points theory (FPT).

Instead of using the inerter, the second part consists in improving the control effect by incorporating a linear negative stiffness between the ground and the tuned mass. Two case studies are conducted based on the non-traditional TMD and inerter-based dynamic vibration absorber (IDVA), whose tuned mass is related to the ground by a viscous damper or an inerter-based mechanical network, respectively. Later, the exact electrical realization of non-traditional configurations with or without negative stiffness is proposed, which is based on the piezoelectric transducer enclosed by a particular shunt circuit. This electromechanical analogy enables to extend the applicability of mechanical control devices and to facilitate the precise tuning.

In the last part, active and semi-active vibration control techniques are developed. The first strategy consists in enhancing the control capability of passive TMD and IDVA by feeding back the displacement signal of mechanical system to the electromagnetic actuator. The proposed controller can be regarded as one or multiple basic units arranged in series, which is featured by one pole at the origin and two coalesced zeros on the real axis. It is analytically proven that such a controller design is always stable if and only if the magnitude of introduced zeros resides within

the magnitudes of the smallest and largest eigenvalues of coupled system, whose expressions are analytically formulated in both cases of TMD and IDVA. Distinguished from the previous strategy, the semi-active control technique is based on electromagnetic shunt damping (EMSD), therefore, no additional sensor is required to measure the information of mechanical system. In order to artificially increase the shunt damping performance, the employment of negative inductance (NI) in the shunt circuit is considered. Three possible layouts of NI in the EMSD are assessed in terms of the electromechanical coupling factor, which quantifies the energy conversion efficiency between mechanical and electrical domains. Finally, six types of shunt circuits are optimally tuned according to the FPT and the beneficial effect of NI and the influence of its layout can be underlined.

# Résumé

Les systèmes mécaniques (e.g. structures flexibles) sont généralement peu amortis, et par conséquent des vibrations de fortes amplitudes peuvent apparaître. Il apparaît nécessaire de développer des stratégies de contrôle vibratoire pour atténuer ces vibrations mécaniques. Cette thèse a pour objectif de développer plusieurs techniques d'amortissement de vibration passives ou actives. Tous les systèmes sont étudiés dans des domaines mécanique et/ou électrique, pour lesquels l'optimisation analytique et les analyses théoriques sont effectuées.

La première partie porte sur l'utilisation d'un “inertier” pour améliorer les performances de contrôle vibratoire de deux dispositifs existants, l'amortisseur à masse accordée (TMD) et deux TMDs placés en série (SDTMD). Dans le cas avec un TMD, on considère un système mécanique avec incertitudes ainsi que son optimisation  $H_\infty$  (worst-case optimization) en adoptant une approche purement algébrique. Dans le cas de SDTMD, on vise à contrôler la vibration d'un système déterministe. Son optimisation  $H_\infty$  s'effectue ici en utilisant une version étendue de la théorie de points fixes (FPT).

Dans une seconde partie, on cherche à améliorer les performances de ce type de dispositif en positionnant un élément linéaire de raideur négative entre la base et la masse accordée. Deux cas d'étude sont menés: le TMD seul et celui basé sur l'inertier (IDVA). Les deux dispositifs ont une configuration non-traditionnelle, dont la masse accordée est liée à la base par l'intermédiaire d'un amortisseur visqueux ou un réseau mécanique basé sur l'inertier. La réalisation de ces dispositifs non-traditionnelles avec ou sans raideur négative et leurs shunts piézoélectriques sont étudiés et une analogie électromécanique est établie. Cette analogie permet d'étendre l'applicabilité des amortisseurs mécaniques et de faciliter les réglages.

Dans la dernière partie, deux techniques d'amortissement actif et semi-actif sont développées. La première stratégie concerne une loi de contrôle hybride applicable au TMD et à l'IDVA. Le contrôleur proposé est composé d'un seul ou plusieurs compensateurs identiques, qui est caractérisé par un pôle à l'origine et deux zéros coïncidents réels. Il est analytiquement prouvé qu'avec ce contrôleur, le système complet est toujours stable si et seulement si le module de ces zéros est compris entre la plus petite et la plus grande des valeurs propres du système. Les expressions

analytiques sont développées dans les deux cas. La seconde technique de contrôle s'appuie sur l'atténuation de vibration par shunt électromagnétique (EMSD), pour laquelle aucun capteur est requis. Une inductance négative (NI) est employée dans les shunts électromagnétiques afin d'améliorer l'amortissement. Trois architectures possibles de NI dans un EMSD sont évaluées à travers le facteur de couplage électromécanique, qui quantifie l'efficacité de conversion énergétique entre les domaines mécanique et électrique. Finalement, six shunts électromagnétiques utilisant des NIs sont optimisés et analysés.

# Contents

<b>Abstract</b>	<b>i</b>
<b>Résumé</b>	<b>iii</b>
<b>Contents</b>	<b>v</b>
<b>List of Figures</b>	<b>ix</b>
<b>List of Tables</b>	<b>xv</b>
<b>List of Abbreviations</b>	<b>xvii</b>
<b>1 Literature Review</b>	<b>1</b>
1.1 Passive vibration control . . . . .	2
1.1.1 Tuned mass damper . . . . .	2
1.1.2 Non-traditional TMD . . . . .	9
1.1.3 Multiple TMDs . . . . .	9
1.1.4 Multiple-DOF TMD . . . . .	11
1.1.5 Inerter . . . . .	12
1.1.6 Negative stiffness mechanism . . . . .	17
1.1.7 Other passive damping mechanisms . . . . .	18
1.2 Electromechanical shunt damper . . . . .	18
1.2.1 Piezoelectric shunt damper . . . . .	19
1.2.2 Electromagnetic shunt damper . . . . .	22
1.3 Active vibration control . . . . .	23
1.4 Dual-functional design . . . . .	26
1.5 Outline of thesis . . . . .	28
<b>2 Worst-Case Optimization of TMDI</b>	<b>29</b>
2.1 Mathematical modeling . . . . .	30
2.1.1 Equations of motion . . . . .	30
2.1.2 Stiffness uncertainty modeling . . . . .	30
2.1.3 Displacement FRF . . . . .	31
2.2 Worst-case optimal design . . . . .	31

2.2.1	Min-max optimization formulation . . . . .	32
2.2.2	Proposed tuning methodology . . . . .	32
2.2.3	Preliminary remarks . . . . .	40
2.3	Numerical investigation . . . . .	41
2.3.1	Validation of derived solutions . . . . .	42
2.3.2	Effectiveness of worst-case design and influence of grounded inerters . . . . .	43
2.3.3	Discussion . . . . .	45
2.4	Concluding remarks . . . . .	46
<b>3</b>	<b>Series Double Tuned Mass Damper with Inerters</b>	<b>47</b>
3.1	Mathematical modeling . . . . .	47
3.1.1	G-SDTMDI . . . . .	48
3.1.2	I-SDTMDI . . . . .	49
3.2	Optimization of G-SDTMDI . . . . .	50
3.2.1	Analytical derivation of optimal parameters . . . . .	51
3.2.2	Validation of derived solutions . . . . .	55
3.2.3	Remarks . . . . .	57
3.3	Optimization of I-SDTMDI . . . . .	59
3.4	Numerical investigation . . . . .	61
3.4.1	Performance index . . . . .	62
3.4.2	Displacement FRF . . . . .	63
3.4.3	Discussion . . . . .	64
3.5	Concluding remarks . . . . .	65
<b>4</b>	<b>Dynamic Vibration Absorber with Negative Stiffness</b>	<b>67</b>
4.1	NSDVA . . . . .	67
4.1.1	Mathematical modeling . . . . .	68
4.1.2	Stability analysis . . . . .	69
4.1.3	Optimization according to the FPT . . . . .	69
4.1.4	Optimization according to the SMC . . . . .	72
4.1.5	Numerical simulations and analyses . . . . .	75
4.2	NSIDVA . . . . .	79
4.2.1	Mathematical modeling . . . . .	80
4.2.2	Optimization according to the SMC . . . . .	81
4.3	Concluding remarks . . . . .	85
<b>5</b>	<b>Electromechanical Analogy</b>	<b>87</b>
5.1	Fundamentals . . . . .	87
5.1.1	Mechanical impedance . . . . .	87
5.1.2	Addition laws of mechanical impedances . . . . .	89
5.1.3	Electrical impedance . . . . .	89
5.1.4	Addition laws of electrical impedances . . . . .	89

---

5.1.5	Subsystem approach . . . . .	90
5.2	Piezoelectric analogous model . . . . .	91
5.3	Electromagnetic analogous model . . . . .	94
5.4	Concluding remarks . . . . .	95
<b>6</b>	<b>A General Control Law for Hybrid DVA and IDVA</b>	<b>97</b>
6.1	Mathematical modeling . . . . .	98
6.1.1	System description . . . . .	98
6.1.2	Generalized equations of motion . . . . .	98
6.1.3	Open-loop and closed-loop FRFs . . . . .	99
6.1.4	Passive IDVA . . . . .	101
6.2	Controller design . . . . .	101
6.2.1	Hyperstability . . . . .	102
6.2.2	Criterion for performance comparison . . . . .	105
6.3	Performance of hybrid control scheme . . . . .	105
6.3.1	Root locus . . . . .	106
6.3.2	Dynamics at specific gains . . . . .	107
6.4	Practical consideration and case study . . . . .	108
6.5	Concluding remarks . . . . .	111
<b>7</b>	<b>Electromagnetic Shunt Damping</b>	<b>113</b>
7.1	Electromechanical coupling factor . . . . .	114
7.1.1	EMCF related to the series layout . . . . .	115
7.1.2	EMCF related to the SP layout . . . . .	116
7.1.3	Remarks . . . . .	117
7.2	EMSD enclosed by series RL and RLC shunts . . . . .	118
7.2.1	Optimization of EMSD with a series RL shunt . . . . .	120
7.2.2	Optimization of EMSD with a series RLC shunt . . . . .	121
7.2.3	Remarks . . . . .	122
7.3	EMSD enclosed by a SP shunt . . . . .	122
7.3.1	Mathematical modeling . . . . .	122
7.4	Discussion . . . . .	125
7.5	Concluding remarks . . . . .	127
<b>8</b>	<b>Conclusions and Future Work</b>	<b>129</b>
8.1	Conclusions . . . . .	129
8.2	Future work . . . . .	131
8.3	Publications . . . . .	132
<b>A</b>	<b>Appendix related to Chapter 2</b>	<b>133</b>
A.1	Partial derivative of $G_{\text{opt}}$ with respect to $\mu$ , $\nu$ and $\eta$ . . . . .	133
A.2	Definition of performance index PI . . . . .	133
<b>B</b>	<b>Appendix related to Chapter 3</b>	<b>135</b>

---

<b>C</b>	<b>Appendix related to Chapter 4</b>	<b>137</b>
C.1	Lower bounds on $\eta$ for NSDVA tuned by the SMC . . . . .	137
C.2	An alternative layout of NSDVA . . . . .	139
<b>D</b>	<b>Appendix related to Chapter 6</b>	<b>141</b>
D.1	Open-loop poles in the worst-case scenario . . . . .	141
D.2	Dynamics of hybrid control scheme based on a DVA . . . . .	141
D.2.1	System description . . . . .	141
D.2.2	Passive design . . . . .	142
D.2.3	Open-loop poles in the worst-case scenario . . . . .	142
D.3	Proof of proposition for the case of $n = 1$ . . . . .	142
<b>E</b>	<b>Appendix related to Chapter 7</b>	<b>145</b>
E.1	$H_2$ Optimization of EMSD coupled with a series RLC shunt . . . . .	145
E.2	Stability analysis for the resistive EMSD enhanced by series and parallel NIs . . . . .	147
	<b>Bibliography</b>	<b>149</b>

# List of Figures

1.1	Schematic diagrams of an undamped SDOF primary system controlled by the TMD of: (a) Frahm; (b) Den Hartog. . . . .	2
1.2	Comparison of displacement FRFs of primary system without any control (dotted line) or coupled with a TMD of either Frahm (thin solid line) or Den Hartog (thick solid line). The mass ratio $\mu$ is of 5%, the frequency tuning ratio $\alpha$ is set as unity and the mechanical damping ratio is equal to 0.1. . . . .	4
1.3	The phenomenon of fixed points. The parameters other than $\xi$ are set as: $\mu = 5\%$ , $\alpha = 1$ . . . . .	5
1.4	Schematic diagram of an undamped SDOF primary system controlled by a non-traditional TMD. . . . .	9
1.5	Schematic diagram of a SDOF primary system controlled by the multiple TMD. . . . .	10
1.6	Schematic diagrams of a SDOF primary system controlled by a: (a) series DTMD; (b) parallel DTMD. . . . .	10
1.7	A SDOF primary system controlled by a two-DOF TMD [32]. . . . .	12
1.8	Schematic diagram of an inerter element. . . . .	13
1.9	Realization mechanisms of inerter: (a) rack and pinion [40]; (b) ball and screw [41]. . . . .	13
1.10	A civil structure installed with either a TMD or a TID [42]. . . . .	14
1.11	Schematic diagram of a SDOF primary system controlled by a TMDI. . . . .	14
1.12	Wind-induced vibration mitigation of a multi-storey building by means of a TMDI [47]. The TMD is connected to the top floor, while the inerter is linked to the penultimate or a lower floor. . . . .	15
1.13	Schematic diagram of a SDOF primary system controlled by an IDVA. . . . .	16
1.14	Electrical models of: (a) piezoelectric transducer; (b) electromagnetic transducer. . . . .	19
1.15	(a) R shunt; (b) series RL shunt; (c) parallel RL shunt; (d) RLC parallel shunt; (e) multi-mode shunt proposed by Hollkamp [92]; (f) Current flowing shunt circuit proposed by Behrens et al. [93]. . . . .	20
1.16	Employment of NCs in PSD: (a) series layout; (b) parallel layout; (c) SP layout. . . . .	21
1.17	A negative impedance converter. . . . .	21

1.18	Schematic representation of active vibration control [118]. . . . .	23
1.19	A SDOF primary system controlled by: (a) an AMD; (b) an ATMD.	24
1.20	The ten tallest completed buildings with dampers in the world [119]. The types of damper include: tuned mass damper (TMD), active tuned mass damper (ATMD) and tuned liquid damper (TLD). . . . .	25
1.21	Schematic diagrams of a SDOF primary system controlled by au- toparametric EH-DVA in the form of: (a) a cantilever beam with a tip mass and embedded piezoelectric layers [150]; (b) a pendulum with a levitating magnet moving freely insides [152]. . . . .	27
2.1	Schematic diagram of a SDOF primary system controlled by a TMDI.	29
2.2	Displacement FRFs of primary system controlled by a TMDI with the classic equal-peak design. The set of parameters is: $\mu = 0.05$ , $\nu = 0.03$ , $\eta = 20\%$ . Thin dash-dotted line: without control, thick dashed line: the deterministic scenario ( $\delta = 0$ ), thick solid line: the worst-case scenario, thin dotted lines: 20 uncertainties $\delta$ randomly sampled in $[-\eta, +\eta]$ . . . . .	32
2.3	Displacement FRFs of primary system controlled by a TMDI corre- sponding to three damping levels: (a) $\delta = -\eta$ ; (b) $\delta = +\eta$ . The set of parameters is: $\mu = 0.05$ , $\nu = 0.03$ , $\eta = 20\%$ and $\alpha^2 = 1.2$ . Dotted line: $\xi = 0$ , solid line: $\xi = 0.6$ and dash-dotted line: $\xi = \infty$ . . . . .	33
2.4	Displacement FRFs of primary system controlled by a TMDI corre- sponding to three damping levels: (a) $\delta = -\eta$ ; (b) $\delta = +\eta$ . The set of parameters is: $\mu = 0.05$ , $\nu = 0.05$ , $\eta = 10\%$ and $\alpha$ is evaluated by Eq.(2.33). Dotted line: $\xi = 0$ , solid line: $\xi = 1$ and dash-dotted line: $\xi = \infty$ . The leftmost and rightmost fixed points locate at (0.81, 5.66) and (1.08, 5.66). . . . .	38
2.5	Displacement FRFs of primary system controlled by a TMDI with the worst-case optimal design. Solid line: $\mu = 0.05$ , $\nu = 0.01$ , $\eta = 20\%$ ; circle markers: $\mu = 0.03$ , $\nu = 0.03$ , $\eta = 20\%$ . C1 and C2 correspond to FRFs with $\delta = -\eta$ and $\delta = +\eta$ , respectively. . . . .	40
2.6	Displacement FRFs of primary system controlled by a TMD related to three levels of stiffness uncertainty: (a) $\delta = -\eta$ ; (b) $\delta = +\eta$ . The TMD is optimized by either the method in [14] (represented by circle marker) or the proposed methodology (marked by lines). The mass ratio is set as $\mu = 0.05$ . Solid line: $\eta = 0$ , dotted line: $\eta = 10\%$ , dash-dotted line: $\eta = 20\%$ . . . . .	41
2.7	Displacement FRFs of primary system controlled by a TMDI corre- sponding to three inertance-to-mass ratios: (a) $\delta = -\eta$ ; (b) $\delta = +\eta$ . The design parameters are either analytically derived (solid lines) or numerically solved (dash-dotted lines). The mass ratio and the un- certainty remain unchanged as: $\mu = 0.05$ and $\eta = 20\%$ , while three values of $\nu$ are used: $\nu = 0$ , 0.05 and 0.10. . . . .	42

2.8	Displacement FRFs of primary system controlled by a: (a) TMD; (b) TMDI. The set of parameters is: $\mu = 0.05$ , $\nu = 0.03$ and $\eta = 20\%$ . Thin solid lines: with the classic design, thick solid lines: with the worst-case optimal design. . . . .	43
2.9	(a) Evolution of performance index PI against the inertance-to-mass ratio $\nu$ for the set of parameters: $\mu = 0.05$ and $\eta = 20\%$ . Thin line: classic TMDI, thick line: robust TMDI, circle markers: $\nu = 0$ . (b) Reduction in PI (in %) for robust TMDI with respect to classic TMDI. (c) Reduction in PI (in %) for TMDI compared to TMD. Thin line: classic design, thick line: robust design. . . . .	45
2.10	Evolution of $\ G\ _\infty$ against actual stiffness uncertainty $\delta$ sweeping within $[-\eta, +\eta]$ : (a) TMD; (b) TMDI. The set of parameters is: $\mu = 0.05$ , $\nu = 0.03$ and $\eta = 20\%$ . Thin solid lines: classic design, thick solid lines: worst-case design. . . . .	46
3.1	Schematic diagrams of a SDOF primary system controlled by a: (a) G-SDTMDI; (b) I-SDTMDI. . . . .	48
3.2	Displacement FRFs of primary system controlled by a G-SDTMDI with three sets of parameters. Only the mechanical damping ratio $\xi_3$ varies, while the other parameters remain unchanged: $\mu = 0.05$ , $\nu = 0.04$ , $\alpha = 1.3$ , $\beta = 0.9$ , $\xi_2 = 0$ and $\eta = \theta = 0.02$ . Dotted line: $\xi_3 = 0$ , solid line: $\xi_3 = 0.2$ , dash-dotted line: $\xi_3 = \infty$ . . . . .	51
3.3	Displacement FRFs of primary system controlled by a SDTMD, whose parameters are tuned by the $H_\infty$ optimization criterion (solid lines) and the extended FPT (dash-dotted lines), respectively. Four sets of simulation are performed corresponding to different mass ratios: $\mu = 0.01, 0.05, 0.10$ and $0.15$ . . . . .	56
3.4	Displacement FRFs of primary system controlled by a G-SDTMDI (solid line: $\xi_2 = 0$ , dash-dotted line: $\xi_2 = 1\%$ ). The tuning parameters are optimized for: $\mu = 0.05$ and $\eta = \theta = 0$ . . . . .	56
3.5	Displacement FRFs of primary system controlled by an optimized G-SDTMDI with different sets of parameters. (a) Solid line: $\mu = 0.05$ , $\eta = 0.02$ and $\theta = 0.01$ ; circle marker: $\mu = 0.04$ , $\eta = 0.03$ and $\theta = 0.01$ . (b) Solid line: $\mu = 0.05$ and $\eta = \theta = 0.02$ ; circle marker: $\mu = 0.05$ , $\eta = 0.02$ and $\theta = 0$ . . . . .	57
3.6	Two variant configurations of G-SDTMDI: (a) type I with only one inerter placed between the TMDA and the ground; (b) type II with only one inerter placed between the TMDB and the ground. . . . .	58
3.7	Comparison of the exact and fitted solutions for $\lambda_3^2$ . Black dots: exact solution at given pairs of $(\mu, \eta)$ ; grid surface: the fitted solutions. . . . .	60

3.8	Displacement FRFs of primary system controlled by a classic SDTMD with optimal parameters derived for G-SDTMDI or I-SDTMDI. The total mass ratio is set as: $\mu = 0.10$ . Solid line: with optimal design for G-SDTMDI, circle marker: with optimal design for I-SDTMDI. . . . .	61
3.9	Evolution of performance indices as a function of $\mu$ or $\gamma = \mu + \eta$ . Solid line: $P\{\text{TMD}, \text{SDTMD}\}$ , circle markers: $P\{\text{TMDI}, \text{G-SDTMDI}\}$ . . . . .	62
3.10	Evolution of performance indices against the total mass ratio $\mu$ and the total inertance-to-mass ratio $\eta$ : (a) $P\{\text{SDTMD}, \text{G-SDTMDI}\}$ ; (b) $P\{\text{SDTMD}, \text{I-SDTMDI}\}$ . . . . .	63
3.11	Displacement FRFs of primary system under harmonic force excitation with $\mu = 0.05$ and $\eta = 0.02$ . (a) Dotted line: without control, thin solid line: classic TMD, thick solid line: TMDI. (b) Dotted line: without control, thin solid line: classic SDTMD, thick solid line: G-SDTMDI, thick dashed line: I-SDTMDI. . . . .	64
4.1	Schematic diagrams of a SDOF undamped primary system controlled by a: (a) non-traditional DVA; (b) NSDVA. . . . .	68
4.2	Displacement FRF surface of primary system controlled by a NSDVA versus the dimensionless frequency $\lambda$ and the negative stiffness ratio $\eta$ . Curve C1: $\eta = 0$ , C2: $\eta = \eta_{\text{fpt}}$ . . . . .	71
4.3	Evolution of peak displacement amplitude of primary system against the negative stiffness ratio $\eta$ when tuned by the FPT. . . . .	72
4.4	Displacement FRF of primary system controlled by a NSDVA. Thin lines: $\eta = 0$ , thick lines: $\eta = \eta_{\text{fpt}}$ . Dashed lines: tuned by the FPT; solid lines: calibrated by the SMC. . . . .	75
4.5	CMSR value of normalized displacement of primary system. Thin lines: $\eta = 0$ , thick lines: $\eta = \eta_{\text{fpt}}$ . Dashed lines: tuned by the FPT; solid lines: calibrated by the SMC. . . . .	76
4.6	FRF of relative displacement between primary and secondary masses. Thin lines: $\eta = 0$ , thick lines: $\eta = \eta_{\text{fpt}}$ . Dashed lines: tuned by the FPT; solid lines: calibrated by the SMC. . . . .	76
4.7	Evolution of system damping ratio $\xi^*$ as a function of the negative stiffness ratio $\eta$ . Dashed lines: tuned by the FPT; solid lines: calibrated by the SMC. . . . .	77
4.8	Root loci of primary system coupled with a NSDVA. Circle marker: tuned by the FPT with $\eta = 0$ ; square marker: calibrated by the SMC with $\eta = 0$ ; diamond marker: optimized by the SMC with critical negative stiffness ratio $\eta_{\text{smc}}^-$ . The performance indices read as: $\Lambda_{\text{fpt}} = 0.067$ , $\Lambda_{\text{smc}} = 0.12$ and $\Lambda_{\text{smc}}^- = 1.35$ . . . . .	78

4.9	Transient responses under free vibration normalized by the initial displacement of primary system $z_0$ : (a) displacement of primary system; (b) stroke length of DVA. The mass ratio is imposed as $\mu = 0.10$ . Dashed line: tuned by the FPT with $\eta = 0$ ; thin solid line: tuned by the SMC with $\eta = 0$ ; thick solid line: calibrated by the SMC with critical negative stiffness ratio $\eta_{\text{smc}}^-$ . . . . .	79
4.10	Schematic diagrams of a SDOF undamped primary system controlled by a: (a) non-traditional IDVA [159]; (b) NSIDVA. . . . .	80
4.11	Displacement FRFs of primary system when controlled by four types of dampers. The mass ratio is set as: $\mu = 5\%$ . Thin lines: without negative stiffness, thick lines: with a negative stiffness ratio of $\eta = -0.02$ . Black lines: DVA, red lines: IDVA. . . . .	85
5.1	A mass element. . . . .	87
5.2	Two subsystems for the configuration of a SDOF primary system controlled by a non-traditional DVA. . . . .	90
5.3	The equivalent model based on the impedance-mobility approach. . . . .	90
5.4	(a) Equivalent model of a SDOF primary system controlled by an electromechanical shunt damper; (b) electrical model of a PSD with a generalized electrical impedance $Z_L$ ; (c) electrical model of an EMSD with an impedance $Z_L$ . . . . .	91
6.1	Schematic diagrams of a SDOF primary system controlled by: (a) a hybrid DVA; (b) a hybrid IDVA. . . . .	98
6.2	Block diagram of the SISO control scheme. . . . .	99
6.3	Dynamics of undamped primary system coupled with a passive DVA or IDVA: (a) normalized FRFs $G_{CL}$ (dotted line: without control, dashed line: DVA, solid line: IDVA); (b) pole-zero plots (black: DVA, red: IDVA). The mass ratio is set as: $\mu = 0.05$ . . . . .	102
6.4	Pole-zero plot for the hybrid control scheme related to IDVA in the worst-case scenario. Zeros are marked by unfilled circles and poles are represented by cross markers. $\phi_1$ and $\phi_3$ are phase angles of the vector joining the coalesced zeros $z_i = -\theta$ ( $i = 4, 5, \dots, 2n + 3$ ) to the poles $p_1$ and $p_3$ , respectively. $\psi_1$ and $\psi_3$ stand for the departure angles of root locus at the open-loop poles $p_1$ and $p_3$ . . . . .	103
6.5	Root locus diagrams of hybrid control scheme based on the IDVA: (a) zeroth-order controller; (b) controller of orders $n = 1$ and $2$ (corresponding to dotted and solid lines, respectively). The normalized magnitude of introduced zeros is set as: $\theta = 1$ . . . . .	106

6.6	Closed-loop FRFs $G_{CL}$ with the passive part being: (a) a DVA; (b) an IDVA. Dotted line: without control, dash-dotted line: passive, dashed line: compensator of order 0, thin solid line: compensator of order 1, thick solid line: compensator of order 2. The set of parameters used for simulation is: $\mu = 0.05$ , $\theta = 1$ , $g_0 = 0.4$ , $g_1 = 0.2$ and $g_2 = 0.1$ . . . . .	107
6.7	FRFs of active force required by controllers $G_{f,n}$ with the passive part being: (a) a DVA; (b) an IDVA. Dashed line: compensator of order 0, thin solid line: compensator of order 1, thick solid line: compensator of order 2. The set of parameters used for simulation is: $\mu = 0.05$ , $\theta = 1$ , $g_0 = 0.4$ , $g_1 = 0.2$ and $g_2 = 0.1$ . . . . .	108
6.8	FRFs of absorber stroke with the passive part being: (a) a DVA; (b) an IDVA. Dashed line: compensator of order 0, thin solid line: compensator of order 1, thick solid line: compensator of order 2. The set of parameters used for simulation is: $\mu = 0.05$ , $\theta = 1$ , $g_0 = 0.4$ , $g_1 = 0.2$ and $g_2 = 0.1$ . . . . .	109
6.9	(a) Schematic diagram of dual transducer; (b) its prototype [134]. . . . .	109
6.10	Temporal responses relevant to passive and hybrid control schemes: (a) displacement of primary system; (b) relative displacement between main and tuned masses (dash-dotted line: passive absorber, solid line: hybrid absorber, black line: DVA-based, red line: IDVA-based). (c) Active force generated by the actuator (black: hybrid DVA, red: hybrid IDVA). (d) Close-up of root locus relevant to first-order hybrid IDVA with high pass filter. The set of parameters used for simulation is: $\mu = 0.0667$ , $\theta = 1$ , $g_1 = 0.2$ , $\lambda = 1$ and $ \tilde{F}_p  = 0.5\text{mm}$ . . . . .	110
7.1	(a) Schematic diagram of mechanical system coupled with an EMSD. Four layouts are investigated: (b) w/o; (c) series; (d) parallel; (e) SP. . . . .	114
7.2	(a) R and RC shunts; (b) series RL and RLC shunts; (c) parallel shunt; (d) SP shunt. . . . .	118
7.3	Displacement FRFs of primary system against the normalized excitation frequency $\lambda$ and the inductance ratio $\alpha$ controlled by a RL EMSD. The set of parameters is: $\theta = 0.2$ and $\kappa = 5$ . . . . .	119
7.4	Displacement FRFs of primary system against $\lambda$ and $\alpha$ controlled by a RLC EMSD. The set of parameters is: $\theta = 0.2$ and $\kappa = 5$ . . . . .	121
7.5	Displacement FRFs of primary system controlled by an EMSD: (a) $\alpha = 1$ (dashed: SC, black: R, cyan: RC, red: parallel); (b) $\alpha = 0.5$ (dashed: SC, black: RL, cyan: RLC, red: SP). The set of parameters is: $\theta = 0.2$ and $\kappa = 5$ . . . . .	126
C.1	Schematic diagram of a SDOF undamped primary system controlled by a traditional NSDVA. . . . .	139

# List of Tables

1.1	Closed-form formulae for optimal parameters of traditional TMD attached to a SDOF undamped primary system under force excitation. Four optimization criteria are considered: FPT, $H_\infty$ and $H_2$ optimization criteria and SMC. . . . .	8
1.2	Closed-form formulae for optimal parameters of non-traditional TMD attached to a SDOF undamped primary system under force excitation. Three optimization criteria are considered: FPT, $H_2$ optimization criterion and SMC. . . . .	8
2.1	Optimal parameters of TMDI for a deterministic and uncertain SDOF primary system under force excitation. Constants $n_i$ and $d_j$ are given in Eqs. (2.42) and (2.43) with $\gamma = \mu + \nu$ and $\kappa = \sqrt{(1 + \eta^2)(1 + \gamma)^2 - 1}$ . 39	
2.2	Optimal parameters of TMD for a deterministic and uncertain SDOF primary system under force excitation. Constants $\hat{n}_i$ and $\hat{d}_j$ are given in Eqs. (2.42) and (2.43) with replacing $\gamma$ by $\mu$ . $\hat{\kappa} = \sqrt{(1 + \eta^2)(1 + \mu)^2 - 1}$ .	41
2.3	Worst-case $H_\infty$ norm of displacement FRFs of primary system controlled by either a TMD or a TMDI with classic or robust optimal design. The set of parameters is: $\mu = 0.05$ , $\nu = 0.03$ and $\eta = 20\%$ . . .	44
3.1	Closed-form formulae to optimal parameters of SDTMD attached to a SDOF undamped primary system under force excitation. . . . .	55
3.2	Exact and approximate parameters of SDTMD based on the $H_\infty$ optimization criterion and the extended FPT, respectively, for four mass ratios: $\mu = 0.01, 0.05, 0.10$ and $0.15$ . . . . .	55
3.3	Analytical formulae to optimal parameters of two variants of G-SDTMDI under force excitation and the allowable bounds on the total inertance-to-mass ratio $\eta$ . . . . .	58
3.4	$H_\infty$ norm of normalized displacement FRF of primary system when controlled by five types of dampers: TMD, TMDI, SDTMD, G-SDTMDI and I-SDTMDI. . . . .	61

3.5	Frequency bandwidths of vibration reduction and peak vibration amplitude of primary system when controlled by five types of dampers for the set of parameters: $\mu = 0.05$ and $\eta = 0.02$ . . . . .	64
4.1	Closed-form formulae to optimal parameters of non-traditional DVA and NSDVA attached to a SDOF undamped primary system under force excitation according to the FPT. . . . .	74
4.2	Closed-form formulae to optimal parameters of non-traditional DVA and NSDVA attached to a SDOF undamped primary system under force excitation according to the SMC. . . . .	74
4.3	Lower bounds on negative stiffness ratio $\eta$ for non-traditional NSDVA when tuned by the FPT and SMC. . . . .	74
4.4	Closed-form formulae to optimal parameters of non-traditional IDVA and NSIDVA based on the SMC. . . . .	85
5.1	Impedances and key characteristics of mechanical elements. . . . .	88
5.2	Total impedances of non-traditional DVA and series-type inertial mechanical network. . . . .	88
5.3	Impedances of three basic electronic components. . . . .	89
5.4	Basic mechanical elements or vibration absorbers and the external shunt circuits of their corresponding PSD. . . . .	92
5.5	Electromagnetic realization of Maxwell unit and inertial mechanical network. . . . .	94
6.1	The evolution of phase angle $\phi_1$ as the coalesced zeros $z_i = -\theta$ ( $i = 4, 5, \dots, 2n+3$ ) move along the negative real axis. The departure angle $\psi_1$ of root locus at the pole $p_1$ is then compared with $3\pi/2$ . . . . .	104
6.2	The evolution of phase angle $\phi_3$ as the coalesced zeros $z_i = -\theta$ ( $i = 4, 5, \dots, 2n+3$ ) move along the negative real axis. The departure angle $\psi_3$ of root locus at the pole $p_3$ is then compared with $\pi/2$ . . . . .	105
7.1	The OC and SC stiffness of various electromechanical systems and their corresponding EMCFs. . . . .	117
7.2	Optimal parameters of an EMSD shunted by a series RLC circuit tuned by the FPT, the $H_2$ optimization criterion and the SMC. . . . .	120
7.3	Normalized peak displacement amplitude of primary system controlled by various shunt circuits tuned by the FPT. . . . .	125
C.1	Closed-form formulae to optimal parameters of traditional DVA and NSDVA attached to a SDOF undamped primary system under force excitation according to the FPT. . . . .	140
C.2	Closed-form formulae to optimal parameters of traditional DVA and NSDVA attached to a SDOF undamped primary system under force excitation according to the SMC. . . . .	140

# List of Abbreviations

<b>AMD</b>	Active mass damper
<b>ATMD</b>	Active tuned mass damper
<b>CMSR</b>	Cumulative mean square response
<b>DOF</b>	Degree of freedom
<b>DTMD</b>	Double tuned mass damper
<b>DVA</b>	Dynamic vibration absorber
<b>DVFC</b>	Direct velocity feedback control
<b>EH-DVA</b>	Energy-harvesting dynamic vibration absorber
<b>EMSD</b>	Electromagnetic shunt damper
<b>EMEH</b>	Electromagnetic energy harvester
<b>EOM</b>	Equation of motion
<b>FPT</b>	Fixed points theory
<b>FRF</b>	Frequency response function
<b>G-SDTMDI</b>	Grounded-type series double tuned mass damper with inerters
<b>HSLD</b>	High-static-low-dynamic
<b>IDVA</b>	Inerter-based dynamic vibration absorber
<b>I-SDTMDI</b>	Inserted-type series double tuned mass damper with inerters
<b>MDOF</b>	Multiple-degree-of-freedom
<b>MTMD</b>	Multiple tuned mass damper
<b>NC</b>	Negative capacitance

<b>NES</b>	Nonlinear energy sink
<b>NI</b>	Negative inductance
<b>NIC</b>	Negative impedance converter
<b>NL-VA</b>	Nonlinear vibration absorber
<b>NR</b>	Negative resistance
<b>NSDVA</b>	Dynamic vibration absorber with negative stiffness
<b>NSIDVA</b>	Inerter-based dynamic vibration absorber with negative stiffness
<b>NSM</b>	Negative stiffness mechanism
<b>OC</b>	Open-circuited
<b>PSD</b>	Piezoelectric shunt damper
<b>QZS</b>	Quasi-zero-stiffness
<b>RLC</b>	Resistive-inductive-capacitive
<b>RMS</b>	Root mean square
<b>SC</b>	Short-circuited
<b>SDOF</b>	Single-degree-of-freedom
<b>SDTMD</b>	Series-type double tuned mass damper
<b>SDTMDI</b>	Series-type double tuned mass damper with inerters
<b>SISO</b>	Single-input-single-output
<b>SMC</b>	Stability maximization criterion
<b>TET</b>	Targeted energy transfer
<b>TID</b>	Tuned inerter damper
<b>TMD</b>	Tuned mass damper
<b>TMDI</b>	Tuned mass damper with inerter
<b>UBB</b>	Uncertain-but-bounded

# Chapter 1

## Literature Review

Vibration control is a critical issue in numerous fields, e.g. mechanical, precision and civil engineering. Excessive vibrations in a structure could cause serviceability problems (such as discomfort for its occupants), accelerate its fatigue and reduces its operational time and life, or even worse, result in the structural failure.

Since the last century, vibration control strategies aiming at improving the structural behaviours under different dynamic loadings have been extensively investigated in the literature and successfully implemented in engineering applications. In general, they can be classified into three categories, passive, active and semi-active vibration control, in the chronological order. Passive control devices are intrinsically stable and their operation does not require energy supply, however, those resonant ones could be only effective at one dominant vibration mode, at which the control efficiency is only optimal for a specific dynamic loading. Meanwhile, active control devices can ensure a considerable effectiveness over a broadband frequency bandwidth under different dynamic loadings. However, they could destabilize the system due to the spillover effect or when a large controller gain is used, meanwhile, they present a greater complexity compared to the passive devices in that sensors, actuators and amplifiers are required and significant energy is indispensable in order to counteract external excitations. Finally, semi-active control devices are developed in the objective of combining the merits of their passive and active counterparts, i.e. the reliability, adaptivity and reduced demand for energy supply.

The shunt damping technique has emerged later as a direct consequence of the ever increasing demand for lightweight, flexible and elastic structures. Such a damping technique consists in integrating a smart material based transducer into the target structure and the electrodes of transducer are enclosed by a properly designed shunt impedance. The mechanical energy of structure is then converted into electrical energy via the electromechanical coupling and is subsequently dissipated through the resistive components in the external shunt circuit.

In this thesis, only literature on the passive and active vibration control will be reviewed in detail, followed by the state of the art of shunt damping techniques based on piezoelectric and electromagnetic transducers. In the end, a brief survey of

control strategies for simultaneous vibration mitigation and energy harvesting will be carried out.

## 1.1 Passive vibration control

### 1.1.1 Tuned mass damper

The first passive device for vibration damping was patented by Frahm [1] in 1911. As illustrated in Figure 1.1a, it is termed as tuned mass damper (TMD) or dynamic vibration absorber (DVA), which is actually a block mass installed on the structure to be controlled via a linear spring. Later, an additional viscous damper was introduced into the TMD by Den Hartog [2], forming the classic layout of mass-spring-damper. In this thesis, the difference between TMD and DVA will not be distinguished. Taking as an example a harmonically forced primary system of single degree of freedom (SDOF), the underlying dynamics of coupled system in Figure 1.1b can be described by the equations of motion (EOMs):

$$m_1\ddot{x}_1 = c_2(\dot{x}_2 - \dot{x}_1) + k_2(x_2 - x_1) - k_1x_1 + f(t) \quad (1.1a)$$

$$m_2\ddot{x}_2 = c_2(\dot{x}_1 - \dot{x}_2) + k_2(x_1 - x_2) \quad (1.1b)$$

where  $m_1$  and  $k_1$  are the mass and stiffness of primary system,  $m_2$ ,  $c_2$  and  $k_2$  are the mass, damping and stiffness of TMD.  $x_1$  and  $x_2$  are displacement of primary and tuned masses, respectively, and the dot over symbol stands for differentiation with respect to the time  $t$ . The primary system is harmonically forced at the angular frequency  $\omega$ . Clearly, Eq. (1.1) reduces to the dynamics of coupled system in Figure 1.1a when removing the damping  $c_2$ . In order to facilitate the following optimization procedure and analyses, the dynamics is nondimensionalized by introducing the dimensionless parameters as follows:

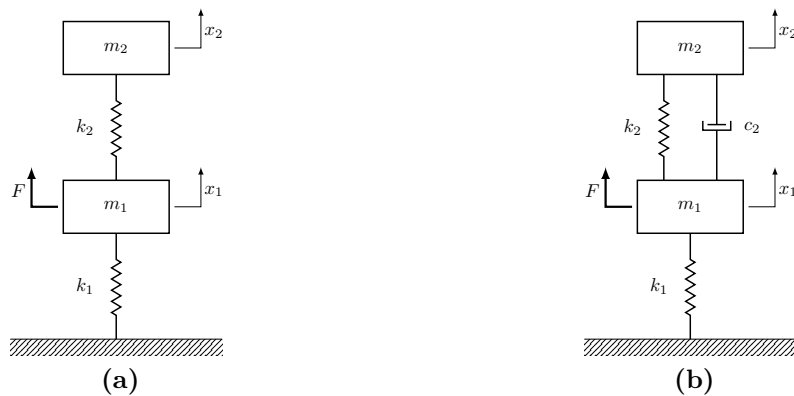


**Figure 1.1:** Schematic diagrams of an undamped SDOF primary system controlled by the TMD of: (a) Frahm; (b) Den Hartog.

$$\left\{ \begin{array}{l} \omega_1 = \sqrt{\frac{k_1}{m_1}}: \text{ Natural frequency of primary system} \\ \omega_2 = \sqrt{\frac{k_2}{m_2}}: \text{ Natural frequency of TMD} \\ \mu = \frac{m_2}{m_1}: \text{ The mass ratio between TMD and primary system} \\ \alpha = \frac{\omega_2}{\omega_1}: \text{ The frequency tuning ratio between TMD and primary system} \\ \xi = \frac{c_2}{2\sqrt{k_2 m_2}}: \text{ The mechanical damping ratio of TMD} \end{array} \right. \quad (1.2)$$

Besides, the time  $t$  is rescaled by  $\omega_1$ , yielding the dimensionless time  $\tau = \omega_1 t$ . One has the following relationship:

$$\frac{d}{dt} = \omega_1 \frac{d}{d\tau}, \quad \frac{d^2}{dt^2} = \omega_1^2 \frac{d^2}{d\tau^2}. \quad (1.3)$$

and the dimensionless excitation frequency is equal to:

$$\lambda = \frac{\omega}{\omega_1} \quad (1.4)$$

By substituting Eqs. (1.2) and (1.3) into (1.1), the EOMs can be recast into the dimensionless form:

$$x_1'' + 2\mu\xi\alpha(x_1' - x_2') + \mu\alpha^2(x_1 - x_2) + x_1 = f(\tau)/k_1 \quad (1.5a)$$

$$x_2'' + 2\xi\alpha(x_2' - x_1') + \alpha^2(x_2 - x_1) = 0 \quad (1.5b)$$

where the prime in the superscript denotes differentiation with respect to the rescaled time  $\tau$ . Hereafter, the complex magnitudes of displacement  $x_1$  and force  $f$  are denoted as  $X_1$  and  $F$ . Therefore, the displacement amplitude of primary system normalized by the static deformation  $F/k_1$ , termed as the normalized displacement frequency response function (FRF), can be formulated as:

$$G(\lambda) = \left| \frac{X_1}{F/k_1} \right| = \sqrt{\frac{(\alpha^2 - \lambda^2)^2 + 4\xi^2\alpha^2\lambda^2}{[(1 - \lambda^2)(\alpha^2 - \lambda^2) - \mu\alpha^2\lambda^2]^2 + 4\xi^2\alpha^2\lambda^2[1 - (1 + \mu)\lambda^2]^2}} \quad (1.6)$$

By setting  $\xi = 0$ , Eq. (1.6) describes the displacement amplitude in Figure 1.1a:

$$G(\lambda) = \left| \frac{X_1}{F/k_1} \right| = \sqrt{\frac{(\alpha^2 - \lambda^2)^2}{[(1 - \lambda^2)(\alpha^2 - \lambda^2) - \mu\alpha^2\lambda^2]^2}} \quad (1.7)$$

One can notice that if the natural frequency of TMD is tuned exactly the same as that of primary system, i.e.  $\alpha = 1$ , the vibration sustained by the primary system is completely attenuated at its resonant frequency, as demonstrated in Figure

1.2. However, there exist two significant peaks at the frequencies  $\lambda_1$  and  $\lambda_2$  in its displacement FRF, with its two resonant frequencies locating at:

$$\lambda_1 = \sqrt{\frac{\mu + 2 - \sqrt{\mu^2 + 4\mu}}{2}}, \quad \lambda_2 = \sqrt{\frac{\mu + 2 + \sqrt{\mu^2 + 4\mu}}{2}}. \quad (1.8)$$

Clearly, the frequency bandwidth between  $\lambda_1$  and  $\lambda_2$  is only dependant of the

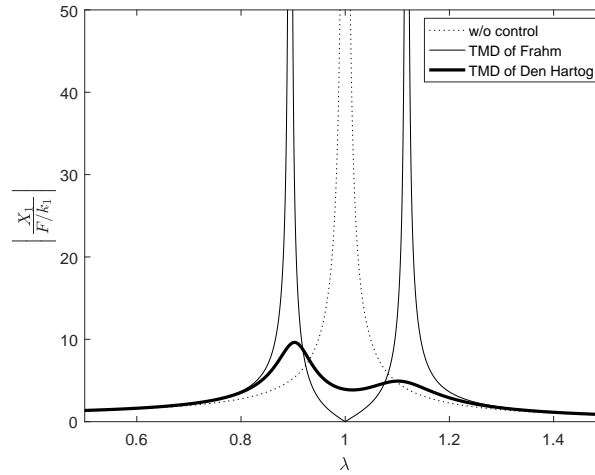


**Figure 1.2:** Comparison of displacement FRFs of primary system without any control (dotted line) or coupled with a TMD of either Frahm (thin solid line) or Den Hartog (thick solid line). The mass ratio  $\mu$  is of 5%, the frequency tuning ratio  $\alpha$  is set as unity and the mechanical damping ratio is equal to 0.1.

mass ratio  $\mu$ , which is generally small due to physical restrictions. Therefore, the TMD of Frahm is only effective in a narrow region around its resonant frequency, while it could amplify the vibration of primary system in the case of detuning. In the contrary, Figure 1.2 suggests that the presence of viscous damper in TMD can effectively reduce the peak vibration amplitude in the whole frequency range to the detriment of vibration cancellation performance at the resonance.

The TMD of Den Hartog is widely used in engineering applications due to its passivity, simplicity and effectiveness [3]. For the purpose of maximizing its control efficiency, numerous researches have been conducted in the literature and various optimization criteria have been proposed for different design objectives. A brief review on this subject is provided below.

#### 1.1.1.1 $H_\infty$ optimization criterion

Proposed by Den Hartog [2], the first design objective of TMD is to minimize the peak displacement amplitude of primary system in the whole frequency range,

namely the  $H_\infty$  norm of its displacement FRF. Indeed, such a  $H_\infty$  optimal design could be posed as a min-max optimization problem, whose objective function is formulated as:

$$\min_{\alpha, \xi} \left\{ \max_{\lambda_r} \left\{ \|G(\mu, \alpha, \xi, \lambda)\|_\infty \right\} \right\} \quad (1.9)$$

subject to:

$$\alpha \geq 0, \quad \xi \geq 0, \quad \lambda \in \mathbb{R}^+. \quad (1.10)$$

where  $\lambda_r$  corresponds to the abscissa of resonance peak, at which the partial derivative of  $G(\lambda)$  with respect to  $\lambda$  is zero, i.e.:

$$\left. \frac{\partial G(\lambda)}{\partial \lambda} \right|_{\lambda=\lambda_r} = 0 \quad (1.11)$$

Therefore, the  $H_\infty$  optimal parameters of TMD, frequency tuning ratio  $\alpha$  and mechanical damping ratio  $\xi$ , can be determined by numerically solving the min-max problem (1.9) in conjunction with the equality constraint (1.11).

Although such a numerical approach can yield exact solutions, it is inefficient to some extent. For example, multiple iterations may be required to yield the optimal values, meanwhile, they correspond exclusively to a specific mass ratio  $\mu$ . To this end, analytical strategies have been developed in the literature so as to derive closed-form formulae for all tuning parameters. It is worth noting that the majority of research works on the analytical design have been carried out under the assumption of an undamped primary system.

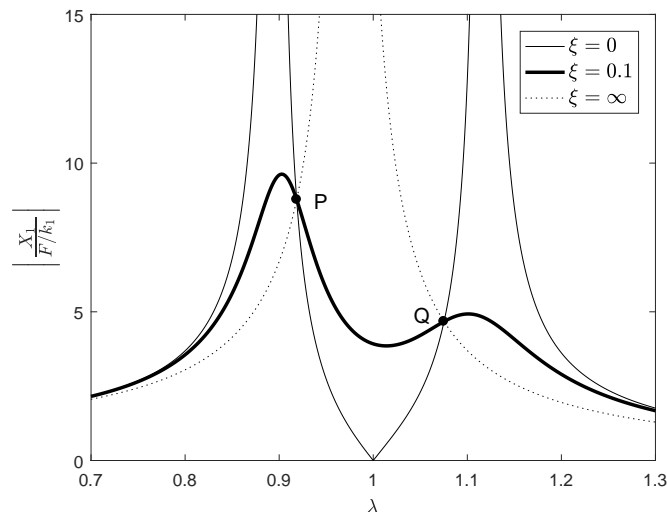


**Figure 1.3:** The phenomenon of fixed points. The parameters other than  $\xi$  are set as:  $\mu = 5\%$ ,  $\alpha = 1$ .

- **Fixed points theory.** The first analytical method to solve the  $H_\infty$  optimization problem is the well-known fixed points theory (FPT) proposed by Den Hartog [2]. This heuristic method is based on the phenomenon that irrespective of the damping values of TMD, the displacement FRF of undamped primary system always passes through two invariant positions  $P$  and  $Q$ , as depicted in Figure 1.3, which are the so-called fixed points. Therefore, the FPT consists in tuning the TMD by equalizing the vibration amplitudes at all invariant points and subsequently by making the displacement FRF passing through them horizontally. Hence, it is also termed as the equal-peak method. Obviously, this analytical approach only yields approximate solutions to the  $H_\infty$  optimization problem, since it works on the invariant points instead of resonance peaks.
- **Algebraic approach.** The exact solutions to the  $H_\infty$  optimization problem could be analytically derived via the entirely algebraic approach developed by Nishihara and Asami [4]. Instead of manipulating the fixed points, they directly worked on the resonance points. By taking the peak amplitude as a design parameter, the displacement FRF of primary system can be transformed into a resultant polynomial as a function of three design parameters: the mechanical damping ratio  $\xi$ , the frequency tuning ratio  $\alpha$  and the peak amplitude. Two optimality conditions can be achieved by factorizing the resultant polynomial into the form of two double roots (corresponding to two resonance points), and the third optimality condition is retained due to the algebraic property of polynomial, i.e. multiplicity of roots. Finally, analytical formulae of design parameters can be achieved by solving simultaneously all three optimality conditions.

The comparison between two analytical approaches implies that the FPT could yield highly accurate solutions to the  $H_\infty$  optimization problem. Due to its simplicity and applicability, the FPT is still widely adopted for optimal tuning of various dampers.

### 1.1.1.2 $H_2$ optimization criterion

When the primary system is randomly excited, a new performance index is defined as the mean square value of a specific motion variable (displacement, velocity or acceleration). Clearly, the objective function is proportional to the area under the FRF curve of the relevant motion. When the mean square displacement of primary system is to be minimized, it is equivalent to minimize the total vibration energy of primary system over the whole frequency range. Warburton [5] derived optimal parameters of TMD when the mean square displacement and velocity of primary system are to be minimized. Asami et al. [6] considered the optimal design for minimizing the mean square acceleration of seismically excited primary system.

### 1.1.1.3 Stability maximization criterion

Apparently, both  $H_\infty$  and  $H_2$  optimization criteria aim at improving the frequency response in the steady state. When the transient response of primary system is to be improved, one should tune the damper according to the stability maximization criterion (SMC). This tuning strategy was first proposed by Yamaguchi [7] who stated that the transient vibration is attenuated in the shortest duration when the logarithmic decrements are maximized. It was later pointed out by Nishihara and Matsuhisa [8] that the design objective is fulfilled if the whole system (i.e. primary system coupled with the TMD) has two coalesced pairs of conjugate eigenvalues.

### 1.1.1.4 Other optimization criteria

The  $H_\infty$ ,  $H_2$  and SMC optimization criteria are the most widely used for optimally tuning the dampers. Meanwhile, there exist other optimization criteria in the literature, which have been proposed for specific engineering applications.

For machining processes, the tuning requirements of TMD differ from the afore-said vibration problems. In the objective of improving the chatter stability and enhancing the vibration suppression, Sims [9] proposed that the TMD should be optimized by minimizing the positive real part of FRF or maximizing the negative real part of FRF. An analytical approach based on the methodology of fixed points was developed, which consists in tuning the TMD in such a way that the positive or negative real parts of FRF have equal real peaks or troughs, respectively.

Zilletti et al. [10] proposed a new tuning criterion, aiming at maximizing the power dissipated by the TMD. It was stated that for a damped primary system, the power injected into the system is solely controlled by the primary mass, therefore, the maximization of power absorbed by the TMD is fulfilled when the kinetic energy of host structure is minimized.

Aforementioned criteria are dedicated to optimization of TMD in the deterministic scenario. Dell'Elce et al. [14] considered the case where the mechanical stiffness of primary system is uncertain-but-bounded (UBB), and proposed the so-called robust equal-peak method. This novel strategy consists in tuning the parameters of TMD in the worst-case scenario, according to which the vibration amplitudes at the leftmost and rightmost fixed points should be equalized in the displacement FRF of primary system.

Viguié and Kerschen [15] proposed a tuning methodology for controlling the vibration of a nonlinear primary system by using a nonlinear vibration absorber (NL-VA), and stated that the NL-VA should possess the same frequency-energy plot as the nonlinear primary system. Later, Habib et al. [16] generalized the Den Hartog's equal-peak method to address the optimization problem of NL-VA for a Duffing mechanical system. Recently, Sun et al. [17] further extended to the case of a more complex primary system with multiple terms of nonlinearity, and a more accurate design method for optimizing the NL-VA was developed based on the nonlinear perturbation theory and bifurcation theory.

Strategy	Frequency tuning ratio $\alpha$	Mechanical damping ratio $\xi$	References
FPT	$\frac{1}{1+\mu}$	$\sqrt{\frac{3\mu}{8(1+\mu)}}$	Den Hartog [2]
$H_\infty$	$\frac{2}{1+\mu} \sqrt{\frac{216+23\mu+9\mu^2+2(2+\mu)\sqrt{4+3\mu}}{64+80\mu+27\mu^2}}$	$\sqrt{\frac{8+9\mu-4\sqrt{4+3\mu}}{16(1+\mu)}}$	Nishihara and Asami [4]
$H_2$	$\frac{1}{1+\mu} \sqrt{\frac{2+\mu}{2}}$	$\sqrt{\frac{\mu(4+3\mu)}{8(1+\mu)(2+\mu)}}$	Warburton [5]
SMC	$\frac{1}{1+\mu}$	$\sqrt{\frac{\mu}{1+\mu}}$	Yamaguchi [7]

**Table 1.1:** Closed-form formulae for optimal parameters of traditional TMD attached to a SDOF undamped primary system under force excitation. Four optimization criteria are considered: FPT,  $H_\infty$  and  $H_2$  optimization criteria and SMC.

Strategy	Frequency tuning ratio $\alpha$	Mechanical damping ratio $\xi$	References
FPT	$\frac{1}{\sqrt{1-\mu}}$	$\sqrt{\frac{3\mu}{4(2-\mu)}}$	Ren [11]
$H_2$	Value as large as possible	$\sqrt{\frac{\alpha^4+(\mu-2)\alpha^2+1}{4\alpha^2}}$	Cheung and Wong [12]
SMC	$\frac{1-\sqrt{1-4\mu}}{2\mu}$	$\sqrt{\frac{1-\sqrt{1-4\mu}}{2}}$	Xiang and Nishitani [13]

**Table 1.2:** Closed-form formulae for optimal parameters of non-traditional TMD attached to a SDOF undamped primary system under force excitation. Three optimization criteria are considered: FPT,  $H_2$  optimization criterion and SMC.

### 1.1.2 Non-traditional TMD

In 2001, Ren [11] proposed a variant design for the TMD of Den Hartog. Termed as the non-traditional TMD, its tuned mass  $m_2$  is linked to the host structure via the spring  $k_2$  solely, meanwhile, it is connected to the base by the viscous damper  $c_2$ , as illustrated in Figure 1.4.

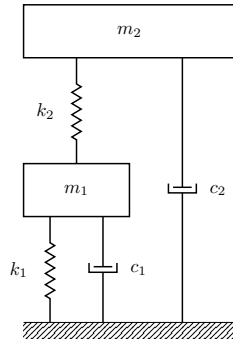


**Figure 1.4:** Schematic diagram of an undamped SDOF primary system controlled by a non-traditional TMD.

Its optimal design has been carried out according to the FPT [11, 18],  $H_2$  optimization criterion [12] and SMC [13, 19]. To this end, analytical formulae for optimal parameters of traditional and non-traditional TMD are summarized in Tables 1.1 and 1.2 according to several aforementioned optimization criteria.

It was demonstrated that the non-traditional layout is slightly more effective than the classic TMD, as reflected by the smaller peak amplitude or mean square value of displacement for the primary system as well as the smaller stroke for the damper. Xiang and Nishitani [13] stated that the non-traditional TMD could be applied to base-isolated structures or central column-equipped high-rise structures with a larger value of permissible mass ratio.

### 1.1.3 Multiple TMDs

Both classic and non-traditional TMDs are effective within a narrow region around the vibration mode of interest. Meanwhile, their effectiveness would be significantly deteriorated when the resonant frequency of structure fluctuates and/or the damping of TMD is detuned.

In order to improve the effectiveness and the robustness, Xu and Igusa [20] proposed to control the vibration of structure by employing multiple TMDs (MTMD) arranged in parallel, as illustrated in Figure 1.5, whose natural frequencies are linearly distributed around the resonant frequency of structure. Following this seminal work, numerous researches have been conducted in the literature, to name a few, Yamaguchi and Harnpornchai [21], Abé and Fujino [22], Jangid [23], Li [24, 25] and Hoang and Warnitchai [26]. Among them, Li [25] investigated the effectiveness of

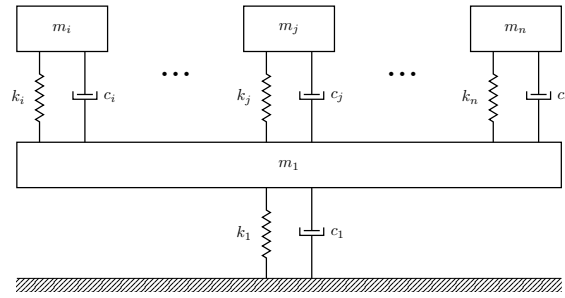


**Figure 1.5:** Schematic diagram of a SDOF primary system controlled by the multiple TMD.

five models of MTMD, which represent five types of combinations of the tuned mass, stiffness and damping values. A conclusion has been therein drawn that in terms of the effectiveness and robustness as well as better constructability, the most preferable model for the MTMD is that all TMD units have the same values of stiffness and damping, while their tuned masses vary. The main differences among these previous works reside in: types of excitation (base or force, harmonic or random), constraints on parameters of each TMD (uniformly or linearly distributed), design objectives (maximum or mean square value of displacement or acceleration) and design methodologies (numerical or analytical). Recently, Kim and Lee [27] provided a general design guide for linear MTMDs in the case of a SDOF primary system under white noise excitation of acceleration type. They validated the remark made by Li [25] that one should use the same spring and damper for each TMD unit in order to achieve a better effectiveness as well as the reduction in the number of design variables. Finally, approximate formulae for optimal parameters were also provided in [27] for the most preferable model of MTMD.

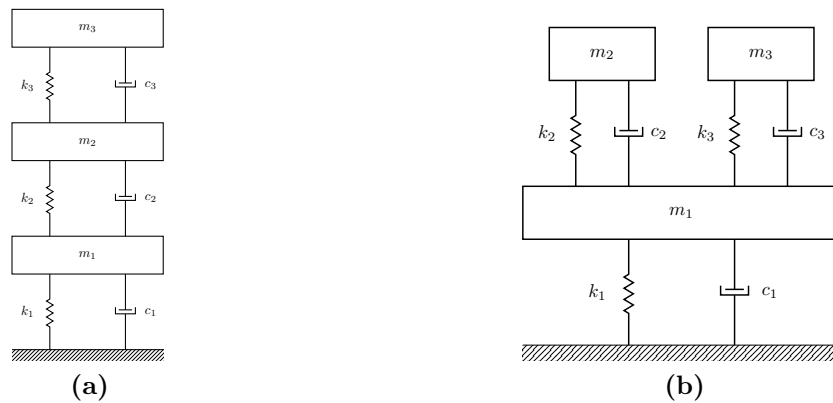


**Figure 1.6:** Schematic diagrams of a SDOF primary system controlled by a: (a) series DTMD; (b) parallel DTMD.

A particular configuration of MTMD is the double TMD (DTMD) arranged either in series or in parallel, as depicted in Figure 1.6. In 2006, Li and Zhu [28]

carried out numerical optimization of the series DTMD attached to a SDOF primary system whose natural frequency is constant or fluctuating. It suggested that the TMD adjacent to the host structure has a much larger mass than the another TMD and the larger TMD should have no damping in the optimal scenario. Besides, it was shown that the series DTMD has the same effectiveness and robustness as the MTMD composed of 5 TMD units in parallel against the detuning effect caused by the drifting of natural frequency, meanwhile it is much more robust than the classic TMD. Later, Zuo [29] adopted the decentralized  $H_\infty$  and  $H_2$  control methods to determine optimal parameters of series DTMD for controlling a SDOF undamped primary system under harmonic and random vibration, respectively. Zuo [29] concluded that the series DTMD is more effective and more robust than the classic TMD, the viscoelastic TMD and the parallel DTMD. Recently, Asami [30] considered the optimal tuning of both series and parallel DTMDs according to three strategies: the  $H_\infty$  and  $H_2$  optimization criteria and the SMC. Optimal parameters based on each optimization criterion were approximately formulated in terms of the mass ratio  $\mu$  with a two-digit accuracy. More recently, Asami et al. [31] analytically derived the exact solutions to the same problem in [30] in the objective of minimizing the mobility transfer function. It was confirmed in [31] that optimality conditions to the  $H_\infty$  optimization of DTMD can be achieved by imposing as zero all minor determinants of the Jacobian matrix related to the coupled system. Meanwhile, such a matrix could be formulated by following the algebraic approach developed by Nishihara and Asami [4]. Finally, these optimality conditions are simultaneously solved by applying the Newton-Raphson method with the  $H_2$  optimal solutions taken as initial values. Although the algebraic approach in [31] could yield exact solutions to the  $H_\infty$  optimization of DTMDs, the derivation process is very sophisticated and the computing cost is huge.

#### 1.1.4 Multiple-DOF TMD

Although a significant improvement in effectiveness and robustness could be achieved, the MTMD may be unsuitable for applications where a limited space is available for accommodating the control device, e.g. a cutting tool embedded with damper. Meanwhile, for all previously reviewed dampers, only the translational DOF is employed to mitigate the translational vibration mode of primary system. To this end, Zuo [32] proposed the concept of multiple-DOF TMD, which could utilize multiple DOFs of a single TMD to damp single or multiple vibration modes of the host structure.

As shown in Figure 1.7, a SDOF primary system controlled by a two-DOF TMD (i.e. translational plus rotational) was investigated by Zuo [32] and its optimal design under harmonic and random excitation was carried out by using the decentralized  $H_\infty$  and  $H_2$  optimization methods, respectively. It was demonstrated that the two-DOF TMD leads to the smallest peak vibration amplitude and mean square displacement when compared to the classic SDOF TMD and the parallel-

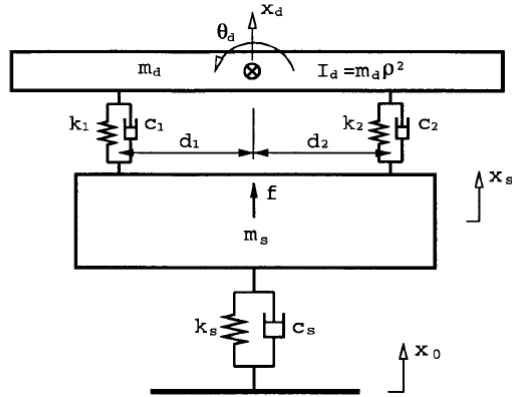


**Figure 1.7:** A SDOF primary system controlled by a two-DOF TMD [32].

type DTMD. The same coupled system was later considered by Jang et al. [33], in which a simple analytical method was proposed to optimize the two-DOF TMD. Jang et al. [33] observed that for different damping levels, the displacement FRFs of undamped primary system always intersect at four invariant positions, implying the existence of four fixed points. Following the methodology of fixed points, a first polynomial function of order 4 in the squared excitation frequency could be achieved. Another fourth-order polynomial was formulated by taking the vibration amplitude at fixed points as design parameters. Consequently, comparing the coefficients of previous two polynomials culminates into four proportional relationships, from which the optimal stiffness and mass distribution can be easily determined. Meanwhile, the optimal value of damping element was numerically solved in [33]. More recently, Ma et al. [34] stated that the maximum available DOFs of TMD for controlling a translational mode are three, which are one translational and two rotational DOFs. A general routine was proposed for the deterministic design of multiple-DOF TMD suppressing single vibration mode, and the  $H_\infty$  optimal design of the three-DOF TMD was numerically addressed via a simulated annealing algorithm. Experimental results demonstrated that the three-DOF TMD can reduce the vibration amplitude of uncontrolled primary system by 86.5% and improve the control performance by 29.5% with respect to that of two-DOF TMD with same mass. Finally, other researches on multiple-DOF TMDs can be referred to [35, 36, 37, 38].

### 1.1.5 Inerter

In 2002, Smith [39] introduced a new mechanical element called the inerter, which allows electrical circuits to be translated over to mechanical ones in a completely analogous way.

As depicted in Figure 1.8, an ideal inerter is a two-terminal and one-port mechanical device, being capable of engendering a resisting force proportional to the

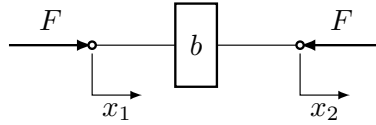


**Figure 1.8:** Schematic diagram of an inerter element.

relative acceleration of its two nodes, i.e.:

$$F = b(\ddot{x}_1 - \ddot{x}_2) \quad (1.12)$$

where the proportionality gain  $b$  is termed as inertance having the same unit as a mass. A key feature of inerter is that its physical mass should be small and is independent of its generated inertance.

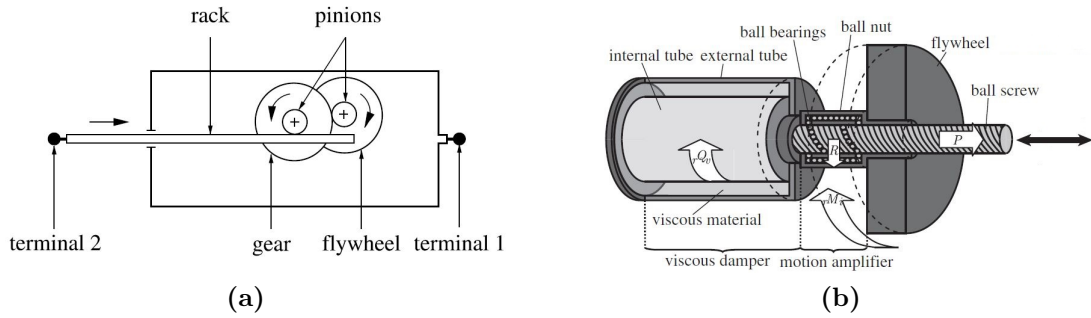


**Figure 1.9:** Realization mechanisms of inerter: (a) rack and pinion [40]; (b) ball and screw [41].

The first mechanism of realizing an inerter was proposed in [39], which is essentially a two-terminal flywheel driven by a rack, pinion and gears, as shown in Figure 1.9a. A prototype was fabricated and tested by Smith and Wang [40], revealing its potential benefits in passive vehicle suspension. An alternative approach is to employ a ball screw mechanism [41]. As illustrated in Figure 1.9b, the ball screw can translate the linear motion to the high-speed rotation of flywheel, thereby generating a large apparent mass.

In what follows, three passive control devices involving inerters will be briefly reviewed, which are the tuned inerter damper, the tuned mass damper with inerter and the inerter-based dynamic vibration absorber, respectively.

### 1.1.5.1 Tuned inerter damper

Considering the similarity between a mass and an inerter, Lazar et al. [43] proposed the tuned inerter damper (TID) by replacing the mass element of classic TMD with an inerter. Due to the two-terminal property of inerter, the TID can be installed between two storeys for mitigating the vibration of civil structures, as shown in Figure 1.10. It was stated in [43] that for a SDOF primary system, the TID and TMD

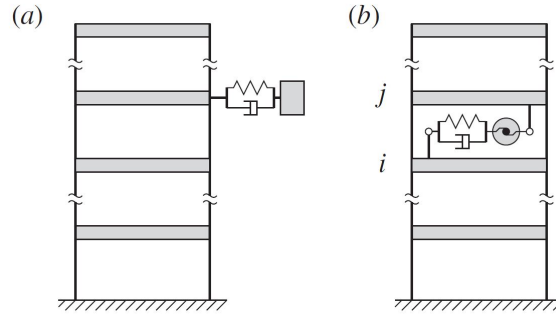


**Figure 1.10:** A civil structure installed with either a TMD or a TID [42].

with the same apparent mass have almost identical vibration control performance, while the small weight and overall size of TID makes it an attractive alternative to the TMD. Besides, Lazar et al. [43] also remarked that for a MDOF system, e.g. a building of multiple storeys, the best control efficiency of TID is obtained when it is installed at the bottom storey with its inerter grounded. It is very attractive since no additional load will be imposed on the structure.

Recently, Gonzalez-Buelga et al. [44] proposed the synthesis of TID by means of an electromagnetic shunt damper connected with a series resonant shunt circuit. A test rig was built and experimental results demonstrated its effectiveness in terms of vibration suppression and self-sufficiency via energy harvesting.

### 1.1.5.2 Tuned mass damper with inerter

Unlike a TID which replaces the mass of TMD with an inerter, Marian and Giaralis [45] incorporated an inerter between the tuned mass and the ground, as shown in Figure 1.11. Such a new control device is termed as the tuned mass damper with inerter (TMDI).

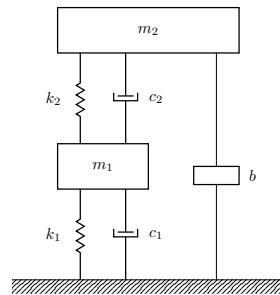


**Figure 1.11:** Schematic diagram of a SDOF primary system controlled by a TMDI.

Closed-form solutions to optimal parameters of TMDI were formulated in [45] for an undamped SDOF primary system under white noise base acceleration excitation. The authors concluded that the inclusion of an inerter can either replace part of the tuned mass for lightweight applications, or improve the control performance for a

given tuned mass. Later, Marian and Giaralis [46] reconsidered the optimization of TMDI under harmonic vibration and optimal parameters were analytically derived by using the FPT. It was suggested from [46] that in both cases of force and base excitation, increasing the inertance leads to the decrease of peak vibration amplitude of primary system, thereby improving the control performance and enhancing the robustness against detuning effect or parametric uncertainty. Giaralis and Petrini [47] further investigated the performance of TMDI on suppressing the excessive wind-induced vibration in a 74-storey building, as shown in Figure 1.12. With the tuned mass connected to the top floor and the inerter linked to the penultimate or a lower floor, it was observed that compared to a TMD of same weight, the TMDI can reduce the peak top-floor acceleration more effectively when the tuned mass is relatively small and the inerter is linked to a much lower floor, i.e. spanning as many storeys as possible. Besides, the inclusion of inerter can significantly reduce the stroke of TMD, thereby facilitating its implementation in environments with a small clearance.

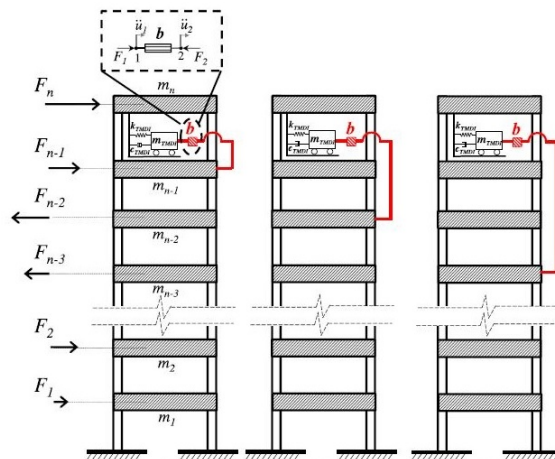


**Figure 1.12:** Wind-induced vibration mitigation of a multi-storey building by means of a TMDI [47]. The TMD is connected to the top floor, while the inerter is linked to the penultimate or a lower floor.

Apart from the classic TMD, Wang et al. [48] also carried out the optimization of non-traditional TMD and viscoelastic TMD with either a grounded inerter or an inerter inserted between the tuned mass and host structure. In general, the inclusion of a grounded inerter can enhance the vibration control performance, however, inserting an inerter between the primary and tuned masses will amplify the vibration amplitude of host structure. Nevertheless, the inserted configuration could be beneficial in specific applications. Chen et al. [49] reported that for a MDOF vibrating system with inerters inserted between any two adjacent lumped masses, increasing the inertance of any inerter can reduce natural frequencies of coupled system. Based on this property, Zilletti [50] used an inerter to relate the proof mass of inertial actuator and the host structure so as to reduce the natural frequency of actuator,

entailing a better stability for the feedback loop and an improved performance.

### 1.1.5.3 Inerter-based dynamic vibration absorber

In 2015, Hu et al. [51] proposed to isolate the vibration of a target structure by incorporating an inerter-based mechanical network between the object and its supporting foundation. An inerter-based mechanical network is actually a mixed connection of an inerter, a spring and a viscous damper. Various configurations of inerter-based isolator were investigated and their optimization was conducted according to the FPT and  $H_2$  optimization criterion successively. Numerical analyses demonstrated the superior performance of inerter-based isolator compared to the TMD under both harmonic and random excitation, meanwhile, no additional mass should be mounted on the target structure. Later, Hu et al. [52] proposed a novel control device termed as inerter-based dynamic vibration absorber (IDVA), which is built by replacing the viscous damper of classic TMD with an inerter-based mechanical network. The  $H_\infty$  and  $H_2$  optimization problem of IDVA installed on a SDOF undamped primary system was numerically solved and it implied that the vibration control performance of an IDVA can be superior to that of a TMD only if the IDVA possesses more DOFs than the TMD. Besides, it was shown that the IDVA with a series connection of an inerter, a spring and a damper (shown in Figure 1.13) always has the best  $H_\infty$  and  $H_2$  control performance within the interval of mass ratio  $\mu \in [0, 1]$ .

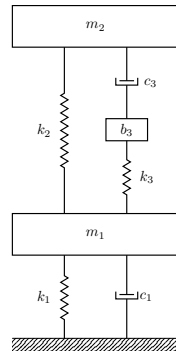


**Figure 1.13:** Schematic diagram of a SDOF primary system controlled by an IDVA.

In light of the introduction of an additional DOF by the inerter-based mechanical network, the coupled system shown in Figure 1.13 has three DOFs and there exists four invariant points in its displacement FRF instead of two. The number of design parameters increases from 2 to 4, therefore, the classic FPT cannot be directly used to conduct approximate solutions to the  $H_\infty$  optimal design of IDVA. Recently, Barredo et al. [53] developed an extended version of FPT, with which the multi-variable optimization problem could be solved efficiently and the closed-form expressions to optimal parameters could be analytically derived. This extended version of FPT is actually based on the method proposed by Jang et al. [33], with which the optimal value of stiffness and inertance can be easily obtained, leaving only the

damping to be determined numerically. On this basis, Barredo et al. [53] proposed that the optimal damping should be chosen as the root mean square (RMS) value of damping levels evaluated at three reference frequencies, the concept of which was initiated by Krenk and Høgsberg [54] for the purpose of flattening the plateau within the fixed points in the displacement FRF curve.

### 1.1.6 Negative stiffness mechanism

The single-axis passive vibration isolation is usually realized by employing a linear viscous damper or a Maxwell damping unit, which is placed between the structure to be isolated and its support [55]. With a conventional linear isolator, the vibration can be completely attenuated when the excitation frequency is beyond  $\sqrt{2}$  times the structural resonant frequency. Hence, reducing the dynamic stiffness of system can broaden the frequency range of vibration isolation, however, the static stiffness of structure should be sufficiently large in avoidance of an excessive static deformation and system instability. Therefore, an ideal isolator should possess both characteristics of high static stiffness and low dynamic stiffness. Such a high-static-low-dynamic (HSLD) stiffness feature could be realized by arranging in parallel a negative stiffness mechanism (NSM) and the support stiffness of controlled structure.

The NSM is featured by a force-displacement curve with a negative slope, signifying that a NSM can generate a force to assist its motion instead of resisting it. The first approach to realize a NSM is to exploit the benefit of buckling of beam-column, which was first proposed by Platus [56]. Later, geometrical nonlinearity is utilized to yield the HSLD or quasi-zero-stiffness (QZS) characteristics, and a common configuration is that two linear mechanical elements are positioned symmetrically with respect to the translational direction of structure. Relevant researches could be categorized into the use of: linear springs (Carrella et al. [57] and Gatti et al. [58]), linear bars (Yang et al. [59]) and linear bars hinged with springs moving perpendicular to the structural motion (Le and Ahn [60, 61, 62] and Wang et al. [63]). The last category of NSM is based on the magnetic repulsion and attraction and related references are referred to [64, 65, 66, 67, 68].

Clearly, most NSMs in aforementioned researches are passive and nonlinear. A convenient approach to realize a linear NSM was proposed and experimentally validated in [69] by using an active control technique with a linear actuator. To summarize, the NSM has widespread application in ameliorating the vibration isolation performance, however, only few studies on enhancing the control effect of DVAs via negative stiffness are available in the literature, as reported below.

Shen et al. [70] first proposed the concept of DVA with negative stiffness (NS-DVA), which was established by incorporating a negative stiffness between the base and the mass of non-traditional DVA. Its optimization according to the FPT was carried out for a SDOF primary system, suggesting that the use of negative stiffness decreases the peak vibration amplitude of primary system and broadens the frequency range of vibration absorption. Similarly, the NSDVA based on the DVA

of Den Hartog was studied by Antoniadis et al. [71], however, the optimal damping value of absorber had not been provided. Later, Huang et al. [72] also addressed the optimal tuning of traditional NSDVA attached to a SDOF primary system, while the optimal damping value of absorber was derived according to the equal damping criterion proposed in [54]. It should be noted that this criterion yielded a larger damping value for DVA and a larger peak amplitude for primary system when compared to the case optimized by the FPT. Finally, Xiuchang et al. [73] carried out the optimal design of traditional NSDVA in terms of controlling the force transmitted to the rigid foundation. The intentional introduction of a grounded negative stiffness into both DVAs does contribute to the improvement of vibration control performance, meanwhile, the coupled system could be potentially destabilized. Nevertheless, the crucial stability analysis and the permissible interval of negative stiffness had not been addressed in aforesaid works and the NSDVAs had been optimized only in terms of suppressing harmonic vibration. Finally, a simple approach for the practical realization of linear NSDVA is still lacking in the literature.

### 1.1.7 Other passive damping mechanisms

Except for aforementioned damping techniques, there exist other passive mechanisms of energy dissipation in the literature, as follows:

- Friction damper [74];
- Eddy current damper [75];
- Constrained layer damping [76];
- Targeted energy transfer (TET): nonlinear energy sink (NES) [77];
- Energy absorption through liquid: tuned liquid damper [78], tuned liquid column damper [79];
- Energy absorption through impact: pounding TMD [80], particle damper [81], asymmetric and symmetric vibro-impact NES [82, 83].

## 1.2 Electromechanical shunt damper

Lightweight solutions for vibration control are of paramount importance in certain engineering applications, e.g. aerospace structures. Such an increasing demand leads to the emergence of various shunt damping techniques, which consist in transforming the mechanical energy of target structure into electrical one via a transducer and subsequently dissipate it in the external shunt circuit. Common transduction mechanisms include: piezoelectric, electromagnetic and electrostatic. This thesis focuses on the applications of piezoelectric and electromagnetic transducers, which will be

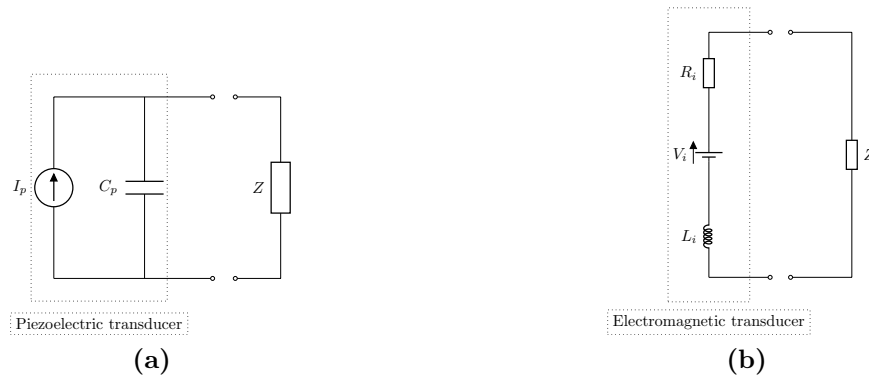


**Figure 1.14:** Electrical models of: (a) piezoelectric transducer; (b) electromagnetic transducer.

briefly reviewed at below. The electrical models of these two types of transducers are schematized in Figures 1.14a and 1.14b, respectively.

### 1.2.1 Piezoelectric shunt damper

In 1979, Forward [84] experimentally demonstrated the feasibility of attenuating mechanical vibrations in optic systems by means of a piezoelectric shunt damper (PSD). In 1991, Hagood and von Flotow [85] established the models of PSD enclosed by two types of circuits, resistive (R) and resistive-inductive in series (series RL), as shown in Figures 1.15a and 1.15b, respectively. The shunt parameters were tuned according to the transfer function technique (i.e. the FPT) and the pole placement technique (i.e. the SMC), respectively, and the proposed models were experimentally validated on a cantilever beam. Following this pioneering work, Wu [86] investigated the parallel arrangement of resistor and inductor (parallel RL), as depicted in Figure 1.15c. A practical limit of typical series or parallel RL networks resides in the requirement of large inductance (up to thousands of henries), which should be either electrically synthesized [87] or generated by closed magnetic cores made of high permeability materials [88]. Fleming et al. [89] pointed out that the required inductance can be reduced by placing an additional positive capacitance across the terminals of piezoelectric transducer. Caruso [90] carried out the comparison of optimal performance delivered by three shunt circuits, series RL, parallel RL and series RL in parallel with a positive capacitor (RLC parallel, shown in Figure 1.15d). It was demonstrated that the series and parallel RL networks have the quasi identical effectiveness, meanwhile the control performance delivered by the RLC parallel circuit turns inferior to that of series RL network as if a positive parallel capacitance is involved. Recently, Soltani et al. [91] derived exact solutions to the  $H_\infty$  optimal design of PSD enclosed by a series RL shunt based on the algebraic approach proposed in [4]. In summary, all these passive shunts can effectively attenuate the vibration around the target mode, however, they are sensitive to parametric

detuning and the control effect on other modes is negligible.

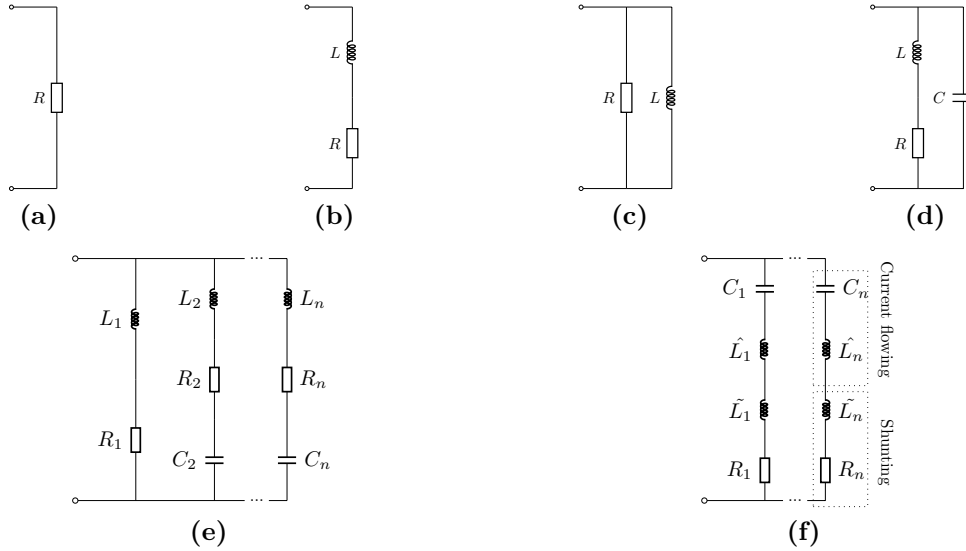


**Figure 1.15:** (a) R shunt; (b) series RL shunt; (c) parallel RL shunt; (d) RLC parallel shunt; (e) multi-mode shunt proposed by Hollkamp [92]; (f) Current flowing shunt circuit proposed by Behrens et al. [93].

Hollkamp [92] proposed the first shunt design for multi-mode vibration control, which is composed of multiple branches of series RLC whose number is equal to that of modes to be damped, as shown in Figure 1.15e. Its effectiveness was experimentally validated, however, the tuning of each resonant branch is not independent so that it is impossible to derive analytical formulae for all tuning parameters when a large number of modes are of interest. Behrens et al. [93] developed the current-flowing shunt technique, consisting in relating each branch to a particular vibration mode so as to tune each branch independently. As depicted in Figure 1.15f, the multi-mode shunt circuit proposed in [93] distinguishes from that of Hollkamp in such a way that each circuit branch is functional at its corresponding resonant frequency, while it is approximately open-circuited at other frequencies. Finally, an adaptive current-flowing shunt damping was introduced in [94], which investigated the online optimal tuning of component values in the presence of shift in structural resonant frequency and variation in transducer capacitance.

Meanwhile, negative capacitance could be also included in electrical networks to improve the damping performance at multiple modes, as reported below.

Tang and Wang [95] added a series negative capacitance (NC) in the shunt circuit of various active-passive hybrid piezoelectric networks. It was found that adding a NC can enhance the electromechanical coupling of integrated system, increase the system damping capability and significantly improve the overall control authority. Later, Behrens et al. [96] proposed an active shunt damping technique based on the NC controller, which was proven to be capable of damping multiple vibration modes and to be less sensitive to environmental variations. Neubauer et al. [97] carried

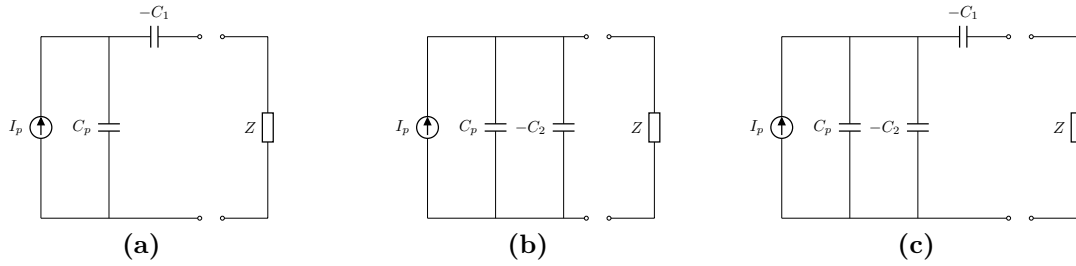


**Figure 1.16:** Employment of NCs in PSD: (a) series layout; (b) parallel layout; (c) SP layout.

out the optimal design of various electrical networks with a series NC based on the FPT, in which the permissible bound on NC and the vibration amplitudes at fixed points are concisely formulated in terms of the electromechanical coupling coefficient. In 2016, Berardengo et al. [98] developed a general analytical formalism for three layouts based on resistive (R) shunts: with one NC in series; with one NC in parallel; with one NC in series to the R load while another NC placed across the piezoelectric transducer (denoted as SP layout), as depicted in Figure 1.16. In this way, the change made to the electromechanical coupling by the NCs can be expressed solely in terms of ratios among NCs and the piezoelectric capacitance. It was numerically and experimentally validated that the main effect of NCs is to artificially enhance the electromechanical coupling, thereby improving the damping performance and leading to a broadband vibration attenuation, and the SP layout can further enhance the electromechanical energy transfer compared to its counterparts with only one NC. Pohl [99, 100] considered the potential saturation of NC under high vibration levels and proposed to improve the damping performance of NC by enlarging the output voltage of the operational amplifier.

Practical applications of PSD cover: chatter reduction [101], acoustic radiation reduction [102], vibration suppression of actuator arm in hard disk drive [103], vibration damping of rotationally periodic structures [104], etc.

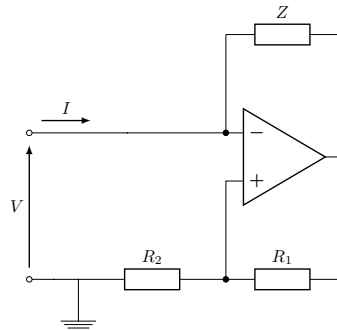


**Figure 1.17:** A negative impedance converter.

As shown in Figure 1.17, a negative impedance converter (NIC) can be used to

synthesize the NC. Due to its requirement of energy input, employing a NC in the shunt impedance is actually a semi-active shunt damping technique. Nevertheless, all shunt designs with NCs in aforementioned researches are passive in nature since no feedback control is involved.

### 1.2.2 Electromagnetic shunt damper

Similar to the PSD technique, Behrens et al. [105, 106] proposed the concept of electromagnetic shunt damping (EMSD), in which an electromagnetic transducer is employed to convert the kinetic energy of mechanical system into electrical energy to be dissipated in the external shunt circuit. An electromagnetic transducer can be modelled as a velocity-controlled voltage source with a resistive-inductive inherent impedance, as illustrated in Figure 1.14b. Compared to its piezoelectric counterpart, an EMSD presents some benefits: smaller shunt voltage and larger strokes.

Due to the resistive-inductive nature of electromagnetic transducer, Behrens et al. [106] added a RC shunt so as to achieve the electrical resonance and a significant vibration reduction of more than 20dB was experimentally observed at the natural frequency of mechanical structure. Similar to the PSD, the online adaptive tuning and current-flowing techniques for EMSD were carried out by Niederberger et al. [107] and Cheng and Oh [108], respectively. Optimal design of EMSD coupled with either R or RC shunt was addressed by Inoue et al. [109] according to the FPT and ready-to-use formulae to optimal parameters were also provided. It was observed in [109] that the optimal value of total resistance is inferior to the inherent resistance of transducer, meanwhile, the authors suggested to include an external inductor for yielding a larger value of optimal resistance at the sacrifice of vibration control performance. Later, exact solutions to the  $H_\infty$  and  $H_2$  optimization of EMSD coupled with a resonant shunt circuit were derived by Tang et al. [110].

Analogous to PSD, negative impedance can be employed in the shunt circuit to enhance the damping performance of EMSD. Niu et al. [111] enclosed the electromagnetic transducer by a positive capacitance and a negative resistance (NR) in series, in which the capacitance is tuned in such a way that the electrical resonance is coincident with the vibration mode of mechanical system. It was shown that increasing the magnitude of NR results in the monotonic decrease of vibration amplitude of primary system and the increase of damping capability. Later, the vibration isolation performance of EMSD shunted with a sole NR was tested on a SDOF primary system (a proof mass suspended by a spring) [112] and on a MDOF system (a beam supported by two springs at its extremities) [113]. Numerical and experimental studies in [112, 113] demonstrated that the use of NR in the shunt impedance can significantly improve the vibration isolation performance at multiple modes. It was later demonstrated in [114, 115] that using a negative inductance (NI) in conjunction with a NR can further improve the damping performance of EMSD and ensure the broadband effect of vibration attenuation. Stabile et al. [116, 117] investigated the potential application of EMSD with a NR for attenuating the micro-vibration

in spacecrafts. More recently, Zheng et al. [68] stated that negative impedances can be employed to electrically tune the natural frequency of coupled system, which could be of special interest for applications of vibration isolation.

Finally, it should be pointed out that the influence of negative shunt impedance on the electromagnetic coupling is still lacking in the literature, which should be addressed in future works.

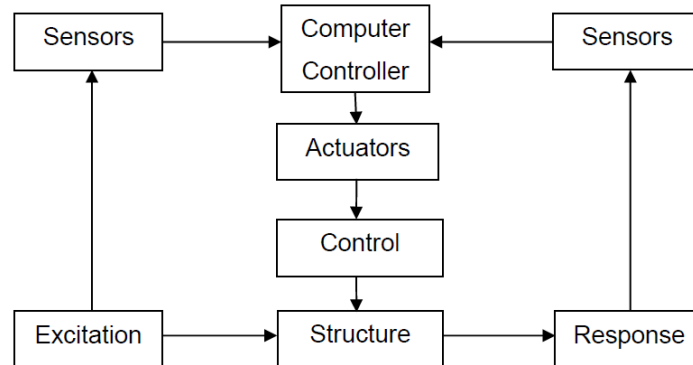


**Figure 1.18:** Schematic representation of active vibration control [118].

### 1.3 Active vibration control

Passive control devices based on mechanical resonance are usually tuned to a specific vibration mode of structure, at which the vibration reduction is proportional to the corresponding modal damping. However, the value of modal damping is directly dependent of the mass ratio between the damper mass and the effective modal mass of structure, which is relatively small. In order to improve the damping capability at multiple modes, active vibration control strategies have been developed in the literature, whose typical schematic representation is depicted in Figure 1.18. The structural responses and/or the external excitation are measure by the sensors, whose signals are fed back to real-time processing devices to calculate the required control force. Finally, the active force acting on the structure is delivered by mechanical actuators. In the past few decades, various active control devices have been developed, among which the active mass damper (AMD) and the active tuned mass damper (ATMD) are in the scope of this thesis, as reported below.

As depicted in Figure 1.19a, an AMD is composed of an auxiliary mass installed on the structure to be controlled and driven by a mechanical actuator. Its inherent damping and stiffness can usually be ignored due to their small influence compared to the actuation force. The first full-scale application of AMD in the world was realized by Kajima Corporation in 1989 [120, 121], which installed two AMDs on the 11-th floor of Kyobashi Seiwa Building in Tokyo, Japan. Later, Dyke et al. [122] developed an acceleration feedback control strategy based on the  $H_2$ /linear



**Figure 1.19:** A SDOF primary system controlled by: (a) an AMD; (b) an ATMD.

quadratic Gaussian technique, demonstrating the effectiveness of AMD at multiple modes for aseismic protection of structure. In 1998, Cao et al. [123] applied an AMD for mitigating the wind-induced vibration of an existing 340-meter-tall TV tower in Nanjing, China, and both the linear quadratic regulator and nonlinear feedback control algorithms were investigated. Recently, Yang et al. [124] proposed a negative acceleration feedback control and experimentally verified the effectiveness of a single AMD for damping multiple vibration modes of a MDOF system.

Unlike the AMD, an ATMD is a hybrid device, as shown in Figure 1.19b, whose stiffness and damping are not neglectable and should be carefully tuned. Nishimura et al. [125, 126] investigated the control efficiency of an ATMD on a SDOF primary system. Based on the direct acceleration feedback control, both the parameters of TMD and the feedback gain were optimized according to the FPT in the objective of minimizing the peak amplitude of displacement FRF of primary system. It was shown that the peak amplitude decreases monotonically as the feedback gain increases, while the TMD stroke is not increased with respect to the passive case. Similarly, numerous researches have been carried out in the literature, which optimize the ATMD in a passive way. To summarize, the design objectives of ATMDs cover: minimizing the peak displacement (i.e.  $H_\infty$  optimization) [127, 128, 129], minimizing the variance of structural motion (i.e.  $H_2$  optimization) [130, 131, 132], maximizing the decay rate of transient response (i.e. the SMC) [127] and minimizing kinetic energy of primary system or maximizing power dissipation [133]. Finally, Figure 1.20 demonstrates the ten tallest completed buildings in the world with clear indication of types of employed dampers.

To summarize, the AMD is actually an inertial actuator whose control force is entirely attributed to the actuator. Hence, it becomes idle when its power supply is turned off. Meanwhile, the passive-alike ATMDs are no longer optimal when the gain deviates from its predefined value. Therefore, they are not suitable for applications where a fail-safe mechanism is a prerequisite, e.g. helicopter vibration control [134]. Moreover, the system controlled by an AMD or ATMD could be destabilized when a large gain is used.

Recently, Collette and Chesné [135] proposed a novel control law for the ATMD

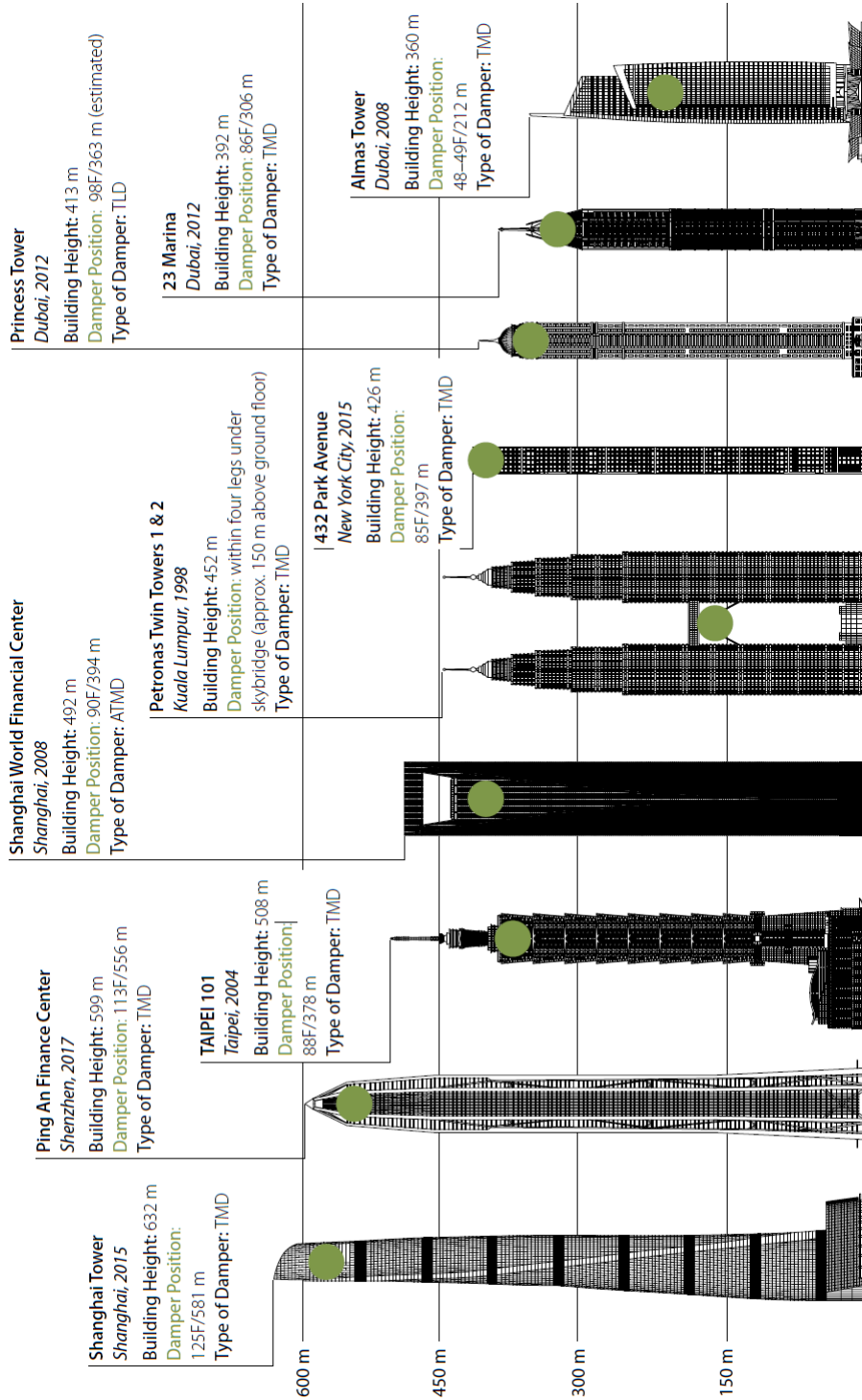


Figure 1.20: The ten tallest completed buildings with dampers in the world [119]. The types of damper include: tuned mass damper (TMD), active tuned mass damper (ATMD) and tuned liquid damper (TLD).

which guarantees simultaneously the fail-safe behaviour and the theoretical *hyper-stability*, namely remaining stable for any controller gain. Hereafter, such a device is referred to as the hybrid DVA in order to tell from the aforementioned ATMDs. The fail-safe property of hybrid DVA is preserved by tuning its passive part independently. Meanwhile, a so-called  $\alpha$ -controller, featured by two coalesced zeros on the real axis and two poles at the origin, is introduced into the direct velocity feedback control (DVFC) loop. By properly positioning the coalesced real zeros, the entire system could remain always stable. Numerical simulation demonstrated its superior performance to the AMD in terms of reduction in both vibration amplitude of structure and required active force around the target mode. Later, this control law was experimentally validated in [136], confirming its significant improvement of control performance and revealing its robustness against parameter detuning.

Finally, the actuator mechanisms are herein briefly mentioned. For controlling the vibration of large-scale structures, e.g. civil buildings, the actuators should have a high force capacity and respond rapidly, covering: hydraulic cylinder [137] and electric servo motor [138]. For small-scale control applications, e.g. thin-walled panels and plates, smart materials based actuators could be employed, such as piezoelectric [139], electromagnetic [140] and shape memory alloy [141], etc.

### 1.4 Dual-functional design

Wireless sensor networks are indispensable in the era of Internet of Things. An efficient and compact solution to their power supply is to enable them to harvest energy from ambient sources, from which arises the concept of energy harvesting. Past few decades have witnessed tremendous development in energy scavenging techniques. Literature reviews on this subject could be referred to [142, 143, 144, 145, 146]. In this section, however, special attention will be given to the state of the art of dual-functional devices, which demonstrate capabilities of both energy harvesting and vibration suppression, as reported below.

The first category is based on the fact that harvesting energy from mechanical systems can generate structural damping effects, which was first initiated by the community working on the energy extraction circuit design. Therefore, semi-active and active control strategies could be developed to suppress the vibrations of flexible structures by using harnessed power as the main source of energy. A detailed survey on this direction was carried out by Wang and Inman [147].

Instead of scavenging energy directly from the structure to be controlled, the second category aims at harvesting energy from a secondary structure, e.g. a DVA, where the energy transferred from the primary system is to be dissipated. Ali and Adhikari [148] proposed the concept of energy-harvesting DVA (EH-DVA), which incorporates a piezoelectric element between the host structure and the absorber mass. An approximate FPT was adopted to derive optimal parameters, and it was shown that with a proper choice of harvester parameters, a broadband energy har-

vesting can be obtained in combination with vibration reduction in primary system. Harne [149] designed an EH-DVA in the form of a distributed mass layer with a corrugated piezoelectric film spring for controlling the surface vibrations of structural panels. It was experimentally tested in both laboratory and field environment, revealing its potential dual-functional applications. Later, an EH-DVA based on the autoparametric resonance was first proposed by Yan and Hajj [150], as depicted in Figure 1.21a. Its optimal dual-functional design was analytically derived by Tan et al. [151] in 2019 by means of the harmonic balance method and the multiple scales method. Numerical and experimental results demonstrated that the autoparametric EH-DVA can not only effectively reduce the vibration of base structure, but also harvest relatively large electrical power at resonance or near resonance. A different configuration of autoparametric EH-DVA was proposed by Kecik [152], who combined the pendulum DVA with an electromagnetic energy harvester (EMEH), as depicted in Figure 1.21b. Distinguished from its piezoelectric counterpart, the electromagnetic EH-DVA proposed in [152] could be potentially implemented in large-scale applications, e.g. civil structures.

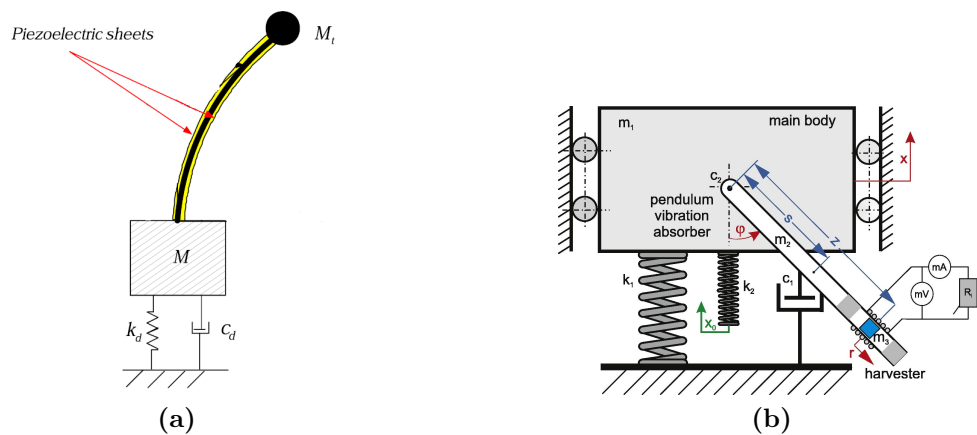


**Figure 1.21:** Schematic diagrams of a SDOF primary system controlled by autoparametric EH-DVA in the form of: (a) a cantilever beam with a tip mass and embedded piezoelectric layers [150]; (b) a pendulum with a levitating magnet moving freely inside [152].

Analogous to the EH-DVA, the vibration energy of mechanical systems can be first localized in an attached NES through the TET mechanism, which will be converted to harvestable electric power subsequently. Kremer and Liu [153, 154] designed a NES whose restoring force is contributed by magnetic repulsion and hardening effect due to lateral deformation of a fixed-fixed thin beam, and experimental validation of dual-functional design was conducted in both transient and harmonic excitation cases. A magnet-strung NES in conjunction with an EMEH was later reported by Pennisi et al. [155] with experimental verification. Finally, a conceptual design of vibro-impact NES combined with an EMEH was proposed by Afsharfard

[156], in which a magnet can freely slide inside a tube wound by coils. Therefore, the vibration energy of primary system is dissipated by the inelastic impact between the magnet and barriers of tube as well as the electric power generated in the coils due to electromagnetic coupling.

### 1.5 Outline of thesis

Having reviewed the literature of passive and active damping techniques, multiple control strategies will be developed in this thesis to attenuate the vibration of a SDOF mechanical system under direct force excitation. Improvements will be achieved in terms of one or multiple criteria, as listed below:

- Increased reduction of peak vibration amplitude and broadened frequency bandwidth of vibration absorption;
- Enhanced robustness against parametric variation;
- Simplicity and ease of practical realization;
- Lightweight application.

For the three following chapters, the proposed control devices are purely passive, which are based on the mechanical TMD or its variants developed in the literature. Precisely, Chapter 2 will focus on the use of grounded inerter for enhancing the effectiveness of traditional TMD against the parametric variation in the mechanical system. Later, the series DTMD instead of the TMD will be employed in Chapter 3 in order to increase the control efficiency for a given amount of tuned mass, and its combination with inerters will be investigated. Finally, Chapter 4 consists in incorporating a linear negative stiffness element in the non-traditional DVA and IDVA. It should be noted that the optimal design of all proposed control devices will be carried out according to specific calibration strategies and the optimal parameters will be analytically formulated.

In Chapter 5, the electromechanical analogy via the piezoelectric and electromagnetic transducers will be established and the possibility of realizing the mechanical devices by means of electromechanical shunt dampers will be investigated.

Advances in active and semi-active vibration damping techniques will be reported in Chapters 6 and 7. A general control law will be proposed in Chapter 6 for both hybrid DVA and IDVA, which assures simultaneously the fail-safe mechanism and the theoretical hyperstability. The next chapter will focus on the electromagnetic shunt damping enhanced by the use of one or two negative inductances, whose influence on the electromechanical coupling will be systematically studied for the first time.

Finally, the general conclusions for this thesis, the major contributions made and some suggestions for future work will be detailed in Chapter 8.

## Chapter 2

# Worst-Case Optimization of TMDI

Mechanical systems are usually modeled as deterministic, whose parameters are employed to evaluate the design parameters of dampers according to a specific optimization criterion, e.g. the FPT. In realistic situations, the physical properties of mechanical system, i.e. stiffness and damping, could fluctuate due to the material degradation and/or environmental variability. In this case, the control device calibrated with respect to the nominal system parameters could lose its effectiveness, or even worse, contributes to vibration amplification due to the detuning effect. Therefore, a novel tuning strategy should be proposed, which takes into consideration the parametric uncertainty.

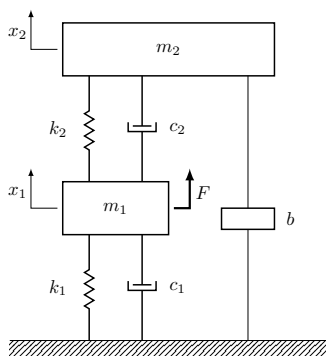


**Figure 2.1:** Schematic diagram of a SDOF primary system controlled by a TMDI.

Dell'Elce et al. [14] investigated the optimization of TMD for controlling the vibration of a SDOF primary system, whose mechanical stiffness is UBB. A robust equal-peak method was therein developed, consisting in tuning the TMD by equalizing the vibration amplitude at the leftmost and rightmost invariant points. Nevertheless, the optimal mechanical damping ratio had not been explicitly formulated. Recalling the salient effects of a grounded inerter, a TMDI is employed in this chapter to damp the forced vibration of uncertain mechanical system, as shown in Figure 2.1. Based on a perturbation approach and the property of multiplicity of polynomials, an entirely algebraic method is developed to analytically derive the

optimal parameters of TMDI, thereby of TMD. Ready-to-use formulae to all optimal parameters will be provided. Finally, the influence of grounded inerter against the detuning effect will be investigated, underlining its capability of decreasing the peak vibration amplitude of primary system in the worst-case scenario.

## 2.1 Mathematical modeling

### 2.1.1 Equations of motion

The underlying dynamics of concerned system can be described by:

$$m_1\ddot{x}_1 = c_2(\dot{x}_2 - \dot{x}_1) + k_2(x_2 - x_1) - c_1\dot{x}_1 - k_1x_1 + F(t) \quad (2.1a)$$

$$m_2\ddot{x}_2 = c_2(\dot{x}_1 - \dot{x}_2) + k_2(x_1 - x_2) - b\ddot{x}_2 \quad (2.1b)$$

where  $b$  is the inertance relating the tuned mass to the ground, meanwhile, other system parameters and displacement variables have been specified in Section 1.1.1.

In the deterministic scenario, it is common practice to neglect the damping of lightly damped structure in order to concisely formulate the expressions of optimal parameters. Meanwhile, Dell'Elce et al. [14] stated that in the uncertain case, the worst-case scenario occurs when the primary system has zero damping. Hereafter, the worst-case optimal design of TMDI will be conducted for a mechanical system under stiffness uncertainty, whose damping is neglected.

### 2.1.2 Stiffness uncertainty modeling

Adopting the UBB model, the mechanical stiffness can be described by an interval variable:

$$k_1^I \triangleq [\underline{k}, \bar{k}] = \{k_1 | \underline{k} \leq k_1 \leq \bar{k}, k_1 \in \mathbb{R}^+\} \quad (2.2)$$

where the superscript  $I$  refers to the interval variable,  $\underline{k}$  and  $\bar{k}$  correspond to its lower and upper bounds. Such an UBB parameter can be also represented by its midpoint  $k^c$  and deviation  $\Delta k$  which are defined as, respectively:

$$k^c = \frac{\bar{k} + \underline{k}}{2}, \quad \Delta k = \frac{\bar{k} - \underline{k}}{2}. \quad (2.3)$$

Therefore, an interval variable reduces to a deterministic value when its deviation is zero. In this study, the nominal stiffness is chosen as the midpoint of  $k_1^I$ , namely:

$$k_1^I = \{k_1 | k_n - \Delta k \leq k_1 \leq k_n + \Delta k, k_1 \in \mathbb{R}^+\} = (1 + \delta)k_n, \quad \delta \in [-\eta, +\eta]. \quad (2.4)$$

where  $\eta = \Delta k/k_n$  denotes the maximum uncertainty magnitude, therefore,  $\eta$  is non-negative in nature. Besides,  $\delta$  is a random variable quantifying the deviation degree of actual mechanical stiffness from its nominal value, which has a constant probability distribution in the whole interval.

### 2.1.3 Displacement FRF

Following the same nondimensionalization procedure in Section 1.1.1 and introducing an inertance-to-mass ratio  $\nu$ :

$$\nu = \frac{b}{m_1} \quad (2.5)$$

The EOMs (2.1) can be recast into the dimensionless form:

$$x_1'' + (\mu + \nu)x_2'' + (1 + \delta)x_1 = F/k_n \quad (2.6a)$$

$$(\mu + \nu)x_2'' + 2\mu\xi\alpha(x_2' - x_1') + \mu\alpha^2(x_2 - x_1) = 0 \quad (2.6b)$$

Therefore, by taking the Laplace transform of Eq. (2.6) and replacing the dimensionless frequency variable by  $j\lambda$  with  $j = \sqrt{-1}$ , the normalized displacement FRF of primary system is formulated as:

$$G = \left| \frac{X_1}{F/k_n} \right| = \sqrt{\frac{A + B\xi^2}{C + D\xi^2}} \quad (2.7)$$

with the four coefficients given by:

$$\begin{cases} A = [\mu\alpha^2 - (\mu + \nu)\lambda^2]^2 \\ B = 4\mu^2\alpha^2\lambda^2 \\ C = [(1 + \delta - \lambda^2)[\mu\alpha^2 - (\mu + \nu)\lambda^2] - \mu(\mu + \nu)\alpha^2\lambda^2]^2 \\ D = 4\mu^2\alpha^2\lambda^2[1 + \delta - (1 + \mu + \nu)\lambda^2]^2 \end{cases} \quad (2.8)$$

Clearly, the normalized displacement amplitude  $G$  is a function of six variables:  $\mu$ ,  $\nu$ ,  $\delta$ ,  $\alpha$ ,  $\xi$  and  $\lambda$ .  $\mu$  and  $\nu$  are given *a priori* and  $\delta$  varies within the specific interval  $[-\eta, +\eta]$  with  $\eta$  being a known constant. Thus,  $\alpha$  and  $\xi$  are design parameters, which aim at minimizing the peak vibration amplitude in the worst-case scenario over the whole frequency range, i.e.  $\lambda \in \mathbb{R}^+$ .

## 2.2 Worst-case optimal design

Figure 2.2 depicts a set of displacement FRFs of primary system controlled by a TMDI, which is tuned by the classic FPT. The responses are simulated for the mass ratio of  $\mu = 5\%$ , an inertance-to-mass ratio of  $\nu = 3\%$  and an uncertainty magnitude of  $\eta = 20\%$ . Apparently, the FRF has two quasi-equal peaks in the nominal case (marked by thick dashed line). Meanwhile, the peak vibration amplitude is inevitably amplified when the stiffness fluctuates, as represented by the 20 FRFs marked by thin dotted lines, which correspond to 20 randomly sampled values of  $\delta$  in the interval  $[-\eta, +\eta]$ . In the worst-case scenario (marked by thick solid line), the deterioration of vibration control performance goes up to 7.2dB, signifying that

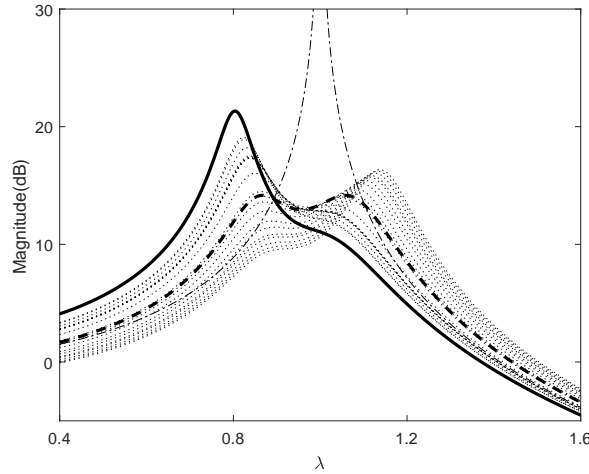


**Figure 2.2:** Displacement FRFs of primary system controlled by a TMDI with the classic equal-peak design. The set of parameters is:  $\mu = 0.05$ ,  $\nu = 0.03$ ,  $\eta = 20\%$ . Thin dash-dotted line: without control, thick dashed line: the deterministic scenario ( $\delta = 0$ ), thick solid line: the worst-case scenario, thin dotted lines: 20 uncertainties  $\delta$  randomly sampled in  $[-\eta, +\eta]$ .

the peak amplitude increases by 129% when compared to the nominal case. Therefore, the classic FPT could not yield favourable result in the presence of parameter fluctuation and a novel tuning rule should be developed in order to minimize the worst-case peak amplitude.

### 2.2.1 Min-max optimization formulation

As presented in Section 1.1.1.1, the  $H_\infty$  optimal design of TMDI can be posed as a min-max optimization problem:

$$\min_{\alpha, \xi} \left\{ \max_{\delta, \lambda_p} \left\{ \|G(\delta, \mu, \nu, \alpha, \xi, \lambda)\|_\infty \right\} \right\} \quad (2.9)$$

subject to:

$$\delta \in [-\eta, +\eta], \quad \eta \geq 0, \quad \alpha \geq 0, \quad \xi \geq 0, \quad \lambda \in \mathbb{R}^+. \quad (2.10)$$

Exact solutions to the min-max problem will be numerically solved, compared to which the accuracy of analytical solutions derived in the following context will be examined.

### 2.2.2 Proposed tuning methodology

The FRFs related to  $G(\lambda)|_{\delta=-\eta}$  and  $G(\lambda)|_{\delta=+\eta}$  are depicted in Figures 2.3a and 2.3b, respectively, for three values of mechanical damping ratio  $\xi$ . Similar to the

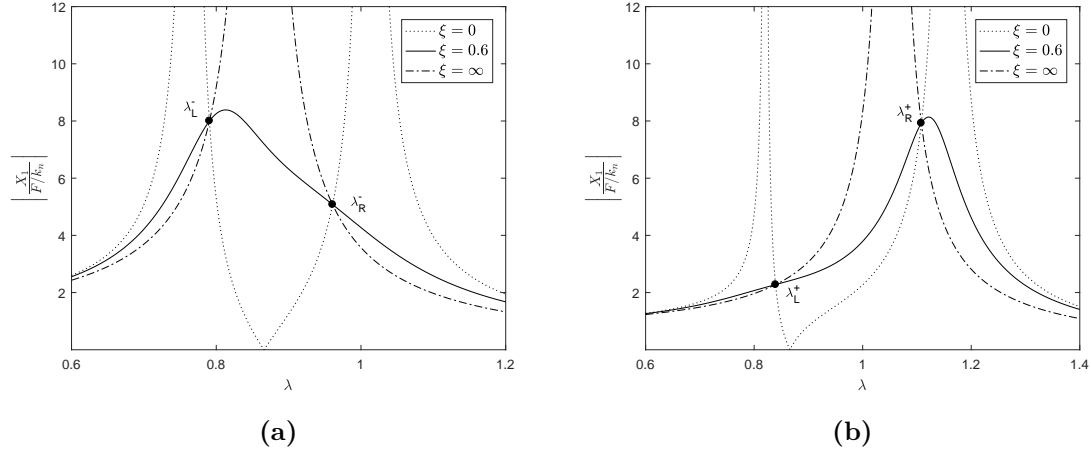


**Figure 2.3:** Displacement FRFs of primary system controlled by a TMDI corresponding to three damping levels: (a)  $\delta = -\eta$ ; (b)  $\delta = +\eta$ . The set of parameters is:  $\mu = 0.05$ ,  $\nu = 0.03$ ,  $\eta = 20\%$  and  $\alpha^2 = 1.2$ . Dotted line:  $\xi = 0$ , solid line:  $\xi = 0.6$  and dash-dotted line:  $\xi = \infty$ .

deterministic scenario, these response curves always intersect at two positions, i.e. invariant points, whose abscissas are denoted as  $\lambda_L^-$  and  $\lambda_R^-$  (or  $\lambda_L^+$  and  $\lambda_R^+$ ).

Dell’Elce et al. [14] stated that the optimal FRF should have the same amplitude at the leftmost and rightmost fixed points,  $\lambda_L^-$  and  $\lambda_R^+$ . In conjunction with Figure 2.3, this optimality condition can be mathematically formulated as:

$$\|G(-\eta, \mu, \nu, \alpha, \xi, \lambda_L^-)\|_\infty = \|G(+\eta, \mu, \nu, \alpha, \xi, \lambda_R^+)\|_\infty \quad (2.11)$$

In the following, the squared vibration amplitude at these two invariant points in the worst-case optimal scenario is denoted as  $h$ , i.e.  $G^2(-\eta, \mu, \nu, \alpha, \xi, \lambda_L^-) = G^2(+\eta, \mu, \nu, \alpha, \xi, \lambda_R^+) = h$ .

Based on the aforementioned optimality condition, an algebraic approach alternative to the robust equal-peak method proposed in [14] is herein outlined. In the worst-case optimal scenario, the optimal mechanical damping ratio  $\xi_{\text{opt}}$  could be expressed in terms of  $\delta$ ,  $\lambda$ ,  $\alpha$  and  $h$  by transforming Eq. (2.7). On this basis, another expression for  $\xi_{\text{opt}}$  could be obtained by employing the perturbation approach as mentioned in [18]. Equating these two expressions of  $\xi_{\text{opt}}$  yields a unique polynomial function which is independent of  $\xi_{\text{opt}}$ . As a consequence, optimal parameters could be determined by virtue of the algebraic properties of the polynomial function, e.g. the multiplicity of roots.

### 2.2.2.1 Polynomial function irrelevant to $\xi$

In the worst-case optimal scenario, the mechanical damping ratio  $\xi$  can be extracted from  $G^2 = h$ :

$$\xi^2 = -\frac{A - hC}{B - hD} \quad (2.12)$$

which can be recast into a polynomial form of:

$$S(\delta, \mu, \nu, \alpha, \xi, \lambda) = (A - hC) + (B - hD)\xi^2 = 0 \quad (2.13)$$

Therefore, the optimality condition (2.11) could be rewritten as:

$$S(-\eta, \mu, \nu, f, \xi, \lambda_L^-) = S(+\eta, \mu, \nu, f, \xi, \lambda_R^+) = 0 \quad (2.14)$$

Meanwhile, one can also tell that their partial derivative with respect to  $\lambda$  should be equal to zero at two invariant points. Therefore, the following conditions should be simultaneously satisfied:

$$S \Big|_{\delta=-\eta, \lambda=\lambda_L^-} = 0, \quad \frac{\partial S}{\partial \lambda} \Big|_{\delta=-\eta, \lambda=\lambda_L^-} = 0. \quad (2.15)$$

and

$$S \Big|_{\delta=+\eta, \lambda=\lambda_R^+} = 0, \quad \frac{\partial S}{\partial \lambda} \Big|_{\delta=+\eta, \lambda=\lambda_R^+} = 0. \quad (2.16)$$

designating that the root  $\lambda_L^-$  (or  $\lambda_R^+$ ) of polynomial function  $S|_{\delta=-\eta}$  (or  $S|_{\delta=+\eta}$ ) is at least of multiplicity 2. Therefore, the discriminant of polynomial function  $S$  is zero, namely:

$$\Delta_\lambda S \Big|_{\delta=-\eta} = 0, \quad \Delta_\lambda S \Big|_{\delta=+\eta} = 0. \quad (2.17)$$

where the subscript  $\lambda$  stands for the variable with respect to which the discriminant is calculated.

Up to now, only two optimality conditions are obtained as given in Eq. (2.17), while there exists three unknown variables in  $S$ :  $f$ ,  $\xi$  and  $h$ . Therefore, one more constraint should be formulated to reduce the number of variables in avoidance of being an underdetermined system.

Recalling the perturbation approach [18], the optimal damping ratio (2.12) can be reformulated by imposing the horizontal tangent constraint on a point (with abscissa  $\lambda + \epsilon$ ) adjacent to the fixed point, and then it could be simplified by approaching the perturbation  $\epsilon$  to zero, i.e.  $\epsilon \rightarrow 0$ . By replacing  $\lambda$  with  $\lambda + \epsilon$ , Eq. (2.12) can be rearranged into the polynomial form in  $\epsilon$ :

$$\xi^2 = \frac{a_0 + a_1\epsilon + a_2\epsilon^2 + \dots}{b_0 + b_1\epsilon + b_2\epsilon^2 + \dots} \quad (2.18)$$

By assuming that the fraction  $a_0/b_0$  is of indeterminate form  $0/0$  and by approaching  $\epsilon$  to zero, an alternative expression for  $\xi^2$  could be obtained according to the *de L'Hospital's* rule:

$$\lim_{\epsilon \rightarrow 0} \xi^2 = \frac{a_1}{b_1} \quad (2.19)$$

with

$$\begin{aligned} a_1 &= 2h [\mu\alpha^2(1+\gamma) + \gamma(1+\delta-2\lambda^2)] [\mu\gamma\alpha^2\lambda^2 - (\mu\alpha^2 - \gamma\lambda^2)(1+\delta-\lambda^2)] \\ &\quad + 2\gamma(\mu\alpha^2 - \gamma\lambda^2) \\ b_1 &= 4\mu^2\alpha^2 - 4h\mu^2\alpha^2 [1+\delta-\lambda^2(1+\gamma)] [1+\delta-3\lambda^2(1+\gamma)] \end{aligned} \quad (2.20)$$

where  $\gamma = \mu + \nu$  stands for the sum of mass ratio and inertance-to-mass ratio. By inserting Eq. (2.19) into Eq. (2.13), the polynomial function  $S$  is rewritten as:

$$S(\delta, \mu, \nu, f, \lambda) = (A - hC)b_1 + (B - hD)a_1 = 0 \quad (2.21)$$

which is independent of  $\xi$  and can be solved together with optimality conditions (2.17).

### 2.2.2.2 Optimal solutions to $\alpha$ and $h$

The discriminant of polynomial  $S$  is proportional to its resultant  $R(S, \partial S/\partial \lambda)$  due to its linearity, as follows:

$$\Delta_\omega(S) = -\frac{1}{s_0} \cdot R\left(S, \frac{\partial S}{\partial \lambda}\right) \quad (2.22)$$

where  $s_0$  is the constant before the highest-order term in  $\lambda$  for the polynomial  $S$ . Therefore, the resultant is set as zero instead of its discriminant. The mathematics software MAPLE is herein employed to yield the resultant expression and thereby conduct its factorization, as follows:

$$R\left(S, \frac{\partial S}{\partial \lambda}\right) = Q_0 \cdot Q_1^3 \cdot Q_2 \cdot Q_3 = 0 \quad (2.23)$$

where  $Q_0$  is independent of  $h$ ,  $Q_3$  is non-factorable and contains too many terms to be appended, which is omitted in this study. The other two factors are herein provided:

$$\begin{aligned} Q_1 &= (1+\delta)^2 h - 1 \\ Q_2 &= -\gamma^4 (1+\delta)^4 h^2 - \gamma^2 (2+\gamma)^2 \\ &\quad + \left[ 2\gamma^2 \left[ 1 + (1+\gamma)^2 \right] (1+\delta)^2 - 8\mu\gamma\alpha^2 (1+\gamma)^2 (1+\delta) + 4\mu^2\alpha^4 (1+\gamma)^4 \right] h \end{aligned} \quad (2.24)$$

It is noticeable that the factor  $Q_1 = 0$  can not be satisfied simultaneously for  $\delta = -\eta$  and  $\delta = +\eta$ , which is then rejected. Therefore, the factor  $Q_2$  should be equal to zero

for lower and upper bound of stiffness uncertainty  $\delta$ . Mathematically, the following constraints should be satisfied:

$$Q_2 \Big|_{\delta=-\eta} = Q_2 \Big|_{\delta=+\eta} = 0 \quad (2.25)$$

which is equivalent to two alternative conditions that

$$Q_2 \Big|_{\delta=-\eta} - Q_2 \Big|_{\delta=+\eta} = 0 \quad (2.26)$$

and

$$Q_2 \Big|_{\delta=-\eta} + Q_2 \Big|_{\delta=+\eta} = 0 \quad (2.27)$$

The condition (2.26) yields the closed-form expression of frequency tuning ratio  $\alpha$  in terms of the squared vibration amplitude  $h$ :

$$\alpha^2 = \frac{\gamma [1 + (1 + \gamma)^2] + h\gamma^3 (1 + \eta^2)}{2\mu(1 + \gamma)^2} \quad (2.28)$$

By inserting Eq. (2.28) into (2.27) and after the manipulation, a quadratic function in  $h$  is retained:

$$\gamma^2 (1 + \eta^2)^2 h^2 + 2 [1 - \eta^2 - (1 + \eta^2)(1 + \gamma)^2] h + (2 + \gamma)^2 = 0 \quad (2.29)$$

which has two possible positive roots given by, respectively:

$$h_{\text{opt},1} = \left( \frac{\kappa - \eta}{\gamma(1 + \eta^2)} \right)^2, \quad h_{\text{opt},2} = \left( \frac{\kappa + \eta}{\gamma(1 + \eta^2)} \right)^2. \quad (2.30)$$

with  $\kappa = \sqrt{(1 + \eta^2)(1 + \gamma)^2 - 1}$ . For any non-negative  $\eta$ , the following inequality always holds:

$$h_{\text{opt},1} \leq h_n = \frac{2 + \gamma}{\gamma} \leq h_{\text{opt},2} \quad (2.31)$$

in which  $h_n$  is the squared vibration amplitude at fixed points in the deterministic scenario [46]. Clearly, three expressions in Eq. (2.31) are equal when  $\eta = 0$ . As the parameter detuning will deteriorate the control effect of TMDI,  $h_{\text{opt},2}$  should be then retained. Therefore, the normalized vibration amplitude at fixed points in the worst-case optimal scenario can be expressed as:

$$G_{\text{opt}} = \sqrt{h_{\text{opt},2}} = \frac{\kappa + \eta}{\gamma(1 + \eta^2)} \quad (2.32)$$

leading to the optimal frequency tuning ratio  $\alpha_{\text{opt}}$ :

$$\alpha_{\text{opt}} = \sqrt{\frac{\gamma(1 - \kappa\eta)}{\mu(1 + \eta^2)(1 + \gamma)^2}} \quad (2.33)$$

In the deterministic scenario, the vibration amplitude (2.32) and frequency tuning ratio (2.33) reduce to, respectively:

$$G = \sqrt{\frac{2+\gamma}{\gamma}}, \quad \alpha = \sqrt{\frac{\gamma}{\mu(1+\gamma)^2}}. \quad (2.34)$$

coinciding with the ones derived in [46].

### 2.2.2.3 Abscissas of fixed points

To date, the only unknown parameter to calculate the optimal damping ratio  $\xi_{\text{opt}}$  is the abscissas of fixed points,  $\lambda_L^-$  and  $\lambda_R^+$ . By inserting Eqs. (2.32) and (2.33) into Eq. (2.21) and after simplification, a polynomial function  $T$  is obtained, which is only dependent of the forcing frequency  $\lambda$  and uncertainty  $\delta$ , i.e.:

$$T(\lambda, \delta) = 0 \quad (2.35)$$

which can be factorized as:

$$\begin{aligned} T(\delta = -\eta) &= \left[ (2+\gamma)(1+\gamma)^2 \lambda^4 + 2(1+\gamma)[\eta(1+\gamma) - 2 - \gamma] \lambda^2 + 2 - 2\eta(1+\gamma) \right]^2 \cdot Q_4 \\ T(\delta = +\eta) &= \left[ (2+\gamma)(1+\gamma)^2 \lambda^4 - 2(1+\gamma)[\eta(1+\gamma) + 2 + \gamma] \lambda^2 + 2 + 2\eta(1+\gamma) \right]^2 \cdot Q_5 \end{aligned} \quad (2.36)$$

where  $Q_4$  and  $Q_5$  are non-factorable and have too many terms, which do not contain useful informations. Therefore, the forcing frequencies at the leftmost and rightmost fixed points should satisfy the following quadratic functions in  $\lambda^2$ :

- $\lambda_L^-$  and  $\lambda_R^-$  satisfy:

$$(2+\gamma)(1+\gamma)^2 \lambda^4 + 2(1+\gamma)[\eta(1+\gamma) - 2 - \gamma] \lambda^2 + 2 - 2\eta(1+\gamma) = 0 \quad (2.37)$$

- $\lambda_L^+$  and  $\lambda_R^+$  satisfy:

$$(2+\gamma)(1+\gamma)^2 \lambda^4 - 2(1+\gamma)[\eta(1+\gamma) + 2 + \gamma] \lambda^2 + 2 + 2\eta(1+\gamma) = 0 \quad (2.38)$$

Therefore, the abscissas of four fixed points can be expressed as, respectively,

$$\begin{aligned} \lambda_L^- &= \sqrt{\frac{1+(1-\eta)(1+\gamma)-\kappa}{(1+\gamma)(2+\gamma)}}, & \lambda_R^- &= \sqrt{\frac{1+(1-\eta)(1+\gamma)+\kappa}{(1+\gamma)(2+\gamma)}}, \\ \lambda_L^+ &= \sqrt{\frac{1+(1+\eta)(1+\gamma)-\kappa}{(1+\gamma)(2+\gamma)}}, & \lambda_R^+ &= \sqrt{\frac{1+(1+\eta)(1+\gamma)+\kappa}{(1+\gamma)(2+\gamma)}}. \end{aligned} \quad (2.39)$$

Figure 2.4 plots three FRFs corresponding to three different values of  $\xi$ . The frequency tuning ratio  $\alpha$  of TMDI is evaluated by using Eq. (2.33) for the set of

parameters:  $(\mu, \nu, \eta) = (0.05, 0.05, 10\%)$ . The coordinates of the leftmost and rightmost fixed points read as, respectively:  $(0.81, 5.66)$  and  $(1.08, 5.66)$ . It is apparent that their abscissas are coincident with the ones computed by using the expressions of  $\lambda_L^-$  and  $\lambda_R^+$  from Eq. (2.39). Besides, their ordinates have the same value and are equal to that determined by Eq. (2.32), validating the derived solutions for  $\alpha$  and  $h$ .

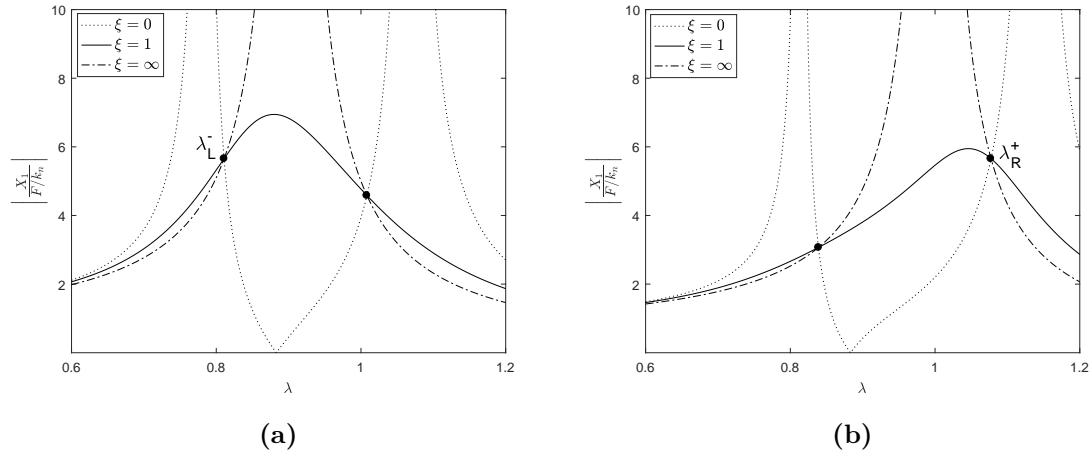


**Figure 2.4:** Displacement FRFs of primary system controlled by a TMDI corresponding to three damping levels: (a)  $\delta = -\eta$ ; (b)  $\delta = +\eta$ . The set of parameters is:  $\mu = 0.05$ ,  $\nu = 0.05$ ,  $\eta = 10\%$  and  $\alpha$  is evaluated by Eq.(2.33). Dotted line:  $\xi = 0$ , solid line:  $\xi = 1$  and dash-dotted line:  $\xi = \infty$ . The leftmost and rightmost fixed points locate at  $(0.81, 5.66)$  and  $(1.08, 5.66)$ .

#### 2.2.2.4 Optimal mechanical damping ratio $\xi$

Finally, one can evaluate the value of mechanical damping ratio by substituting the abscissas of fixed points (2.39), the squared vibration amplitude at fixed points (2.32) and the frequency tuning ratio (2.33) into Eq. (2.19). At the leftmost and rightmost invariant points, their corresponding damping ratios are computed as:

$$\xi_L^2 = \frac{a_1}{b_1} \bigg|_{\lambda=\lambda_L^-, \delta=-\eta, \alpha=\alpha_{\text{opt}}, h=h_{\text{opt}}}, \quad \xi_R^2 = \frac{a_1}{b_1} \bigg|_{\lambda=\lambda_R^+, \delta=-\eta, \alpha=\alpha_{\text{opt}}, h=h_{\text{opt}}}. \quad (2.40)$$

It is noticeable that the damping ratios evaluated at each invariant point are slightly different with each other. Therefore, the optimal mechanical damping ratio  $\xi_{\text{opt}}$

could be chosen as their root mean square value, i.e.:

$$\xi_{\text{opt}} = \sqrt{\frac{\xi_L^2 + \xi_R^2}{2}} = \sqrt{\frac{\gamma(1+\eta^2) \sum_{j=0}^8 n_j \kappa^j}{8\mu(1-\kappa\eta)(1+\kappa^2)^2 \sum_{j=0}^4 d_j \kappa^j}} \quad (2.41)$$

with the constants in numerator and denominator given as, respectively,

$$\begin{cases} n_0 = \gamma^5 + 5\gamma^4 + 5\gamma^3 + \gamma^2 \\ n_1 = -2\gamma^2\eta(1+\gamma)(2\gamma^2 + 8\gamma + 5) \\ n_2 = -6\gamma^5 - 30\gamma^4 - 47\gamma^3 - 15\gamma^2 + 2\gamma \\ n_3 = 2\eta(1+\gamma)(2\gamma^4 + 8\gamma^3 + 16\gamma^2 + 4\gamma - 1) \\ n_4 = \gamma^5 + 5\gamma^4 + 27\gamma^3 + 55\gamma^2 + 12\gamma - 2 \\ n_5 = -2\eta(1+\gamma)(3\gamma^2 + 12\gamma + 2) \\ n_6 = -\gamma^3 - 9\gamma^2 - 30\gamma - 4 \\ n_7 = 6\eta(1+\gamma) \\ n_8 = 6 \end{cases} \quad (2.42)$$

and

$$\begin{cases} d_0 = \gamma^2 + \gamma \\ d_1 = -\eta(1+\gamma)(2\gamma + 1) \\ d_2 = -\gamma^2 - 3\gamma - 1 \\ d_3 = \eta(1+\gamma) \\ d_4 = 1 \end{cases} \quad (2.43)$$

Parameters	Deterministic model [46]	Uncertain model
$\alpha$	$\sqrt{\frac{\gamma}{\mu(1+\gamma)^2}}$	$\sqrt{\frac{\gamma(1-\kappa\eta)}{\mu(1+\eta^2)(1+\gamma)^2}}$
$\xi$	$\sqrt{\frac{3\gamma^2}{8\mu(1+\gamma)}}$	$\sqrt{\frac{\gamma(1+\eta^2) \sum_{i=0}^8 n_i \kappa^i}{8\mu(1-\kappa\eta)(1+\kappa^2)^2 \sum_{j=0}^4 d_j \kappa^j}}$
$G _{\lambda=\lambda_L^-, \lambda_R^+}$	$\sqrt{\frac{2+\gamma}{\gamma}}$	$\frac{\kappa + \eta}{\gamma(1+\eta^2)}$

**Table 2.1:** Optimal parameters of TMDI for a deterministic and uncertain SDOF primary system under force excitation. Constants  $n_i$  and  $d_j$  are given in Eqs. (2.42)

and (2.43) with  $\gamma = \mu + \nu$  and  $\kappa = \sqrt{(1+\eta^2)(1+\gamma)^2 - 1}$ .

### 2.2.3 Preliminary remarks

Up to now, all optimal parameters of TMDI are derived for a SDOF uncertain mechanical system. Their analytical formulae in both deterministic and uncertain scenarios are summarized in Table 2.1. By vanishing the stiffness uncertainty (i.e.  $\eta = 0$ ), the proposed optimal parameters reduce to those derived by Marian and Giaralis [46], validating the proposed optimal design.

An observation could be made by regarding Eq. (2.32) that for a given bound on stiffness uncertainty  $\eta$ , the vibration amplitude at fixed points is solely controlled by  $\gamma$ , i.e. the sum of mass ratio and inertance-to-mass ratio. Figure 2.5 shows two identical FRFs corresponding to different sets of parameters:  $\mu = 0.05$ ,  $\nu = 0.01$ ,  $\eta = 20\%$  (represented by solid lines);  $\mu = 0.03$ ,  $\nu = 0.03$ ,  $\eta = 20\%$  (represented by circle markers). Therefore, one can infer that in the harmonically forced case, the global vibration control effect remains unchanged as if the total amount of tuned mass and inertance is unchanged. In other words, the tuned mass and the grounded inertance are interchangeable so that the need for the tuned mass could be partially diminished by increasing the amount of inertance.

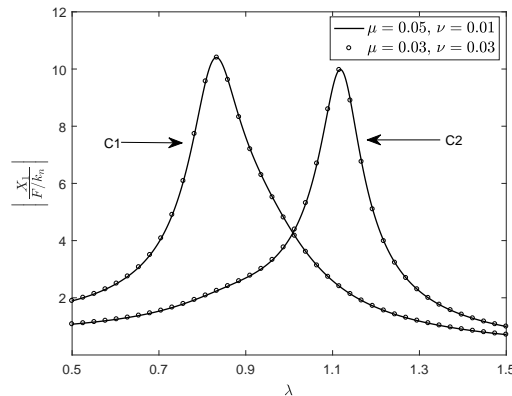


**Figure 2.5:** Displacement FRFs of primary system controlled by a TMDI with the worst-case optimal design. Solid line:  $\mu = 0.05$ ,  $\nu = 0.01$ ,  $\eta = 20\%$ ; circle markers:  $\mu = 0.03$ ,  $\nu = 0.03$ ,  $\eta = 20\%$ . C1 and C2 correspond to FRFs with  $\delta = -\eta$  and  $\delta = +\eta$ , respectively.

Finally, the optimal parameters of TMD in the worst-case optimal scenario could be achieved from those of TMDI with removing the grounded inerter (i.e.  $\nu = 0$  and  $\gamma = \mu$ ), which are given in Table 2.2. Again, their analytical expressions reduce to the long-established formulae of Den Hartog [2] in the deterministic scenario. However, it is worth noting that the worst-case optimal parameters of TMDI could not be obtained by extending those of TMD with simply replacing  $\mu$  by  $\gamma$ , due to the fact that the two optimal tuning parameters in Eqs. (2.33) and (2.41) of TMDI are not dictated by  $\gamma$  but a function of  $\mu$  and  $\gamma$  simultaneously.

Parameters	Deterministic model [2]	Uncertain model
$\alpha$	$\frac{1}{1+\mu}$	$\sqrt{\frac{(1-\hat{\kappa}\eta)}{(1+\eta^2)(1+\mu)^2}}$
$\xi$	$\sqrt{\frac{3\mu}{8(1+\mu)}}$	$\sqrt{\frac{1+\eta^2}{8(1-\hat{\kappa}\eta)(1+\hat{\kappa}^2)^2} \frac{\sum_{i=0}^8 \hat{n}_i \hat{\kappa}^i}{\sum_{j=0}^4 \hat{d}_j \hat{\kappa}^j}}$
$G _{\lambda=\lambda_L^-, \lambda_R^+}$	$\sqrt{\frac{2+\mu}{\mu}}$	$\frac{\hat{\kappa} + \eta}{\mu(1+\eta^2)}$

**Table 2.2:** Optimal parameters of TMD for a deterministic and uncertain SDOF primary system under force excitation. Constants  $\hat{n}_i$  and  $\hat{d}_j$  are given in Eqs. (2.42) and (2.43) with replacing  $\gamma$  by  $\mu$ .  $\hat{\kappa} = \sqrt{(1+\eta^2)(1+\mu)^2} - 1$ .

## 2.3 Numerical investigation

In this section, the proposed tuning methodology is validated by comparing with existing or numerical solutions. Furthermore, we will highlight the effectiveness of proposed worst-case optimum design and the favourable effect of grounded inerter against parameter detuning.

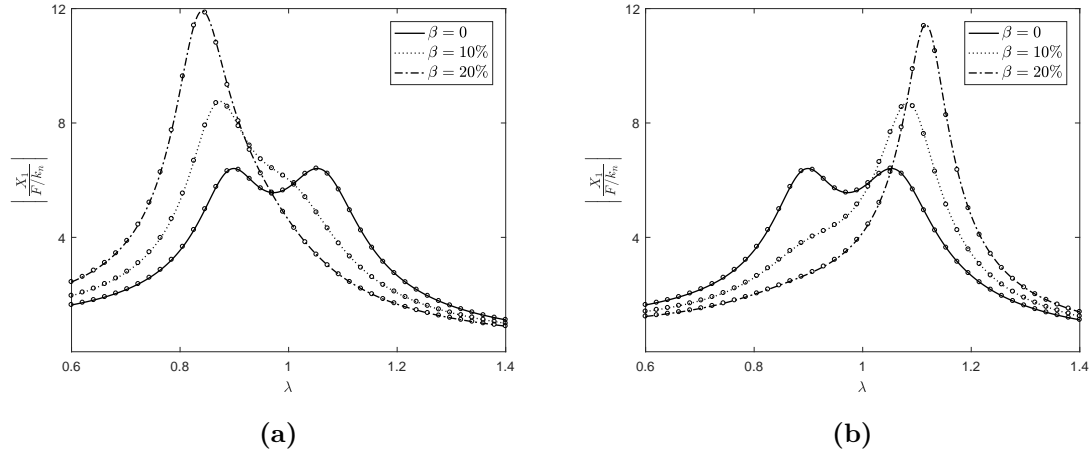


**Figure 2.6:** Displacement FRFs of primary system controlled by a TMD related to three levels of stiffness uncertainty: (a)  $\delta = -\eta$ ; (b)  $\delta = +\eta$ . The TMD is optimized by either the method in [14] (represented by circle marker) or the proposed methodology (marked by lines). The mass ratio is set as  $\mu = 0.05$ . Solid line:  $\eta = 0$ , dotted line:  $\eta = 10\%$ , dash-dotted line:  $\eta = 20\%$ .

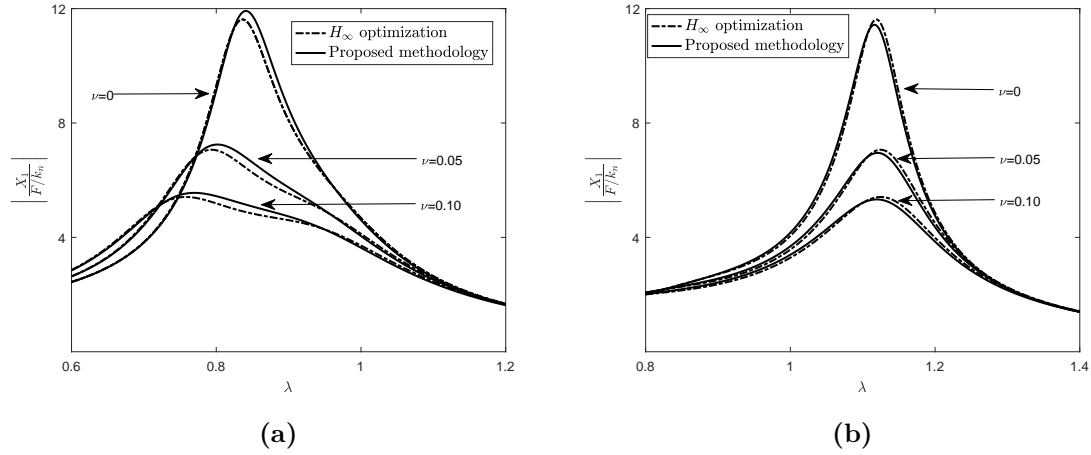


**Figure 2.7:** Displacement FRFs of primary system controlled by a TMDI corresponding to three inertia-to-mass ratios: (a)  $\delta = -\eta$ ; (b)  $\delta = +\eta$ . The design parameters are either analytically derived (solid lines) or numerically solved (dash-dotted lines). The mass ratio and the uncertainty remain unchanged as:  $\mu = 0.05$  and  $\eta = 20\%$ , while three values of  $\nu$  are used:  $\nu = 0, 0.05$  and  $0.10$ .

### 2.3.1 Validation of derived solutions

#### 2.3.1.1 Case of TMD

Figure 2.6 depicted frequency responses corresponding to TMD optimized either by the proposed methodology or the method in [14], which are marked by solid lines and circle markers, respectively. The mass ratio is set as  $\mu = 0.05$  and three values of  $\eta$  are used for simulation:  $\eta = 0, 10\%$  and  $20\%$ . As evident from Figure 2.6, the TMD calibrated by two methods yields exactly the same dynamics responses for all uncertainty magnitudes.

It should be mentioned that closed-form solutions to the mechanical damping ratio  $\xi$  and the vibration amplitude at fixed points  $h$  are lacking in [14], which are herein provided in Table 2.2.

#### 2.3.1.2 Case of TMDI

The design proposed for TMDI will be validated by comparing with numerical solutions to its worst-case  $H_\infty$  optimization. Their relevant FRFs are plotted in Figure 2.7. The mass ratio and the uncertainty magnitude are constant:  $\mu = 0.05$  and  $\eta = 20\%$ , while three inertia-to-mass ratios are used:  $\nu = 0, 0.05$  and  $0.10$ . Clearly, the response curves with analytical solutions deviate slightly from the ones with numerically obtained parameters, which is attributed to the suboptimal nature of methodologies based on fixed points. Nevertheless, the maximum difference in peak amplitude is of merely 2.7%. Therefore, the proposed methodology could yield

accurate solutions to the worst-case optimal design of TMDI.

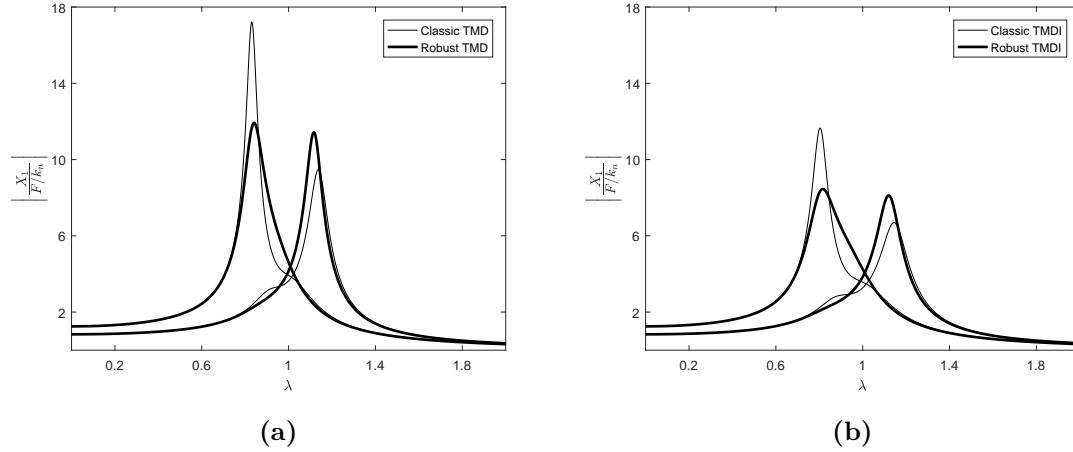


**Figure 2.8:** Displacement FRFs of primary system controlled by a: (a) TMD; (b) TMDI. The set of parameters is:  $\mu = 0.05$ ,  $\nu = 0.03$  and  $\eta = 20\%$ . Thin solid lines: with the classic design, thick solid lines: with the worst-case optimal design.

## 2.3.2 Effectiveness of worst-case design and influence of grounded inerter

### 2.3.2.1 Harmonic excitation scenario

Figures 2.8a and 2.8b demonstrate the displacement FRFs of primary system controlled by a TMD and TMDI, respectively, with classic equal-peak tuning (marked by thin solid lines) or the proposed design (represented by thick solid lines). The worst-case  $H_\infty$  norm of normalized vibration amplitude is listed in Table 2.3 for all four cases. It clearly suggests that for both TMD and TMDI, the worst-case optimal design leads to a pair of quasi-equal peaks evidently lower than the maximum amplitude with the classic design. More precisely, the proposed calibration strategy contributes to the reduction of worst-case peak amplitude by 30.7% (or 27.5%) for the primary system controlled by a TMD (or TMDI). Furthermore, the TMDI with either classic or proposed design always conducts to a smaller peak amplitude than its counterpart without inerter, implying that the incorporation of grounded inerter could render the detuning effect on the frequency response less important. With an inertance-to-mass ratio  $\nu$  being 0.03, the classic and robust TMDI can decrease the peak amplitude by 32.3% and 29.1%, respectively, when compared to their TMD counterpart. Finally, the robust TMDI could reduce the worst-case peak vibration amplitude by 50.9% compared to the case of classic TMD.

	Classic TMD	Robust TMD	Classic TMDI	Robust TMDI
$\ G\ _\infty$	17.21	11.92	11.65	8.45

**Table 2.3:** Worst-case  $H_\infty$  norm of displacement FRFs of primary system controlled by either a TMD or a TMDI with classic or robust optimal design. The set of parameters is:  $\mu = 0.05$ ,  $\nu = 0.03$  and  $\eta = 20\%$ .

In fact, one can analytically investigate the influence of mass ratio  $\mu$ , inertance-to-mass ratio  $\nu$  and the uncertainty magnitude  $\eta$  on the vibration control performance. The partial derivative of vibration amplitude at fixed points  $G_{\text{opt}}$  with respect to these variables are provided in Appendix A.1. It suggests that  $G_{\text{opt}}$  is a monotonically decreasing function of  $\gamma$  (thereby  $\mu$  and  $\nu$ ), while it increases monotonically as  $\eta$  increases. Therefore, for a given uncertainty  $\eta$ , increasing the total amount of tuned mass and inertance could contribute to compensate the deterioration of vibration control effect incurred by the uncertainty present in the host structure, which is also reflected in Figure 2.7. More precisely, for a given mass ratio of 0.05 and a 20% uncertainty, increasing the inertance-to-mass ratio  $\nu$  from 0 to 0.05 can reduce the worst-case peak amplitude by 39.2%. Furthermore, a reduction of 53.4% could be achieved when  $\nu$  arrives at 0.10, where the worst-case peak amplitude decreases to 5.56, inferior to 6.41 which is the peak amplitude with a TMD in the deterministic scenario. Reminding the mass amplification effect of inertial devices, a large value of  $\gamma$  can be easily achieved without increasing considerably the total weight of TMDI.

### 2.3.2.2 Random excitation scenario

Of a special interest is to examine the applicability of proposed robust design in the case of random excitation. In an effort to quantify the vibration sustained by the broadband-excited host structure, a performance index PI related to its mean square displacement is herein adopted, as defined in Appendix A.2.

Figure 2.9a plots the evolution of PIs for TMDIs with either classic or robust design against the inertance-to-mass ratio  $\nu$ . The mass ratio and the uncertainty magnitude are set as:  $\mu = 0.05$  and  $\eta = 20\%$ . Clearly, the worst-case optimal TMDI always yields a smaller value of PI in the whole range of  $\nu$  when compared to its counterpart with classic design. Alternatively speaking, the primary system vibrates less importantly when tuned by the proposed strategy, signifying its effectiveness in the random vibration case. However, the two curves in Figure 2.9a approach each other as the amount of inertance increases, suggesting that the control performance improvement introduced by the robust design is minor for a large inertance, as confirmed by Figure 2.9b. Finally, the positive influence brought by the grounded inertance is demonstrated in Figure 2.9c, in which is plotted the reduction in PI for TMDI with either classic or robust design when compared to their TMD counterpart. With an inertance-to-mass ratio being 0.05, the TMDI with classic (or robust) design

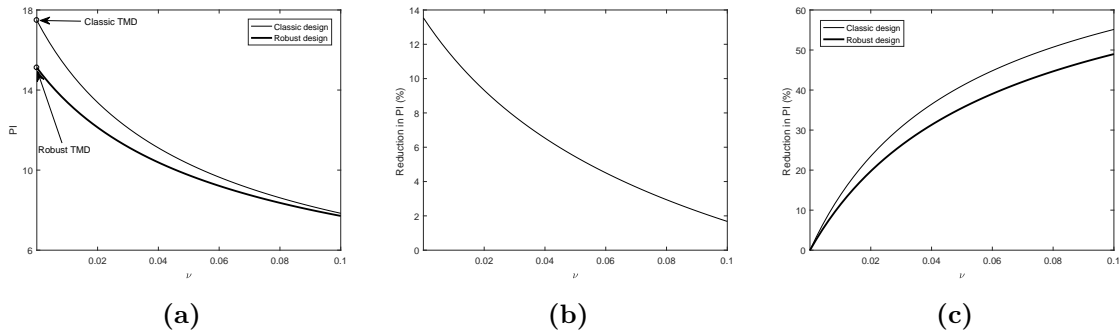


**Figure 2.9:** (a) Evolution of performance index PI against the inertia-to-mass ratio  $\nu$  for the set of parameters:  $\mu = 0.05$  and  $\eta = 20\%$ . Thin line: classic TMDI, thick line: robust TMDI, circle markers:  $\nu = 0$ . (b) Reduction in PI (in %) for robust TMDI with respect to classic TMDI. (c) Reduction in PI (in %) for TMDI compared to TMD. Thin line: classic design, thick line: robust design.

can decrease the root mean displacement of primary system by 41.0% (or 35.5%, respectively) compared to a TMD.

### 2.3.3 Discussion

A remark can be first made that the proposed design is always more effective than the classic design in terms of confining the vibration of host structure under both harmonic and random excitation. Besides, the incorporation of a grounded inerter always contribute to the improvement of vibration control performance.

The proposed optimal design is proven to be effective in terms of controlling the worst-case vibration amplitude of uncertain primary system, corresponding to the scenario at lower and upper bounds of uncertainty, i.e.  $\delta = \pm\eta$ . Meanwhile, it is also of interest to inspect the performance within the interval  $[-\eta, +\eta]$ . As depicted in Figure 2.10, the peak vibration amplitude of primary system  $\|G\|_\infty$  varies as the actual stiffness uncertainty  $\delta$  sweeps from  $-\eta$  to  $+\eta$ . More precisely,  $\|G\|_\infty$  is bounded by  $[5.12, 11.65]$  and  $[6.60, 8.45]$  (or  $[6.44, 17.21]$  and  $[8.67, 11.92]$ ) when classic and robust designs are applied to the TMDI (or TMD), respectively. Therefore, the first observation could be made in conjunction with Figures 2.10a and 2.10b that the robust design leads to a smaller variability in  $\|G\|_\infty$  for a given uncertainty interval. Moreover, the vibration amplification for a mechanical system controlled by a classic TMDI could go up to 127.5% when its stiffness is largely softened (insides the zone I). Meanwhile, the robust design could reduce the worst-case peak vibration amplitude by 27.5%, however, at the expense of amplifying the vibration insides the zone II where the actual stiffness of mechanical system is stiffened or lightly softened. Hence, a remark is herein drawn that the TMDI with robust design could lose its effectiveness, or even worse, bring damaging effects into the vibration control performance when the stiffness uncertainty is overestimated,

namely a too large value of  $\eta$  imposed for a small  $\delta$ . All aforementioned observations also hold for the case with a TMD.

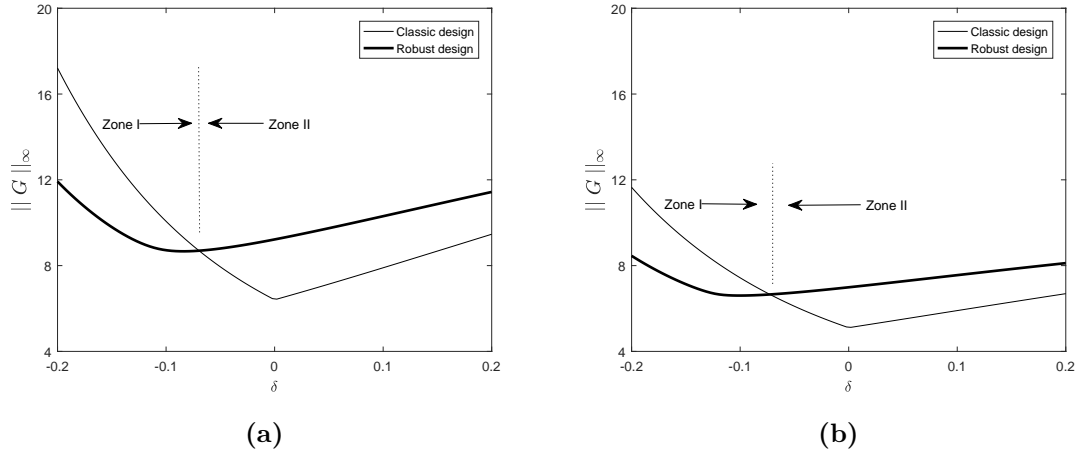


**Figure 2.10:** Evolution of  $\|G\|_\infty$  against actual stiffness uncertainty  $\delta$  sweeping within  $[-\eta, +\eta]$ : (a) TMD; (b) TMDI. The set of parameters is:  $\mu = 0.05$ ,  $\nu = 0.03$  and  $\eta = 20\%$ . Thin solid lines: classic design, thick solid lines: worst-case design.

## 2.4 Concluding remarks

This chapter investigates the optimal design of TMDI for controlling a mechanical system under UBB stiffness uncertainty. Posed as a min-max optimization problem, its analytical solutions are derived by applying a novel algebraic method, which is based on the philosophy of robust equal peaks and the perturbation approach. Ready-to-use formulae to the optimal parameters of TMDI (and also TMD) are then provided in this chapter.

The presence of uncertainty always leads to the parameter mismatch, thereby entailing a deteriorated performance of vibration control. Nevertheless, increasing the total amount of tuned mass and inertance is a favourable way to resist the detuning effect. Numerical results demonstrate that for a primary system with a 20% stiffness uncertainty and with a mass ratio of 0.05, incorporating a grounded inerter with an inertance-to-mass ratio of 0.10 can decrease the worst-case peak amplitude by 53.4%, engendering a vibration control performance superior to the TMD with the same mass ratio in the deterministic scenario.

In the next chapter, inerters will be employed in conjunction with two TMDs arranged in series, whose vibration control performance will be compared with its counterpart with a single TMD.

## Chapter 3

# Series Double Tuned Mass Damper with Inerters

It was reported in Chapter 1 that with the same amount of tuned mass, a series DTMD (SDTMD) is more effective and robust than its parallel counterpart, the classic TMD and the viscoelastic TMD. Nevertheless, a simple and effective analytical approach had not been yet developed in the literature to derive its optimal parameters. Besides, the beneficial effects of inerter on structural vibration control have been extensively investigated and industrial applications of inerter could be found in both fields of automotive and civil engineering.

Enlightened by the layout of TMDI, a novel control device, termed as the SDTMD with inerters (SDTMDI), is proposed for the first time. It is expected to make use of benefits of both SDTMD and inerter in terms of vibration control, namely the enhanced effectiveness and the lightweight potential. Depending on the positions of inerters, the SDTMDI could have two different configurations: grounded type (G-SDTMDI) and inserted type (I-SDTMDI). For the former layout, two inerters relate each tuned mass to the ground, while they are inserted between any two adjacent masses in the latter layout, as depicted in Figures 3.1a and 3.1b, respectively. Furthermore, it will be demonstrated that the phenomena of invariant points are encountered in the displacement FRFs of primary system for both configurations, suggesting that the methodology based on fixed points can be applied to carry out their optimization analytically and efficiently. Finally, ready-to-use formulae to optimal parameters of both SDTMDIs and subsequently the SDTMD will be provided and their control performance will be assessed by comparing with some well-known control devices.

### 3.1 Mathematical modeling

The host structure is modeled by a mass-spring-damper system ( $m_1-k_1-c_1$ ), which is of SDOF and is lightly damped. The SDTMD is composed of two TMDs arranged

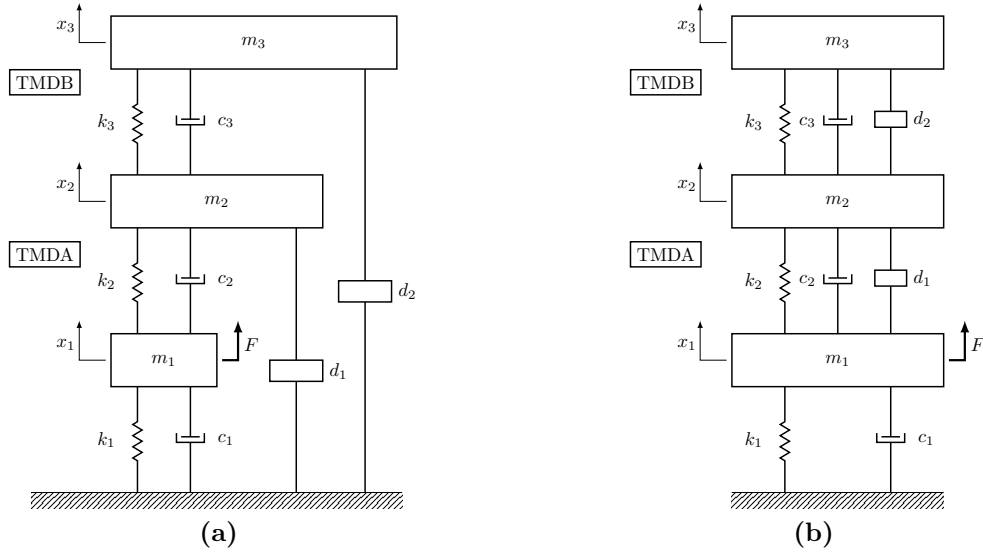


**Figure 3.1:** Schematic diagrams of a SDOF primary system controlled by a: (a) G-SDTMDI; (b) I-SDTMDI.

in series, in which the TMD adjacent to host structure is denoted as TMDA, while another TMD is denoted as TMDB.  $m_2$ ,  $k_2$  and  $c_2$  (or  $m_3$ ,  $k_3$  and  $c_3$ ) are the lumped mass, stiffness and viscous damping of TMDA (or TMDB), respectively. Meanwhile, two inerters  $d_1$  and  $d_2$  are linked to the tuned masses  $m_2$  and  $m_3$ , respectively, and their another terminals are either connected to the ground or to the adjacent masses. In the next, the underlying dynamics related to two configurations will be described and all dimensionless parameters will be introduced.

### 3.1.1 G-SDTMDI

The dynamics of whole system depicted in Figure 3.1a is governed by the EOMs:

$$m_1 \ddot{x}_1 = c_2(\dot{x}_2 - \dot{x}_1) + k_2(x_2 - x_1) - c_1 \dot{x}_1 - k_1 x_1 + F(t) \quad (3.1a)$$

$$m_2 \ddot{x}_2 = c_2(\dot{x}_1 - \dot{x}_2) + k_2(x_1 - x_2) + c_3(\dot{x}_3 - \dot{x}_2) + k_3(x_3 - x_2) - d_1 \ddot{x}_2 \quad (3.1b)$$

$$m_3 \ddot{x}_3 = c_3(\dot{x}_2 - \dot{x}_3) + k_3(x_2 - x_3) - d_2 \ddot{x}_3 \quad (3.1c)$$

where  $x_1$ ,  $x_2$  and  $x_3$  are the displacements of  $m_1$ ,  $m_2$  and  $m_3$ , respectively. Meanwhile, the natural frequencies of each subsystem can be computed by:

$$\omega_1 = \sqrt{\frac{k_1}{m_1}}, \quad \omega_2 = \sqrt{\frac{k_2}{m_2}}, \quad \omega_3 = \sqrt{\frac{k_3}{m_3}}. \quad (3.2)$$

And their mechanical damping ratios are evaluated by:

$$\xi_1 = \frac{c_1}{2\sqrt{k_1 m_1}}, \quad \xi_2 = \frac{c_2}{2\sqrt{k_2 m_2}}, \quad \xi_3 = \frac{c_3}{2\sqrt{k_3 m_3}}. \quad (3.3)$$

Based on these mechanical properties, the following dimensionless parameters and constants are introduced in order to facilitate the optimization.

$$\left\{ \begin{array}{l} \nu = \frac{m_2}{m_1}: \text{ The mass ratio between TMDA and primary system} \\ \mu - \nu = \frac{m_3}{m_1}: \text{ The mass ratio between TMDB and primary system} \\ \mu = \frac{m_2 + m_3}{m_1}: \text{ The mass ratio between total tuned mass and primary system} \\ \theta = \frac{d_1}{m_1}: \text{ The inertance-to-mass ratio related to the inerter } d_1 \\ \eta - \theta = \frac{d_2}{m_1}: \text{ The inertance-to-mass ratio related to the inerter } d_2 \\ \eta = \frac{d_1 + d_2}{m_1}: \text{ The total inertance-to-mass ratio} \\ \alpha = \frac{\omega_2}{\omega_1}: \text{ The frequency tuning ratio between TMDA and primary system} \\ \beta = \frac{\omega_3}{\omega_1}: \text{ The frequency tuning ratio between TMDB and primary system} \end{array} \right. \quad (3.4)$$

Finally, the EOMs (3.1) can be recast into the dimensionless form:

$$x_1'' + 2\xi_1 x_1' + x_1 + (\nu + \theta) x_2'' + (\mu + \eta - \nu - \theta) x_3'' = F/k_1 \quad (3.5a)$$

$$(\nu + \theta) x_2'' + (\mu + \eta - \nu - \theta) x_3'' + 2\xi_2 \nu \alpha (x_2' - x_1') + \nu \alpha^2 (x_2 - x_1) = 0 \quad (3.5b)$$

$$(\mu + \eta - \nu - \theta) x_3'' + 2\xi_3 \beta (\mu - \nu) (x_3' - x_2') + \beta^2 (\mu - \nu) (x_3 - x_2) = 0 \quad (3.5c)$$

where the prime stands for differentiation with respect to the scaled time  $\tau$ .

### 3.1.2 I-SDTMDI

The whole system related to I-SDTMDI is shown in Figure 3.1b, whose dynamics is described by:

$$\begin{aligned} m_1 \ddot{x}_1 &= d_1 (\ddot{x}_2 - \ddot{x}_1) + c_2 (\dot{x}_2 - \dot{x}_1) + k_2 (x_2 - x_1) - c_1 \dot{x}_1 - k_1 x_1 + F(t) \\ m_2 \ddot{x}_2 &= d_1 (\ddot{x}_1 - \ddot{x}_2) + c_2 (\dot{x}_1 - \dot{x}_2) + k_2 (x_1 - x_2) + d_2 (\ddot{x}_3 - \ddot{x}_2) + c_3 (\dot{x}_3 - \dot{x}_2) + k_3 (x_3 - x_2) \\ m_3 \ddot{x}_3 &= d_2 (\ddot{x}_2 - \ddot{x}_3) + c_3 (\dot{x}_2 - \dot{x}_3) + k_3 (x_2 - x_3) \end{aligned} \quad (3.6)$$

By taking the same procedure, Eq. (3.6) can be transformed into the dimensionless form as follows:

$$\begin{aligned} x_1'' + 2\xi_1 x_1' + x_1 + \nu x_2'' + (\mu - \nu) x_3'' &= F/k_1 \\ \nu x_2'' + (\mu - \nu) x_3'' + \theta (x_2'' - x_1'') + 2\xi_2 \nu \alpha (x_2' - x_1') + \nu \alpha^2 (x_2 - x_1) &= 0 \\ (\mu - \nu) x_3'' + (\eta - \theta) (x_3'' - x_2'') + 2\xi_3 \beta (\mu - \nu) (x_3' - x_2') + \beta^2 (\mu - \nu) (x_3 - x_2) &= 0 \end{aligned} \quad (3.7)$$

By vanishing the inertance-to-mass ratios  $\eta$  and  $\theta$ , Eqs. (3.5) and (3.7) reduce to the same set of equation, describing the underlying dynamics of a forced SDOF primary system controlled by a SDTMD.

## 3.2 Optimization of G-SDTMDI

For deriving concise solutions to optimal parameters of dampers, it is common practice to take the assumption of an undamped primary system (i.e.  $c_1 = \xi_1 = 0$ ). Meanwhile, it was confirmed in [28, 29, 30, 31] that in the optimal scenario, the TMDB of SDTMD should have zero damping, which will be used as a precondition for the optimal design of SDTMDIs. By taking into consideration the previous facts and taking the Laplace transform of Eq. (3.5), the normalized displacement FRF of primary system controlled by G-SDTMDI can be formulated as:

$$G = \left| \frac{X_1}{F/k_1} \right| = \sqrt{\frac{A + B\xi_3^2}{C + D\xi_3^2}} \quad (3.8)$$

with its four coefficients given by:

$$\left\{ \begin{array}{l} A = \left[ \beta^2 (\mu - \nu) (\nu\alpha^2 - (\mu + \eta)\lambda^2) - (\mu + \eta - \nu - \theta)\lambda^2 (\nu\alpha^2 - (\nu + \theta)\lambda^2) \right]^2 \\ B = 4\beta^2\lambda^2 (\mu - \nu)^2 \left[ \nu\alpha^2 - (\mu + \eta)\lambda^2 \right]^2 \\ C = \left[ \lambda^2 (1 - \lambda^2) \left[ \beta^2 (\mu - \nu) (\mu + \eta) - (\nu + \theta) (\mu + \eta - \nu - \theta)\lambda^2 \right] + \right. \\ \left. \nu\alpha^2\lambda^2 (\mu + \eta - \nu - \theta) \left[ 1 - (1 + \nu + \theta)\lambda^2 \right] - \nu\alpha^2\beta^2 (\mu - \nu) \left[ 1 - (1 + \mu + \eta)\lambda^2 \right] \right]^2 \\ D = 4\beta^2\lambda^2 (\mu - \nu)^2 \left[ (1 - \lambda^2) \left[ \nu\alpha^2 - (\mu + \eta)\lambda^2 \right] - \nu\alpha^2\lambda^2 (\mu + \eta) \right]^2 \end{array} \right. \quad (3.9)$$

Three sets of simulation are performed by varying the mechanical damping ratio  $\xi_3$  of TMDB, and the displacement FRFs of primary system are demonstrated in Figure 3.2. Clearly, the response curves corresponding to different damping levels always intersect at four positions, signifying the existence of four invariant points. Therefore, methodologies based on fixed points could be applied to derive its optimal design. Apparently, the FPT of Den Hartog could not be directly employed, as it is dedicated to systems characterized by two fixed points. Nevertheless, its extended version proposed in [53] can efficiently tackle the optimization problem of systems featured by four invariant points, which will be used to optimize both SDTMDIs hereafter.

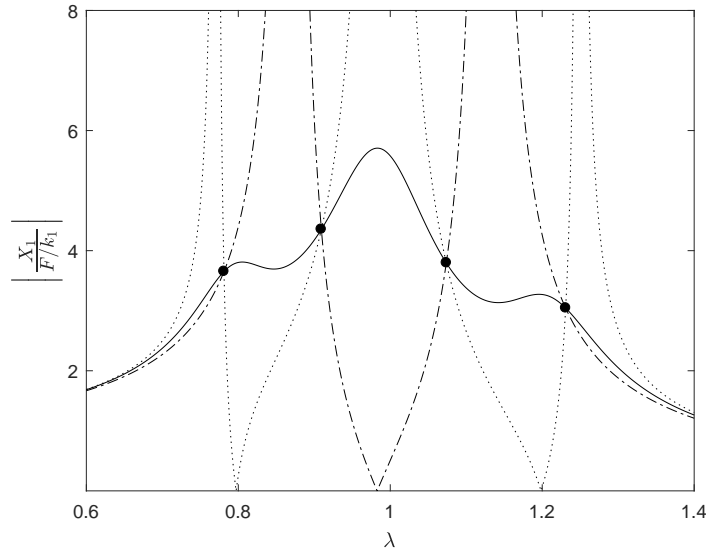


**Figure 3.2:** Displacement FRFs of primary system controlled by a G-SDTMDI with three sets of parameters. Only the mechanical damping ratio  $\xi_3$  varies, while the other parameters remain unchanged:  $\mu = 0.05$ ,  $\nu = 0.04$ ,  $\alpha = 1.3$ ,  $\beta = 0.9$ ,  $\xi_2 = 0$  and  $\eta = \theta = 0.02$ . Dotted line:  $\xi_3 = 0$ , solid line:  $\xi_3 = 0.2$ , dash-dotted line:  $\xi_3 = \infty$ .

### 3.2.1 Analytical derivation of optimal parameters

The total mass ratio  $\mu$  and the total inertance-to-mass ratio  $\eta$  are generally imposed by practical constraints. Therefore, design parameters are the mass ratio  $\nu$  between TMDB and primary system, the natural frequency ratios  $\alpha$  and  $\beta$  between two TMDs and primary system, and the mechanical damping ratio  $\xi_3$  of TMDB.

#### 3.2.1.1 Optimal solutions to $\nu$ , $\alpha$ and $\beta$

The first step is to find the optimal values of  $\nu$ ,  $\alpha$  and  $\beta$  which lead to an identical vibration amplitude at four invariant points. Considering two extreme cases,  $\xi_3 = 0$  and  $\xi_3 \rightarrow \infty$ , one has:

$$G|_{\xi_3=0} = \sqrt{\frac{A}{C}}, \quad G|_{\xi_3 \rightarrow \infty} = \sqrt{\frac{B}{D}}. \quad (3.10)$$

By equating this two expressions, a quartic equation in  $\lambda^2$  is obtained:

$$a_4\lambda^8 + a_3\lambda^6 + a_2\lambda^4 + a_1\lambda^2 + a_0 = 0 \quad (3.11)$$

with coefficients of all terms given by:

$$\left\{ \begin{array}{l} a_4 = -2(\mu + \eta)(\nu + \theta)(\mu + \eta - \nu - \theta) \\ a_3 = 2(\mu + \eta - \nu - \theta) \left[ (\mu + \eta)(\theta + \nu + \nu\alpha^2) + \nu\alpha^2(\nu + \theta)(1 + \mu + \eta) \right] \\ \quad + 2(\mu - \nu)(\mu + \eta)^2\beta^2 \\ a_2 = -2\beta^2(\mu - \nu)(\mu + \eta) \left[ 2\nu\alpha^2 + (\mu + \eta)(1 + \nu\alpha^2) \right] \\ \quad - \nu\alpha^2(\mu + \eta - \nu - \theta) \left[ 2\nu\alpha^2 + (\mu + \eta + \nu + \theta)(2 + \nu\alpha^2) \right] \\ a_1 = 2\nu\alpha^2 \left[ \beta^2(\mu - \nu)(\mu + \eta)(2 + \nu\alpha^2) + \nu\alpha^2\beta^2(\mu - \nu) + \nu\alpha^2(\mu + \eta - \nu - \theta) \right] \\ a_0 = -2\alpha^4\beta^2\nu^2(\mu - \nu) \end{array} \right. \quad (3.12)$$

Let denote the squared vibration amplitude at fixed points as  $h$ , i.e.  $G^2 \Big|_{\xi_3=0} = G^2 \Big|_{\xi_3 \rightarrow \infty} = h$ , which yields another optimality condition in the form of a fourth degree polynomial in  $\lambda^2$ :

$$b_4\lambda^8 + b_3\lambda^6 + b_2\lambda^4 + b_1\lambda^2 + b_0 = 0 \quad (3.13)$$

with five coefficients given as a function of  $\alpha$ ,  $\beta$ ,  $\nu$  and  $h$ :

$$\left\{ \begin{array}{l} b_4 = h(\mu + \eta)^2 \\ b_3 = -2h(\mu + \eta) \left[ (1 + \mu + \eta)\nu\alpha^2 + \mu + \eta \right] \\ b_2 = h\nu^2(1 + \mu + \eta)^2\alpha^4 + 2h\nu(\mu + \eta)(2 + \mu + \eta)\alpha^2 + (h - 1)(\mu + \eta)^2 \\ b_1 = -2\nu\alpha^2 \left[ h\nu(1 + \mu + \eta)\alpha^2 + (h - 1)(\mu + \eta) \right] \\ b_0 = \nu^2\alpha^4(h - 1) \end{array} \right. \quad (3.14)$$

In order to yield the same invariant points, the coefficients of like power of  $\lambda^2$  in Eqs. (3.11) and (3.13) should satisfy the proportionality relationship imposed by the Vieta's theorem, which cumulates into four equations:

$$a_4b_3 - b_4a_3 = 0 \quad (3.15a)$$

$$a_4b_2 - b_4a_2 = 0 \quad (3.15b)$$

$$a_4b_1 - b_4a_1 = 0 \quad (3.15c)$$

$$a_4b_0 - b_4a_0 = 0 \quad (3.15d)$$

By solving simultaneously the four equations in (3.15), the optimal values of  $\alpha$ ,  $\beta$ ,  $\nu$  and  $h$  can be determined and their closed-form formulae are given as a function of the total mass ratio  $\mu$  and two inertance-to-mass ratios  $\eta$  and  $\theta$ , as follows:

- The natural frequency ratio  $\alpha$  between TMDA and primary system is formulated as:

$$\alpha = \sqrt{\frac{(\mu + \eta) [1 + 2(\mu + \eta)]}{(1 + \mu + \eta) [(\mu + \eta)(1 - 2\theta) - \theta]}} \quad (3.16)$$

In order to yield a real value for  $\alpha$ , the inertance-to-mass ratio  $\theta$  should be bounded by:

$$0 = \theta_1^- < \theta < \theta_1^+ = \frac{\mu + \eta}{1 + 2(\mu + \eta)} \quad (3.17)$$

- The natural frequency ratio  $\beta$  between TMDB and primary system is formulated as:

$$\beta = (\mu + \eta) \sqrt{\frac{2}{(1 + \mu + \eta) [1 + 2(\mu + \eta)] [2(\mu + \eta)(\mu + \theta) + \theta - \eta]}} \quad (3.18)$$

Similarly, there exists another constraint for  $\theta$ :

$$\theta > \theta_2^- = \frac{\eta - 2\mu(\mu + \eta)}{1 + 2(\mu + \eta)} \quad (3.19)$$

- The mass ratio  $\nu$  between tuned mass  $m_2$  and primary mass  $m_1$  is equal to:

$$\nu = \frac{\mu + \eta}{1 + 2(\mu + \eta)} - \theta \quad (3.20)$$

whose non-negativity is automatically guaranteed when Eq. (3.17) is satisfied.

- Finally, the squared vibration amplitude  $h$  at four invariant points can be expressed as:

$$h = \frac{1 + \mu + \eta}{\mu + \eta} \quad (3.21)$$

Without loss of generality, the vibration amplitude at fixed points is considered as the  $H_\infty$  norm of primary system in the following context, namely  $\sqrt{h} = \|G\|_\infty$ .

### 3.2.1.2 Optimal solution to $\xi_3$

Up to now, the only parameter to be determined is the mechanical damping ratio  $\xi_3$  which has an important influence on the shape of frequency response curve of primary system. With the knowledge of  $\alpha$ ,  $\beta$ ,  $\nu$  and  $h$ , the mechanical damping ratio can be evaluated by transforming Eq. (3.8) into the following form:

$$\xi_3 = \sqrt{-\frac{A - hC}{B - hD}} \quad (3.22)$$

### 3. Series Double Tuned Mass Damper with Inerters

---

where the only unknown parameter is the frequency  $\lambda$ , which should be properly chosen. According to the extended fixed points technique [53], the optimal  $\xi_3$  should be imposed as the RMS value of damping levels evaluated at three reference frequencies  $\lambda_1$ ,  $\lambda_2$  and  $\lambda_3$ . According to [54], the reference frequencies correspond to the real eigenvalues of two particular dynamical systems,  $G|_{\xi_3 \rightarrow \infty}$  and  $G|_{\xi_3=0}$ . The characteristic equation relevant to  $G|_{\xi_3 \rightarrow \infty}$  is a quadratic polynomial in  $\lambda^2$ , i.e.:

$$P_1(\lambda^2) = (\mu + \eta + 1)(\lambda^2)^2 - 2(\mu + \eta + 1)\lambda^2 + 1 = 0 \quad (3.23)$$

from which two reference frequencies can be obtained, as follows:

$$\lambda_1^2 = 1 - \sqrt{\frac{\mu + \eta}{\mu + \eta + 1}}, \quad \lambda_2^2 = 1 + \sqrt{\frac{\mu + \eta}{\mu + \eta + 1}}. \quad (3.24)$$

And the eigenvalue of  $G|_{\xi_3=0}$  should satisfy the following expression of order 3 in  $\lambda^2$ :

$$P_2(\lambda^2) = (\gamma + 1)^2(\lambda^2)^3 - (\gamma + 1)(4\gamma + 3)(\lambda^2)^2 + (\gamma + 1)(2\gamma + 3)\lambda^2 - 1 = 0 \quad (3.25)$$

where an intermediate variable  $\gamma = \mu + \eta$  is introduced in order to facilitate the curve fitting process, which stands for the sum of the total mass ratio and the total inertance-to-mass ratio. Clearly, Eq. (3.25) has three possible roots, however, only the one between  $\lambda_1$  and  $\lambda_2$  is chosen as the third reference frequency  $\lambda_3$  [53]. Although the exact solutions to the roots of  $P_2(\lambda^2)$  could be analytically derived, their formulae are extremely cumbersome and irreducible. Therefore, only the curve-fitted solution is retained, which is in the form of linear polynomial in  $\gamma$ :

$$\lambda_3^2 = 1 - \frac{\gamma}{4} = 1 - \frac{\mu + \eta}{4} \quad (3.26)$$

The non-negativity of  $\lambda_3^2$  imposes that  $\mu + \eta \leq 4$ , which is satisfied for most engineering applications. After finding the expressions of three reference frequencies, Eq. (3.22) can be employed to evaluate their corresponding mechanical damping ratios,  $\xi|_{\lambda_1}$ ,  $\xi|_{\lambda_2}$  and  $\xi|_{\lambda_3}$ . Finally, the optimal mechanical damping ratio  $\xi_3$  is calculated as their RMS value, namely:

$$\xi_3 = \sqrt{\frac{\xi^2|_{\lambda_1} + \xi^2|_{\lambda_2} + \xi^2|_{\lambda_3}}{3}} = \sqrt{\frac{\gamma^3(\gamma^3 + 34\gamma^2 - 111\gamma - 160)}{24(\gamma - 4)(\gamma + 1)(2\gamma + 1)[2\gamma(\mu + \theta) + \theta - \eta]}} \quad (3.27)$$

which remains real if Eq. (3.19) is satisfied. In summary, the allowable interval for the inertance-to-mass ratio  $\theta$  is given by  $\theta \in (\theta^-, \theta^+)$  with its lower and upper bounds defined as:

$$\theta^- = \max\{\theta_1^-, \theta_2^-\}, \quad \theta^+ = \theta_1^+. \quad (3.28)$$

### 3.2.2 Validation of derived solutions

It is of a primary importance to validate the proposed optimal design of G-SDTMDI. To this end, it is pertinent to reduce the G-SDTMDI to a SDTMD by vanishing the inertance, i.e.  $\eta = \theta = 0$  and compare its dynamics response to that whose parameters are tuned by using the  $H_\infty$  optimization criterion. The optimal parameters of SDTMD based on the extended FPT are summarized in Table 3.1. Meanwhile, exact solutions to its  $H_\infty$  optimal design will be numerically solved.

$\nu$	$\alpha$	$\beta$	$\xi_2$	$\xi_3$	$\ G\ _\infty$
$\frac{\mu}{1+2\mu}$	$\sqrt{\frac{1+2\mu}{1+\mu}}$	$\sqrt{\frac{1}{(1+\mu)(1+2\mu)}}$	0	$\sqrt{\frac{\mu(\mu^3 + 34\mu^2 - 111\mu - 160)}{48(\mu-4)(\mu+1)(2\mu+1)}}$	$\sqrt{\frac{1+\mu}{\mu}}$

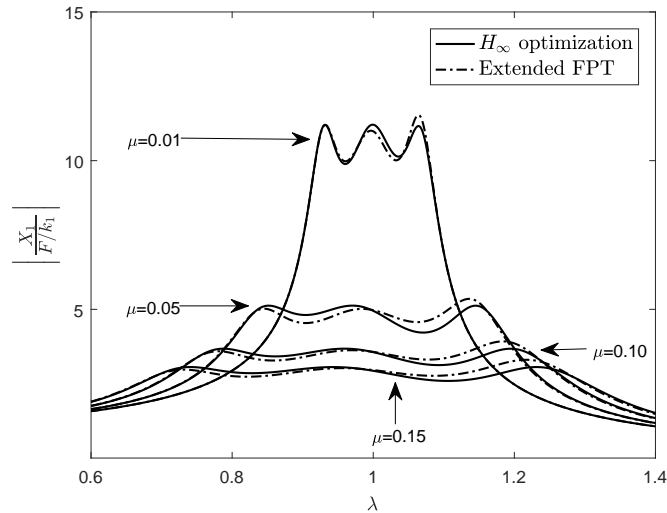
**Table 3.1:** Closed-form formulae to optimal parameters of SDTMD attached to a SDOF undamped primary system under force excitation.

$\mu = 0.01$	$\nu$	$\alpha$	$\beta$	$\xi_2$	$\xi_3$	$\ G\ _\infty$
$H_\infty$ optimization	0.0098	1.0057	0.9871	0	0.0904	11.2093
Extended FPT	0.0098	1.0049	0.9852	0	0.0904	11.5344
$\mu = 0.05$	$\nu$	$\alpha$	$\beta$	$\xi_2$	$\xi_3$	$\ G\ _\infty$
$H_\infty$ optimization	0.0455	1.0303	0.9278	0	0.1923	5.1251
Extended FPT	0.0455	1.0235	0.9305	0	0.1944	5.3527
$\mu = 0.10$	$\nu$	$\alpha$	$\beta$	$\xi_2$	$\xi_3$	$\ G\ _\infty$
$H_\infty$ optimization	0.0833	1.0554	0.8717	0	0.2628	3.6778
Extended FPT	0.0833	1.0445	0.8704	0	0.2629	3.9222
$\mu = 0.15$	$\nu$	$\alpha$	$\beta$	$\xi_2$	$\xi_3$	$\ G\ _\infty$
$H_\infty$ optimization	0.1154	1.0784	0.8210	0	0.3094	3.0598
Extended FPT	0.1154	1.0632	0.8179	0	0.3090	3.3036

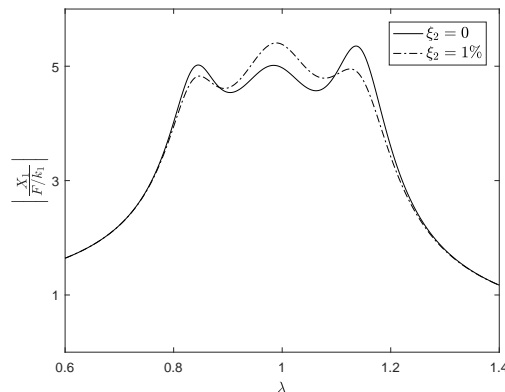
**Table 3.2:** Exact and approximate parameters of SDTMD based on the  $H_\infty$  optimization criterion and the extended FPT, respectively, for four mass ratios:  $\mu = 0.01$ , 0.05, 0.10 and 0.15.

Table 3.2 summarizes the exact and approximate values for all parameters of SDTMD, which are derived according to the  $H_\infty$  optimization criterion and the extended FPT, respectively. Four values of mass ratio are considered,  $\mu = 0.01$ , 0.05, 0.10 and 0.15, and their corresponding FRFs are depicted in Figure 3.3. One can observe that with the  $H_\infty$  optimal design, the FRFs are featured by three distinct peaks having the same amplitude, while there exists a slight misalignment

among these peaks when analytically obtained parameters are used. In general, the extended FPT yields approximate but highly accurate solutions, due to which this method can be employed for optimizing a coupled system featured by four invariant points.



**Figure 3.3:** Displacement FRFs of primary system controlled by a SDTMD, whose parameters are tuned by the  $H_\infty$  optimization criterion (solid lines) and the extended FPT (dash-dotted lines), respectively. Four sets of simulation are performed corresponding to different mass ratios:  $\mu = 0.01, 0.05, 0.10$  and  $0.15$ .



**Figure 3.4:** Displacement FRFs of primary system controlled by a G-SDTMDI (solid line:  $\xi_2 = 0$ , dash-dotted line:  $\xi_2 = 1\%$ ). The tuning parameters are optimized for:  $\mu = 0.05$  and  $\eta = \theta = 0$ .

Besides, the phenomenon of zero damping for  $\xi_2$  is encountered in both numerical

and analytical designs for all mass ratios, proving that no optimal value exists for  $c_2$  when bounded by the non-negativity constraint. In practice, the zero-damping situation never occurs, therefore, the influence of damping in TMDA on the global dynamics should be studied. In Figure 3.4, the FRFs of primary system are depicted when controlled by an optimized G-SDTMDI with zero damping for TMDA (marked by solid line) or with an inherent damping ratio of 1% (marked by dash-dotted line). Clearly, the global frequency response slightly changes, with the difference between peak vibration amplitudes being of only 1%. Hence, the proposed analytical design can be still used in practical applications.

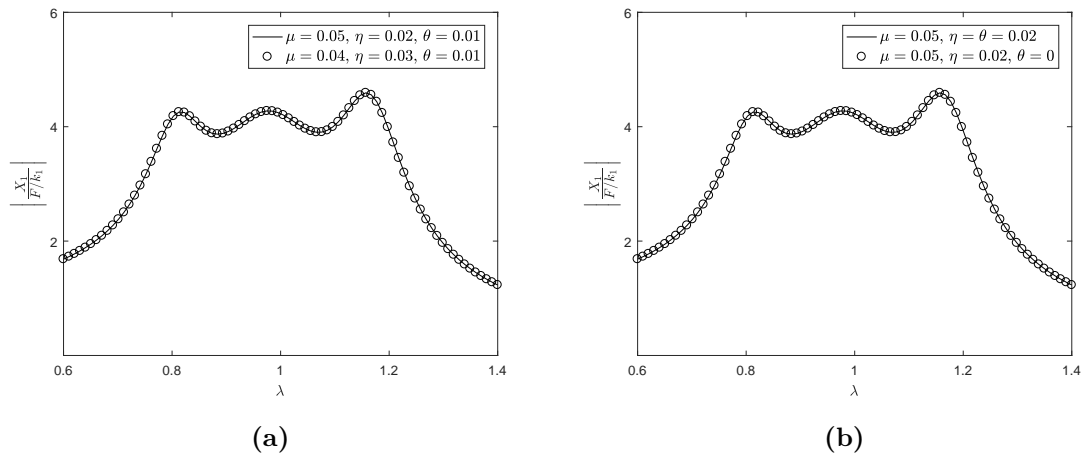


**Figure 3.5:** Displacement FRFs of primary system controlled by an optimized G-SDTMDI with different sets of parameters. (a) Solid line:  $\mu = 0.05$ ,  $\eta = 0.02$  and  $\theta = 0.01$ ; circle marker:  $\mu = 0.04$ ,  $\eta = 0.03$  and  $\theta = 0.01$ . (b) Solid line:  $\mu = 0.05$  and  $\eta = \theta = 0.02$ ; circle marker:  $\mu = 0.05$ ,  $\eta = 0.02$  and  $\theta = 0$ .

### 3.2.3 Remarks

As evident from Eq. (3.21), the normalized displacement amplitude at fixed points is dictated by the sum of the total mass ratio  $\mu$  and the total inertance-to-mass ratio  $\eta$ . Therefore, one can imagine that the vibration control performance of G-SDTMDI will be maintained if and only if this specific value,  $\mu + \eta$ , remains unchanged. This prediction is confirmed by Figure 3.5a, in which the dynamics response of primary system does not change as the mass ratio  $\mu$  decreases while the total inertance-to-mass ratio  $\eta$  increases in order to keep the same amount of  $\mu + \eta$ .

Another important finding to be mentioned is that the vibration control capability of G-SDTMDI is irrelevant to the distribution of inertance in the control scheme. As demonstrated in Figure 3.5b, the FRF of primary system remains unchanged either by vanishing the inertance  $d_1$  (i.e.  $\theta = 0$ ) or removing the inertance  $d_2$  (i.e.  $\eta = \theta$ ). Therefore, the G-SDTMDI can be simplified into two configurations: type I

### 3. Series Double Tuned Mass Damper with Inerters

with only one inverter placed between the TMDB and the ground (depicted in Figure 3.6a), and type II with only one inverter relating the TMDB to the ground (shown in Figure 3.6b). For the purpose of completeness, the analytical formulae of optimal parameters for two variants are provided in Table 3.3 with allowable bounds on  $\eta$  specified.

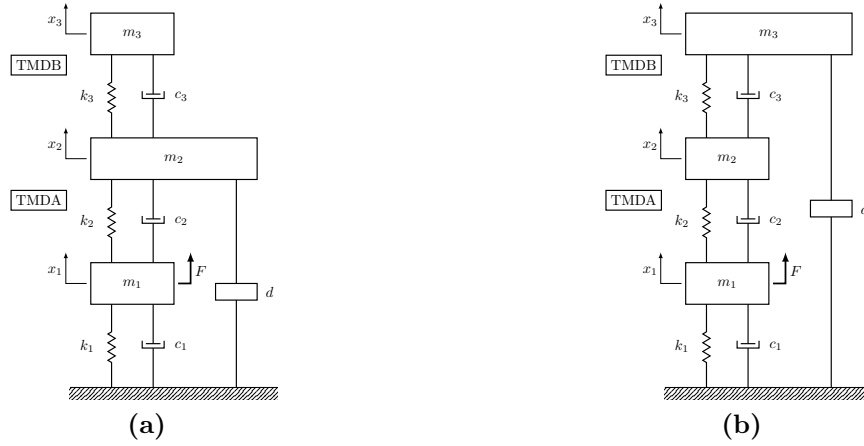


**Figure 3.6:** Two variant configurations of G-SDTMDI: (a) type I with only one inverter placed between the TMDB and the ground; (b) type II with only one inverter placed between the TMDB and the ground.

Parameters	Type I	Type II
$\nu$	$\frac{\mu - 2\eta\gamma}{2\gamma + 1}$	$\frac{\gamma}{2\gamma + 1}$
$\alpha$	$\sqrt{\frac{\gamma(2\gamma + 1)}{(\gamma + 1)(\mu - 2\eta\gamma)}}$	$\sqrt{\frac{2\mu + 2\eta + 1}{\mu + \eta + 1}}$
$\beta$	$\sqrt{\frac{1}{(\gamma + 1)(2\gamma + 1)}}$	$\sqrt{\frac{2\gamma^2}{(\gamma + 1)(2\gamma + 1)(2\mu\gamma - \eta)}}$
$\xi_2$	0	0
$\xi_3$	$\sqrt{\frac{\gamma(\gamma^3 + 34\gamma^2 - 111\gamma - 160)}{48(\gamma - 4)(\gamma + 1)(2\gamma + 1)}}$	$\sqrt{\frac{\gamma^3(\gamma^3 + 34\gamma^2 - 111\gamma - 160)}{24(\gamma - 4)(\gamma + 1)(2\gamma + 1)(2\mu\gamma - \eta)}}$
$\eta \in (\eta^-, \eta^+)$	$\eta^- = 0, \eta^+ = \frac{-\mu + \sqrt{\mu^2 + 2\mu}}{2}$	$\eta^- = 0, \eta^+ = \frac{2\mu^2}{1 - 2\mu}$ with $\mu < 0.5$ .

**Table 3.3:** Analytical formulae to optimal parameters of two variants of G-SDTMDI under force excitation and the allowable bounds on the total inertance-to-mass ratio  $\eta$ .

### 3.3 Optimization of I-SDTMDI

The optimal design of I-SDTMDI will be carried out by employing the same procedure in Section 3.2. For the purpose of brevity, the detailed optimization process is omitted and only the expressions of different constants are provided in Appendix B. By applying the proportionality relationship (3.15) with constants  $a_i$  and  $b_i$  ( $i = 0, \dots, 4$ ) given in Eqs. (B.4) and (B.3), the optimal solutions for  $\alpha$ ,  $\beta$ ,  $\nu$  and  $h$  could be analytically obtained. Specifically, the squared displacement amplitude at fixed points is expressed as:

$$h = \frac{(1+\mu)[\theta + \mu(1+\theta)]}{\mu^2(1+\theta)} = \left[1 + \frac{\theta}{\mu(1+\theta)}\right] \frac{1+\mu}{\mu} \quad (3.29)$$

suggesting that  $h > (1+\mu)/\mu$  always holds for any positive  $\theta$ . Reminding that  $(1+\mu)/\mu$  is exactly the squared vibration amplitude at fixed points related to the SDTMD (as given in Table 3.1), a conclusion could be then drawn that the vibration control performance of a SDTMD will be deteriorated by inserting an inerter between the primary mass  $m_1$  and tuned mass  $m_2$  of TMDA. This finding will be examined by looking at the frequency response of primary system under the condition that all optimal parameters are obtained.

Furthermore, it clearly suggests that the vibration amplitude at fixed points is solely controlled by the total mass ratio  $\mu$  and the inertance-to-mass ratio  $\theta$ . Alternatively speaking, the inerter  $d_2$  incorporated between masses of TMDA and TMDB has no influence on the global vibration control effect of I-SDTMDI. In the objective of reducing the structural complexity and simplifying the optimization procedure, the inerter  $d_2$  is then removed in the following context by imposing  $\theta = \eta$ .

After the simplification, closed-form solutions to the optimal  $\alpha$ ,  $\beta$  and  $\nu$  are formulated as a function of the total mass ratio  $\mu$  and the inertance-to-mass ratio  $\eta$ :

$$\alpha = \sqrt{\frac{(\mu + \eta + 2\mu\eta)[2\mu(\mu\eta + \mu + \eta) + \mu + \eta]}{\mu(\mu + 1)(\mu + \eta)}} \quad (3.30)$$

$$\beta = \sqrt{\frac{\mu + \eta + 2\mu\eta}{(\mu + 1)[2\mu(\mu\eta + \mu + \eta) + \mu + \eta]}} \quad (3.31)$$

$$\nu = \frac{\mu(\mu + \eta)}{2\mu(\mu\eta + \mu + \eta) + \mu + \eta} \quad (3.32)$$

By vanishing the inertance, i.e.  $\eta = 0$ , the expressions of  $h$ ,  $\alpha$ ,  $\beta$  and  $\nu$  in Eqs. (3.29)-(3.32) are exactly the same as optimal parameters of SDTMD, as given in Table 3.1.

Again, the optimal mechanical damping ratio  $\xi_3$  is chosen as the RMS value of three mechanical damping ratios evaluated at reference frequencies, which are the

### 3. Series Double Tuned Mass Damper with Inerters

---

real roots of characteristic equations of  $G|_{\xi_3 \rightarrow \infty}$  and  $G|_{\xi_3=0}$ , respectively:

$$P_3(\lambda^2) = (\mu + 1)(\mu + \eta + \mu\eta)(\lambda^2)^2 - 2(\mu + 1)(\mu + \eta + \mu\eta)\lambda^2 + 2\mu\eta + \mu + \eta = 0 \quad (3.33)$$

and

$$\begin{aligned} P_4(\lambda^2) = & (\mu + 1)^2(\mu\eta + \mu + \eta)(2\mu\eta + \mu + \eta)(\lambda^2)^3 \\ & - (\mu + 1)(\mu\eta + \mu + \eta)(6\eta\mu^2 + 8\eta\mu + 4\mu^2 + 3\mu + 3\eta)(\lambda^2)^2 \\ & + (\mu + 1)(2\mu\eta + \mu + \eta)(2\eta\mu^2 + 4\eta\mu + 2\mu^2 + 3\mu + 3\eta)\lambda^2 - (2\mu\eta + \mu + \eta)^2 = 0 \end{aligned} \quad (3.34)$$

The first characteristic equation (3.33) yields two reference frequencies described by:

$$\lambda_1^2 = 1 - \mu\sqrt{\frac{\eta + 1}{(\mu + 1)(\mu\eta + \mu + \eta)}}, \quad \lambda_2^2 = 1 + \mu\sqrt{\frac{\eta + 1}{(\mu + 1)(\mu\eta + \mu + \eta)}}. \quad (3.35)$$

while Eq. (3.34) is a cubic polynomial in  $\lambda^2$  and its constants before terms are dependent of two variables,  $\mu$  and  $\eta$ . Therefore, under no circumstance, the concise solution of the third reference frequency  $\lambda_3^2$  could be achieved. In this context, the surface fitting technique is applied to provide an approximate solution of  $\lambda_3^2$  in terms of both  $\mu$  and  $\eta$ , as follows:

$$\lambda_3^2 = 1.00 - 0.16\mu + 0.24\eta - 1.19\mu^2 + 2.75\mu\eta - 1.97\eta^2 \quad (3.36)$$

This surface-fitted solution is a polynomial of second degree in both  $\mu$  and  $\eta$  and

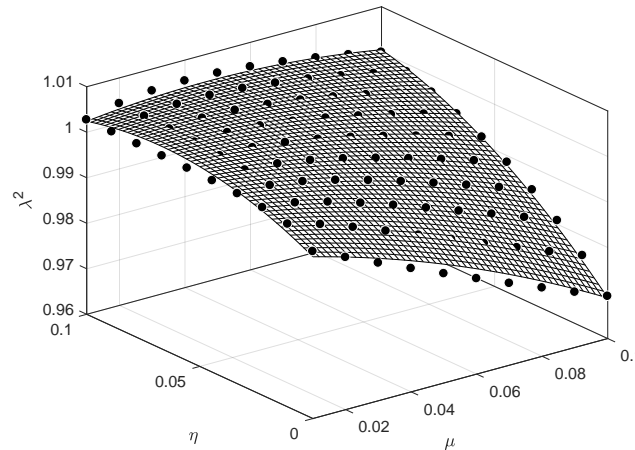


**Figure 3.7:** Comparison of the exact and fitted solutions for  $\lambda_3^2$ . Black dots: exact solution at given pairs of  $(\mu, \eta)$ ; grid surface: the fitted solutions.

are evaluated for  $\mu \in [0.01, 0.10]$  and  $\eta \in [0, 0.10]$ , which is represented by the grid

surface in Figure 3.7, while the exact solutions are marked by black dots. It should be mentioned that for a larger interval of both  $\mu$  and  $\eta$ , more accurate solutions could be obtained by increasing the degree of employed polynomial model. With the knowledge of three reference frequencies, one can calculate the optimal value for  $\xi_3$  by employing Eq. (3.27), whose analytical formulation is, however, omitted in this thesis.

Figure 3.8 demonstrates the FRFs of primary system coupled with a SDTMD, whose parameters correspond to those reduced from a G-SDTMDI or I-SDTMDI. Their coincidence validates the proposed optimal design for the I-SDTMDI.

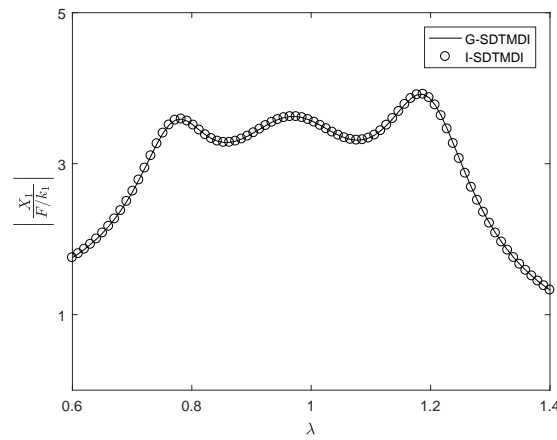


**Figure 3.8:** Displacement FRFs of primary system controlled by a classic SDTMD with optimal parameters derived for G-SDTMDI or I-SDTMDI. The total mass ratio is set as:  $\mu = 0.10$ . Solid line: with optimal design for G-SDTMDI, circle marker: with optimal design for I-SDTMDI.

	TMD [2]	TMDI [46]	SDTMD	G-SDTMDI	I-SDTMDI
$\ G\ _\infty$	$\sqrt{\frac{\mu+2}{\mu}}$	$\sqrt{\frac{\mu+\eta+2}{\mu+\eta}}$	$\sqrt{\frac{\mu+1}{\mu}}$	$\sqrt{\frac{\mu+\eta+1}{\mu+\eta}}$	$\sqrt{\left(1 + \frac{\eta}{\mu(1+\eta)}\right) \frac{\mu+1}{\mu}}$

**Table 3.4:**  $H_\infty$  norm of normalized displacement FRF of primary system when controlled by five types of dampers: TMD, TMDI, SDTMD, G-SDTMDI and I-SDTMDI.

### 3.4 Numerical investigation

Up to now, the optimal design of both types of SDTMDIs is conducted based on the extended FPT. Table 3.4 summarizes all normalized displacement amplitudes of

primary system at fixed points when controlled by five types of damper, i.e. TMD [2], TMDI [46], SDTMD, G-SDTMDI and I-SDTMDI.

A first observation is that in the case of a SDOF primary system under force excitation, the SDTMD leads to the same vibration amplitude at invariant points as the IDVA plotted in Figure 1.13 (i.e. the IDVA-C3 in [53]). Therefore, one can conclude that the SDTMD and the IDVA are equivalent in terms of vibration control.

#### 3.4.1 Performance index

In order to quantify the improvement of vibration control effect of damper II over the damper I, it is pertinent to introduce a performance index  $P$  defined as:

$$P\{I, II\} = \left(1 - \frac{\|G\|_{\infty, II}}{\|G\|_{\infty, I}}\right) \times 100\% \quad (3.37)$$

The damper II outperforms the damper I when their relevant performance index is positive, and the larger the positive value of  $P\{I, II\}$  is, the more significant this outperformance is. It is the opposite case if a negative value is encountered.

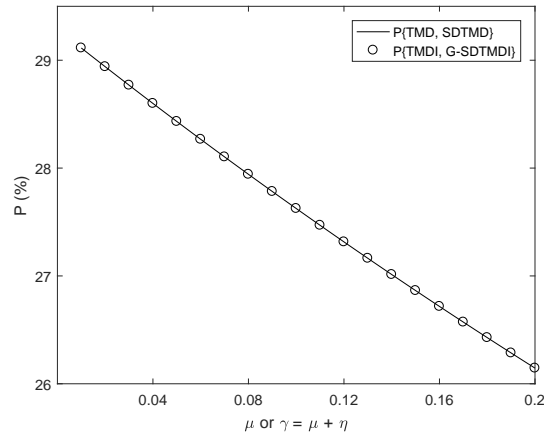


**Figure 3.9:** Evolution of performance indices as a function of  $\mu$  or  $\gamma = \mu + \eta$ . Solid line:  $P\{\text{TMD}, \text{SDTMD}\}$ , circle markers:  $P\{\text{TMDI}, \text{G-SDTMDI}\}$ .

Let first look at the evolution of performance index relevant to the TMD and SDTMD and their counterpart with grounded inerter as a function of the mass ratio  $\mu$  and  $\mu + \eta$ , respectively. As demonstrated in Figure 3.9, the curve of  $P\{\text{TMD}, \text{SDTMD}\}$  is coincident with that of  $P\{\text{TMDI}, \text{G-SDTMDI}\}$ . Therefore, it suggests that for both classic TMD and SDTMD, the incorporation of a grounded inerter is equivalent to increase the physical mass of absorber by the same amount of the added inertance. Moreover, one can remark from Figure 3.9 that with the same

value of  $\mu$  or  $\mu + \eta$ , the configuration of SDTMD can decrease the peak vibration amplitude of primary system by 26 – 29% when compared to the TMD.

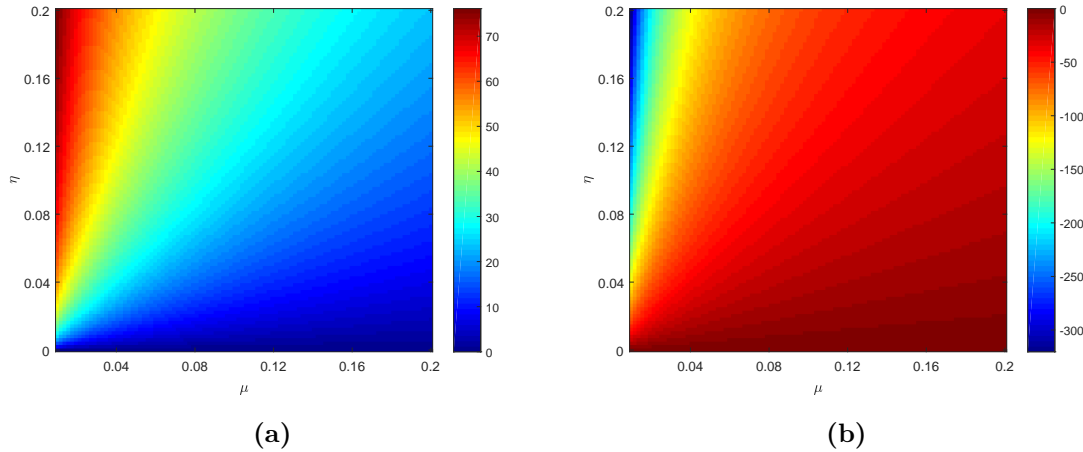


**Figure 3.10:** Evolution of performance indices against the total mass ratio  $\mu$  and the total inertance-to-mass ratio  $\eta$ : (a)  $P\{\text{SDTMD, G-SDTMDI}\}$ ; (b)  $P\{\text{SDTMD, I-SDTMDI}\}$ .

The performance indices relating two types of SDTMDIs and the SDTMD are also investigated, as depicted in Figure 3.10. Apparently, the G-SDTMDI always yields a positive performance index, while those related to the I-SDTMDI are always negative. Thus, one can conclude that a grounded inerter contributes to the improvement of vibration control performance of SDTMD, while only potential detrimental effect is observed if one incorporates an inerter between the primary system and the TMDA. Moreover, for both configurations, changes made to the control effects of a SDTMD are much pronounced when a considerable value of the ratio  $\eta/\mu$  is present. In the extreme case where a small mass ratio  $\mu$  combined with a large inertance-to-mass ratio  $\eta$  is encountered, the performance index could go up to 70% for the G-SDTMDI, and migrates towards  $-300\%$  for the I-SDTMDI.

### 3.4.2 Displacement FRF

The displacement FRFs of primary system are plotted in Figure 3.11 when controlled by five aforementioned types of damper. The mass ratio and the inertance-to-mass ratio are imposed as:  $\mu = 0.05$  and  $\eta = 0.02$ . The vibration control performance of a damper is characterized by two features: the peak vibration amplitude of target system and the frequency bandwidth of vibration reduction, the definition of which is demonstrated in Figure 3.11a. Accordingly, their values corresponding to different dampers are summarized in Table 3.5. Clearly, the G-SDTMDI has the best capability of vibration control, featured by the broadest reduction bandwidth and the minimal vibration amplitude of controlled system. More precisely, compared to the

classic TMD and SDTMD, the G-SDTMDI can enlarge the reduction bandwidth by 54.2% and 17.8%, and reduce the peak amplitude by 28.3% and 14.2%, respectively. One can image that with a larger inertance, the improvement will become more significant. Meanwhile, the I-SDTMDI leads to a peak amplitude similar to the classic TMD, and decreases the reduction bandwidth by 15.3% compared with the classic SDTMD, confirming the previous remark that incorporating an inerter between the main system and tuned mass of TMDA could bring detrimental effect to the vibration control performance.

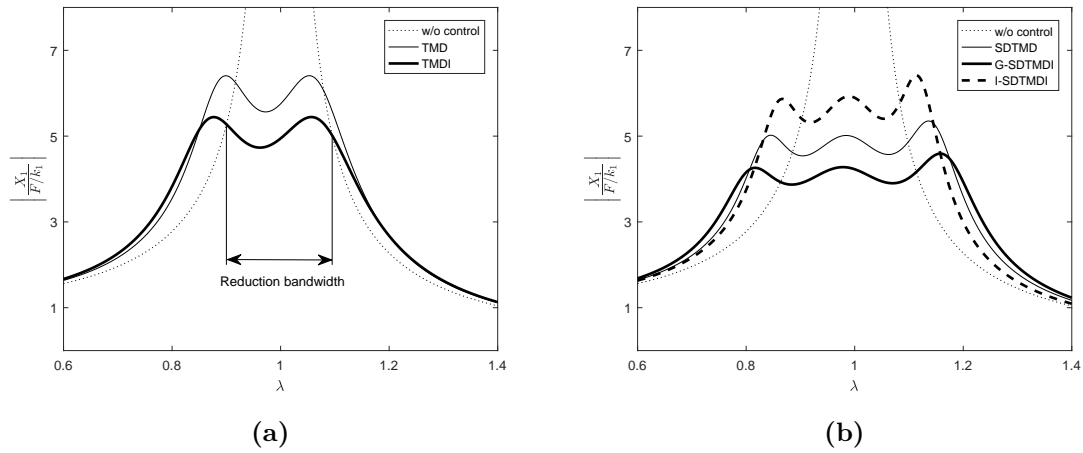


**Figure 3.11:** Displacement FRFs of primary system under harmonic force excitation with  $\mu = 0.05$  and  $\eta = 0.02$ . (a) Dotted line: without control, thin solid line: classic TMD, thick solid line: TMDI. (b) Dotted line: without control, thin solid line: classic SDTMD, thick solid line: G-SDTMDI, thick dashed line: I-SDTMDI.

	TMD [2]	TMDI [46]	SDTMD	G-SDTMDI	I-SDTMDI
Reduction bandwidth	0.1625	0.1948	0.2128	0.2506	0.1803
Peak amplitude	6.4084	5.4443	5.3527	4.5923	6.4170

**Table 3.5:** Frequency bandwidths of vibration reduction and peak vibration amplitude of primary system when controlled by five types of dampers for the set of parameters:  $\mu = 0.05$  and  $\eta = 0.02$ .

### 3.4.3 Discussion

It should be mentioned that the primary system under investigation is of SDOF and the best control performance is observed when the inerter is grounded. The control performance of a TMDI on a MDOF primary system was considered by Masri et al.

[157], revealing that the control efficiency under stationary excitation is maximized when the inerter is placed between the tuned mass and the ground. When a civil structure of multiple storeys is to be controlled, the proposed G-SDTMDI can be installed in such a way that the SDTMD is connected to a specific floor (usually the top floor) via the spring  $k_2$  and damper  $c_2$ , meanwhile, the inerter  $d$  relates one of its two tuned masses to a penultimate or lower floor. Such an implementation was also considered in [158], in which a TMDI is employed to mitigate the wind-induced vibration of a tall building.

### 3.5 Concluding remarks

Two types of SDTMDIs are investigated in this chapter, and their optimal design is conducted according to the extended FPT for an harmonically forced SDOF primary system. Therefore, closed-form solutions to the optimal parameters of SDTMD could be also obtained by vanishing the inertance, whose accuracy is validated by comparing with numerical solutions to the relevant  $H_\infty$  optimization problem.

The G-SDTMDI contributes to the decrease of peak vibration amplitude of primary system and the broadening of frequency range of vibration reduction, thereby entailing a better performance of vibration control. Moreover, its control effect is only influenced by the total mass ratio  $\mu$  and the total inertance-to-mass ratio  $\eta$ . Therefore, two variant layouts can be developed by combining the two grounded inerters into one in order to keep the structural simplicity.

Distinguished from the G-SDTMDI, the two inerters positioned between three vibrating masses are not interchangeable in the case of I-SDTMDI. It is hinted that its control effect is solely controlled by the inerter between the primary mass and its adjacent TMDA, while it is irrelevant to the inerter relating two TMDs. Nevertheless, the vibration amplitude of main system is amplified compared to the SDTMD and the effective frequency bandwidth of vibration mitigation is decreased. Therefore, only adverse effect on the vibration control performance could be introduced by incorporating an inerter between vibrating masses, for which this configuration should not be considered for further applications of vibration control.

Finally, other calibration strategies could be applied in future work to tune the G-SDTMDI for different design objectives.

Instead of using the inerter, the next chapter will consist in incorporating a linear negative stiffness element in existing control devices and its influence on control efficiency will be investigated.



## Chapter 4

# Dynamic Vibration Absorber with Negative Stiffness

The previous two chapters demonstrated that the employment of grounded inerter can enhance the vibration control performance of DVA due to its effect of mass amplification. Meanwhile, it was remarked in [70] that incorporating a negative stiffness between the tuned mass of absorber and the base can also improve the vibration attenuation of primary system. Distinguished from a grounded inerter, the mechanism related to the negative stiffness can be described as: the inclusion of a negative stiffness will amplify the relative motion across the two terminals of viscous damper, therefore, more energy from the mechanical system can be dissipated, entailing a reduced vibration amplitude.

In this chapter, the NSDVA based on the non-traditional DVA will be first investigated, whose optimal design will be carried out according to the FPT and the SMC. The advantage of such a non-traditional configuration will be discussed in the next chapter. Since the inclusion of negative stiffness could destabilize the whole system, a thorough stability analysis will be performed and its allowable bounds will be explicitly specified in each optimal scenario. Finally, the control capability of NSDVA could be further enhanced by replacing its viscous damper with an inerter-based mechanical network, yielding a novel control device termed as the non-traditional IDVA with negative stiffness (NSIDVA). In the end, its optimal design will be carried out based on the SMC. Considering that the SDOF primary system coupled with the NSIDVA is of three DOFs, an optimality condition will be first postulated and will be analytically proven in this chapter.

### 4.1 NSDVA

The undamped primary system controlled by a non-traditional DVA and the NSDVA is depicted in Figures 4.1a and 4.1b, respectively. Clearly, the NSDVA is based on the DVA with a supplemental negative stiffness  $k_n$  relating its mass to the base.

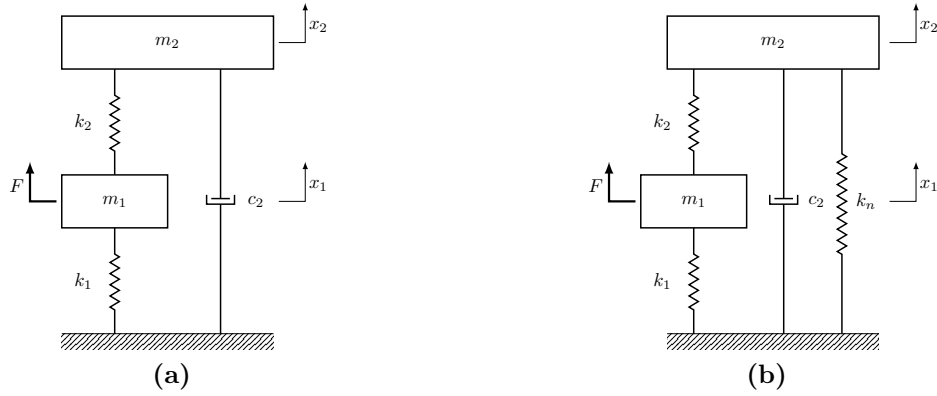


**Figure 4.1:** Schematic diagrams of a SDOF undamped primary system controlled by a: (a) non-traditional DVA; (b) NSDVA.

### 4.1.1 Mathematical modeling

The dynamics of whole system in Figure 4.1b is governed by:

$$m_1 \ddot{x}_1 = k_2(x_2 - x_1) - k_1 x_1 + F(t) \quad (4.1a)$$

$$m_2 \ddot{x}_2 = k_2(x_1 - x_2) - k_n x_2 - c_2 \dot{x}_2 \quad (4.1b)$$

in which all designations are given in Section 1.1.1. An additional dimensionless parameter  $\eta$  is herein introduced, which is defined as the ratio of negative stiffness and the mechanical stiffness of primary system:

$$\eta = \frac{k_n}{k_1} \quad (4.2)$$

with  $\eta \leq 0$ . Then, the EOMs (4.1) can be transformed into:

$$x_1'' + (1 + \mu\alpha^2)x_1 - \mu\alpha^2 x_2 = F(\tau)/k_1 \quad (4.3a)$$

$$x_2'' + 2\xi\alpha x_2' + \alpha^2(x_2 - x_1) + \frac{\eta}{\mu} x_2 = 0 \quad (4.3b)$$

The dimensionless frequency variable, complex magnitudes of displacement  $x_1$  and external force  $F(\tau)$  are denoted by  $\bar{s}$ ,  $X_1$  and  $F$ , respectively. Therefore, the normalized displacement FRF of primary system can be expressed as:

$$\begin{aligned} G(\bar{s}) &= \frac{X_1}{F/k_1} \\ &= \frac{\mu\bar{s}^2 + 2\mu\xi\alpha\bar{s} + \eta + \mu\alpha^2}{\mu\bar{s}^4 + 2\mu\xi\alpha\bar{s}^3 + (\eta + \mu + \mu\alpha^2 + \mu^2\alpha^2)\bar{s}^2 + 2\mu\xi\alpha(1 + \mu\alpha^2)\bar{s} + \eta + \mu\alpha^2(1 + \eta)} \end{aligned} \quad (4.4)$$

where  $F/k_1$  corresponds to its static deflection controlled by a DVA (namely  $\eta = 0$ ). It is worth noting that as a negative stiffness is present, the static displacement of primary system is no longer equal to  $F/k_1$ , as evident from  $G(\bar{s} = 0) \neq 1$ .

### 4.1.2 Stability analysis

In light of the inclusion of negative stiffness, it is of a special importance to specify the allowable bound on the value of negative stiffness, within which the coupled system remains stable.

According the Routh-Hurwitz stability criterion, a system is asymptotically stable if and only if all its eigenvalues lie in the left half of the complex plane. Denoted by  $\lambda$ , eigenvalues can be determined by the characteristic polynomial  $P(\lambda)$  of the two DOF system in the form of:

$$P(\lambda) = \lambda^4 + \delta_1\lambda^3 + \delta_2\lambda^2 + \delta_3\lambda + \delta_4 \quad (4.5)$$

and the stability of coupled system is guaranteed when the following necessary and sufficient conditions are satisfied:

$$\delta_1 > 0, \quad \delta_3 > 0, \quad \delta_4 > 0, \quad \delta_1\delta_2\delta_3 > \delta_3^2 + \delta_1^2\delta_4. \quad (4.6)$$

where all real coefficients of the characteristic polynomial  $P(\lambda)$  correspond to the ones in the denominator of the FRF  $G(\bar{s})$ , recasting into the monic form. Therefore, these coefficients are given by

$$\delta_1 = 2\xi\alpha, \quad \delta_2 = 1 + \frac{\eta}{\mu} + (1 + \mu)\alpha^2, \quad \delta_3 = 2\xi\alpha(1 + \mu\alpha^2), \quad \delta_4 = \frac{\eta}{\mu} + (1 + \eta)\alpha^2. \quad (4.7)$$

By substituting Eq. (4.7) into (4.6), the constraint on negative stiffness ratio  $\eta$  is determined:

$$\eta > -\frac{\mu\alpha^2}{\mu\alpha^2 + 1} = -1 + \frac{1}{\mu\alpha^2 + 1} \quad (4.8)$$

where the expression of lower bound on  $\eta$  is implicit due to the probable dependence between the frequency tuning ratio  $\alpha$  and the negative stiffness ratio  $\eta$ . Nevertheless, it is evident from Eq. (4.8) that  $\eta$  should be always greater than  $-1$  for any positive mass ratio  $\mu$ , signifying that the absolute value of negative stiffness  $k_n$  should be always inferior to that of primary system  $k_1$ . The explicit expression for lower limit of  $\eta$  will be derived in the following study under the condition that the analytical formulation of frequency tuning ratio  $\alpha$  is sought and expressed as a function of  $\eta$ .

### 4.1.3 Optimization according to the FPT

In this section, the NSDVA will be tuned according to the FPT in the objective of minimizing the peak vibration amplitude of displacement FRF.

Considering that the primary system is harmonically excited at the forcing frequency  $\omega$ , the squared amplitude of its displacement FRF can be written by substituting  $\bar{s} = j\omega/\omega_1 = j\lambda$  into Eq. (4.4):

$$G^2(\Omega) = \left| \frac{X_1}{F/k_1} \right|^2 = \frac{A + 4\xi^2 B}{C + 4\xi^2 D} \quad (4.9)$$

with  $j = \sqrt{-1}$  and  $\lambda$  designating the excitation frequency normalized by the natural frequency of primary system. And the four components are given by:

$$\begin{aligned} A &= [\eta + \mu(\alpha^2 - \lambda^2)]^2, & B &= \mu^2 \alpha^2 \lambda^2, \\ C &= \left[ [\eta + \mu(\alpha^2 - \lambda^2)](1 - \lambda^2) + \mu \alpha^2 (\eta - \mu \lambda^2) \right]^2, & D &= \mu^2 \alpha^2 \lambda^2 (1 + \mu \alpha^2 - \lambda^2)^2. \end{aligned} \quad (4.10)$$

#### 4.1.3.1 Optimal design parameters

The derivation process based on the FPT has been detailed in previous chapters, therefore, it is omitted in the optimization of NSDVA for brevity and the expressions of all design parameters are directly given below.

- The optimal frequency tuning ratio  $\alpha$  and mechanical damping ratio  $\xi$  are:

$$\alpha_{\text{fpt}} = \sqrt{\frac{\mu - \eta}{\mu(1 - \mu)}}, \quad \xi_{\text{fpt}} = \sqrt{\frac{3\mu(1 - \eta)(\mu - \eta)^3}{4[2\mu(1 - \eta)^2(\mu - \eta)^2 - (\mu - \eta)^4]}}. \quad (4.11)$$

- The normalized displacement amplitude at fixed points is:

$$\|G\|_{\infty} = (1 - \mu) \sqrt{\frac{2\mu}{(\mu - \eta)^2}} \quad (4.12)$$

Clearly, all optimal parameters are expressed in terms of the mass ratio  $\mu$  and the negative stiffness ratio  $\eta$ .

#### 4.1.3.2 Lower limit and optimal value of $\eta$

By substituting the optimal frequency tuning ratio into the general stability condition (4.8), the upper and lower limits of  $\eta$  can be obtained:

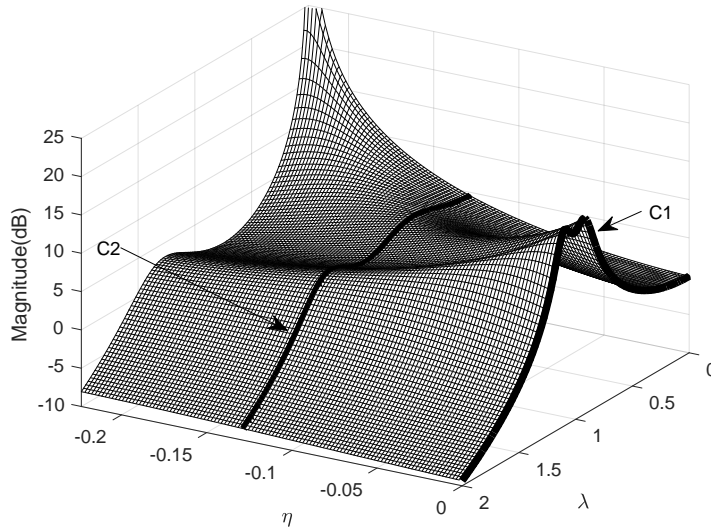
$$\eta \in (\eta_{\text{fpt}}^-, 0] = (-\sqrt{\mu}, 0] \quad (4.13)$$

Figure 4.2 depicts the FRF surface of primary system against the dimensionless excitation frequency  $\lambda$  and the negative stiffness ratio  $\eta$ . The curve C1 corresponds to the FRF in the case of a DVA ( $\eta = 0$ ). Clearly, the inclusion of negative stiffness does contribute to the decreasing of peak vibration amplitude and the increasing of absorbing frequency range. Nevertheless, the static displacement  $X_{st}$  of primary system attached with a NSDVA increases monotonically as the negative stiffness ratio  $\eta$  approaches to its lower limit  $\eta_{\text{fpt}}^-$ , which is in contrast with the trend of the magnitude at fixed points. Therefore, it could be postulated that the optimal negative stiffness ratio  $\eta_{\text{fpt}}$  is achieved when the static deflection  $X_{st}$  and the peak

magnitude  $\|G\|_\infty$  are equalized. The normalized static deformation  $X_{st}$  can be obtained from Eq. (4.9) by imposing  $\lambda = 0$ :

$$X_{st} = G \Big|_{\lambda=0} = \frac{\mu(1-\eta)}{\mu-\eta^2} \quad (4.14)$$

It is worth noting that  $X_{st}$  deviates from unity if  $\eta \neq 0$ , implying that the static



**Figure 4.2:** Displacement FRF surface of primary system controlled by a NSDVA versus the dimensionless frequency  $\lambda$  and the negative stiffness ratio  $\eta$ . Curve C1:

$$\eta = 0, \text{ C2: } \eta = \eta_{\text{fpt}}.$$

deflection of primary system is also influenced by the secondary oscillator. Equating Eqs. (4.12) and (4.14) yields four rational values of  $\eta_{\text{fpt}}$ , respectively:

$$\begin{aligned} \eta_1 &= \frac{-1 - (1-\mu)\sqrt{2\mu}}{1-2\mu}, & \eta_2 &= \frac{-1 + (1-\mu)\sqrt{2\mu}}{1-2\mu}, \\ \eta_3 &= \frac{\mu - (1-\mu)\sqrt{2\mu}}{2-\mu}, & \eta_4 &= \frac{\mu + (1-\mu)\sqrt{2\mu}}{2-\mu}. \end{aligned} \quad (4.15)$$

where  $\eta_2$  and  $\eta_4$  are greater than zero for any positive  $\mu$  and  $\eta_1 < \eta_{\text{fpt}}^-$  always holds for  $\mu < 0.25$ . The last possible solution satisfies:  $\eta_{\text{fpt}}^- < \eta_3 < 0, \forall \mu \in (0, 0.25)$ , which should be then retained. Finally, the optimal negative stiffness ratio  $\eta_{\text{fpt}}$  for the NSDVA is expressed as:

$$\eta_{\text{fpt}} = \frac{\mu - (1-\mu)\sqrt{2\mu}}{2-\mu} \quad (4.16)$$

Marked by C2, the FRF of primary system with the optimal value  $\eta_{fpt}$  is drawn in Figure 4.2, where an equilibrium is established between the increasing of static displacement and the decreasing of vibration amplitude at fixed points as the negative stiffness goes up to its lower limit.

Figure 4.3 depicts the evolution of peak vibration amplitude of primary system with respect to the stiffness ratio  $\eta$ . A minimum is observed in the peak amplitude curve within the stability region, at which the optimal negative stiffness ratio is defined and coincides with the one predicted by Eq. (4.16).

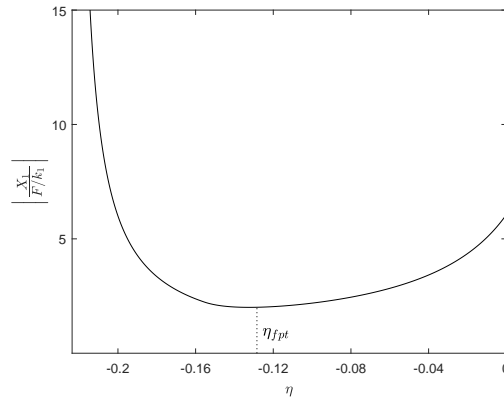


**Figure 4.3:** Evolution of peak displacement amplitude of primary system against the negative stiffness ratio  $\eta$  when tuned by the FPT.

#### 4.1.4 Optimization according to the SMC

When the transient response of primary system is to optimally shaped in terms of fast attenuation and low peak response, the NSDVA should be tuned according to the SMC.

##### 4.1.4.1 Optimal design parameters

Give that the coupled system is of two DOFs, there exist four eigenvalues for its characteristic polynomial, denoted by  $z_1$ ,  $z_2$ ,  $z_3$  and  $z_4$ . Therefore, the transient response of primary system under free vibration can be expressed in the form of:

$$x_1(\tau) = A_1 e^{z_1 \tau} + A_2 e^{z_2 \tau} + A_3 e^{z_3 \tau} + A_4 e^{z_4 \tau} \quad (4.17)$$

where  $A_1$ ,  $A_2$ ,  $A_3$  and  $A_4$  are coefficients in terms of rescaled time  $\tau$  and are dependent of the initial state of the system. As proposed in [8], a performance index, degree of stability, is defined as the absolute value of the maximal real part of all eigenvalues, i.e.:

$$\Lambda = -\max_i \left\{ \text{Re}(z_i) \right\} \quad (4.18)$$

indicating the slowest speed of convergence of the free vibration response. Therefore, the SMC aims at maximizing the degree of stability  $\Lambda$ , namely all eigenvalues should locate as far as possible away from the imaginary axis in the left half complex plane.

As stated in [8], the design objective is fulfilled when the eigenvalues of coupled system take the form of a double pair of complex conjugates. Denoting the eigenvalues by  $z_1 = z_3 = -p + jq$  and  $z_2 = z_4 = -p - jq$ ,  $p$  must be positive in order to locate at the left half complex plane and is exactly the degree of stability  $\Lambda$ . Thus, the characteristic polynomial can be factorized in terms of its eigenvalues:

$$(z - z_1) \cdot (z - z_2) \cdot (z - z_3) \cdot (z - z_4) = 0 \quad (4.19)$$

which can be expanded and further rearranged in the polynomial form of  $z$  as:

$$z^4 + 4pz^3 + (4p^2 + 2r^2)z^2 + 4pr^2z + r^4 = 0 \quad (4.20)$$

with  $r = \sqrt{p^2 + q^2}$  being the modulus of complex poles. By comparing coefficients in Eqs. (4.7) and (4.20), four conditions should be satisfied simultaneously:

$$4p = 2\xi\alpha \quad (4.21a)$$

$$4p^2 + 2r^2 = 1 + \frac{\eta}{\mu} + (1 + \mu)\alpha^2 \quad (4.21b)$$

$$4pr^2 = 2\xi\alpha(1 + \mu\alpha^2) \quad (4.21c)$$

$$r^4 = \frac{\eta}{\mu} + (1 + \eta)\alpha^2 \quad (4.21d)$$

from which one can determine the SMC-based optimal parameters as:

$$\alpha_{\text{smc}} = \sqrt{\frac{1 + \eta - 2\mu - \sqrt{(1 + \eta)^2 - 4\mu}}{2\mu^2}}, \quad \xi_{\text{smc}} = \sqrt{\frac{1 - \eta - \sqrt{(1 + \eta)^2 - 4\mu}}{2}}. \quad (4.22)$$

with the modulus and real part of eigenvalues given by:

$$r = \sqrt{\frac{1 + \eta - \sqrt{(1 + \eta)^2 - 4\mu}}{2\mu}}, \quad \Lambda = p = \sqrt{\frac{1 + \eta - (3 - \eta)\mu - (1 - \mu)\sqrt{(1 + \eta)^2 - 4\mu}}{8\mu^2}}. \quad (4.23)$$

It is remarked that the lower threshold of  $\eta$  is not unique for  $\mu \in [0, 1/4]$ , which should be investigated per segment of  $\mu$ . The detailed deduction is provided in Appendix C.1, leading to the following lower bounds on negative stiffness ratio:

$$\eta_{\text{smc}}^- = \begin{cases} \frac{\mu + 2\sqrt{\mu}(5\mu - 1)}{1 - 4\mu}, & 0 \leq \mu < \frac{1}{9}; \\ \frac{7\mu - 1}{1 - 3\mu}, & \frac{1}{9} \leq \mu \leq \frac{1}{7}; \\ 2\sqrt{\mu} - 1, & \frac{1}{5} \leq \mu \leq \frac{1}{4}. \end{cases} \quad (4.24)$$

Damper	Frequency tuning ratio $\alpha$	Mechanical damping ratio $\xi$	$\ G\ _{\infty}$
DVA	$\frac{1}{\sqrt{1-\mu}}$	$\sqrt{\frac{3\mu}{4(2-\mu)}}$	$(1-\mu)\sqrt{\frac{2}{\mu}}$
NSDVA	$\sqrt{\frac{\mu-\eta}{\mu(1-\mu)}}$	$\sqrt{\frac{3\mu(1-\eta)(\mu-\eta)^3}{4[2\mu(1-\eta)^2(\mu-\eta)^2-(\mu-\eta)^4]}}$	$(1-\mu)\sqrt{\frac{2\mu}{(\mu-\eta)^2}}$

**Table 4.1:** Closed-form formulae to optimal parameters of non-traditional DVA and NSDVA attached to a SDOF undamped primary system under force excitation according to the FPT.

Damper	Frequency tuning ratio $\alpha$	Mechanical damping ratio $\xi$	Degree of stability $\Lambda$
DVA	$\frac{1-\sqrt{1-4\mu}}{2\mu}$	$\frac{\sqrt{1-\sqrt{1-4\mu}}}{2}$	$\frac{\sqrt{1-3\mu-(1-\mu)\sqrt{1-4\mu}}}{8\mu^2}$
NSDVA	$\sqrt{\frac{1+\eta-2\mu-\sqrt{(1+\eta)^2-4\mu}}{2\mu^2}}$	$\frac{\sqrt{1-\eta-\sqrt{(1+\eta)^2-4\mu}}}{2}$	$\frac{\sqrt{1+\eta-(3-\eta)\mu-(1-\mu)\sqrt{(1+\eta)^2-4\mu}}}{8\mu^2}$

**Table 4.2:** Closed-form formulae to optimal parameters of non-traditional DVA and NSDVA attached to a SDOF undamped primary system under force excitation according to the SMC.

FPT	SMC
$\eta > \eta_{\text{fpt}}^- = -\sqrt{\mu}$	$\eta \geq \eta_{\text{smc}}^-$ given in Eq. (4.24)

**Table 4.3:** Lower bounds on negative stiffness ratio  $\eta$  for non-traditional NSDVA when tuned by the FPT and SMC.

Analytical formulae to optimal parameters of both non-traditional DVA and NSDVA according to the FPT and the SMC are summarized in Tables 4.1 and 4.2, respectively. Clearly, the parameters of NSDVA reduce to those of DVA when  $\eta = 0$ . Besides, the lower thresholds of negative stiffness ratio  $\eta$  in two optimal scenarios are summarized in Table 4.3.

An alternative configuration of NSDVA based on the DVA of Den Hartog is provided in Appendix C.2, where its all optimal parameters according to the FPT and the SMC are analytically formulated and the corresponding lower bounds on  $\eta$  are specified.

#### 4.1.5 Numerical simulations and analyses

In this section, numerical simulations will be performed in order to illustrate the effect of negative stiffness on vibration control performance in both harmonic and transient scenarios by comparing with the DVA. In the following study, the results are obtained with the mass ratio being  $\mu = 0.05$  except for specific cases.

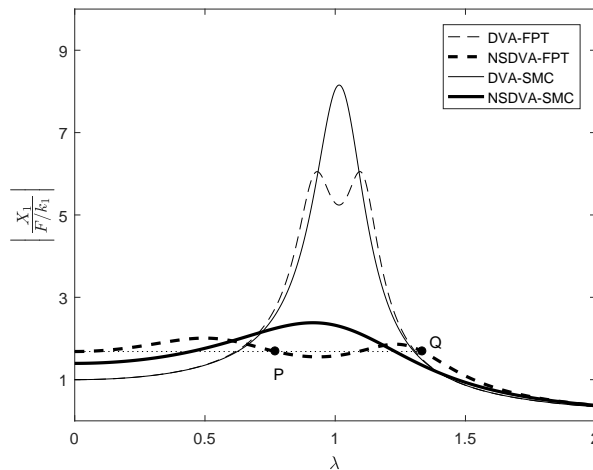
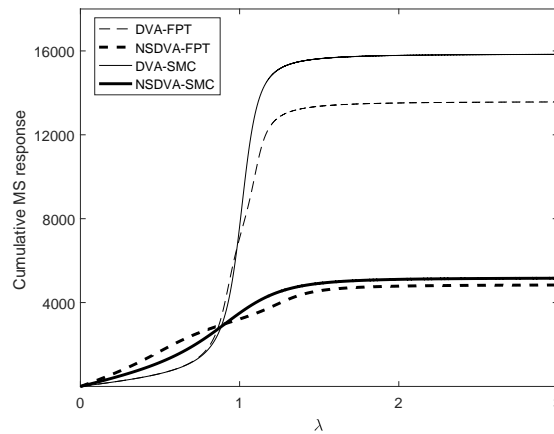


**Figure 4.4:** Displacement FRF of primary system controlled by a NSDVA. Thin lines:  $\eta = 0$ , thick lines:  $\eta = \eta_{\text{fpt}}$ . Dashed lines: tuned by the FPT; solid lines: calibrated by the SMC.

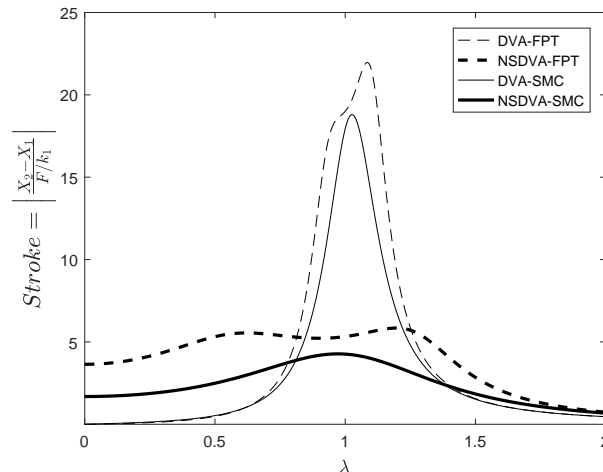
##### 4.1.5.1 Harmonic vibration case

Figure 4.4 depicts the displacement FRFs of primary system controlled by either a DVA (marked by thin lines) or a NSDVA with optimal negative stiffness ratio  $\eta_{\text{fpt}}$  (marked by thick lines). Meanwhile, the dashed and solid curves correspond to DVAs optimized by the FPT and the SMC, respectively. It is evident that compared to the SMC, the FPT contributes to the minimizing of peak vibration amplitude of primary

system in the steady state and to a relatively large frequency bandwidth of vibration suppression. Moreover, in the FRFs related to NSDVAs, the vibration amplitude at fixed points P and Q is equal to the static deformation (i.e. at  $\lambda = 0$ ), validating the aforementioned postulation on optimality condition. Finally, comparison between FRFs relevant to DVA and NSDVA suggests that the addition of negative stiffness leads to the decrease of peak vibration amplitude, the broadening of suppression bandwidth and the left shifting of resonance area.



**Figure 4.5:** CMSR value of normalized displacement of primary system. Thin lines:  $\eta = 0$ , thick lines:  $\eta = \eta_{fpt}$ . Dashed lines: tuned by the FPT; solid lines: calibrated by the SMC.



**Figure 4.6:** FRF of relative displacement between primary and secondary masses. Thin lines:  $\eta = 0$ , thick lines:  $\eta = \eta_{fpt}$ . Dashed lines: tuned by the FPT; solid lines: calibrated by the SMC.

The main drawback of negative stiffness is to amplify the vibration amplitude of primary system in low frequency region. Nevertheless, the justification of its use in control scheme could be twofold: improved frequency responses over a larger area around resonance as previously discussed and reduced cumulative mean square response (CMSR) of primary mass, which is illustrated in Figure 4.5. The dimensionless CMSR is defined as the integrated value of squared normalized displacement of primary system over a certain frequency range [55], standing for the total kinetic energy of primary mass when undergoing a broadband excitation. Figure 4.5 clearly suggests that both NSDVAs can reduce the peak value of CMSR by a factor close to 3, signifying that the use of negative stiffness can enhance significantly the system damping capability against external disturbance.

More benefit could be introduced into the control performance by using the negative stiffness. Figure 4.6 demonstrates FRFs of relative motion between primary and secondary masses, also termed as the stroke of DVA. One can remark that the NSDVA can reduce significantly the peak stroke amplitude compared to their DVA counterparts, which facilitates their practical implementation in a more strict environment.

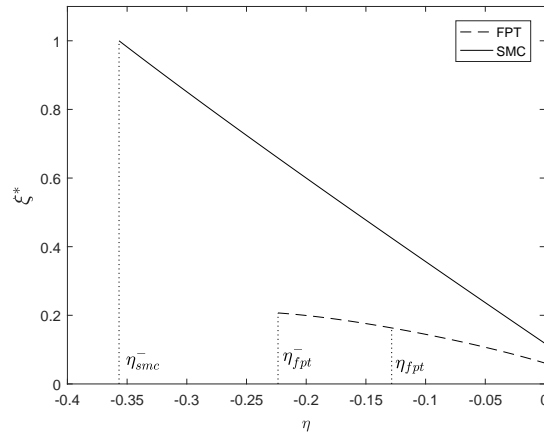


**Figure 4.7:** Evolution of system damping ratio  $\xi^*$  as a function of the negative stiffness ratio  $\eta$ . Dashed lines: tuned by the FPT; solid lines: calibrated by the SMC.

Nevertheless, the FPT is not oriented towards the optimization of damping ratio  $\xi^*$  of coupled system, which is defined as the minimal value of all modal damping ratios. The modal damping ratio associated with a specific eigenvalue is determined as the absolute value of ratio between its real part and its complex modulus. Therefore, increasing  $\xi^*$  leads to the decrease of damped natural frequency so that the required oscillation cycle for decaying the disturbance to zero is reduced. Figure 4.7 demonstrates the evolution of system damping ratio  $\xi^*$  as a function of negative stiffness ratio  $\eta$ . Compared to the SMC, the FPT always yields a smaller value of  $\xi^*$

over the whole range of  $\eta$ , implying that the SMC is more preferable when a larger damping ratio is needed. Moreover, one can observe that the system damping value at the optimal negative stiffness ratio  $\eta_{II,fpt}$  is not the largest, validating the fact that the FPT aims at improving the steady state response instead of maximizing the damping capability.

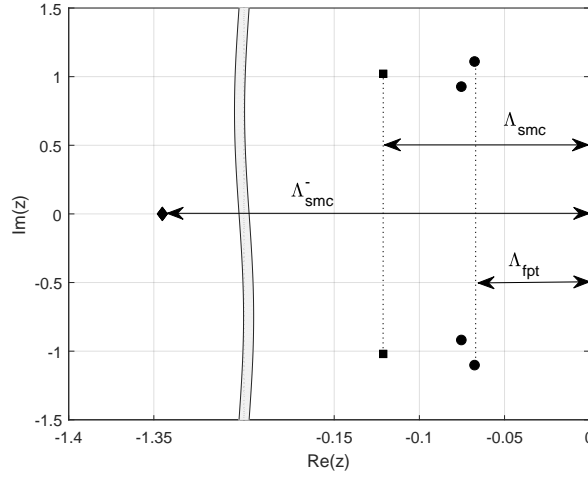


**Figure 4.8:** Root loci of primary system coupled with a NSDVA. Circle marker: tuned by the FPT with  $\eta = 0$ ; square marker: calibrated by the SMC with  $\eta = 0$ ; diamond marker: optimized by the SMC with critical negative stiffness ratio  $\eta_{smc}^-$ . The performance indices read as:  $\Lambda_{fpt} = 0.067$ ,  $\Lambda_{smc} = 0.12$  and  $\Lambda_{smc}^- = 1.35$ .

#### 4.1.5.2 Transient vibration case

The capability of decaying transient disturbances can be also quantified by taking the degree of stability  $\Lambda$  as the performance index. In fact,  $\Lambda$  represents the slowest exponential decay speed of transient response, therefore, a larger value of  $\Lambda$  corresponds to a faster decay of disturbance. Figure 4.8 depicts the eigenvalues of coupled system. With the definition of degree of stability given in Eq. (4.18), the performance indices read as:  $\Lambda_{fpt} = 0.067$ ,  $\Lambda_{smc} = 0.12$  and  $\Lambda_{smc}^- = 1.35$ . Performance indices without any superscript are related to DVAs without negative stiffness, while those with the superscript,  $-$ , are related to NSDVA with critical negative stiffness ratio  $\eta_{smc}^-$ . It clearly suggests that the SMC always conducts to a double pair of complex eigenvalues and a larger performance index than the FPT, namely a faster convergence of transient response. In the ultimate scenario with SMC-based optimization, all the eigenvalues are coincident with each other and locates at the real axis of the complex plane, at which the largest degree of stability can be achieved.

A numerical simulation in the temporal domain is also carried out to investigate the control performance of various DVAs with respect to transient vibration. Figure

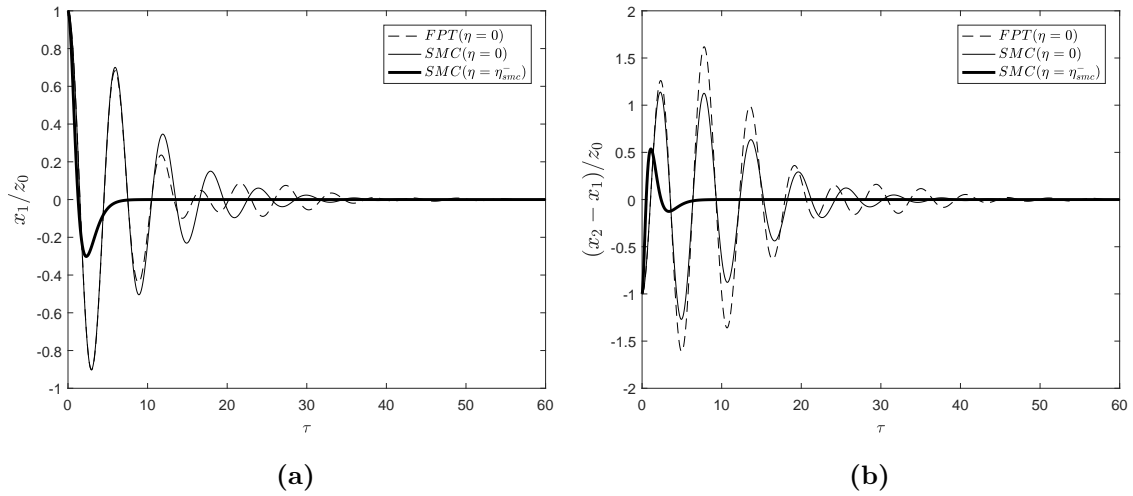


**Figure 4.9:** Transient responses under free vibration normalized by the initial displacement of primary system  $z_0$ : (a) displacement of primary system; (b) stroke length of DVA. The mass ratio is imposed as  $\mu = 0.10$ . Dashed line: tuned by the FPT with  $\eta = 0$ ; thin solid line: tuned by the SMC with  $\eta = 0$ ; thick solid line: calibrated by the SMC with critical negative stiffness ratio  $\eta_{\text{smc}}^-$ .

4.9 plots the temporal responses of primary system and stroke of DVA. The simulation is performed under free vibration (namely  $F(\tau) = 0$ ) with a relatively large mass ratio  $\mu = 0.1$  for a better visual effect. The initial states of two DOFs are imposed as:  $x_1(0) = z_0 = 0.1$  and  $x_1'(0) = x_2(0) = x_2'(0) = 0$ . The temporal solutions related to the dimensionless ordinary differential equations (4.3) are obtained by adopting the fourth order Runge-Kutta method with a fixed time step  $1e-4$  for a simulation duration of 60. As evident from Figure 4.9a, DVA tuned by the FPT and SMC render a similar attenuation performance of transient response of primary system in terms of the peak vibration amplitude and the settling time, which is consistent with the prediction according to the performance index. Meanwhile, the use of negative stiffness can significantly reduce both peak amplitudes of primary system and stroke of DVA and can accelerate the decay rate of transient disturbance.

## 4.2 NSIDVA

In this section, a novel control device termed as NSIDVA is proposed, which can be built by replacing the viscous damper of NSDVA with a series-type inerter-based mechanical network, as shown in Figure 4.10b. The NSIDVA is supposed to combine the beneficial effects brought by both the negative stiffness and the inertial mechanical network. By removing the negative stiffness, the NSIDVA reduces to a non-traditional IDVA (as shown in Figure 4.10a), whose optimal design had been

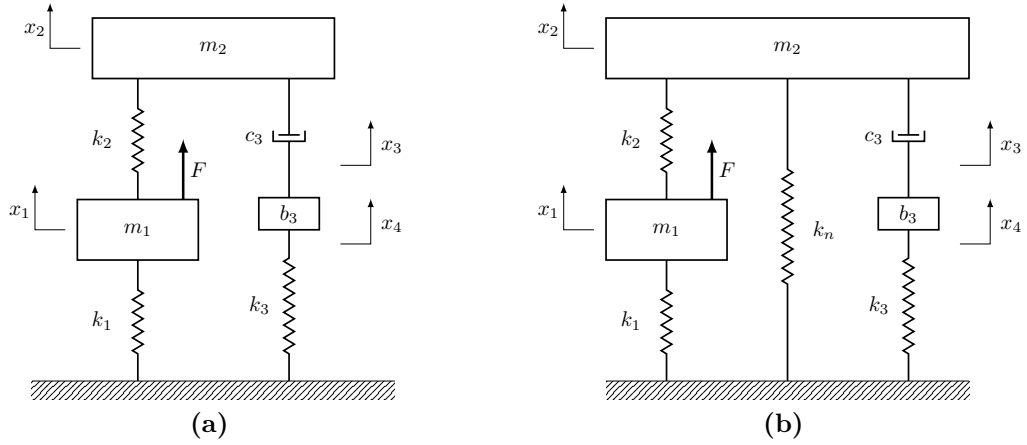


**Figure 4.10:** Schematic diagrams of a SDOF undamped primary system controlled by a: (a) non-traditional IDVA [159]; (b) NSIDVA.

carried out according to the FPT and the SMC in my published work [159].

### 4.2.1 Mathematical modeling

The dynamics of whole system in Figure 4.10b can be described by the EOMs:

$$m_1 \ddot{x}_1 = k_2(x_2 - x_1) - k_1 x_1 + F(t) \quad (4.25a)$$

$$m_2 \ddot{x}_2 = k_2(x_1 - x_2) - k_n x_2 + c_3(\dot{x}_3 - \dot{x}_2) \quad (4.25b)$$

$$0 = b_3(\ddot{x}_4 - \ddot{x}_3) + c_3(\dot{x}_2 - \dot{x}_3) \quad (4.25c)$$

$$0 = b_3(\ddot{x}_3 - \ddot{x}_4) - k_3 x_4 \quad (4.25d)$$

where  $x_3$  and  $x_4$  are the displacements at two terminals of inerter. Besides,  $b_3$ ,  $k_3$  and  $c_3$  denote the inertance, stiffness and viscous damping of the series-type inerter-based mechanical network, respectively. The following natural frequencies are first defined:

$$\omega_1 = \sqrt{\frac{k_1}{m_1}}, \quad \omega_2 = \sqrt{\frac{k_2}{m_2}}, \quad \omega_3 = \sqrt{\frac{k_3}{b_3}}. \quad (4.26)$$

with  $\omega_3$  being the corner frequency of mechanical network. On this basis, the following dimensionless parameters are introduced:

$$\mu = \frac{m_2}{m_1}, \quad \nu = \frac{b_3}{m_1}, \quad \xi = \frac{c_3}{2\sqrt{k_2 m_2}}, \quad \alpha = \frac{\omega_2}{\omega_1}, \quad \beta = \frac{\omega_3}{\omega_1}, \quad \eta = \frac{k_n}{k_1}. \quad (4.27)$$

Apparently, the design parameters to be optimized are the inertance-to-mass ratio  $\nu$ , mechanical damping ratio  $\xi$  and two frequency tuning ratios  $\alpha$  and  $\beta$ . Finally,

the dimensionless EOMs read as:

$$x_1'' + x_1 + \mu\alpha^2(x_1 - x_2) = F(\tau)/k_1 \quad (4.28a)$$

$$\mu x_2'' + \eta x_2 + 2\xi\mu\alpha(x_2' - x_3') + \mu\alpha^2(x_2 - x_1) = 0 \quad (4.28b)$$

$$\nu(x_4'' - x_3'') + 2\xi\mu\alpha(x_2' - x_3') = 0 \quad (4.28c)$$

$$x_3'' - x_4'' - \beta^2 x_4 = 0 \quad (4.28d)$$

from which the normalized displacement FRF of primary system can be formulated in the form of:

$$\frac{X_1}{F/k_1} = \frac{B_4\bar{s}^4 + B_3\bar{s}^3 + B_2\bar{s}^2 + B_1\bar{s} + B_0}{A_6\bar{s}^6 + A_5\bar{s}^5 + A_4\bar{s}^4 + A_3\bar{s}^3 + A_2\bar{s}^2 + A_1\bar{s} + A_0} \quad (4.29)$$

with the coefficients in the numerator and denominator given by:

$$\begin{cases} B_4 = 2\mu^2\xi\alpha \\ B_3 = \mu\nu\beta^2 \\ B_2 = 2\mu\xi\alpha [\eta + \mu\alpha^2 + (\mu + \nu)\beta^2] \\ B_1 = \nu\beta^2 (\eta + \mu\alpha^2) \\ B_0 = 2\mu\xi\alpha\beta^2 (\eta + \mu\alpha^2) \end{cases} \quad (4.30)$$

$$\begin{cases} A_6 = 2\mu^2\xi\alpha \\ A_5 = \mu\nu\beta^2 \\ A_4 = 2\mu\xi\alpha [\mu + \eta + (1 + \mu)\mu\alpha^2 + (\mu + \nu)\beta^2] \\ A_3 = \nu\beta^2 [\mu + \eta + (1 + \mu)\mu\alpha^2] \\ A_2 = 2\mu\xi\alpha [\eta + (1 + \eta)\mu\alpha^2 + (\mu + \nu + \eta)\beta^2 + (1 + \mu + \nu)\mu\alpha^2\beta^2] \\ A_1 = \nu\beta^2 [\eta + (1 + \eta)\mu\alpha^2] \\ A_0 = 2\mu\xi\alpha\beta^2 [\eta + (1 + \eta)\mu\alpha^2] \end{cases} \quad (4.31)$$

As evident from Eq. (4.29), the characteristic polynomial is of degree six in terms of  $\bar{s}$ , implying the existence of six distinct poles for the whole system.

## 4.2.2 Optimization according to the SMC

Similar to the case of traditional IDVA [53], the displacement FRF of primary system is featured by four invariant points when controlled by a non-traditional IDVA (and thereby the NSIDVA), thus their  $H_\infty$  optimization can be conducted according to the extended FPT. However, it is remarked that the derivation process is very sophisticated, which is omitted in this section. Meanwhile, the optimal design of NSIDVA according to the SMC will be carried out.

For a coupled system of two DOFs, i.e. a SDOF primary structure controlled by a SDOF DVA, the design objective of optimizing the transient response is fulfilled by coinciding the two pairs of complex conjugate eigenvalues. Therefore, it can be herein postulated that:

**Proposition 1** *For a coupled system of three DOFs, the transient response of primary system is optimized when it has three coalesced pairs of conjugate poles.*

The proof of this proposition is detailed as follows.

**Proof 1** *The characteristic equation is actually the monic form of the denominator in Eq. (4.29), i.e.:*

$$f(\bar{s}) = \bar{s}^6 + \tilde{A}_5\bar{s}^5 + \tilde{A}_4\bar{s}^4 + \tilde{A}_3\bar{s}^3 + \tilde{A}_2\bar{s}^2 + \tilde{A}_1\bar{s} + \tilde{A}_0 \quad (4.32)$$

with the normalized coefficients being:  $\tilde{A}_i = A_i/A_6, i = 0, 1, \dots, 5$ . Let denote its six poles as:  $s_{1,2} = -p_1 \pm jq_1$ ,  $s_{3,4} = -p_2 \pm jq_2$  and  $s_{5,6} = -p_3 \pm jq_3$ , the characteristic polynomial can be then written in a factorization form of its eigenvalues such that:

$$\begin{aligned} f(\bar{s}) &= (\bar{s} - s_1)(\bar{s} - s_2)(\bar{s} - s_3)(\bar{s} - s_4)(\bar{s} - s_5)(\bar{s} - s_6) \\ &= \bar{s}^6 + D_5\bar{s}^5 + D_4\bar{s}^4 + D_3\bar{s}^3 + D_2\bar{s}^2 + D_1\bar{s} + D_0 \end{aligned} \quad (4.33)$$

with the coefficients  $D_i, i = 0, 1, \dots, 5$  given by:

$$\begin{cases} D_5 = 2(p_1 + p_2 + p_3) \\ D_4 = 4(p_1p_2 + p_1p_3 + p_2p_3) + r_1^2 + r_2^2 + r_3^2 \\ D_3 = 8p_1p_2p_3 + 2p_1(r_2^2 + r_3^2) + 2p_2(r_1^2 + r_3^2) + 2p_3(r_1^2 + r_2^2) \\ D_2 = 4(p_2p_3r_1^2 + p_1p_3r_2^2 + p_1p_2r_3^2) + r_1^2r_2^2 + r_1^2r_3^2 + r_2^2r_3^2 \\ D_1 = 2(p_1r_2^2r_3^2 + p_2r_1^2r_3^2 + p_3r_1^2r_2^2) \\ D_0 = r_1^2r_2^2r_3^2 \end{cases} \quad (4.34)$$

where  $p_1, p_2$  and  $p_3$  must be positive due to the stability requirement, and  $r_i = \sqrt{p_i^2 + q_i^2}$  denotes the complex magnitude of poles. By balancing coefficients in Eqs. (4.32) and (4.33), six equations should be satisfied:

$$\tilde{A}_i = D_i, \quad i = 0, 1, \dots, 5. \quad (4.35)$$

By inspecting the coefficients in Eq. (4.32), a constraint relating  $\tilde{A}_0$ ,  $\tilde{A}_5$  and  $\tilde{A}_1$  can be obtained:

$$\tilde{A}_0\tilde{A}_5 - \beta^2\tilde{A}_1 = 0 \quad (4.36)$$

which is equivalent to

$$D_0D_5 - \beta^2D_1 = 2p_1r_2^2r_3^2(r_1^2 - \beta^2) + 2p_2r_1^2r_3^2(r_2^2 - \beta^2) + 2p_3r_1^2r_2^2(r_3^2 - \beta^2) = 0 \quad (4.37)$$

With all coefficients before brackets being positive, Eq. (4.37) is satisfied when three terms in bracket do not have the same sign simultaneously. As the magnitude of pole signifies the dimensionless natural frequency of corresponding mode, a larger value of  $r_i$  is always preferred for faster transient response. Therefore, the optimal scenario occurs when

$$r_1 = r_2 = r_3 = r = \beta \quad (4.38)$$

With the equality between magnitudes of poles, the condition  $\tilde{A}_0 = D_0$  yields the expression of  $\alpha$  in terms of  $r$ :

$$\alpha^2 = \frac{\mu r^4 - \eta}{\mu(1 + \eta)} \quad (4.39)$$

Subsequently,  $\tilde{A}_3$  is proportional to  $\tilde{A}_5$  in such a way that:

$$\tilde{A}_3 = \tilde{A}_5 \frac{\mu + \eta^2 + (\mu^2 + \mu)r^4}{\mu(1 + \eta)} \quad (4.40)$$

Alternatively, one has:

$$D_3 - D_5 \frac{\mu + \eta^2 + (\mu^2 + \mu)r^4}{\mu(1 + \eta)} = \frac{8}{3}p_1(p_2p_3 - p^2) + \frac{8}{3}p_2(p_1p_3 - p^2) + \frac{8}{3}p_3(p_1p_2 - p^2) = 0 \quad (4.41)$$

with

$$p^2 = \frac{3\eta^2 - 2\mu r^2\eta + \mu^2 r^4 + \mu(r^2 - 1)^2}{4\mu(1 + \eta)} \quad (4.42)$$

Given that  $p_i$  is positive and denotes the exponential decay rate of transient response, thus a larger value of  $p_i$  is always beneficial. Again, the same observation can be made for Eq. (4.41) that the design objective is achieved when  $p_1p_3 = p_1p_2 = p_2p_3 = p^2$ , which is equivalent to the following expression:

$$p_1 = p_2 = p_3 = p = \sqrt{\frac{3\eta^2 - 2\mu r^2\eta + \mu^2 r^4 + \mu(r^2 - 1)^2}{4\mu(1 + \eta)}} \quad (4.43)$$

Therefore, the aforementioned statement is justified that the transient response of primary system is optimized when the six distinct poles of the coupled system coalesce into three identical pairs of complex conjugate eigenvalues.

By substituting Eqs. (4.38) and (4.43) into (4.34) and considering the optimality conditions (4.35), a quadratic equation in  $r^2$  can be obtained:

$$\mu r^4 - (1 + \eta)r^2 + 1 = 0 \quad (4.44)$$

where real roots could be retained if the mass ratio satisfies:  $\mu \leq 0.25$ , which is generally the case in practical applications. In this case, two possible solutions of  $r^2$  exist, respectively:

$$r_L^2 = \frac{1 + \eta - \sqrt{(1 + \eta)^2 - 4\mu}}{2\mu}, \quad r_U^2 = \frac{1 + \eta + \sqrt{(1 + \eta)^2 - 4\mu}}{2\mu}. \quad (4.45)$$

Under no circumstance, the absolute value of real part of conjugate eigenvalues  $p$  could be greater than their magnitude  $r$ , viz.  $p \leq r$  as required by the complex poles assumption, which yields an inequality expression solely in  $r$  as:

$$3(\mu^2 + \mu)r^4 - 10\mu(1 + \eta)r^2 + 3\eta^2 + 3\mu \leq 0 \quad (4.46)$$

from which the allowable bound on  $r^2$  can be specified as:  $r^2 \in [r_-^2, r_+^2]$  with its lower and upper threshold expressed by:

$$\begin{aligned} r_-^2 &= \frac{5\mu(1+\eta) - \sqrt{\mu[(16\mu-9)\eta^2 + 50\mu\eta + \mu(16-9\mu)]}}{3(\mu^2 + \mu)}, \\ r_+^2 &= \frac{5\mu(1+\eta) + \sqrt{\mu[(16\mu-9)\eta^2 + 50\mu\eta + \mu(16-9\mu)]}}{3(\mu^2 + \mu)}. \end{aligned} \quad (4.47)$$

where  $\eta$  should satisfy  $\eta_- \leq \eta \leq 0$  for having real solutions for  $r^2$ , with

$$\eta_- = \frac{12(\mu+1)\sqrt{\mu} - 25\mu}{16\mu - 9} \quad (4.48)$$

It is apparent that  $r_-^2 \leq r_L^2 \leq r_+^2$  and  $r_U^2 > r_+^2$  always hold for any  $\mu \leq 0.25$ . Thus,  $r_L^2$  should be retained and taken as the optimal magnitude of poles. Furthermore, the inertance-to-mass ratio is given by:

$$\nu_{\text{smc}} = \frac{8[(\mu^2 + \mu)r^4 - 2\mu(1+\eta)r^2 + \mu + \eta^2]}{r^2(1+\eta)} \quad (4.49)$$

Finally, the optimal mechanical damping ratio is formulated as:

$$\xi_{\text{smc}} = \frac{4\sqrt{3}}{9} \sqrt{\frac{(\mu^2 + \mu)r^4 - 2\mu(1+\eta)r^2 + \mu + \eta^2}{\mu r^4 - \eta}}. \quad (4.50)$$

Finally, optimal parameters of both non-traditional IDVA and NSIDVA according to the SMC are summarized in Table 4.4. By imposing  $\eta = 0$ , the analytical expressions of NSIDVA reduce to those of non-traditional IDVA.

The displacement FRFs of primary system controlled by the non-traditional DVA, NSDVA, non-traditional IDVA and NSIDVA optimized by the SMC are depicted in Figure 4.11. The mass ratio and negative stiffness ratio are set as:  $\mu = 5\%$  and  $\eta = -0.02$ . Clearly, there exists a mono-peak in all four FRF curves since the SMC is not oriented towards the optimization of steady state responses. Precisely, the peak values are 8.1544, 5.7765, 6.3878 and 4.6040, respectively. It suggests that with a 2% negative stiffness, the NSDVA can further reduces the peak vibration by 29.2% compared to the non-traditional DVA. Meanwhile, with respect to the non-traditional DVA, IDVA and NSDVA, the NSIDVA can reduce the peak amplitude by 43.5%, 27.9% and 20.3%, respectively.

	Non-traditional IDVA [159]	NSIDVA
$r$	$\sqrt{\frac{1 - \sqrt{1 - 4\mu}}{2\mu}}$	$\sqrt{\frac{1 + \eta - \sqrt{(1 + \eta)^2 - 4\mu}}{2\mu}}$
$\alpha$	$r^2$	$\sqrt{\frac{\mu r^4 - \eta}{\mu(1 + \eta)}}$
$\beta$	$r$	$r$
$\nu$	$\frac{8 [(\mu^2 + \mu) r^4 - 2\mu r^2 + \mu]}{r^2}$	$\frac{8 [(\mu^2 + \mu) r^4 - 2\mu(1 + \eta) r^2 + \mu + \eta^2]}{r^2(1 + \eta)}$
$\xi$	$\frac{4\sqrt{3}}{9} \sqrt{\frac{(1 + \mu) r^4 - 2r^2 + 1}{r^4}}$	$\frac{4\sqrt{3}}{9} \sqrt{\frac{(\mu^2 + \mu) r^4 - 2\mu(1 + \eta) r^2 + \mu + \eta^2}{\mu r^4 - \eta}}$

**Table 4.4:** Closed-form formulae to optimal parameters of non-traditional IDVA and NSIDVA based on the SMC.

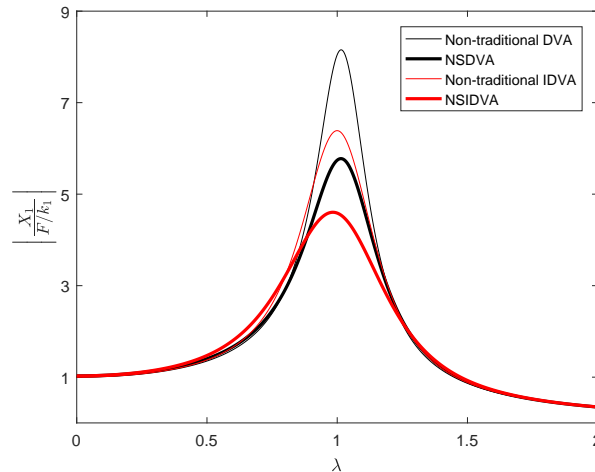


**Figure 4.11:** Displacement FRFs of primary system when controlled by four types of dampers. The mass ratio is set as:  $\mu = 5\%$ . Thin lines: without negative stiffness, thick lines: with a negative stiffness ratio of  $\eta = -0.02$ . Black lines: DVA, red lines: IDVA.

### 4.3 Concluding remarks

In this chapter, the optimal design of NSDVA is carried out based on the FPT and the SMC. Ready-to-use formulae to all design parameters are provided and allowable bound on negative stiffness is specified in each optimal scenario based

on the stability requirement. Besides, an optimal negative stiffness ratio is defined when the NSDVA is optimized according to the FPT.

Numerical simulation results demonstrate that under harmonic excitation, the inclusion of negative stiffness can reduce significantly the maximum vibration amplitude of primary system and the stroke length of DVA and increase the frequency bandwidth of vibration suppression. Moreover, it is shown that the system damping increases as the negative stiffness approaches to its lower limit. Finally, temporal responses under free vibration suggest that in the ultimate scenario, the SMC-based NSDVAs can attenuate the transient response in an extremely short duration.

The control effect of NSDVA can be further improved by incorporating an inerter-based mechanical network, leading to the NSIDVA. Since the whole system is of three DOFs, it is postulated and later proven that the transient response is optimally shaped when three coalesced pairs of conjugate poles are observed. Finally, its optimal parameters according to the SMC are analytically derived and numerical results confirm its superior control effect with respect to the NSDVA.

In the next chapter, the electrical analogous models in the framework of PSD will be established for both NSDVA and NSIDVA, facilitating their application for controlling the vibration of flexible structures.

# Chapter 5

## Electromechanical Analogy

In previous chapters, several non-traditional configurations of passive dampers have been investigated, whose tuned masses are related to the base by either a viscous damper or an inerter-based mechanical network. It was later proven that incorporating a linear negative stiffness in parallel to the ground-hook component is beneficial in terms of enhancing the vibration attenuation performance of existing control devices. Their optimal design had been addressed in the literature or have been newly carried out in this thesis. To facilitate their implementation and to extend their applicability, the possibility of accurately realizing these mechanical dampers by means of piezoelectric and electromagnetic shunt dampers will be investigated. Some fundamentals of structural dynamics will be first presented.

### 5.1 Fundamentals

#### 5.1.1 Mechanical impedance

Consider that a linear generalized mechanical structure is forced at the frequency  $\omega$ , its velocity is denoted as  $\dot{x}$ . Therefore, its impedance can be defined in terms of the complex magnitudes of force  $F$  and its velocity  $\dot{X}$  in such a way that:

$$Z(s) = \frac{F}{\dot{X}} \quad (5.1)$$

with  $s = j\omega$  and  $j = \sqrt{-1}$ .

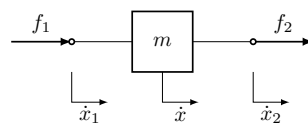


Figure 5.1: A mass element.

For the mass element shown in Figure 5.1,  $f_1$  is the force input at one of its terminals and  $f_2$  is the force output at another terminal. Clearly, one has:

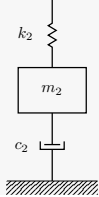
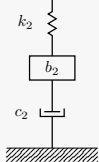
$$\dot{x}_1 = \dot{x}_2 = \dot{x} \quad (5.2a)$$

$$m\ddot{x} = f_2 + f_1 \quad (5.2b)$$

Therefore, the mass element is rigid since no relative motion could be generated across its two terminals, meanwhile, the force transmitted through it will be attenuated since  $f_2 = m\ddot{x} - f_1$ . Following the same way, the impedances of four mechanical elements, mass, inerter, spring and damper, and their corresponding characteristics of force transmission can be obtained, as summarized in Table 5.1. Although the mass and inerter have the same form of impedance, the inerter is a two-terminal device, through which the force transmitted is unattenuated. Their difference can be further observed in the impedances of non-traditional DVA and grounded series-type inertial mechanical network, as provided in Table 5.2.

Element	Symbol	Impedance	Force transmitted
Mass	m	$s \cdot m$	Attenuated
Inerter	b	$s \cdot b$	Unattenuated
Spring	k	$\frac{k}{s}$	Unattenuated
Damper	c	c	Unattenuated

**Table 5.1:** Impedances and key characteristics of mechanical elements.

	Mechanical model	Total impedance
Non-traditional DVA		$\left( \frac{s}{k_2} + \frac{1}{m_2 s + c_2} \right)^{-1}$
Inertial mechanical network		$\left( \frac{1}{b_2 s} + \frac{s}{k_2} + \frac{1}{c_2} \right)^{-1}$

**Table 5.2:** Total impedances of non-traditional DVA and series-type inertial mechanical network.

### 5.1.2 Addition laws of mechanical impedances

The total impedance of  $n$  mechanical elements in series is computed by:

$$\frac{1}{Z_{\text{series}}} = \sum_{i=1}^n \frac{1}{Z_i} \quad (5.3)$$

Meanwhile, the total impedance of  $n$  elements in parallel is equal to:

$$Z_{\text{parallel}} = \sum_{i=1}^n Z_i \quad (5.4)$$

### 5.1.3 Electrical impedance

The impedance of an electronic component can be expressed in terms of the complex magnitudes of the voltage  $V$  across its two terminals and the current  $I$  flowing through it, as follows:

$$Z(s) = \frac{V}{I} \quad (5.5)$$

The electrical impedances of inductor, capacitor and resistor are given in Table 5.3.

Component	Symbol	Impedance
Inductor	L	$s \cdot L$
Capacitor	C	$\frac{1}{s \cdot C}$
Resistor	R	R

**Table 5.3:** Impedances of three basic electronic components.

### 5.1.4 Addition laws of electrical impedances

The total impedance of  $n$  electronic components in series is determined as:

$$Z_{\text{series}} = \sum_{i=1}^n Z_i \quad (5.6)$$

The total impedance of  $n$  electronic components in parallel is described by:

$$\frac{1}{Z_{\text{parallel}}} = \sum_{i=1}^n \frac{1}{Z_i} \quad (5.7)$$

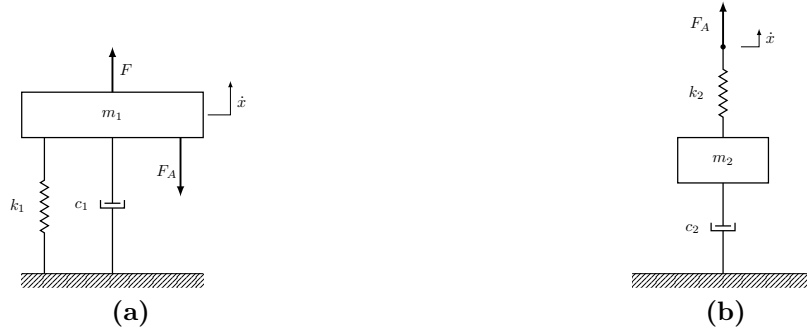


**Figure 5.2:** Two subsystems for the configuration of a SDOF primary system controlled by a non-traditional DVA.

### 5.1.5 Subsystem approach

Consider the case where a SDOF primary system under force excitation is controlled by a non-traditional DVA, the whole system can be partitioned into two subsystems, as depicted in Figures 5.2a and 5.2b. Based on the impedance-mobility approach, the structural dynamics could be concisely represented by Figure 5.3, in which  $Z_S$  and  $Z_A$  are arranged in parallel and correspond to the impedances of primary structure and absorber, respectively. Therefore, its relevant EOMs can be expressed as:

$$F_S + F_A = Z_S \dot{X} + Z_A \dot{X} = F \quad (5.8)$$

with

$$Z_S = m_1 s + \frac{k_1}{s} + c_1, \quad Z_A = \frac{1}{\frac{s}{k_2} + \frac{1}{m_2 s + c_2}}. \quad (5.9)$$

In what follows, one consists in finding the piezoelectric analogous model of non-traditional DVA, whose equivalent mechanical impedance should be equal to  $Z_A$ .

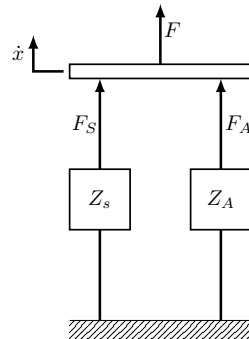


**Figure 5.3:** The equivalent model based on the impedance-mobility approach.

## 5.2 Piezoelectric analogous model

The piezoelectric transducer can generate a voltage across its terminals when a mechanical force is exerted on it, and vice versa. Meanwhile, its generated current is controlled by the mechanical velocity. Therefore, electromechanical analogy via the piezoelectric transducer follows the principle of direct analogy, namely the mechanical force is related to the electric voltage and the mechanical velocity is related to the electric current.

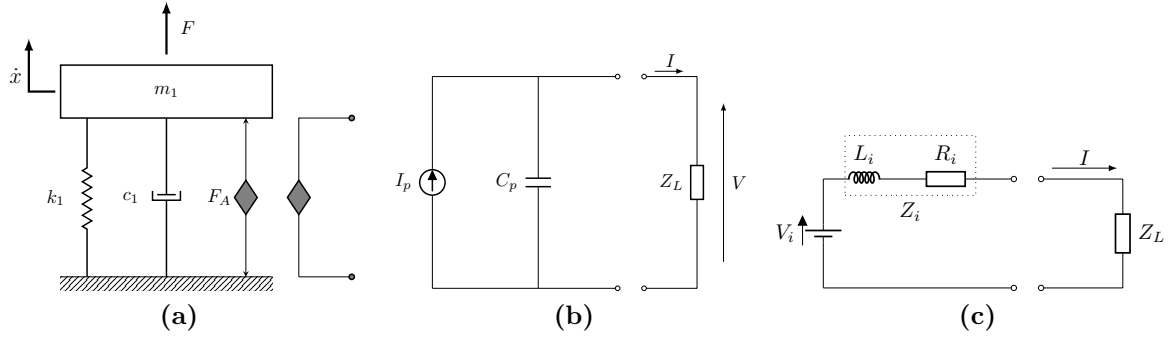


**Figure 5.4:** (a) Equivalent model of a SDOF primary system controlled by an electromechanical shunt damper; (b) electrical model of a PSD with a generalized electrical impedance  $Z_L$ ; (c) electrical model of an EMSD with an impedance  $Z_L$ .

If one replaces the mechanical absorber by a PSD with a generalized electrical impedance  $Z_L$ , as depicted in Figures 5.4a and 5.4b, the dynamics of electromechanical system can be described by [160]:

$$Z_S \dot{X} + F_A = F \quad (5.10a)$$

$$Z_L I = V \quad (5.10b)$$

with

$$F_A = \frac{k_p}{s} \dot{X} + \phi_{pe} V \quad (5.11a)$$

$$I = \phi_{pe} \dot{X} - C_p s V \quad (5.11b)$$

where  $k_p$  is the mechanical stiffness of short-circuited piezoelectric element and  $\phi_{pe}$  is the piezoelectric coupling coefficient. Therefore, the EOMs (5.10) can be recast into the form of Eq. (5.8):

$$\bar{Z}_S \dot{X} + Z_{pe} \dot{X} = F \quad (5.12)$$

where  $\bar{Z}_S$  is the modified mechanical impedance of structure due to the inclusion of piezoelectric transducer and  $Z_{pe}$  is the equivalent mechanical impedance of PSD, with their expressions given by:

$$\bar{Z}_S = m_1 s + \frac{k_1 + k_p}{s} + c_1, \quad Z_{pe} = \frac{1}{\frac{C_p s}{\phi_{pe}^2} + \frac{1}{\phi_{pe}^2 \cdot Z_L}}. \quad (5.13)$$

	Mechanical model	External shunt circuit
Maxwell unit		
Inertial mechanical network		
Non-traditional DVA		
NSDVA		
Non-traditional IDVA		
NSIDVA		

**Table 5.4:** Basic mechanical elements or vibration absorbers and the external shunt circuits of their corresponding PSD.

Therefore, the piezoelectric analogous model of non-traditional DVA should satisfy the relationship  $Z_A = Z_{pe}$ , leading to the expression of shunt impedance  $Z_L$ :

$$Z_L = \frac{m_2}{\phi_{pe}^2} s + \frac{c_2}{\phi_{pe}^2} \quad (5.14)$$

According to the addition laws for electrical impedances,  $Z_L$  is the total impedance of an inductor  $L_2$  and a resistor  $R_2$  in series, whose values are related to the mechanical mass and damper by, respectively:

$$L_2 = \frac{m_2}{\phi_{pe}^2}, \quad R_2 = \frac{c_2}{\phi_{pe}^2}. \quad (5.15)$$

Meanwhile, the piezoelectric capacitance  $C_p$  is analogous to the mechanical stiffness  $k_2$  with  $C_p = \phi_{pe}^2/k_2$ .

To this end, one can remark that the non-traditional DVA can be accurately realized by a PSD with a series RL shunt circuit. However, the use of PSD will increase the equivalent mechanical stiffness of primary structure, thereby altering its natural frequency. Thus, one should substitute  $k_1$  by  $k_1 + k_p$  when determining the parameters of shunt circuit by means of electromechanical analogy.

Following the same approach, six configurations of basic mechanical elements or vibration absorbers and the shunt circuits of their corresponding analogous PSD are summarized in Table 5.4. In summary, the values of electronic components are related to those of mechanical elements by:

$$L_i = \frac{m_i}{\phi_{pe}^2} \text{ or } \frac{b_i}{\phi_{pe}^2}, \quad R_i = \frac{c_i}{\phi_{pe}^2}, \quad C_i = \frac{\phi_{pe}^2}{k_i}. \quad (5.16)$$

Employing a Maxwell unit or an inertial mechanical network between the proof mass of primary structure to its base forms the so-called relaxation isolator [55] or inerter-based isolator [51]. It is worth mentioning that their realization via piezoelectric transducer may not be an attractive option, since the static stiffness of coupled system is increased, leading to a reduced frequency range of vibration isolation.

Besides, analogous PSDs of both NSDVA and NSIDVA are also provided, in which the effect of negative stiffness is realized by the negative capacitance  $C_n$  in series with the transducer. Given that the analogous relationship is established and their optimal design have been accomplished in previous chapter, the application of both NSDVA and NSIDVA can be extended to vibration control of flexible structures. Their optimal design based on different tuning strategies will be experimentally validated in future works.

### 5.3 Electromagnetic analogous model

When an EMSD is employed, its equivalent electrical model is depicted in Figure 5.4c and the structural dynamics of system can be expressed as:

$$Z_S \dot{X} + F_A = F \quad (5.17a)$$

$$(Z_i + Z_L) I = V_i \quad (5.17b)$$

with

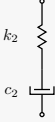
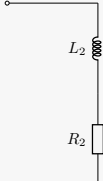
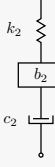
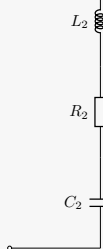
$$F_A = \phi_{em} I \quad (5.18a)$$

$$V_i = \phi_{em} \dot{X} \quad (5.18b)$$

where  $Z_i = L_i s + R_i$  are the inherent impedances of electromagnetic transducer and  $\phi_{em}$  is the electromagnetic coupling coefficient. In this case, the mechanical force is correlated to the electric current, while the voltage is controlled by the mechanical velocity. Thus, the analogous relationship via the electromagnetic transducer follows the principle of inverse analogy, with the correspondence between electric and mechanical elements given as below:

$$L = \frac{\phi_{em}^2}{k}, \quad R = \frac{\phi_{em}^2}{c}, \quad C = \frac{m}{\phi_{em}^2} \text{ or } \frac{b}{\phi_{em}^2}. \quad (5.19)$$

Finally, the structural dynamics can be transformed into the following form:

	Mechanical model	External shunt circuit
Maxwell unit		
Inertial mechanical network		

**Table 5.5:** Electromagnetic realization of Maxwell unit and inertial mechanical network.

$$Z_S \dot{X} + \frac{\phi_{em}^2}{L_i s + R_i + Z_L} \dot{X} = F \quad (5.20)$$

Clearly, the structural impedance  $Z_S$  does not change due to the inclusion of electromagnetic transducer in the idealized scenario. Nevertheless, the possible configurations of mechanical analogous models are restricted by the presence of inherent impedances  $Z_i$ . In Table 5.5, the accurate realization of Maxwell unit and inertial mechanical network via EMSD is provided. Finally, it should be mentioned that other dampers can be imitated if negative impedances are used to compensate the electrical losses of transducer.

## 5.4 Concluding remarks

In this chapter, the mobility-impedance and subsystem approaches are employed to describe the structural dynamics. The possibility of realizing several non-traditional mechanical dampers by means of PSD is investigated, and their corresponding shunt circuit is provided. Such an electromechanical equivalence enables to develop new shunt damping techniques in the framework of PSD, to facilitate the implementation and precise tuning of proposed concepts of mechanical absorbers as well as to deliver the same damping performance in a more lightweight way.

The next chapter will investigate a novel hybrid IDVA, in which the passive part will be realized by means of an EMSD enclosed by a series RLC shunt circuit.



## Chapter 6

# A General Control Law for Hybrid DVA and IDVA

The mechanical control devices investigated in previous chapters are all passive, therefore, their maximal control efficiency is dictated by their amount of equivalent tuned mass, which is relatively small due to practical constraints. Thus, active control force can be introduced into the passive control devices in order to enhance their capability of counteracting the vibration induced by external disturbances. Nevertheless, such a control scheme, i.e. the hybrid vibration control, could considerably improve the damping performance at the expense of potential destabilization of whole system.

Recently, Collette and Chesné [135] proposed an  $\alpha$ -controller for the hybrid DVA, which can assure the fail-safe behaviour and the theoretical hyperstability simultaneously. Recalling the advantage claimed for the IDVA over the DVA and its possible realization via the resonant electromagnetic shunt damper, this chapter consists in proposing an hybrid IDVA based on the generalized  $\alpha$ -controller. In this configuration, the electromagnetic actuator is driven by the position signal of primary system and the controller can be regarded as  $n$  identical units arranged in series in the feedback control loop, each of which introduces two coalesced real zeros and a single pole at the origin. Compared to the hybrid DVA, the hybrid IDVA will lead to a reduced vibration for primary system when the controller is failed or switched off. Moreover, one of major contributions of this chapter is the proposition and theoretical proof of a uniform limit for the magnitude of intentionally introduced zeros, irrespective of the controller order. Finally, a criterion is set to compare compensators of different orders by equalizing their corresponding active force at the natural frequency of primary system, therefore, the influence of controller order on the control performance could be revealed.

## 6.1 Mathematical modeling

### 6.1.1 System description

The configuration related to hybrid IDVA is depicted in Figure 6.1b. The mass and stiffness of primary system are  $m_1$  and  $k_1$ , respectively. Directly excited by a primary force  $f_p$ , the vibration of main system is confined by two subsystems simultaneously. The passive control effect is attributed to the auxiliary IDVA, composed of a block mass  $m_2$  attached to the target structure via a spring  $k_2$  and an inerter-based mechanical network in parallel. The inertial device is actually a series connection of a spring  $k_3$ , an inerter  $b_3$  and a damper  $c_3$ . In order to reinforce the disturbance rejection performance, the structural position is fed back to the actuator via a controller  $-H$ , exerting an active force  $f_a$  on both the primary system and the tuned mass of IDVA.

### 6.1.2 Generalized equations of motion

The underlying dynamics of whole system in Figure 6.1b could be described by:

$$m_1 \ddot{x}_1 = k_2(x_2 - x_1) + k_3(x_3 - x_1) - k_1 x_1 + f_p(t) - f_a(t) \quad (6.1a)$$

$$m_2 \ddot{x}_2 = k_2(x_1 - x_2) + c_3(\dot{x}_4 - \dot{x}_2) + f_a(t) \quad (6.1b)$$

$$0 = b_3(\ddot{x}_3 - \ddot{x}_4) + c_3(\dot{x}_2 - \dot{x}_4) \quad (6.1c)$$

$$0 = b_3(\ddot{x}_4 - \ddot{x}_3) + k_3(x_1 - x_3) \quad (6.1d)$$

where  $x_1$  and  $x_2$  are displacement of inertial masses of primary system and IDVA, respectively.  $x_3$  and  $x_4$  are the displacement at two terminals of inerter  $b_3$ . Finally, the dot over symbol represents differentiation with respect to unscaled time  $t$ .

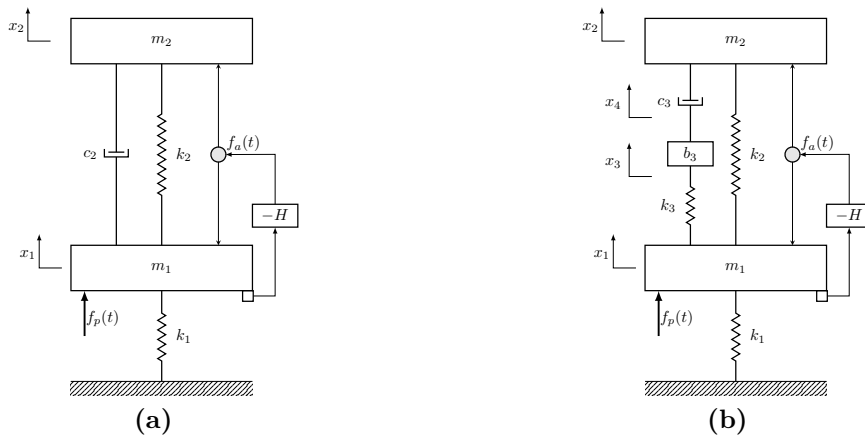


**Figure 6.1:** Schematic diagrams of a SDOF primary system controlled by: (a) a hybrid DVA; (b) a hybrid IDVA.

Since the current system is different from those investigated in precedent chapters, the complete nondimensionalization procedure is herein detailed. A series of dimensionless parameters are first introduced:

$$\begin{aligned} \omega_1 &= \sqrt{\frac{k_1}{m_1}}, & \omega_2 &= \sqrt{\frac{k_2}{m_2}}, & \omega_3 &= \sqrt{\frac{k_3}{b_3}}, & \xi &= \frac{c_3}{2\sqrt{k_2 m_2}}, \\ \mu &= \frac{m_2}{m_1}, & \nu &= \frac{b_3}{m_1}, & \alpha &= \frac{\omega_2}{\omega_1}, & \beta &= \frac{\omega_3}{\omega_1}. \end{aligned} \quad (6.2)$$

where  $\omega_1$  and  $\omega_2$  are natural frequency of primary and auxiliary systems, and  $\omega_3$  is the corner frequency of mechanical network.  $\xi$  denotes the passive mechanical damping ratio of absorber.  $\mu$  and  $\nu$  stands for the mass ratio and the inertance-to-mass ratio. Besides,  $\alpha$  (or  $\beta$ ) is frequency ratio between  $\omega_2$  (or  $\omega_3$ , respectively) and  $\omega_1$ . Moreover, the time is scaled by  $\omega_1$ , i.e.  $\tau = \omega_1 t$ .

Finally, the EOMs (6.1) are transformed into:

$$x_1'' + \mu x_2'' + x_1 + 2\mu\xi\alpha(x_2' - x_4') + \nu\beta^2(x_1 - x_3) = \tilde{f}_p(\tau) \quad (6.3a)$$

$$\mu x_2'' + 2\mu\xi\alpha(x_2' - x_4') + \mu\alpha^2(x_2 - x_1) = \tilde{f}_a(\tau) \quad (6.3b)$$

$$\nu(x_3'' - x_4'') + 2\mu\xi\alpha(x_2' - x_4') = 0 \quad (6.3c)$$

$$x_4'' - x_3'' + \beta^2(x_1 - x_3) = 0 \quad (6.3d)$$

where the prime in the superscript denotes differentiation with respect to the rescaled time  $\tau$ . Besides, the normalized primary and active forces are related to the original ones by:  $\tilde{f}_p = f_p/k_1$  and  $\tilde{f}_a = f_a/k_1$ . In the following context, the complex magnitudes of  $x_1$ ,  $\tilde{f}_p$  and  $\tilde{f}_a$  are denoted as  $X_1$ ,  $\tilde{F}_p$  and  $\tilde{F}_a$ , respectively.

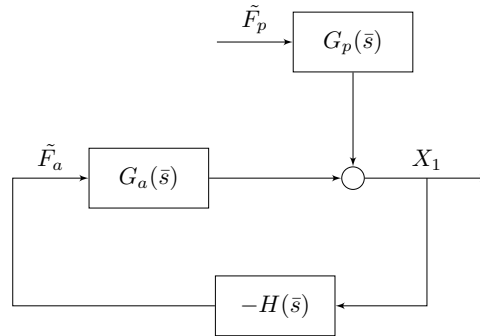


**Figure 6.2:** Block diagram of the SISO control scheme.

### 6.1.3 Open-loop and closed-loop FRFs

In fact, the hybrid control system in Figure 6.1b can be classified as a single-input-single-output (SISO) feedback control scheme, where the primary disturbance  $\tilde{F}_p$  constitutes the only input and the output is the position of primary system  $X_1$ .

Consequently, its corresponding block diagram can be drawn as in Figure 6.2, where  $G_p(\bar{s})$  and  $G_a(\bar{s})$  are two FRFs relating the structural position  $X_1$  and the primary and active forces,  $\tilde{F}_p$  and  $\tilde{F}_a$ . Besides,  $\bar{s}$  is the dimensionless Laplace variable, i.e.  $\bar{s} = j\lambda$  with  $j = \sqrt{-1}$  and  $\lambda$  being the excitation frequency normalized by the natural frequency  $\omega_1$ . As evident from Figure 6.2,  $X_1$ ,  $G_p(\bar{s})$  and  $G_a(\bar{s})$  satisfy the following relationship:

$$X_1 = G_p(\bar{s})\tilde{F}_p + G_a(\bar{s})\tilde{F}_a \quad (6.4)$$

Meanwhile,  $G_p(\bar{s})$  and  $G_a(\bar{s})$  can be achieved by setting as zero  $\tilde{f}_a$  and  $\tilde{f}_p$  in Eq. (6.3), respectively. After taking the Laplace transform, one has:

$$\begin{aligned} G_p &= \frac{B_4\bar{s}^4 + B_3\bar{s}^3 + B_2\bar{s}^2 + B_1\bar{s} + B_0}{A_6\bar{s}^6 + A_5\bar{s}^5 + A_4\bar{s}^4 + A_3\bar{s}^3 + A_2\bar{s}^2 + A_1\bar{s} + A_0}, \\ G_a &= \frac{-\bar{s}^2(C_2\bar{s}^2 + C_1\bar{s} + C_0)}{A_6\bar{s}^6 + A_5\bar{s}^5 + A_4\bar{s}^4 + A_3\bar{s}^3 + A_2\bar{s}^2 + A_1\bar{s} + A_0}. \end{aligned} \quad (6.5)$$

with the coefficients in the denominator being:

$$\begin{cases} A_6 = 2\mu\xi\alpha \\ A_5 = \nu\beta^2 \\ A_4 = 2\xi\alpha [\mu + (\mu^2 + \mu)\alpha^2 + (\mu + \nu + \mu\nu)\beta^2] \\ A_3 = \nu\beta^2 [1 + (1 + \mu)\alpha^2] \\ A_2 = 2\xi\alpha [\mu\alpha^2 + (\mu + \nu)\beta^2 + (\mu^2 + \mu)\alpha^2\beta^2] \\ A_1 = \nu\alpha^2\beta^2 \\ A_0 = 2\mu\xi\alpha^3\beta^2 \end{cases} \quad (6.6)$$

and those in the numerator given by:

$$\begin{cases} B_4 = 2\mu\xi\alpha \\ B_3 = \nu\beta^2 \\ B_2 = 2\xi\alpha(\mu\alpha^2 + \mu\beta^2 + \nu\beta^2) \\ B_1 = \nu\alpha^2\beta^2 \\ B_0 = 2\mu\xi\alpha^3\beta^2 \end{cases} \quad \begin{cases} C_2 = 2\mu\xi\alpha \\ C_1 = \nu\beta^2 \\ C_0 = 2\mu\xi\alpha\beta^2 \end{cases} \quad (6.7)$$

Therefore, the closed-loop FRF from the input  $\tilde{F}_p$  to the output  $X_1$  can be described in terms of  $G_p(\bar{s})$ ,  $G_a(\bar{s})$  and  $H(\bar{s})$ , as follows:

$$G_{CL} = \frac{X_1}{\tilde{F}_p} = \frac{G_p(\bar{s})}{1 + G_a(\bar{s})H(\bar{s})} \quad (6.8)$$

Furthermore, one can read from Eq. (6.8) that the open-loop FRF of control system is expressed as:

$$G_{OL} = G_a(\bar{s})H(\bar{s}) \quad (6.9)$$

by which the stability of control scheme will be assessed. Finally, it should be mentioned that the block diagram in Figure 6.2 is idealized due to the fact that the dynamics of actuator and the measurement noise are not taken into consideration.

### 6.1.4 Passive IDVA

When the controller is switched off, i.e.  $H = 0$ , the vibration is attenuated entirely via passive IDVA. In this case, the closed-loop FRF of system (6.8) is reduced to:  $G_{CL} = G_p$ . The closed-form solutions to the  $H_\infty$  optimization of passive IDVA were conducted by Barredo et al. [53] by using a methodology based on fixed points. The optimal parameters of IDVA are herein provided [53]:

$$\nu = \frac{2\mu^2}{\mu+1}, \quad \alpha = \frac{1}{\mu+1}, \quad \beta = \sqrt{\frac{1}{\mu+1}}, \quad \xi = \sqrt{\frac{11\mu}{36(\mu+1)}}. \quad (6.10)$$

With a mass ratio of 5%, the vibration control performance of passive DVA and IDVA are compared in terms of steady state FRFs (in Figure 6.3a) and damping capability (in Figure 6.3b). It suggests from Figure 6.3a that compared to the passive DVA, the IDVA can reduce the peak vibration amplitude by 19.4% in the steady state. However, the IDVA has an inferior capability than the DVA in terms of decaying transient disturbances, as reflected by the smaller damping ratio.

## 6.2 Controller design

The hyperstable controller proposed in this chapter has the following formulation:

$$-H(\bar{s}) = g_n \left[ \frac{(\bar{s} + \theta)^2}{\bar{s}} \right]^n, \quad n = 1, 2, \dots \quad (6.11)$$

where  $g_n$  and  $\theta$  are the normalized gain and magnitude of introduced zeros, with  $g_n \geq 0$  and  $\theta > 0$ . They are related to the dimensional parameters,  $\hat{g}_n$  and  $\hat{\theta}$ , by:

$$g_n = \frac{\hat{g}_n}{m_1 \omega_1^{2-n}}, \quad \theta = \frac{\hat{\theta}}{\omega_1}. \quad (6.12)$$

suggesting that  $g_n$  is related to the order of controller, while  $\theta$  is not. As evident from Eq. (6.11), the controller of order  $n$  introduces  $2n$  zeros and  $n$  poles to structural dynamics. In practice, the maximum value of  $n$  should not be superior to the number of poles in excess of zeros relevant to the FRF,  $G_a(\bar{s})$ . Finally, the compensator (6.11) reduces to a proportional feedback controller when the zero-th order is considered.

To this end, the major objective of this present study is twofold. First, find the allowable bound on the magnitude of coalesced zeros  $\theta$  for all admissible orders  $n$  of compensator, which renders the control system always stable in the whole range of gain  $g_n$ . Second, investigate the influence of compensator order on the resultant disturbance rejection performance.

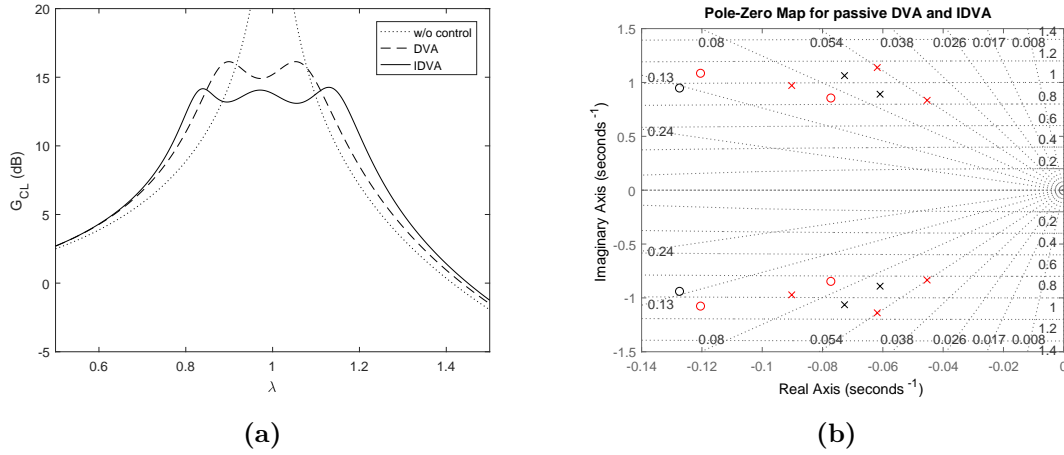


**Figure 6.3:** Dynamics of undamped primary system coupled with a passive DVA or IDVA: (a) normalized FRFs  $G_{CL}$  (dotted line: without control, dashed line: DVA, solid line: IDVA); (b) pole-zero plots (black: DVA, red: IDVA). The mass ratio is set as:  $\mu = 0.05$ .

### 6.2.1 Hyperstability

As illustrated in Figure 6.3b, the three pairs of conjugate poles do not locate on the imaginary axis, the deviation of which depends on the viscous damper  $c_3$  and the inherent damping of target structure (which is not modelled in this chapter). The presence of mechanical damping increases the gain margin, thereby improving the relative stability, however, it renders more complicated the deduction of hyperstability limits for  $\theta$ .

In the objective of simplifying the deduction analysis, it is pertinent to consider the worst-case scenario, in which all three pairs of conjugate poles lie on the imaginary axis, thus, the linear system is marginally stable. Nevertheless, it should be mentioned that such a simplification will result in a more strict bound on  $\theta$ . In fact, the worst-case scenario occurs when an undamped primary system is considered and the damper  $c_3$  is intentionally disabled by restricting the relative motion of its two terminals, i.e. by imposing  $c_3 = \infty$ . By doing so, the open-loop FRF  $G_a(\bar{s})$  has three pairs of conjugate poles on the imaginary axis, which are denoted as  $\pm j\lambda_1$ ,  $\pm j\lambda_2$  and  $\pm j\lambda_3$  with  $0 < \lambda_1 < \lambda_2 < \lambda_3$ , respectively. Their magnitudes are analytically formulated in Appendix D.1, which are only dependent of the mass ratio  $\mu$ . Meanwhile, the dynamics of coupled system related to hybrid DVA (shown in Figure 6.1a) and its open-loop poles in the worst-case scenario are also provided in Appendix D.2.

**Proposition 2** *For the proposed compensator (6.11) of any order  $n$ , the allowable bound on  $\theta$  guaranteeing an infinite gain margin is given by:*

$$\lambda_1 \leq \theta \leq \lambda_3 \quad (6.13)$$

in which  $\lambda_1$  and  $\lambda_3$  are the smallest and largest eigenvalues.

**Proof 2** The path of proving the proposition (6.13) could follow two routes: applying the Routh-Hurwitz stability criterion; determining the departure angles at all open-loop poles. In what follows, these two approaches will be employed for the case of  $n = 1$  and  $n \geq 2$  successively.

- $n = 1$ . Detailed proof is given in Appendix D.3.
- $n \geq 2$ . The same deduction procedure as the case of  $n = 1$  can be still employed. Meanwhile, one can prove the proposition by calculating the departure angles at these open-loop poles on the imaginary axis. Alternatively speaking, the system remains stable if all closed-loop poles go immediately inside the left-half complex plane.

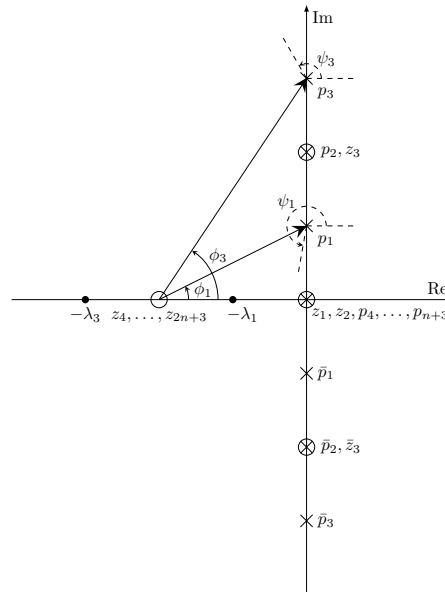


**Figure 6.4:** Pole-zero plot for the hybrid control scheme related to IDVA in the worst-case scenario. Zeros are marked by unfilled circles and poles are represented by cross markers.  $\phi_1$  and  $\phi_3$  are phase angles of the vector joining the coalesced zeros  $z_i = -\theta$  ( $i = 4, 5, \dots, 2n + 3$ ) to the poles  $p_1$  and  $p_3$ , respectively.  $\psi_1$  and  $\psi_3$  stand for the departure angles of root locus at the open-loop poles  $p_1$  and  $p_3$ .

As depicted in Figure 6.4, the passive system in the worst-case scenario has three pairs of conjugate poles ( $p_i = +j\lambda_i, \bar{p}_i = -j\lambda_i$ ), two coalesced zeros at the origin ( $z_1$  and  $z_2$ ) and a pair of conjugate zeros ( $z_3$  and  $\bar{z}_3$ ). Meanwhile, the integrated compensator of order  $n$  introduces  $2n$  coincident zeros on the real axis ( $z_4, z_5, \dots, z_{2n+3}$ ) and  $n$  coalesced poles at the origin ( $p_4, \dots, p_{n+3}$ ). For all poles at the origin, the departure angles of their corresponding root loci are equal to  $\pi$  due to the symmetry of other poles and zeros about the real axis.

Besides, the pole  $p_2$  and zero  $z_3$  coincide with each other, engendering a pole-zero cancellation. Therefore, one should only inspect the departure angles of root loci relevant to  $p_1$  and  $p_3$ , which could potentially destabilize the control scheme.

Clearly, the phase angle of the vector joining each imaginary pole/zero to a specific pole  $p_i$  is equal to  $\pm\pi/2$  (the sign depends on their position relationship). Let denote  $\phi_1$  and  $\phi_3$  as the phase angles relating the zeros  $z_4, z_5, \dots, z_{2n+3}$  to the pole  $p_1$  and  $p_3$ , as illustrated in Figure 6.4. Then, the departure angles,  $\psi_1$  and  $\psi_3$ , of root locus starting at  $p_1$  and  $p_3$  can be formulated as, respectively:

$$\psi_1 = 2k\pi + \frac{3\pi}{2} + 2n \left( \phi_1 - \frac{\pi}{4} \right), \quad (6.14a)$$

$$\psi_3 = 2k\pi + \frac{\pi}{2} + 2n \left( \phi_3 - \frac{\pi}{4} \right), \quad k = 0, \pm 1, \pm 2, \dots \quad (6.14b)$$

with  $\phi_1$  and  $\phi_3$  determined as:

$$\phi_1 = \tan^{-1} \left( \frac{\lambda_1}{\theta} \right), \quad \phi_3 = \tan^{-1} \left( \frac{\lambda_3}{\theta} \right). \quad (6.15)$$

Apparently, the phase angles  $\phi_1$  and  $\phi_3$  fluctuate as the introduced zeros  $z_i = -\theta$  ( $i = 4, 5, \dots, 2n+3$ ) move along the negative real axis. Their magnitudes corresponding to different intervals of  $z_i$  are summarized in Tables 6.1 and 6.2, in which the magnitudes of departure angles are also provided. In order to keep the whole root loci in the left-half complex plane, the departure angles  $\psi_1$  and  $\psi_3$  should be constrained by:  $\psi_1 \leq 3\pi/2$  and  $\psi_3 \geq \pi/2$ . According to Tables 6.1 and 6.2, the coalesced zeros should locate within the interval  $z_i \in [-\lambda_3, -\lambda_1]$  (namely  $\lambda_1 \leq \theta \leq \lambda_3$ ), validating the proposition for the case of  $n \geq 2$ .

Until now, a simple and uniform limit for  $\theta$  is proposed and analytically proven, within which the theoretical hyperstability is preserved for the proposed controller. It should be mentioned that the aforementioned proof is conducted for the hybrid control scheme related to the IDVA, however, such a proposition can be also extended to the case of hybrid DVA.

$z_i$	$(-\infty, -\lambda_1)$	$-\lambda_1$	$(-\lambda_1, 0)$
$\phi_1$	$\left(0, \frac{\pi}{4}\right)$	$\frac{\pi}{4}$	$\left(\frac{\pi}{4}, \frac{\pi}{2}\right)$
$\psi_1$	$< \frac{3\pi}{2}$	$= \frac{3\pi}{2}$	$> \frac{3\pi}{2}$

**Table 6.1:** The evolution of phase angle  $\phi_1$  as the coalesced zeros  $z_i = -\theta$  ( $i = 4, 5, \dots, 2n+3$ ) move along the negative real axis. The departure angle  $\psi_1$  of root locus at the pole  $p_1$  is then compared with  $3\pi/2$ .

$z_i$	$(-\infty, -\lambda_3)$	$-\lambda_3$	$(-\lambda_3, 0)$
$\phi_3$	$\left(0, \frac{\pi}{4}\right)$	$\frac{\pi}{4}$	$\left(\frac{\pi}{4}, \frac{\pi}{2}\right)$
$\psi_3$	$< \frac{\pi}{2}$	$= \frac{\pi}{2}$	$> \frac{\pi}{2}$

**Table 6.2:** The evolution of phase angle  $\phi_3$  as the coalesced zeros  $z_i = -\theta$  ( $i = 4, 5, \dots, 2n + 3$ ) move along the negative real axis. The departure angle  $\psi_3$  of root locus at the pole  $p_3$  is then compared with  $\pi/2$ .

### 6.2.2 Criterion for performance comparison

In order to fairly compare the control performances delivered by controllers of different orders, a criterion is herein chosen by equalizing their active forces  $\tilde{f}_a$  at the natural frequency of primary system. Denoting  $(\bar{s} + \theta)^2 / \bar{s}$  as  $\bar{H}$ , the FRF of active force required by a controller of order  $n$ ,  $G_{f,n}$ , is formulated as follows:

$$G_{f,n} = \frac{F_a}{F_p} = \frac{\tilde{F}_a}{\tilde{F}_p} = g_n \bar{H}^n G_{CL} = \frac{g_n \bar{H}^n G_p}{1 - g_n \bar{H}^n G_a} \quad (6.16)$$

Considering two controllers of arbitrary orders,  $i$  and  $j$  with  $i \neq j$ , equating their corresponding active forces at fundamental frequency leads to:

$$|G_{f,i}| = \left| \frac{g_i \bar{H}^i G_p}{1 - g_i \bar{H}^i G_a} \right| = \left| \frac{g_j \bar{H}^j G_p}{1 - g_j \bar{H}^j G_a} \right| = |G_{f,j}| \quad (6.17)$$

with  $g_i$  and  $g_j$  being positive. A rational solution to Eq. (6.17) is:  $g_i \bar{H}^i = g_j \bar{H}^j$ , with which the corresponding closed-loop FRFs have the same magnitude at the resonant frequency. With  $|\bar{H}(\bar{s} = j1)| = 1 + \theta^2$ , the gains  $g_i$  and  $g_j$  are then related by the following relationship:

$$g_i = g_j (1 + \theta^2)^{j-i} \quad (6.18)$$

Therefore, for a given amount of active force at the resonance, the vibration control performance of a compensator is only dependant of its order  $n$  and the magnitude of zeros  $\theta$ .

Clearly, the relationship (6.18) is satisfied when the same type of absorber is used. Nevertheless, it is impossible to derive such a closed-form expression when different types of passive absorber are engaged.

## 6.3 Performance of hybrid control scheme

In the following study, the absorber mass  $m_2$  is of only 5% of the main mass  $m_1$  and the normalized magnitude of introduced zeros is set as  $\theta = 1$  (namely  $\hat{\theta} = \omega_1$ ), which is within the hyperstability limit of  $\theta$  for both hybrid DVA and IDVA.

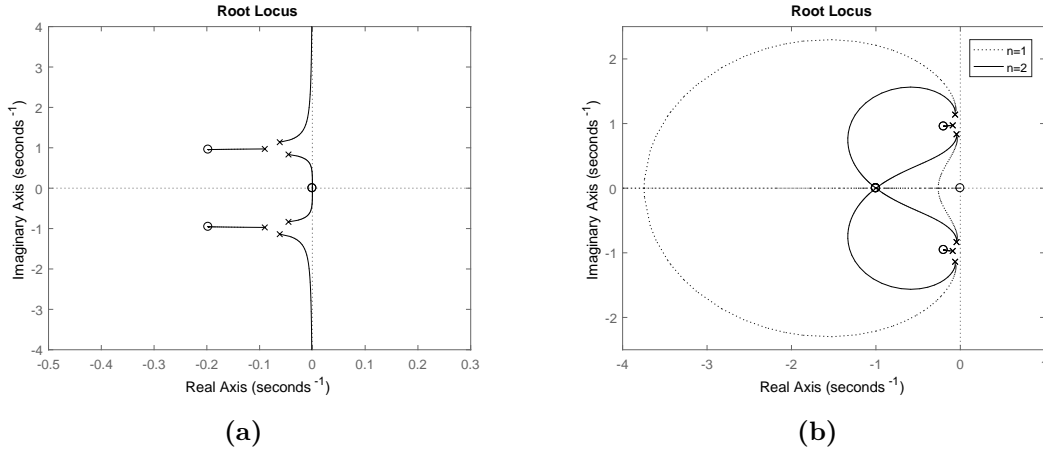


**Figure 6.5:** Root locus diagrams of hybrid control scheme based on the IDVA: (a) zeroth-order controller; (b) controller of orders  $n = 1$  and  $2$  (corresponding to dotted and solid lines, respectively). The normalized magnitude of introduced zeros is set as:  $\theta = 1$ .

### 6.3.1 Root locus

As confirmed by the root loci in Figure 6.5, the coupled system controlled by hybrid IDVAs of order  $n = 0, 1, 2$  remains always stable. With the hyperstability guaranteed, however, the zeroth-order controller (i.e. the direct position feedback control) could not deliver satisfactory control performance, as reflected in Figure 6.5a where its two pairs of conjugate poles migrate towards the imaginary axis when the gain increases. On the contrary, the closed-loop poles shift to the left of their corresponding open-loop poles when a compensator of higher order is used, as illustrated in Figure 6.5b. In fact, this is due to the attraction of coalesced zeros on the real axis, which keeps the whole root locus in the left-half complex plane and improves the control performance simultaneously. Finally, a remark can be made that:

**Remark 1** *The two branches of root locus starting at open-loop poles  $p_1$  and  $p_3$  get closer when the controller order is higher.*

This can be explained by looking at the difference between their corresponding departure angles  $\psi_1$  and  $\psi_3$ , which could be approximated by the ones in the worst-case scenario. According to Eq. (6.14), their difference for a controller of order  $n$  can be analytically formulated as:

$$\psi_1 - \psi_3 = (2l + 1)\pi - 2n(\phi_3 - \phi_1), \quad l = 0, \pm 1, \pm 2, \dots \quad (6.19)$$

in which  $\phi_3 - \phi_1 = \tan^{-1}(\lambda_3/\theta) - \tan^{-1}(\lambda_1/\theta)$  is constant and positive, as  $\lambda_3 > \lambda_1$  always holds for any mass ratio  $\mu$ . When  $n = 0$ , the angle difference is  $\pi$ , as confirmed in Figure 6.5a. Moreover, the difference between  $\psi_1$  and  $\psi_3$  decreases monotonically

as the increase of compensator order  $n$ . Therefore, One can conclude that for a compensator of higher order, the intentionally introduced zeros have a stronger attraction for the root locus.

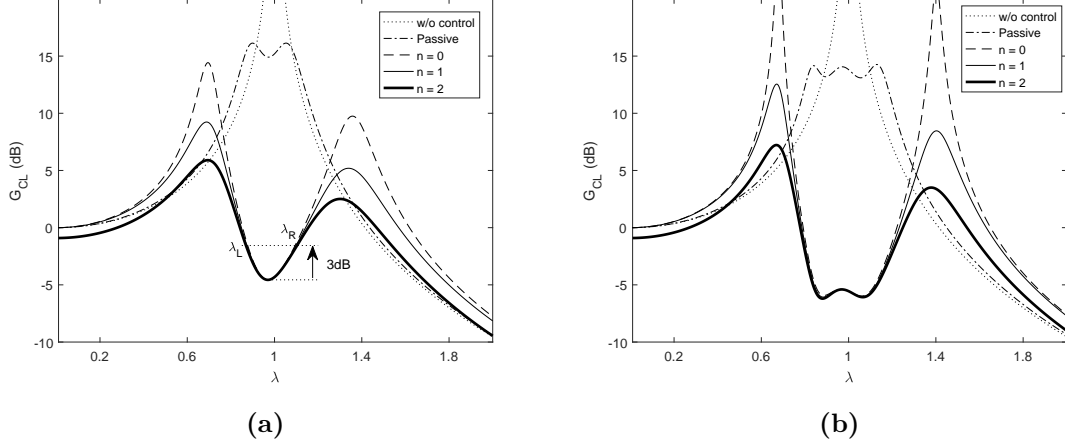


**Figure 6.6:** Closed-loop FRFs  $G_{CL}$  with the passive part being: (a) a DVA; (b) an IDVA. Dotted line: without control, dash-dotted line: passive, dashed line: compensator of order 0, thin solid line: compensator of order 1, thick solid line: compensator of order 2. The set of parameters used for simulation is:  $\mu = 0.05$ ,  $\theta = 1$ ,  $g_0 = 0.4$ ,  $g_1 = 0.2$  and  $g_2 = 0.1$ .

### 6.3.2 Dynamics at specific gains

Hereafter, the gains corresponding to controllers of orders  $n = 0, 1, 2$  are set as:  $g_0 = 0.4$ ,  $g_1 = 0.2$  and  $g_2 = 0.1$ . Note that their values satisfy the relationship (6.18).

The closed-loop FRFs,  $G_{CL}$ , relevant to the DVA and IDVA are depicted in Figs. 6.6a and 6.6b, respectively. In both cases, the hybrid control schemes can reduce the vibration by nearly 20dB in the proximity of fundamental frequency, however, two distinct peaks arise at two sides of the target mode. Moreover, one can notice that the two peaks approach each other when the order of compensator increases, validating the remark made in Section 6.3.1. Finally, a remark can be made in conjunction with Figure 6.6 regarding the peak vibration amplitude that:

**Remark 2** *The increase of compensator order results in the monotonically decreasing vibration amplitudes at the two peaks.*

Comparing now the performance of different absorbers, the advantages claimed for IDVA over DVA reside in two aspects: smaller peak amplitude and larger frequency bandwidth of vibration mitigation in the passive control mode; a broadband col (in the form of double wells) in the frequency response around the target mode in the hybrid control mode. More precisely, the  $-3\text{dB}$  bandwidth  $\lambda_R - \lambda_L$  can be used to

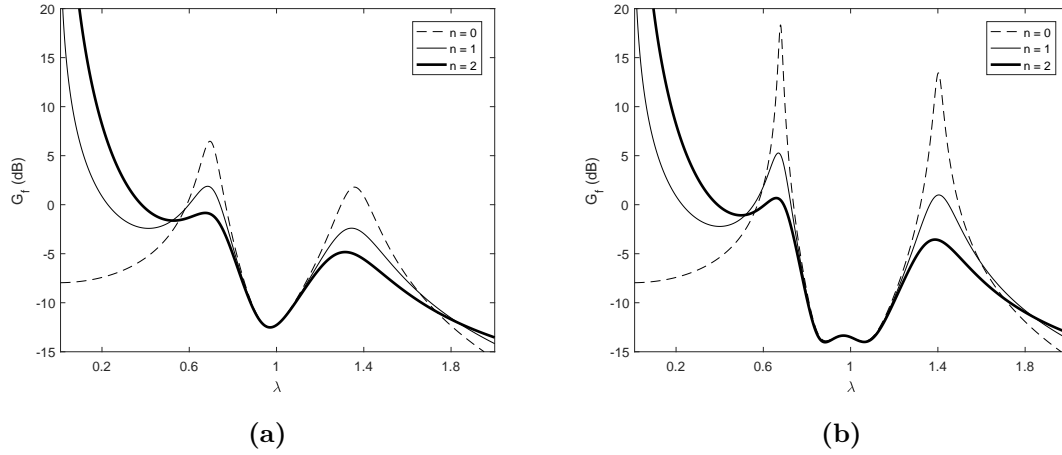


**Figure 6.7:** FRFs of active force required by controllers  $G_{f,n}$  with the passive part being: (a) a DVA; (b) an IDVA. Dashed line: compensator of order 0, thin solid line: compensator of order 1, thick solid line: compensator of order 2. The set of parameters used for simulation is:  $\mu = 0.05$ ,  $\theta = 1$ ,  $g_0 = 0.4$ ,  $g_1 = 0.2$  and  $g_2 = 0.1$ .

quantify the col width, as illustrated in Figure 6.6a. Accordingly, the widths corresponding to hybrid DVA and IDVA of order 2 are 0.234 and 0.365, signifying that the IDVA can broaden the frequency bandwidth of significant vibration reduction by 56% compared to the DVA. Nevertheless, the IDVA results in larger amplitudes at two arising peaks than the DVA when the same controller is used.

The remarks made for the displacement of primary system also hold for the active force required by the controller, as demonstrated in Figure 6.7.

The frequency responses of relative displacement between the primary and tuned masses, also termed as the stroke, are plotted in Figure 6.8. Compared to their passive counterparts, the hybrid control schemes lead to a similar stroke around the natural frequency of main system, however, they yield a much larger stroke at frequencies outside the resonance region. Besides, the strokes at two arising peaks reduce monotonically as the controller order increases.

## 6.4 Practical consideration and case study

In practice, the directly measured signal of main system is usually its acceleration, therefore, two integrators are needed to yield the position signal to drive the actuator in this study. Moreover, the proposed controller of order  $n$  introduces  $n$  more integrators, leading to the phenomenon of stroke saturation and actuator force overloading at the low-frequency region, as shown in Figures 6.7 and 6.8. In avoidance of such a phenomenon, a high pass filter should be introduced in the feedback loop,

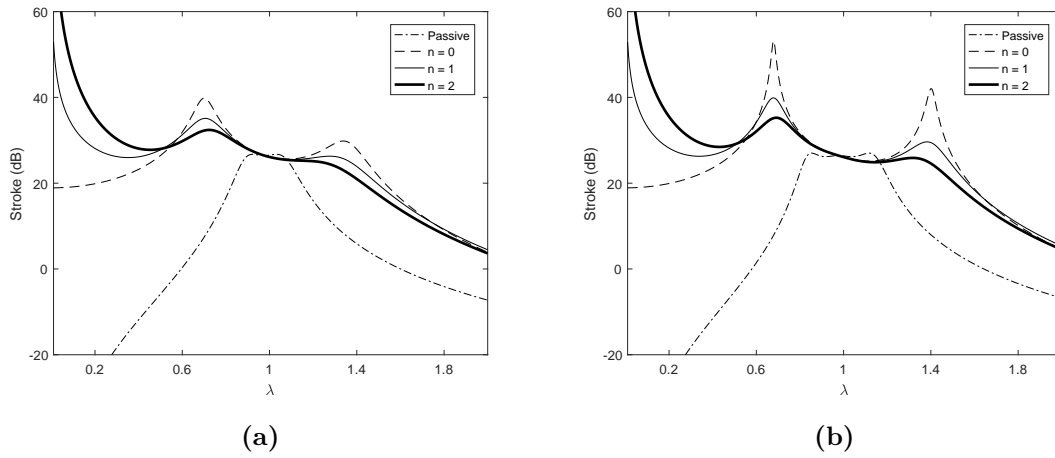


**Figure 6.8:** FRFs of absorber stroke with the passive part being: (a) a DVA; (b) an IDVA. Dashed line: compensator of order 0, thin solid line: compensator of order 1, thick solid line: compensator of order 2. The set of parameters used for simulation is:  $\mu = 0.05$ ,  $\theta = 1$ ,  $g_0 = 0.4$ ,  $g_1 = 0.2$  and  $g_2 = 0.1$ .

which has the form of:

$$H_f(\bar{s}) = \left( \frac{\bar{s}}{\bar{s} + \lambda_c} \right)^{n+2} \quad (6.20)$$

where  $\lambda_c$  is the normalized cut-off frequency of high pass filter and is set as  $\theta/50$  in this paper. Therefore, the open-loop FRF is changed to:  $G_{OL} = G_a(\bar{s})H(\bar{s})H_f(\bar{s})$ .

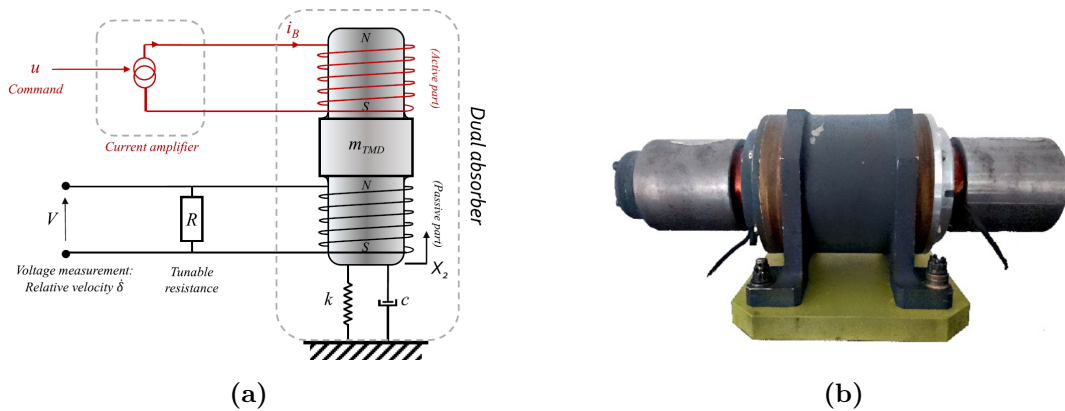


**Figure 6.9:** (a) Schematic diagram of dual transducer; (b) its prototype [134].

## 6. A General Control Law for Hybrid DVA and IDVA

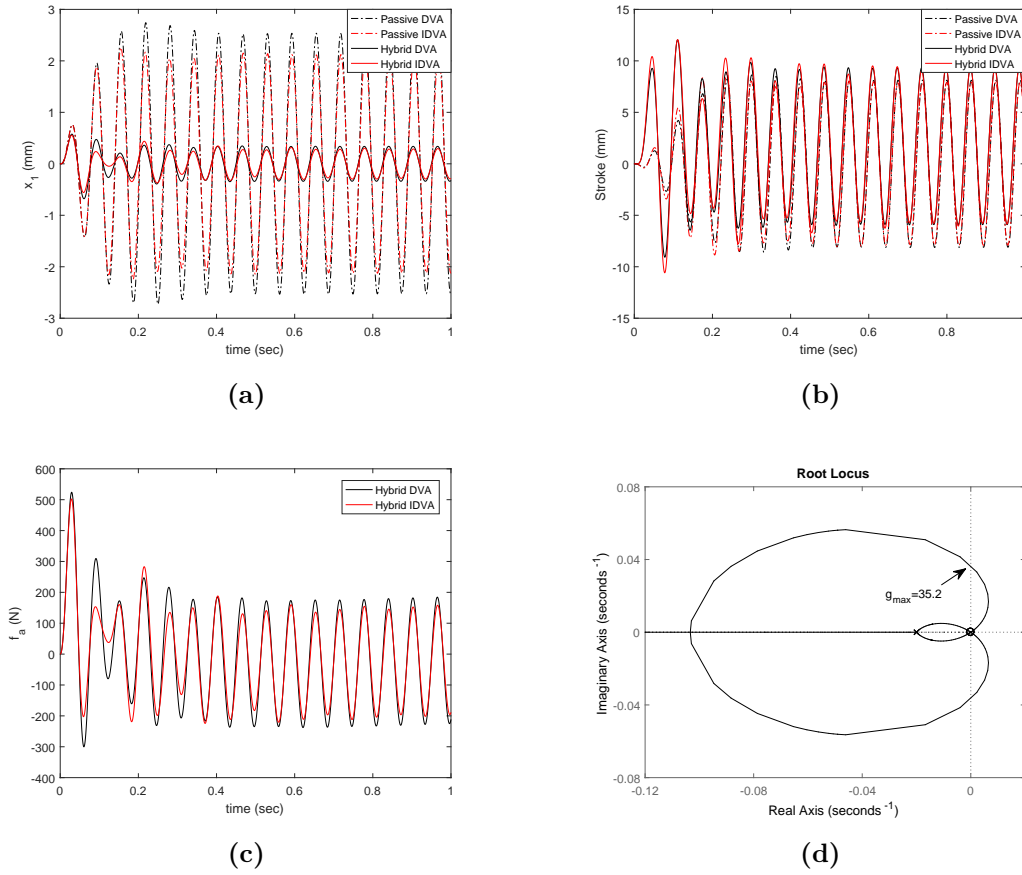


**Figure 6.10:** Temporal responses relevant to passive and hybrid control schemes: (a) displacement of primary system; (b) relative displacement between main and tuned masses (dash-dotted line: passive absorber, solid line: hybrid absorber, black line: DVA-based, red line: IDVA-based). (c) Active force generated by the actuator (black: hybrid DVA, red: hybrid IDVA). (d) Close-up of root locus relevant to first-order hybrid IDVA with high pass filter. The set of parameters used for simulation is:  $\mu = 0.0667$ ,  $\theta = 1$ ,  $g_1 = 0.2$ ,  $\lambda = 1$  and  $|\tilde{F}_p| = 0.5\text{mm}$ .

The main system and the absorber investigated in [134] is chosen as the case study. The absorber can be represented by a mass-spring model with negligible damping and is integrated with two electromagnetic transducers at its two extremities, as depicted in Figure 6.9. Therefore, one of its dual transducer can be served as the actuator, while another can be used to realize the inerter-based mechanical network analogously. The main system has a mass of 150kg, its natural frequency is 16Hz and is weakly damped (0.8%). The absorber mass is 10kg, leading to a mass ratio of 6.67%. Finally, the force constant of actuator is  $k_e = 65\text{N A}^{-1}$ . In the next, the primary system is harmonically excited at its natural frequency and the amplitude of external force is 758N, namely the primary system has a static displacement of  $|\tilde{F}_p| = 0.5\text{mm}$ . Results in previous section show that the same performance is

achieved at the natural frequency when the gains of different controllers satisfy Eq. (6.18). Hereafter, only the first-order controller is considered and its normalized gain is unchanged:  $g_1 = 0.2$ .

The temporal responses of coupled system under harmonic force excitation are depicted in Figure 6.10. It suggests from Figure 6.10a that compared to their passive counterpart, both hybrid control schemes can reduce the vibration amplitude of primary system by 17dB, meanwhile, they do not increase the stroke amplitude significantly, as shown in Figure 6.10b. Moreover, Figure 6.10c illustrates that the hybrid DVA requires an active force slightly greater than the hybrid IDVA. More precisely, the maximum current amplitude required by hybrid DVA in the steady state can be calculated as:  $I = f_a/k_e = 3.5\text{A}$ . Note that this value does not exceed its upper threshold  $I_{\max} = 6\text{A}$ , which was experimentally calibrated. Finally, Figure 6.10d depicts a close-up of root locus related to hybrid IDVA around the origin. One can notice that with the inclusion of high pass filter in the feedback loop, the root locus goes inside the right-half complex plane when the gain is greater than the critical value  $g_{\max} = 35.2$ , therefore, the controller is no longer hyperstable. Nevertheless, this upper threshold is sufficiently large for the proposed controller to deliver a superior control performance in practice, recalling that the controller with a gain of 0.2 can already improve the control performance significantly.

## 6.5 Concluding remarks

This chapter theoretically investigates a simple control law for designing a hybrid control scheme based on either a classic DVA or an IDVA. The position signal of primary system is fed back to drive the actuator and is filtered by a compensator of order  $n$ , which introduces  $2n$  coalesced zeros on the real axis and  $n$  poles at the origin.

For possessing an infinite gain margin, a uniform limit for the magnitude of introduced real zeros is proposed for a controller of arbitrary order and is theoretically proven. It is suggested that the hyperstability is guaranteed when the magnitude of introduced zeros lies between the smallest and largest magnitudes of all open-loop poles, whose closed-form expressions are analytically derived for both DVA and IDVA. Besides, a criterion is proposed to compare the performance delivered by controllers of different orders. Numerical examples demonstrate that increasing the controller order can reduce monotonically the vibration amplitudes at the two arising peaks around the natural frequency of primary system, however, the phenomenon of stroke saturation and active force overloading is encountered at low frequencies due to the increasing integrators in the control loop. Finally, a case study is carried out and some practical issues are discussed.

Future work will be dedicated to the realization of inerter-based mechanical network via electromechanical analogy and the experimental validation of proposed control law.

In the next chapter, a family of semi-active control techniques will be developed, which is based on the EMSD in conjunction with negative inductance. Unlike the hybrid control scheme in this chapter, no additional sensor will be needed to feedback the information of target structure.

# Chapter 7

## Electromagnetic Shunt Damping

Passive vibration control techniques have been developed in Chapters 2, 3 and 4, while Chapter 6 proposed a simple controller design for actively controlling the vibration. The current chapter will focus on the semi-active vibration damping.

The shunt damping techniques based on smart materials are gaining momentum due to the trends towards lightweight structures. Instead of dissipating the mechanical energy of the target structure through a viscous damper, a shunt damper consist in converting it into electrical energy and dissipating it in the external shunt circuit. In this chapter, the shunt damping technique with the use of electromagnetic transducer is of interest.

In the field of PSD, it is a long established fact that adding a NC in series and/or parallel with the piezoelectric transducer can artificially enhance the control performance. In fact, it is attributed to the fact that the use of NCs contributes to the improvement of energy conversion efficiency between mechanical and electrical domains, which is quantified and denoted as the electromechanical coupling factor (EMCF) hereafter. Meanwhile, the current literature on EMSD has reported theoretical and experimental studies on the feasibility of enhancing the damping capability by employing negative impedances (NI and/or NR) in series with the electromagnetic transducer. Nevertheless, the influence of negative impedances on the EMCF related to EMSD is still lacking in the current literature. Besides, no attempt has been made to the employment of negative impedances in parallel with the electromagnetic transducer.

To this end, this chapter consists in carrying out a systematic study on the influence of negative impedances on the EMSD in terms of the EMCF and the confinement of peak structural vibration. All possible layouts of EMSD with a NI in series, in parallel and combination thereof will be first investigated within the same framework and their corresponding EMCFS will be analytically formulated. Finally, six types of shunt circuit design will be applied to the EMSD and their  $H_\infty$  optimization will be conducted for a SDOF primary system, whose control performance will be compared with each other.

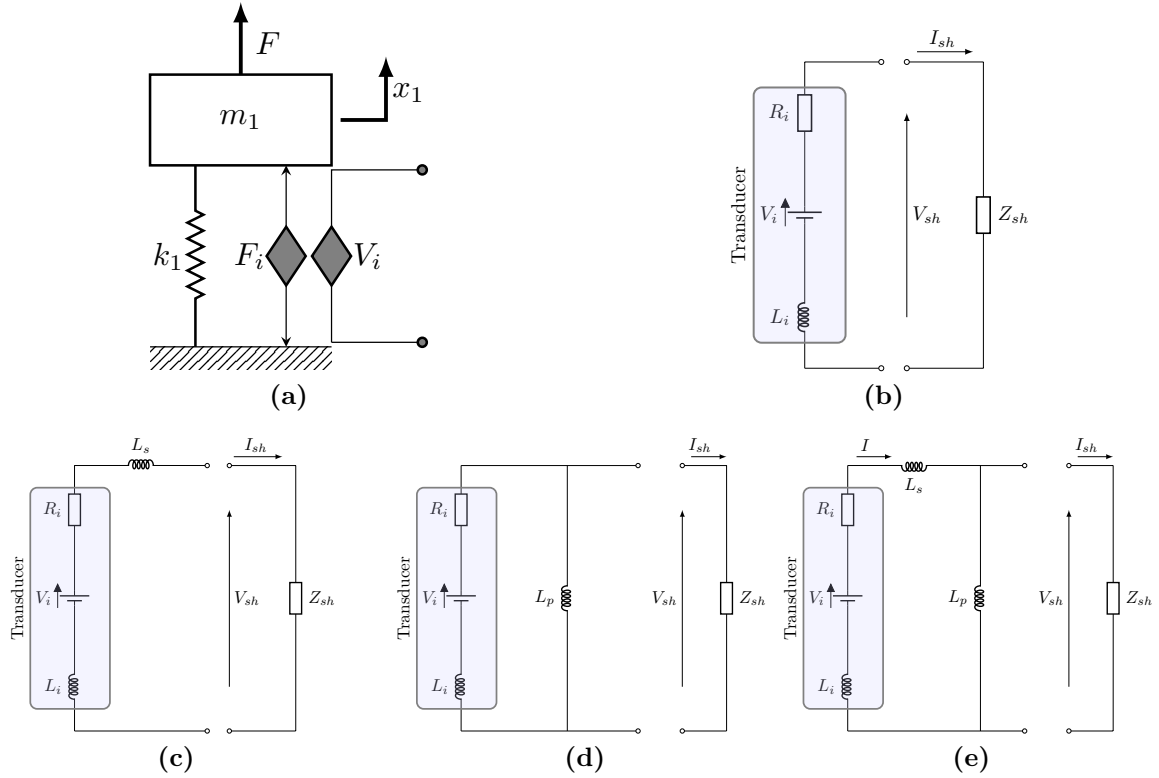


**Figure 7.1:** (a) Schematic diagram of mechanical system coupled with an EMSD. Four layouts are investigated: (b) w/o; (c) series; (d) parallel; (e) SP.

## 7.1 Electromechanical coupling factor

In what follows, the mechanical system under investigation is undamped and is of SDOF, as depicted in Figure 7.1a. To confine its vibration, an electromagnetic transducer is incorporated between its proof mass and the supporting foundation, whose two terminals are connected to a properly designed shunt impedance  $Z_{sh}$ , as shown in Figure 7.1b, which is denoted as the w/o layout hereafter. Meanwhile, adding a NI  $L_s$  in series with the external impedance forms the series layout, as demonstrated in Figure 7.1c. Similarly, a single NI  $L_p$  can be placed in parallel with the generalized impedance  $Z_{sh}$ , yielding the parallel configuration as plotted in Figure 7.1d. Finally, it was suggested from [98] that in the case of PSD, the employment of two NCs in series and parallel connection can further increase the EMCF, thereby improving the effectiveness of PSD. Therefore, a novel SP layout is herein proposed for the EMSD for the first time, in which a NI  $L_s$  is placed in series with the electromagnetic transducer and another NI  $L_p$  is positioned across the two terminals of external shunt circuit, as illustrated in Figure 7.1e.

Clearly, the series and SP layouts will reduce to the w/o and parallel configurations, respectively, when the series NI  $L_s$  is vanished, i.e.  $L_s = 0$ . Therefore, only

investigation of series and SP layouts will be detailed below. In order to facilitate the analysis, two dimensionless parameters are introduced:

$$\alpha = \frac{L_i + L_s}{L_i}, \quad \gamma = \frac{L_p}{L_i}. \quad (7.1)$$

in which  $\alpha - 1$  and  $\gamma$  represent the ratio between the series and parallel NIs and the internal inductance of transducer, respectively.

### 7.1.1 EMCF related to the series layout

For the coupled system shown in Figures 7.1a and 7.1c, its dynamics can be described by the EOMs:

$$m_1 \ddot{x}_1 + k_1 x_1 + \phi_{em} I_{sh} = F \quad (7.2a)$$

$$(L_i + L_s) \dot{I}_{sh} + R_i I_{sh} + V_{sh} = \phi_{em} \dot{x}_1 \quad (7.2b)$$

where  $m_1$  and  $k_1$  are the mass and the stiffness of primary system,  $L_i$  and  $R_i$  are the internal impedances of transducer,  $V_{sh}$  is the voltage across the generalized impedance  $Z_{sh}$  and  $I_{sh}$  is the current flowing through it.

The EMCF of electromechanical system can be defined as [161]:

$$\Psi = \frac{(\omega^{sc})^2 - (\omega^{oc})^2}{(\omega^{oc})^2} = \frac{k^{sc} - k^{oc}}{k^{oc}} \quad (7.3)$$

where  $\omega^{oc}$  and  $\omega^{sc}$  are the open-circuited (OC) and short-circuited (SC) resonant frequencies of electromechanical system, which are related to the OC and SC stiffness,  $k^{oc}$  and  $k^{sc}$ , respectively. For the purpose of simplification, the internal resistance  $R_i$  is strategically neglected when calculating the OC and SC stiffness.

- SC stiffness. Clearly, the voltage  $V_{sh}$  should be equal to zero if the transducer is SC. Therefore, the SC stiffness corresponds to the constant before the displacement term in the mechanical equation, in which the only explicit state variables are  $x_1$  and  $V_{sh}$ . Accordingly, the mechanical equation in Eq. (7.2) can be transformed into:

$$m_1 \ddot{x}_1 + \left( k_1 + \frac{\phi_{em}^2}{L_i + L_s} \right) x_1 - \int \frac{\phi_{em}}{L_i + L_s} V_{sh} dt = F \quad (7.4)$$

implying that the SC stiffness is expressed as:

$$k_S^{sc} = k_1 + \frac{\phi_{em}^2}{L_i + L_s} \quad (7.5)$$

- OC stiffness. When the transducer is OC, the electric current  $I_{sh}$  is vanished. Hence, the OC stiffness will present in the mechanical equation which is explicitly expressed in terms of  $x_1$  and  $I_{sh}$  solely. As evident from Eq. (7.2), the OC stiffness is equal to the stand-alone structural stiffness, namely:

$$k_S^{oc} = k_1 \quad (7.6)$$

As a consequence, the EMCF related to the series layout can be determined as:

$$\Psi_S = \frac{k_S^{\text{sc}} - k_S^{\text{oc}}}{k_S^{\text{oc}}} = \frac{\phi_{em}^2}{k_1(L_i + L_s)} = \frac{\theta}{\alpha} \quad (7.7)$$

where  $\theta$  corresponds to the EMCF of w/o layout:

$$\Psi_{\text{w/o}} = \theta = \frac{\phi_{em}^2}{k_1 L_i} \quad (7.8)$$

which will be termed as the nominal value of EMCF hereafter. According to the analogous relationship (5.19),  $\theta$  represents the ratio between the equivalent electrical stiffness and the mechanical stiffness of primary system.

### 7.1.2 EMCF related to the SP layout

Following the same procedure, the SC and OC stiffness will be determined for the coupled system depicted in Figures 7.1a and 7.1e.

- SC stiffness. According to the Kirchhoff's voltage law, the electrical equation can be written in terms of voltage across the external impedance  $V_{\text{sh}}$ , i.e.:

$$V_i = \phi_{em} \dot{x}_1 = (L_i + L_s) \dot{I} + V_{\text{sh}} \quad (7.9)$$

where  $I$  is the electric current flowing out of the transducer. Therefore, the mechanical equation in Eq. (7.2) can be recast into:

$$m_1 \ddot{x}_1 + \left( k_1 + \frac{\phi_{em}^2}{L_i + L_s} \right) x_1 - \int \frac{\phi_{em}}{L_i + L_s} V_{\text{sh}} dt = F \quad (7.10)$$

When the external impedance is SC, the SC stiffness reads as:

$$k_{\text{SP}}^{\text{sc}} = k_1 + \frac{\phi_{em}^2}{L_i + L_s} \quad (7.11)$$

- OC stiffness. The dynamics in the electrical domain can be formulated in terms of  $I_{\text{sh}}$ :

$$V_i = \phi_{em} \dot{x}_1 = (L_i + L_s + L_p) \dot{I} - L_p \dot{I}_{\text{sh}} \quad (7.12)$$

Hence, one can transform the mechanical equation in Eq. (7.2) into the following form:

$$m_1 \ddot{x}_1 + \left( k_1 + \frac{\phi_{em}^2}{L_i + L_s + L_p} \right) x_1 + \frac{\phi_{em} L_p}{L_i + L_s + L_p} I_{\text{sh}} = F \quad (7.13)$$

By vanishing the current flowing into the external impedance, i.e.  $I_{\text{sh}} = 0$ , the OC stiffness is then achieved:

$$k_{\text{SP}}^{\text{oc}} = k_1 + \frac{\phi_{em}^2}{L_i + L_s + L_p} \quad (7.14)$$

Layout	w/o	Series	Parallel	SP
OC stiffness	$k_1$	$k_1$	$k_1 + \frac{\phi_{em}^2}{L_i + L_p}$	$k_1 + \frac{\phi_{em}^2}{L_i + L_s + L_p}$
SC stiffness	$k_1 + \frac{\phi_{em}^2}{L_i}$	$k_1 + \frac{\phi_{em}^2}{L_i + L_s}$	$k_1 + \frac{\phi_{em}^2}{L_i}$	$k_1 + \frac{\phi_{em}^2}{L_i + L_s}$
EMCF	$\theta$	$\frac{\theta}{\alpha}$	$\frac{\gamma\theta}{1 + \gamma + \theta}$	$\frac{\gamma\theta}{\alpha(\alpha + \gamma + \theta)}$

**Table 7.1:** The OC and SC stiffness of various electromechanical systems and their corresponding EMCFs.

One can remark that for the EMSD of SP configuration, the SC stiffness is influenced by the series inductance  $L_s$ , while its OC stiffness is controlled by both series and parallel inductances  $L_s$  and  $L_p$ . Finally, the EMCF related to the SP layout can be formulated as:

$$\Psi = \frac{k_{SP}^{sc} - k_{SP}^{oc}}{k_{SP}^{oc}} = \frac{\gamma\theta}{\alpha(\alpha + \gamma + \theta)} \quad (7.15)$$

### 7.1.3 Remarks

The EMCFs corresponding to the w/o and parallel layouts can be obtained from those of series and SP layouts by removing the series inductance  $L_s$ , i.e. by imposing  $\alpha = 1$ . Table 7.1 summarizes the OC and SC stiffness of electromechanical system related to various layouts and their corresponding EMCFs.

Apparently, the series configuration can turn superior to the w/o layout in terms of EMCF when  $\alpha$  is bounded by:

$$\alpha \in (\alpha_S^-, \alpha_S^+) = (0, 1) \quad (7.16)$$

where the signs  $-$  and  $+$  refer to the lower and upper limit, respectively. Given that the EMCF characterizes the energy conversion efficiency between electrical and mechanical domains, a larger value of EMCF for an EMSD signifies more mechanical energy dissipated in the electrical circuit, implying that adding a NI in series can entail a better shunt damping performance.

Similarly, the parallel configuration is more preferable than the w/o layout when  $\gamma$  satisfies:

$$\gamma < \gamma_P^+ = -1 - \theta \quad (7.17)$$

while the SP layout outperforms the series counterpart as if the following condition is met:

$$\gamma < \gamma_{SP}^+ = -\alpha - \theta, \forall \alpha \in (0, 1). \quad (7.18)$$

The previous analysis theoretically reveals the potential benefit of introducing NIs into the existing shunt circuit so as to improve the attenuation performance. However, it should be mentioned that all EMCFs are calculated by neglecting the coil resistance. In what follows, the complete dynamics of electromechanical systems will be modeled, on the basis of which the optimal design of various shunt circuits will be carried out.

A series NI will be first inserted in existing R and RC shunt circuits (as depicted in Figure 7.2a), forming the series RL and RLC shunt circuits (as shown in Figure 7.2b). Later, the SP shunt will be investigated, as plotted in Figure 7.2d, which is based on the R shunt with two NIs positioned in series and in parallel with it. Removing the series NI, the SP shunt reduces to the parallel shunt, as illustrated in Figure 7.2c. Finally, the optimized shunt circuits will be compared with each other in terms of shunt damping performance.

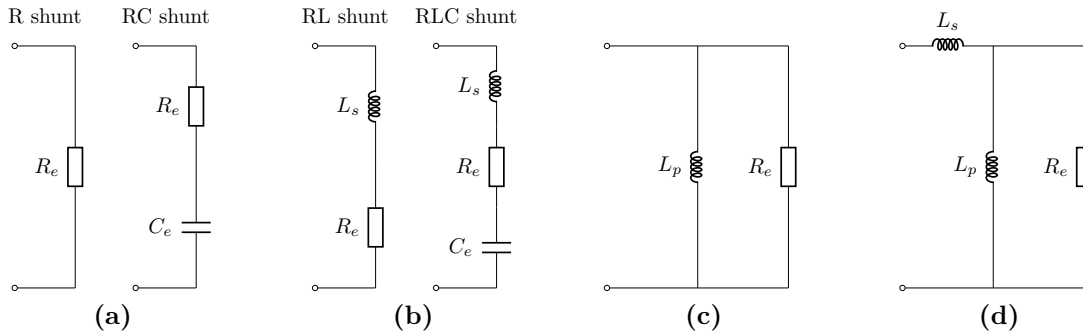


**Figure 7.2:** (a) R and RC shunts; (b) series RL and RLC shunts; (c) parallel shunt; (d) SP shunt.

## 7.2 EMSD enclosed by series RL and RLC shunts

The dynamics of primary system controlled by an EMSD with a series RLC shunt circuit can be described by:

$$m_1 \ddot{x}_1 + k_1 x_1 + \phi_{em} I_{sh} = F \quad (7.19a)$$

$$(L_i + L_s) \dot{I}_{sh} + (R_i + R_e) I_{sh} + \int \frac{1}{C_e} I_{sh} dt = \phi_{em} \dot{x}_1 \quad (7.19b)$$

while it reduces to the EOMs in the case of a series RL shunt circuit when  $C_e$  approaches to infinity. To simplify the optimal design, the following dimensionless parameters are introduced:

$$\beta = \frac{R_e}{R_i}, \quad \kappa = \frac{R_i}{L_i \omega_1}, \quad \omega_e = \sqrt{\frac{1}{L_i C_e}}, \quad \phi = \frac{\omega_e}{\omega_1}. \quad (7.20)$$

where  $\beta$  is the ratio between external and internal resistances,  $\kappa$  is a constant dependent of the internal impedances of transducer and the natural frequency of primary system,  $\omega_e$  is the pseudo electrical resonant frequency and  $\phi$  is the frequency tuning ratio. Therefore, the normalized displacement FRFs of primary system can be expressed as follows:

- Series RL shunt:

$$G(\bar{s}) = \frac{X_1}{F/k_1} = \frac{\alpha\bar{s} + \kappa(1 + \beta)}{\alpha\bar{s}^3 + \kappa(1 + \beta)\bar{s}^2 + (\alpha + \theta)\bar{s} + \kappa(1 + \beta)} \quad (7.21)$$

- Series RLC shunt:

$$G(\bar{s}) = \frac{X_1}{F/k_1} = \frac{\alpha\bar{s}^2 + \kappa(1 + \beta)\bar{s} + \phi^2}{\alpha\bar{s}^4 + \kappa(1 + \beta)\bar{s}^3 + (\alpha + \theta + \phi^2)\bar{s}^2 + \kappa(1 + \beta)\bar{s} + \phi^2} \quad (7.22)$$

According to the Routh-Hurwitz criterion, the stability of whole system is guaranteed when the following conditions are satisfied:

$$\alpha > \alpha_S^- = 0, \beta > \beta_S^- = -1. \quad (7.23)$$

implying that in the series layout, the magnitudes of negative impedances should be always inferior to the internal impedances of transducer.

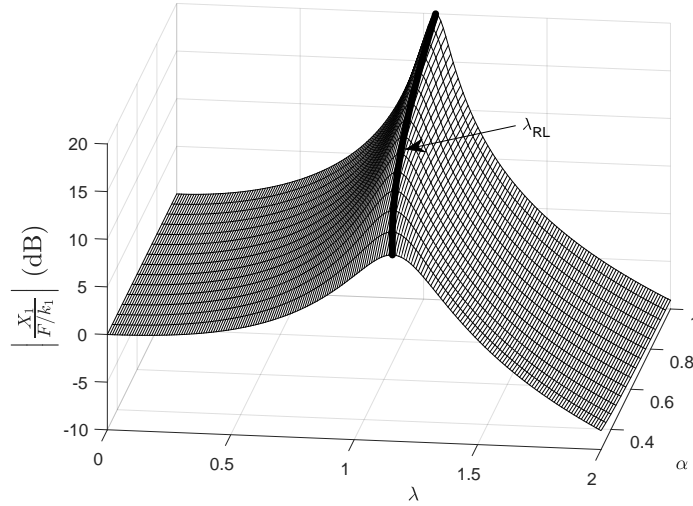


**Figure 7.3:** Displacement FRFs of primary system against the normalized excitation frequency  $\lambda$  and the inductance ratio  $\alpha$  controlled by a RL EMSD. The set of parameters is:  $\theta = 0.2$  and  $\kappa = 5$ .

### 7.2.1 Optimization of EMSD with a series RL shunt

For the electromechanical system related to the series RL shunt, the displacement FRFs of primary system always pass through an invariant position when the external resistance varies, therefore, the FPT can be applied to optimally tune the non-resonant EMSD. The optimization procedure had been detailed in previous chapters and is herein omitted for brevity. The optimal parameters and some characteristics are directly given at below.

- The abscissa of fixed point  $\lambda_{\text{RL}}$  and its normalized displacement amplitude  $\|G\|_{\infty, \text{RL}}$  are:

$$\lambda_{\text{RL}} = \sqrt{1 + \frac{\theta}{2\alpha}}, \quad \|G\|_{\infty, \text{RL}} = \frac{2\alpha}{\theta}. \quad (7.24)$$

Clearly, the dynamics of optimal EMSD coupled with series RL shunt is dominated by two key parameters, the total inductance ratio  $\alpha$  and the nominal EMCF  $\theta$ . As evident from Figure 7.3, the fixed point shifts to higher frequency when the negative inductance  $L_s$  approaches to the internal inductance of coil  $L_i$ , meanwhile, the peak vibration amplitude decreases monotonically.

- The optimal resistance ratio  $\beta_{\text{RL}}$  is equal to:

$$\beta_{\text{RL}} = \frac{1}{\kappa} \sqrt{\alpha^2 + \frac{\theta}{2}\alpha} - 1 \quad (7.25)$$

Therefore, the stability margin can be read as:  $\beta_{\text{RL}} - \beta_{\text{S}}^- = \sqrt{\alpha^2 + \theta\alpha/2}/\kappa$ . For a given transducer and primary system, the stability margin decreases monotonically as the total inductance ratio  $\alpha$  decreases, namely the negative impedances get closer to the internal impedances, which could destabilize the system in realistic applications.

By imposing  $\alpha = 1$ , the optimal parameters of series RL shunt reduce to those of R shunt.

Strategy	FPT	$H_2$ optimization	SMC
Inductance ratio $\alpha$	$\left[\frac{\theta}{2}, +\infty\right)$	$\left[\frac{\theta}{2}, +\infty\right)$	$\left[\frac{\theta}{4}, +\infty\right)$
Resistance ratio $\beta$	$\frac{1}{\kappa} \sqrt{\frac{3}{2}\theta\alpha} - 1$	$\frac{1}{\kappa} \sqrt{\alpha\theta - \frac{\theta^2}{4}} - 1$	$\frac{2}{\kappa} \sqrt{\theta\alpha} - 1$
Frequency tuning ratio $\phi$	$\sqrt{\alpha - \frac{\theta}{2}}$	$\sqrt{\alpha - \frac{\theta}{2}}$	$\sqrt{\alpha}$

**Table 7.2:** Optimal parameters of an EMSD shunted by a series RLC circuit tuned by the FPT, the  $H_2$  optimization criterion and the SMC.

## 7.2.2 Optimization of EMSD with a series RLC shunt

The EMSD shunted by a series RLC circuit is optimized according to the FPT, the  $H_2$  optimization criterion and the SMC, respectively. The derivation process related to the  $H_2$  optimization criterion is detailed in Appendix E.1, while those based on the FPT and the SMC are omitted for brevity. To summarize, the optimal parameters of resonant EMSD are provided in Table 7.2, with the allowable bound on total inductance ratio  $\alpha$  specified in each optimal scenario.

Besides, some key characteristics when tuned by the FPT and the SMC are given at below.

- The FPT-base optimal design. The two fixed points locate at:

$$\lambda_{\text{RLC},1} = \sqrt{1 - \frac{\theta}{2\alpha}}, \quad \lambda_{\text{RLC},2} = \sqrt{1 + \frac{\theta}{2\alpha}}. \quad (7.26)$$

at which the normalized displacement amplitude is expressed as:

$$\|G\|_{\infty, \text{RLC}} = \sqrt{\frac{2\alpha}{\theta}} \quad (7.27)$$

It suggests from Figure 7.4 that the reduction of  $\alpha$  (i.e. the increase of negative inductance  $L_s$ ) leads to the spreading of fixed points and the decreasing of peak vibration amplitudes, thereby entailing a better effectiveness and an enhanced robustness.

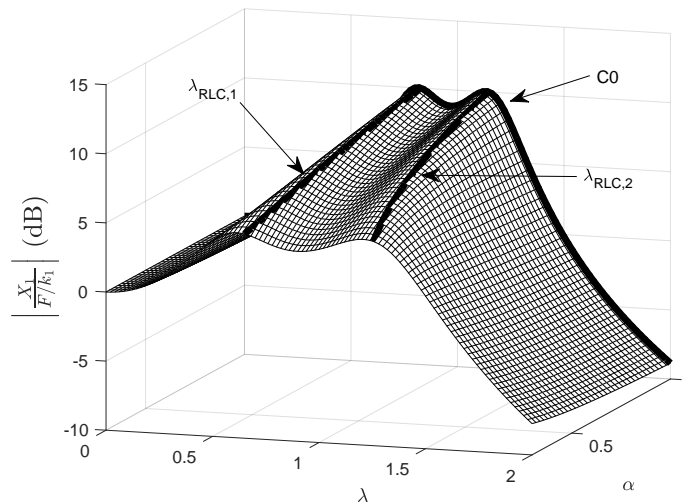


**Figure 7.4:** Displacement FRFs of primary system against  $\lambda$  and  $\alpha$  controlled by a RLC EMSD. The set of parameters is:  $\theta = 0.2$  and  $\kappa = 5$ .

- The SMC-base optimal design. The real part of coalesced pairs of conjugate poles, i.e. the degree of stability, is formulated as:

$$p = \Lambda = \sqrt{\frac{\theta}{4\alpha}} \quad (7.28)$$

Meanwhile, all poles of whole system when tuned by the SMC locate on a circle whose centre is the origin of complex plane and whose radius is equal to unity, namely  $r = 1$ . As  $\alpha$  decreases gradually, the coalesced poles move on the circle in such a way that they move away from the imaginary axis and migrate towards the real axis, entailing a faster attenuation rate of transient response and a smaller oscillation cycle.

### 7.2.3 Remarks

For both EMSDs coupled with a series RL and RLC shunt circuit, the optimal values of resistance and capacitance are formulated in terms of the series NI  $L_s$ , which could be adjusted within a certain interval.

In the optimal scenario, the vibration amplitude of primary system at fixed points is only dependent of the nominal EMCF  $\theta$  and the inductance ratio  $\alpha$ . Moreover, the vibration amplitude when controlled by the RC or series RLC shunt circuit is the square root of that when shunted by a R or series RL circuit, respectively.

## 7.3 EMSD enclosed by a SP shunt

### 7.3.1 Mathematical modeling

The EOMs of electromechanical system related to the SP layout are formulated as:

$$m_1 \ddot{x}_1 + k_1 x_1 + \phi_{em} I = F \quad (7.29a)$$

$$(L_i + L_s) \dot{I} + R_i I + V_{sh} = \phi_{em} \dot{x}_1 \quad (7.29b)$$

$$\frac{\dot{V}_{sh}}{R_e} + \frac{V_{sh}}{L_p} = \dot{I} \quad (7.29c)$$

By employing the aforementioned dimensionless parameters and taking the Laplace transform, the displacement FRF of primary system is simplified as:

$$\begin{aligned} G(\bar{s}) &= \frac{X_1}{F/k_1} \\ &= \frac{\alpha\gamma\bar{s}^2 + \kappa(\alpha\beta + \gamma + \beta\gamma)\bar{s} + \beta\kappa^2}{\alpha\gamma\bar{s}^4 + \kappa(\alpha\beta + \gamma + \beta\gamma)\bar{s}^3 + (\alpha\gamma + \theta\gamma + \beta\kappa^2)\bar{s}^2 + \kappa(\alpha\beta + \gamma + \beta\gamma + \beta\theta)\bar{s} + \beta\kappa^2} \end{aligned} \quad (7.30)$$

As evident from the denominator, the coupled system has four eigenvalues, suggesting that an additional DOF could be introduced by employing the SP layout. This could be confirmed by computing the equivalent mechanical impedance of EMSD, namely:

$$\frac{F_i}{\dot{X}_1} = \phi_{em} \frac{I}{\dot{X}_1} = k_1 \theta \frac{\gamma \bar{s} + \beta \kappa}{\alpha \gamma \bar{s}^2 + \kappa(\alpha \beta + \gamma + \beta \gamma) \bar{s} + \beta \kappa^2} \quad (7.31)$$

whose denominator is a second order polynomial, implying that the resistive shunt enhanced by two NIs in series and parallel could behave as a mass-spring-damper system, which will be theoretically proven at below. Finally, the squared amplitude of displacement FRF of primary system could be achieved by substituting  $\bar{s} = j\lambda$  into Eq. (7.30), yielding:

$$\begin{aligned} G^2 &= \left| \frac{X_1}{F/k_1} \right|^2 \\ &= \frac{(\beta \kappa^2 - \alpha \gamma \lambda^2)^2 + \lambda^2 \kappa^2 (\alpha \beta + \gamma + \beta \gamma)^2}{\left[ (\beta \kappa^2 - \alpha \gamma \lambda^2)(1 - \lambda^2) - \theta \gamma \lambda^2 \right]^2 + \lambda^2 \kappa^2 \left[ \beta \theta + (\alpha \beta + \gamma + \beta \gamma)(1 - \lambda^2) \right]^2} \end{aligned} \quad (7.32)$$

### 7.3.1.1 Optimal design based on the FPT

To apply the FPT, an electrical damping ratio  $\xi_e$  should be first defined for the EMSD coupled with a SP shunt in a similar manner to a second-order mechanical oscillator:

$$\xi_e = \frac{|\alpha \beta + \gamma + \beta \gamma|}{2\sqrt{\alpha \beta \gamma}} \quad (7.33)$$

which should be subject to:

$$\alpha \beta \gamma > 0 \quad (7.34)$$

Therefore, the squared amplitude of displacement FRF (7.32) corresponding to two extreme cases,  $\xi_e = 0$  and  $\xi_e \rightarrow \infty$ , could be simplified as:

$$G^2 \Big|_{\xi_e=0} = \frac{(\beta \kappa^2 - \alpha \gamma \lambda^2)^2}{\left[ (\beta \kappa^2 - \alpha \gamma \lambda^2)(1 - \lambda^2) - \theta \gamma \lambda^2 \right]^2 + (\theta \kappa \beta)^2 \lambda^2}, \quad G^2 \Big|_{\xi_e \rightarrow \infty} = \left( \frac{1}{1 - \lambda^2} \right)^2. \quad (7.35)$$

Equating the two expressions yields a quadratic equation in  $\lambda^2$  as:

$$a_2 \lambda^4 + a_1 \lambda^2 + a_0 = 0 \quad (7.36)$$

whose coefficients are given by:

$$a_2 = \alpha \gamma^2, \quad a_1 = -\beta \gamma \kappa^2 - \alpha \gamma^2 - \frac{1}{2} \theta \gamma^2, \quad a_0 = \beta \gamma \kappa^2 - \frac{1}{2} \theta \beta^2 \kappa^2. \quad (7.37)$$

from which one can obtain the sum of its two roots  $\lambda_1^2$  and  $\lambda_2^2$  as:

$$\lambda_1^2 + \lambda_2^2 = -\frac{a_1}{a_2} \quad (7.38)$$

Besides, another constraint on their sum can be achieved by balancing  $G^2 \Big|_{\xi_e \rightarrow \infty, \lambda = \lambda_1}$  and  $G^2 \Big|_{\xi_e \rightarrow \infty, \lambda = \lambda_2}$ , leading to:

$$\lambda_1^2 + \lambda_2^2 = 2 \quad (7.39)$$

By combining Eqs. (7.38) and (7.39), the optimal resistance ratio  $\beta$  is determined as a function of two inductance ratios  $\alpha$  and  $\gamma$ :

$$\beta = \frac{\gamma}{\kappa^2} \left( \alpha - \frac{\theta}{2} \right) \quad (7.40)$$

By back-substituting Eq. (7.40) into (7.36), its two real roots read

$$\lambda_1^2 = 1 - \sqrt{\frac{4\theta\kappa^2 + \theta(\theta - 2\alpha)^2}{8\alpha\kappa^2}}, \quad \lambda_2^2 = 1 + \sqrt{\frac{4\theta\kappa^2 + \theta(\theta - 2\alpha)^2}{8\alpha\kappa^2}}. \quad (7.41)$$

which imposes the positivity on series inductance ratio  $\alpha$ . Meanwhile, the normalized displacement amplitude of primary system at fixed points is formulated as:

$$\|G\|_{\infty, SP} = \sqrt{\frac{8\alpha\kappa^2}{4\theta\kappa^2 + \theta(\theta - 2\alpha)^2}} \quad (7.42)$$

According to the FPT, the subsequent approach consists in calculating the optimal damping ratio by imposing a zero tangent for the displacement FRF at  $\lambda_1^2$  and  $\lambda_2^2$ , which is very sophisticated. For the sake of convenience, the vibration amplitudes at fixed point and at a reference frequency are equalized. In this study, the reference frequency is set as the natural frequency, i.e.  $\lambda_{\text{ref}} = 1$ , at which the vibration amplitude is equal to:

$$G \Big|_{\lambda = \lambda_{\text{ref}}} = \sqrt{\frac{(\beta\kappa^2 - \alpha\gamma)^2 + \kappa^2(\alpha\beta + \gamma + \beta\gamma)^2}{\theta^2\gamma^2 + \kappa^2\beta^2\theta^2}} \quad (7.43)$$

Then, balancing Eqs. (7.42) and (7.43) conducts to a quadratic equation in  $\gamma$ :

$$b_2\gamma^2 + b_1\gamma + b_0 = 0 \quad (7.44)$$

whose coefficients are equal to:

$$\begin{cases} b_2 = (\theta - 2\alpha)^2 \\ b_1 = -2(\theta - 2\alpha)(2\alpha^2 + 2\kappa^2 - \alpha\theta) \\ b_0 = 4\alpha^4 - 4\theta\alpha^3 + (\theta^2 + 8\kappa^2)\alpha^2 - 12\theta\kappa^2\alpha + 4\kappa^4 + \kappa^2\theta^2 \end{cases} \quad (7.45)$$

Hence, two possible solutions for the inductance ratio  $\gamma$  can be obtained, as follows:

$$\gamma_1 = -\alpha - \frac{2\kappa^2}{2\alpha - \theta} - \frac{\kappa|2\alpha - \theta|}{(2\alpha - \theta)^2} \sqrt{8\alpha\theta - \theta^2}, \quad \gamma_2 = -\alpha - \frac{2\kappa^2}{2\alpha - \theta} + \frac{\kappa|2\alpha - \theta|}{(2\alpha - \theta)^2} \sqrt{8\alpha\theta - \theta^2}. \quad (7.46)$$

Shunt	R	RL	RC	RLC	Parallel	SP
$\ G\ _\infty$	$\frac{2}{\theta}$	$\frac{2\alpha}{\theta}$	$\sqrt{\frac{2}{\theta}}$	$\sqrt{\frac{2\alpha}{\theta}}$	$\sqrt{\frac{2}{\theta} \frac{1}{1 + \frac{(\theta-2)^2}{4\kappa^2}}}$	$\sqrt{\frac{2\alpha}{\theta} \frac{1}{1 + \frac{(\theta-2\alpha)^2}{4\kappa^2}}}$

**Table 7.3:** Normalized peak displacement amplitude of primary system controlled by various shunt circuits tuned by the FPT.

Clearly, only the one satisfying the stability requirement should be retained. According to the Routh-Hurwitz criterion, the optimal inductance ratio  $\beta$  is formulated as:

$$\gamma = -\alpha - \frac{2\kappa^2}{2\alpha - \theta} + \frac{\kappa}{2\alpha - \theta} \sqrt{8\alpha\theta - \theta^2} \quad (7.47)$$

with the stability analysis detailed in the Appendix E.2.

## 7.4 Discussion

To this end, it is pertinent to compare the vibration damping performance of various shunt circuits. Table 7.3 summarizes the analytical formulae of peak displacement amplitudes of primary system normalized by its static deflection when controlled by R, RL, RC, RLC, parallel and SP shunt circuits. It is interesting that for all series layouts, the peak amplitude of primary system is solely controlled by the corresponding EMCF,  $\Psi_S$  in Eq. (7.7), in such a way that:

- For non-resonant shunt circuits (R, RL):

$$\|G\|_\infty = \frac{2}{\Psi_S} \quad (7.48)$$

- For resonant shunt circuits (RC, RLC):

$$\|G\|_\infty = \sqrt{\frac{2}{\Psi_S}} \quad (7.49)$$

For all series layouts, the use of a series NI will increase the EMCF, thereby reducing the peak vibration amplitude of primary system.

In the framework of electromagnetic shunt damping, a criterion could be herein proposed to assess the electromagnetic coupling strength by comparing the nominal value of EMCF and 2, as follows:

$$\begin{cases} \theta < 2: \text{ weakly coupled;} \\ \theta = 2: \text{ critically coupled;} \\ \theta > 2: \text{ strongly coupled.} \end{cases} \quad (7.50)$$

Following this criterion, the optimal RC shunt for a critically coupled system is actually a R shunt, whose left fixed point has an abscissa of zero. Meanwhile, the peak vibration amplitude of primary system is equal to its static deflection. Therefore, the aforementioned optimal design based on the FPT is not applicable to a strongly coupled system, due to the fact that the vibration amplitudes at invariant points are no longer global maximum.

In general, the electromechanical system is weakly coupled. Therefore, the peak displacement amplitude of primary system should always be greater than its static deflection, meanwhile, an optimal resonant shunt circuit (RC or RLC) should always be superior to its non-resonant counterpart (R or RL) in terms of shunt damping performance. Finally, one can observe from Table 7.3 that compared to the RLC shunt, the R shunt enhanced by series and parallel NIs can lead to a slightly smaller vibration amplitude of primary system at fixed points.

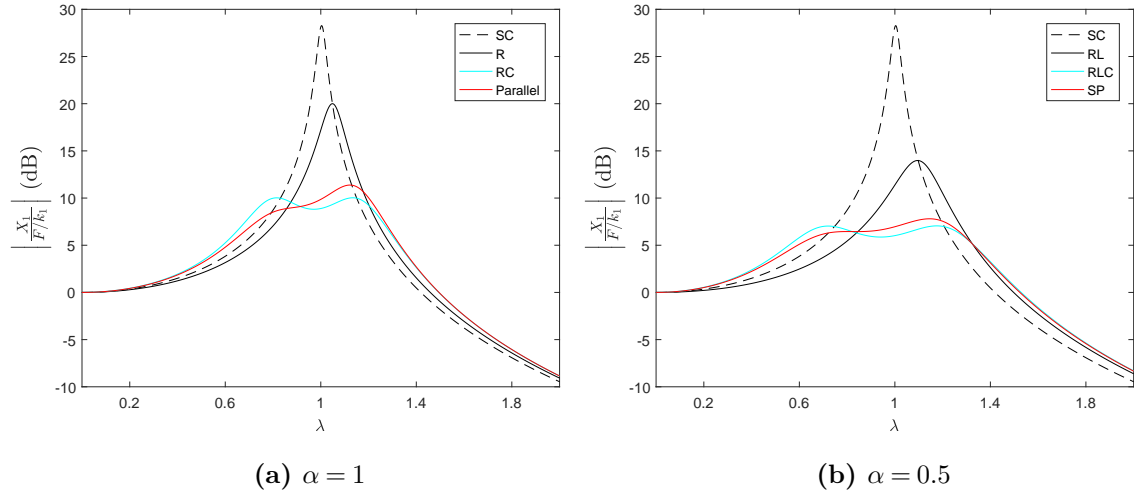


**Figure 7.5:** Displacement FRFs of primary system controlled by an EMSD: (a)  $\alpha = 1$  (dashed: SC, black: R, cyan: RC, red: parallel); (b)  $\alpha = 0.5$  (dashed: SC, black: RL, cyan: RLC, red: SP). The set of parameters is:  $\theta = 0.2$  and  $\kappa = 5$ .

Figure 7.5a depicts the displacement FRFs of primary system when the EMSD is SC or enclosed by a R, RC or parallel shunt. The nominal EMCF and the system constant are set as:  $\theta = 0.2$  and  $\kappa = 5$ . When the transducer is SC, the peak vibration amplitude of primary system is 28.3dB, while it reduces to 20dB, 10dB and 11.4dB when controlled by an EMSD coupled with a R, RC and parallel shunt, respectively. Employing a NI with  $\alpha = 0.5$  in series with previous shunt circuits, the peak vibration amplitudes are further decreased to 14dB, 7dB and 7.8dB, respectively, as plotted in Figure 7.5b. Clearly, an evident misalignment of vibration amplitudes at fixed points is observed in both FRFs related to the parallel and SP shunts, which is attributed to the fact that the damping value had not been optimized according to the classic FPT. Besides, three more remarks can be made, as listed below:

- The SC vibration amplitude of primary system can be approximated by that at its natural frequency, i.e.:

$$\|G\|_{\infty, \text{SC}} = G \Big|_{\lambda=1} = \frac{\sqrt{1 + \kappa^2}}{\theta} \quad (7.51)$$

If the two parameters  $\theta$  and  $\kappa$  are known, one can estimate the attainable vibration reduction from a specific shunt circuit with respect to the SC case.

- By comparing the vibration attenuation performance of the series RL and the parallel shunts, it suggests that adding a single NI in parallel with the purely resistive shunt could present more benefit than the series layout.
- The R shunt in conjunction with a parallel NI has a similar damping capability as the RC shunt, meanwhile, the SP shunt can lead to a shunt damping performance comparable to that of RLC shunt.

## 7.5 Concluding remarks

In this chapter, a systematic study on improving the shunt damping performance by using NIs has been conducted. To this end, three possible layouts have been proposed for the NIs, which are in series, parallel or series-parallel with the external shunt. Their corresponding EMCFs have been analytically determined and are concisely formulated in terms of the nominal EMCF  $\theta$  and two inductance ratios  $\alpha$  and  $\gamma$ . It implies that the inclusion of one or two NIs can artificially enhance the energy conversion efficiency between mechanical and electrical domains, and the smallest and largest EMCF is achieved by employing the series and SP layout, respectively.

For the series layout, the optimal design of EMSD enclosed by a series RL and RLC shunt circuit have been carried out according to the FPT. It is observed that the normalized displacement amplitude of primary system at fixed points can be concisely expressed as their corresponding EMCF. Therefore, the vibration decreases monotonically as the EMCF increases, which could be achieved by increasing the magnitude of series NI.

Finally, the optimal tuning of parallel and SP shunts have been performed by using an approximate FPT. It is noticeable that the purely resistive shunt in parallel with a single NI can deliver a vibration attenuation performance similar to the RC shunt. Meanwhile, the R shunt enhanced by two NIs has the same effectiveness as a series RLC shunt. Thus, one can conclude that employing the parallel or SP layout constitutes an alternative approach to introduce the electrical resonance into the circuit.



# Chapter 8

## Conclusions and Future Work

### 8.1 Conclusions

Excessive vibrations in a structure could have detrimental effects, ranging from lowering of vibrational and acoustic comfort, performance degradation of precision mechatronics to the loss of structural integrity. Therefore, persistent efforts have been devoted to developing vibration control devices with an enhanced effectiveness and robustness. In this thesis, some advances in passive and active vibration damping techniques are reported. The conclusions and original contributions of this thesis are listed as below.

Firstly, the optimal design of TMDI is carried out for minimizing the peak vibration amplitude of a mechanical system under UBB stiffness uncertainty. To address this worst-case optimization problem, a purely algebraic method is developed, which is based on the perturbation approach combined with properties of polynomial. Both optimal parameters of TMDI (thereby TMD) and the peak vibration amplitude of primary system are analytically formulated for the first time. Finally, the analytical study suggests that the proposed design can minimize the peak amplitude of primary system in the worst-case scenario, meanwhile, the control efficiency can be increased by using the grounded inerter.

Secondly, a novel control device SDTMDI based on the series DTMD in conjunction with inerters is investigated. The  $H_\infty$  optimization of its all possible configurations is conducted via an extended FPT, revealing that the best control efficiency is achieved when the inerters are incorporated between two tuned masses and the ground. Meanwhile, the global effectiveness is irrespective of the distribution of inertance in the control scheme, therefore, two equivalent variants of SDTMDI are then proposed by removing one of the two grounded inerters. Finally, it suggests that with the same amount of tuned mass and inertance, the SDTMDI can further reduce the peak amplitude of host structure by more than 25% with respect to the TMDI.

Thirdly, the possibility of enhancing the control performance of existing dampers via a linear negative stiffness is investigated. Optimal design is carried out for both

non-traditional NSDVA and NSIDVA, whose viscous damper or inerter-based mechanical network is grounded. It is underlined that the inclusion of negative stiffness can effectively reduce both the peak vibration amplitude of primary system and the stroke of damper, meanwhile, it leads to an enhanced damping capability. Furthermore, the piezoelectric shunt dampers analogous to both NSDVA and NSIDVA (thereby the non-traditional DVA and IDVA) are proposed, by which the applicability of aforementioned mechanical devices could be largely extended. Therefore, one of advantages claimed for the non-traditional configuration of existing dampers resides in the fact that it allows an exact electrical realization of the mechanical dampers by means of piezoelectric transducer.

Fourthly, a simple hybrid control scheme based on optimized DVA or IDVA is proposed. The feedback signal is the position of mechanical system and is filtered by a single or multiple identical compensators in series, each of which is featured by a single pole at the origin and two coalesced real zeros. The simplicity of such a controller design is attributed to the fact that the stability is dictated by the position of introduced zeros, and the hybrid control scheme remains stable for any controller gain if and only if the magnitude of real zeros is bounded by those of the smallest and largest system eigenvalues. For both hybrid DVA and IDVA, the corresponding allowable bounds are analytically formulated in terms of the mass ratio  $\mu$  solely. Compared to the DVA counterpart, a hybrid IDVA can maintain the significant vibration reduction over a much broader frequency bandwidth around the natural frequency of primary system. In general, the increase of compensator can decrease monotonically the peak amplitude of primary system. However, the potential stroke saturation and active force overloading at low frequency should be addressed in practical implementation.

Finally, the employment of NIs in electromagnetic shunt damping is considered and all possible layouts are investigated in the same framework for the first time. The shunt damping capability of various layouts is first assessed by means of the EMCF, suggesting that adding a NI in series with the transducer can increase the energy conversion efficiency, while it can be further enhanced by employing another NI in parallel with the external impedance. The preliminary remark is later confirmed by comparing the peak amplitudes of primary system when controlled by different shunt circuits tuned by the FPT. A general characteristics for all optimized shunts is that for a given coupled system, the peak vibration amplitude of primary system is only influenced by the NI in series, and the increasing of its magnitude improves monotonically the effectiveness. Besides, for a weakly coupled system, a series resonant shunt always demonstrates a superior shunt damping performance than its non-resonant counterpart. Finally, employing a NI in parallel with the resistive shunt constitutes an effective alternative to the resonant shunt damping.

## 8.2 Future work

Future work could be dedicated to the following issues:

- All optimal designs in this thesis were conducted in the case of force excitation. Therefore, similar studies could be carried out for a seismically excited primary system, which is usually the case in the field of civil engineering.
- The worst-case optimization in Chapter 2 could be further extended to the cases where uncertainty is present in system property other than stiffness and/or the uncertain parameter is asymmetric.
- The  $H_\infty$  optimization of series DTMD carried out in Chapter 3 suggests that the TMD adjacent to the primary system has zero damping. Therefore, one can propose a non-traditional configuration for the series DTMD by grounding the viscous damper of smaller TMD, which can be electrically realized by means of piezoelectric shunt damper with a high-order circuit. Its effectiveness could be first assessed by the displacement amplitude of primary system at fixed points. Furthermore, a negative stiffness element could be also incorporated in order to enhance the performance of vibration attenuation.
- The NSIDVA was only optimized according to the SMC, therefore, its FPT-based optimal design could be addressed in future work. Meanwhile, the electromechanical analogous models of non-traditional DVA and IDVA, NSDVA and NSIDVA proposed in Chapter 5 should be experimentally verified.
- It was demonstrated in Chapter 7 that a purely resistive shunt enhanced by NIs in series and parallel configuration can deliver a shunt damping performance similar to that of a series RLC shunt circuit. Thus, it is reasonable to expect a better effect of vibration reduction when the R shunt is replaced by a resonant shunt circuit, i.e. a RC shunt either in series or in parallel.
- The  $H_\infty$  optimal design of a passive damper for controlling the vibration of a SDOF mechanical system is usually accomplished by means of methodologies based on the fixed points. For any coupled system in which the displacement FRF of primary system is characterized by one, two, three or four invariant points, analytical optimization procedure has been already reported in the current literature. Therefore, attention could be paid in the future to the development of analytical approaches based on fixed points, which are capable of addressing the optimization of coupled system characterized by five or more invariant points, e.g. a SDOF primary system controlled by a MTMD.

In general, this thesis has focused on the theoretical investigation of multiple vibration damping techniques, whose applicability should be further experimentally validated. Moreover, the realization of mechanical absorbers by means of smart

material based shunt dampers constitutes a compact and lightweight solution for vibration control, therefore, a periodic array of shunt dampers with the advanced damping techniques can be applied to attenuate the broadband vibration of thin-walled or periodic structures. Finally, attentions could be paid to the possibility of energy harvesting via the proposed absorbers in quest of a dual-functional application.

### 8.3 Publications

Until July 2019, part of my research work has appeared in the following publications:

#### Journal papers

- [1] **S. Zhou**, C. Jean-Mistral, and S. Chesné. Influence of internal electrical losses on optimization of electromagnetic energy harvesting. *Smart Materials and Structures*, 27(8):085015, 2018.
- [2] **S. Zhou**, C. Jean-Mistral, and S. Chesné. Electromagnetic shunt damping with negative impedances: Optimization and analysis. *Journal of Sound and Vibration*, 445:188-203, 2019.
- [3] **S. Zhou**, C. Jean-Mistral, and S. Chesné. Closed-form solutions to optimal parameters of dynamic vibration absorbers with negative stiffness under harmonic and transient excitation. *International Journal of Mechanical Sciences*, 157-158:528-541, 2019.
- [4] **S. Zhou**, C. Jean-Mistral, and S. Chesné. Optimal design of an inerter-based dynamic vibration absorber connected to ground. *Journal of Vibration and Acoustics, Transactions of the ASME*, 141(5):051017, 2019.
- [5] **S. Zhou**, C. Jean-Mistral, and S. Chesné. Influence of inerters on the vibration control effect of series double tuned mass dampers: Two layouts and analytical study. *Structural Control and Health Monitoring*, accepted for publication.

#### Conference papers

**S. Zhou**, C. Jean-Mistral, and S. Chesné. Design of a nonlinear shunt circuit for dual applications: energy harvesting and vibration damping. Paper presented at the *25th International Congress on Sound and Vibration 2018, ICSV 2018: Hiroshima Calling*, July 2018, Hiroshima, Japan.

# Appendix A

## Appendix related to Chapter 2

### A.1 Partial derivative of $G_{\text{opt}}$ with respect to $\mu$ , $\nu$ and $\eta$

With  $\gamma = \mu + \nu$ , both partial derivatives of  $G_{\text{opt}}$  with respect to  $\mu$  and  $\nu$  are equal to that with respect to  $\gamma$ , namely:

$$\frac{\partial G_{\text{opt}}}{\partial \mu} = \frac{\partial G_{\text{opt}}}{\partial \nu} = \frac{\partial G_{\text{opt}}}{\partial \gamma} \quad (\text{A.1})$$

where

$$\frac{\partial G_{\text{opt}}}{\partial \gamma} = -\frac{(1+\gamma)\eta^2 + \kappa\eta + \gamma}{\kappa\gamma^2(1+\eta^2)} \quad (\text{A.2})$$

with  $\kappa = \sqrt{(1+\eta^2)(1+\gamma)^2 - 1}$ . For any positive  $\gamma$  and  $\eta$ ,  $\partial G_{\text{opt}}/\partial \gamma < 0$  always holds, therefore,  $G_{\text{opt}}$  is a monotonically decreasing function of  $\gamma$ , thereby of  $\mu$  or  $\nu$ . Meanwhile, its partial derivative in terms of  $\eta$  is formulated as follows:

$$\frac{\partial G_{\text{opt}}}{\partial \eta} = \frac{\kappa(1-\eta^2) + \eta(1-\kappa^2)}{\gamma\kappa(1+\eta^2)^2} \quad (\text{A.3})$$

Generally, the mass ratio or inertance-to-mass ratio is very small and the stiffness uncertainty could not be superior to unity, as required by its definition. Therefore,  $\partial G_{\text{opt}}/\partial \eta$  is always non-negative in realistic situations, signifying that  $G_{\text{opt}}$  increases monotonically as  $\eta$  becomes larger.

### A.2 Definition of performance index PI

Considering that the primary system is excited by a random force having a constant power spectral density over the whole range of frequency, an intermediate

performance index  $I$  can be first defined as:

$$I = \frac{1}{\pi} \int_{-\infty}^{+\infty} \left| \frac{X_1}{F/k_n} \right|^2 d\lambda = \frac{1}{\pi} \int_{-\infty}^{+\infty} \left| \frac{\sum_{i=0}^3 p_i (j\lambda)^i}{\sum_{i=0}^4 q_i (j\lambda)^i} \right|^2 d\lambda \quad (\text{A.4})$$

with the constants in numerator and denominator given by:

$$\begin{cases} p_0 = \mu\alpha^2 \\ p_1 = 2\mu\xi\alpha \\ p_2 = \mu + \nu \\ p_3 = 0 \end{cases} \quad \begin{cases} q_0 = \mu\alpha^2(1 + \delta) \\ q_1 = 2\mu\xi\alpha(1 + \delta) \\ q_2 = (1 + \delta)(\mu + \nu) + \mu\alpha^2(1 + \mu + \nu) \\ q_3 = 2\mu\xi\alpha(1 + \mu + \nu) \\ q_4 = \mu + \nu \end{cases} \quad (\text{A.5})$$

Then, the indefinite integral (A.4) can be calculated by employing the analytical formula provided in [162]. Finally, the performance index PI is chosen as the worst-case value of  $I$  for the stiffness uncertainty  $\delta$  varying within the interval  $[-\eta, +\eta]$ , i.e.:

$$\text{PI} = \max_{-\eta \leq \delta \leq +\eta} \{I(\delta)\} \quad (\text{A.6})$$

## Appendix B

### Appendix related to Chapter 3

The four expressions in the normalized vibration amplitude (3.8) are:

$$\begin{cases} A = \left[ \beta^2 (\mu - \nu) (\nu \alpha^2 - (\mu + \theta) \lambda^2) - (\mu - \nu) \lambda^2 (\nu \alpha^2 - (\nu + \eta) \lambda^2) \right. \\ \quad \left. - (\eta - \theta) \lambda^2 (\nu \alpha^2 - (\nu + \theta) \lambda^2) \right]^2 \\ B = 4\beta^2 \lambda^2 (\mu - \nu)^2 \left[ \nu \alpha^2 - (\mu + \theta) \lambda^2 \right]^2 \\ C = (e_3 \lambda^6 + e_2 \lambda^4 + e_1 \lambda^2 + e_0)^2 \\ D = 4\beta^2 \lambda^2 (\mu - \nu)^2 \left[ (1 - \lambda^2) [\nu \alpha^2 - (\mu + \theta) \lambda^2] - \mu \lambda^2 (\nu \alpha^2 - \theta \lambda^2) \right]^2 \end{cases} \quad (\text{B.1})$$

with the constants before terms  $e_i, i = 0, \dots, 3$  given by:

$$\begin{cases} e_3 = (1 + \mu)\theta^2 + (1 + \theta) [\nu(\nu - \mu) - \mu\eta] + \theta(\nu - \eta) \\ e_2 = \nu (\eta\mu + \mu\nu - \mu\theta - \nu^2 + \eta + \mu - \nu - \theta) \alpha^2 + \beta^2 (\mu\theta + \mu + \theta) (\mu - \nu) \\ \quad + \eta\mu + \eta\theta + \mu\nu - \nu^2 - \nu\theta - \theta^2 \\ e_1 = -\nu\alpha^2 (\mu + \eta - \nu - \theta) - (\mu - \nu) \beta^2 [\mu + \theta + \nu\alpha^2 (1 + \mu)] \\ e_0 = \alpha^2 \beta^2 \nu (\mu - \nu) \end{cases} \quad (\text{B.2})$$

The constants in Eq. (3.13) change to:

$$\begin{cases} b_4 = h(\mu\theta + \mu + \theta)^2 \\ b_3 = -2h(\mu\theta + \mu + \theta) (\alpha^2 \mu\nu + \alpha^2 \nu + \mu + \theta) \\ b_2 = h\nu^2 (\mu + 1)^2 \alpha^4 + 2h\nu (\mu^2 + 2\mu\theta + 2\mu + 2\theta) \alpha^2 + (\mu + \theta)^2 (h - 1) \\ b_1 = -2\alpha^2 \nu (\alpha^2 h\mu\nu + \alpha^2 h\nu + h\mu + h\theta - \mu - \theta) \\ b_0 = \nu^2 \alpha^4 (h - 1) \end{cases} \quad (\text{B.3})$$

$$\left\{ \begin{array}{l}
 a_4 = 2(\mu+1)\theta^3 + (-2\mu\eta + \mu^2 + v^2 - 2\eta + 2\mu + 2\nu)\theta^2 \\
 + (-2\eta\mu^2 - 2\mu^2\nu + 2\mu\nu^2 - 4\mu\eta + 2v^2)\theta - 2\mu(\mu\eta + \mu\nu - v^2) \\
 a_3 = 2\beta^2(\theta + \mu)(\mu\theta + \mu + \theta)(\mu - \nu) + 2(\theta + \mu)(\mu\eta + \eta\theta + \mu\nu - v^2 - \theta\nu - \theta^2) \\
 + (2\eta\mu^2\nu + 4\eta\mu\nu\theta + 2\mu^2v^2 - 2\mu\nu^3 - 4\mu\nu\theta^2 - 2v^3\theta + 4\eta\nu\theta + 2\mu^2\nu - 2v^3 - 4v^2\theta - 4v\theta^2)\alpha^2 \\
 a_2 = -v^2(2\mu\eta + \mu^2 - 2\mu\theta - v^2 + 2\eta + 2\mu - 2\nu - 2\theta)\alpha^4 - 2\beta^2(\theta + \mu)^2(\mu - \nu) \\
 - 2\nu[\beta^2(\mu^2 + 2\mu\theta + 2\mu + 2\theta)(\mu - \nu) + 2\mu\eta + 2\eta\theta + \mu^2 - v^2 - 2\theta\nu - 2\theta^2]\alpha^2 \\
 a_1 = 2v^2\alpha^4(\beta^2(\mu + 1)(\mu - \nu) + \mu + \eta - \nu - \theta) + 4\nu\alpha^2\beta^2(\theta + \mu)(\mu - \nu) \\
 a_0 = -2\alpha^4\beta^2v^2(\mu - \nu)
 \end{array} \right. \tag{B.4}$$

The constants in Eq. (3.11) change to:

# Appendix C

## Appendix related to Chapter 4

### C.1 Lower bounds on $\eta$ for NSDVA tuned by the SMC

Multiple constraints exist on the negative stiffness ratio  $\eta$ , as discussed one by one in the following study.

1. The stability requirement. The substitution of optimal frequency tuning ratio  $\alpha_{\text{smc}}$  into the general stability condition (4.8) yields:

$$(1 + \eta)^2 - 2\mu > (1 + \eta)\sqrt{(1 + \eta)^2 - 4\mu} \quad (\text{C.1})$$

which results in a possible bound on  $\eta$ :  $\eta > \eta_1 = \sqrt{2\mu} - 1$ .

2.  $\alpha_{\text{smc}}^2 \geq 0$ . This condition imposes that:

$$\left. \begin{array}{l} 1 + \eta \geq 2\mu \\ (1 + \eta)^2 \geq 4\mu \\ (1 + \eta - 2\mu)^2 \geq (1 + \eta)^2 - 4\mu \end{array} \right\} \implies \left\{ \begin{array}{l} \eta \geq \eta_2 = 2\mu - 1 \\ \eta \geq \eta_3 = 2\sqrt{\mu} - 1 \end{array} \right. \quad (\text{C.2})$$

One can tell that  $\eta_3 > \eta_1 > \eta_2$  always holds for any positive  $\mu \leq 0.5$  and the mass ratio should be inferior to 0.25. Up to now, the negative stiffness ratio  $\eta$  should be bounded by:  $\eta \geq \eta_3 = 2\sqrt{\mu} - 1$ .

3. The complex eigenvalue assumption  $p^2 \leq r^2$ . The inequality conducts to  $t_1 \leq t_2$  with the two polynomials given by:

$$t_1 = 1 - 7\mu + \eta(1 - 3\mu), \quad t_2 = (1 - 5\mu)\sqrt{(1 + \eta)^2 - 4\mu}. \quad (\text{C.3})$$

It is remarkable that the signs of  $t_1$  and  $t_2$  depend on the mass ratio  $\mu$  so that the lower bound on  $\eta$  should be deducted per segment of  $\mu$ . The coefficient  $t_1$  will be positive if  $\eta > \eta_4 = (7\mu - 1)/(1 - 3\mu)$  and  $t_2$  remains positive when  $\mu$  is less than 1/5. Besides, one can tell that  $\eta_3 \geq \eta_4$  for any  $\mu \in [0, 1/9]$ . Therefore, three possible cases where a negative stiffness could be employed in the DVA, i.e.  $\eta < 0$ , are listed as follows:

- Case 1:  $\eta \geq \eta_3$ ,  $\eta_3 \leq 0$ ,  $0 \leq t_1 \leq t_2$ ,  $\forall \mu \in \left[0, \frac{1}{9}\right]$ ,
- Case 2:  $\eta \geq \eta_4$ ,  $\eta_4 \leq 0$ ,  $0 \leq t_1 \leq t_2$ ,  $\forall \mu \in \left[\frac{1}{9}, \frac{1}{5}\right]$ ,
- Case 3:  $\eta \geq \eta_3$ ,  $\eta_3 \leq 0$ ,  $t_1 \leq t_2 \leq 0$ ,  $\forall \mu \in \left[\frac{1}{5}, \frac{1}{4}\right]$ .

each of which will be investigated in order to obtain the lower bound on  $\eta$  with respect to the segment of mass ratio  $\mu$ .

- Case 1.  $\eta < 0$  always holds for  $\mu \in [0, 1/9]$ . Moreover, the condition  $0 \leq t_1 \leq t_2$  results in:

$$(1 - 4\mu)\eta^2 - 2\mu\eta + 25\mu^2 - 4\mu \leq 0 \quad (\text{C.4})$$

It is noticeable that the upper limit of this inequality is always positive, therefore, the corresponding bound on  $\eta$  is:  $\eta_5 \leq \eta \leq 0$  with

$$\eta_5 = \frac{\mu + 2\sqrt{\mu}(5\mu - 1)}{1 - 4\mu} \quad (\text{C.5})$$

With  $\eta_5$  being superior to  $\eta_3$  in the very range of mass ratio, the allowable bound on  $\eta$  is:

$$\eta_5 \leq \eta \leq 0, \forall \mu \in \left[0, \frac{1}{9}\right]. \quad (\text{C.6})$$

- Case 2. In this range of mass ratio, the condition  $0 \leq t_1 \leq t_2$  will be satisfied if  $\eta \geq \eta_4$  holds. Nevertheless,  $\eta_4$  will be positive when the mass ratio is greater than  $1/7$ . Therefore, no negative stiffness could be employed in the range of  $[1/7, 1/5]$  and the permissible bound on  $\eta$  is expressed as:

$$\eta_4 \leq \eta \leq 0, \forall \mu \in \left[\frac{1}{9}, \frac{1}{7}\right]. \quad (\text{C.7})$$

- Case 3. The constraint of  $t_1 \leq t_2 \leq 0$  gives rise to

$$\eta \leq \eta^- = \frac{\mu - 2\sqrt{\mu}(5\mu - 1)}{1 - 4\mu}, \quad \eta \geq \eta^+ = \frac{\mu + 2\sqrt{\mu}(5\mu - 1)}{1 - 4\mu} \quad (\text{C.8})$$

In the mass ratio range of  $[1/5, 1/4]$ ,  $\eta^+ > \eta^- > 0$  always holds. Therefore, the corresponding interval of  $\eta$  is given as:

$$\eta_3 \leq \eta \leq 0, \forall \mu \in \left[\frac{1}{5}, \frac{1}{4}\right]. \quad (\text{C.9})$$

Finally, the lower thresholds of negative stiffness ratio  $\eta$  are found for each segment of mass ratio  $\mu$  and are summarized in Eq. (4.24).

## C.2 An alternative layout of NSDVA

Figure C.1 represents a different configuration of NSDVA based on the DVA of Den Hartog. Its dimensionless EOMs are given by:

$$x_1'' + x_1 + \mu x_2'' + \eta x_2 = F(\tau)/k_1 \quad (\text{C.10a})$$

$$x_2'' + 2\xi\alpha(x_2' - x_1') + \alpha^2(x_2 - x_1) + \frac{\eta}{\mu}x_2 = 0 \quad (\text{C.10b})$$

Besides, its normalized displacement FRF of primary system is written as:

$$G(\bar{s}) = \frac{X_1}{F/k_1} = \frac{\mu\bar{s}^2 + 2\mu\xi\alpha\bar{s} + \eta + \mu\alpha^2}{\mu\bar{s}^4 + 2\mu\xi\alpha(1 + \mu)\bar{s}^3 + (\eta + \mu + \mu\alpha^2 + \mu^2\alpha^2)\bar{s}^2 + 2\mu\xi\alpha(1 + \eta)\bar{s} + \eta + \mu\alpha^2(1 + \eta)} \quad (\text{C.11})$$

Finally, its squared magnitude of displacement FRF has the same form as Eq. (4.9) with the four coefficients expressed as:

$$A = [\eta + \mu(\alpha^2 - \lambda^2)]^2, \quad B = \mu^2\alpha^2\lambda^2, \\ C = \left[ [\eta + \mu(\alpha^2 - \lambda^2)](1 - \lambda^2) + \mu\alpha^2(\eta - \mu\lambda^2) \right]^2, \quad D = \mu^2\alpha^2\lambda^2(1 - \lambda^2 + \eta - \mu\lambda^2)^2. \quad (\text{C.12})$$

Following the same procedure in Section 4.1, ready-to-use formulae to optimal parameters of NSDVA according to the FPT and the SMC are summarized in Tables C.1 and C.2, respectively. Meanwhile, the lower bounds on negative stiffness ratio  $\eta$  in both optimal scenarios are given by:

$$\eta_{\text{fpt}}^- = \frac{\mu^2 + 3\mu - \sqrt{(\mu^2 + 3\mu)^2 + 4\mu}}{2}, \quad \eta_{\text{smc}}^- = \frac{\mu - 2\sqrt{\mu}}{1 + 2\sqrt{\mu}}. \quad (\text{C.13})$$

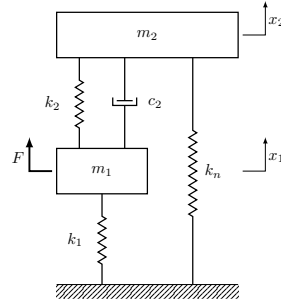


**Figure C.1:** Schematic diagram of a SDOF undamped primary system controlled by a traditional NSDVA.

Damper	Frequency tuning ratio $\alpha$	Mechanical damping ratio $\xi$	$\ G\ _\infty$
DVA	$\frac{1}{1+\mu}$	$\sqrt{\frac{3\mu}{8(1+\mu)}}$	$\sqrt{\frac{\mu+2}{\mu}}$
NSDVVA	$\sqrt{\frac{\mu-\eta}{\mu(1+\mu)^2}}$	$\sqrt{\frac{\mu(2\eta\mu+5\eta+3)(\mu-\eta)^3}{4(\mu+1)[\mu(\mu+2)(\eta+1)^2(\mu-\eta)^2-(\mu-\eta)^4]}}$	$\sqrt{\frac{\mu(\mu+2)}{(\mu-\eta)^2}}$

**Table C.1:** Closed-form formulae to optimal parameters of traditional DVA and NSDVVA attached to a SDOF undamped primary system under force excitation according to the FPT.

Damper	Frequency tuning ratio $\alpha$	Mechanical damping ratio $\xi$	Degree of stability $\Lambda$
DVA	$\frac{1}{1+\mu}$	$\sqrt{\frac{\mu}{1+\mu}}$	$\sqrt{4(1+\mu)}$
NSDVVA	$\sqrt{\frac{(\mu-\eta)(1-\eta\mu)}{\mu(1+\eta)(1+\mu)^2}}$	$\sqrt{\frac{\mu-\eta}{(1+\mu)(1-\eta\mu)}}$	$\sqrt{\frac{(\mu-\eta)^2}{4\mu(1+\mu)(1+\eta)}}$

**Table C.2:** Closed-form formulae to optimal parameters of traditional DVA and NSDVVA attached to a SDOF undamped primary system under force excitation according to the SMC.

# Appendix D

## Appendix related to Chapter 6

### D.1 Open-loop poles in the worst-case scenario

In the worst-case scenario, the characteristic equation of system,  $P(\bar{s})$ , corresponds to the coefficients of  $\xi$  in the denominator of Eq. (6.5). By substituting the optimal formulae (6.10), the characteristic polynomial can be simplified as:

$$P(\bar{s}) = [(\mu + 1)\bar{s}^2 + 1] [(\mu + 1)^2\bar{s}^4 + (\mu + 1)(3\mu + 2)\bar{s}^2 + 1] = 0 \quad (\text{D.1})$$

Meanwhile,  $P(\bar{s})$  can be also written in the factorized form in terms of its all imaginary poles, i.e.:

$$\begin{aligned} P(\bar{s}) &= (\bar{s} + j\lambda_1)(\bar{s} - j\lambda_1)(\bar{s} + j\lambda_2)(\bar{s} - j\lambda_2)(\bar{s} + j\lambda_3)(\bar{s} - j\lambda_3) \\ &= (\bar{s}^2 + \lambda_1^2)(\bar{s}^2 + \lambda_2^2)(\bar{s}^2 + \lambda_3^2) = 0 \end{aligned} \quad (\text{D.2})$$

By comparing Eqs. (D.1) and (D.2), the magnitudes of imaginary poles are determined as, respectively:

$$\lambda_1 = \sqrt{\frac{3\mu + 2 - \sqrt{3\mu(3\mu + 4)}}{2(\mu + 1)}}, \quad \lambda_2 = \sqrt{\frac{1}{\mu + 1}}, \quad \lambda_3 = \sqrt{\frac{3\mu + 2 + \sqrt{3\mu(3\mu + 4)}}{2(\mu + 1)}}. \quad (\text{D.3})$$

with  $0 < \lambda_1 < \lambda_2 < \lambda_3$  always holding for any value of mass ratio  $\mu$ .

### D.2 Dynamics of hybrid control scheme based on a DVA

#### D.2.1 System description

The control scheme related to hybrid DVA is depicted in Figure 6.1a. By applying the same nondimensionalization procedure as in Section 6.1, the underlying dynamics of a SDOF undamped primary system controlled by a hybrid DVA is governed

by the dimensionless equations of motion:

$$x_1'' + x_1 + \mu x_2'' = \tilde{f}_p(\tau) \quad (\text{D.4a})$$

$$\mu x_2'' + 2\mu\xi\alpha(x_2' - x_1') + \mu\alpha^2(x_2 - x_1) = \tilde{f}_a(\tau) \quad (\text{D.4b})$$

Therefore, its corresponding FRFs,  $G_p(\bar{s})$  and  $G_a(\bar{s})$ , are formulated as:

$$G_p = \frac{\bar{s}^2 + 2\xi\alpha\bar{s} + \alpha^2}{\bar{s}^4 + 2\xi\alpha(\mu+1)\bar{s}^3 + [1 + (\mu+1)\alpha^2]\bar{s}^2 + 2\xi\alpha\bar{s} + \alpha^2}, \quad (\text{D.5a})$$

$$G_a = \frac{-\bar{s}^2}{\bar{s}^4 + 2\xi\alpha(\mu+1)\bar{s}^3 + [1 + (\mu+1)\alpha^2]\bar{s}^2 + 2\xi\alpha\bar{s} + \alpha^2}. \quad (\text{D.5b})$$

### D.2.2 Passive design

The optimal design of a classic DVA in terms of minimizing the peak vibration amplitude of primary system is long established. Analytical formulae of its optimal parameters were derived by applying the well-known fixed points theory [2]:

$$\alpha = \frac{1}{\mu+1}, \quad \xi = \sqrt{\frac{3\mu}{8(\mu+1)}}. \quad (\text{D.6})$$

### D.2.3 Open-loop poles in the worst-case scenario

Distinguished from the hybrid IDVA where we disable the damping element by restricting the relative motion of its two terminals, the worst-case scenario for a hybrid DVA occurs by removing the viscous damper  $c_3$  (i.e.  $c_3 = \xi = 0$ ). Therefore, its simplified characteristic equation can be read from the denominator of Eq. (D.5) and further factorized as:

$$P(\bar{s}) = \bar{s}^4 + [1 + (\mu+1)\alpha^2]\bar{s}^2 + \alpha^2 = (\bar{s}^2 + \lambda_1^2)(\bar{s}^2 + \lambda_3^2) = 0 \quad (\text{D.7})$$

By substituting Eq. (D.6), the open-loop poles locate at  $\pm j\lambda_1$  and  $\pm j\lambda_3$  on the imaginary axis, with  $\lambda_1$  and  $\lambda_3$  formulated as, respectively:

$$\lambda_1 = \sqrt{\frac{\mu+2 - \sqrt{\mu^2+4\mu}}{2(\mu+1)}}, \quad \lambda_3 = \sqrt{\frac{\mu+2 + \sqrt{\mu^2+4\mu}}{2(\mu+1)}}. \quad (\text{D.8})$$

## D.3 Proof of proposition for the case of $n = 1$

By substituting Eq. (6.11) into (6.8) with  $n = 1$  and by approaching  $\xi$  to infinity, the closed-loop FRF can be further simplified as:

$$\lim_{\xi \rightarrow \infty} G_{CL} = \lim_{\xi \rightarrow \infty} \frac{N_1\xi + N_0}{D_1\xi + D_0} = \frac{N_1}{D_1} \quad (\text{D.9})$$

where the denominator  $D_1$  is a polynomial function of degree 6 in  $\bar{s}$ , i.e.  $D_1 = \sum_{i=0}^6 E_i \bar{s}^i$  with its coefficients given by:

$$\begin{cases} E_6 = 2\mu\alpha \\ E_5 = 2g\mu\alpha \\ E_4 = 2\alpha [\mu(1 + 2g\theta) + (\mu^2 + \mu)\alpha^2 + (\mu + \nu + \mu\nu)\beta^2] \\ E_3 = 2g\mu\alpha(\beta^2 + \theta^2) \\ E_2 = 2\alpha [\mu\alpha^2 + (\mu + \nu + 2g\mu\theta)\beta^2 + (\mu^2 + \mu)\alpha^2\beta^2] \\ E_1 = 2g\mu\alpha\beta^2\theta^2 \\ E_0 = 2\mu\alpha^3\beta^2 \end{cases} \quad (\text{D.10})$$

Then, the stability of hybrid system can be assessed from its characteristic equation, which is exactly the denominator in Eq. (D.9). According to the Routh Hurwitz stability criterion, a system is stable if its all poles have negative real parts. One can also judge its stability by inspecting if there exists sign changes for coefficients in the first array of Routh table relevant to the characteristic equation. By substituting the formulae of optimal parameters in Eq. (6.10) and after simplification, the stability requirement culminates into two conditions:

$$2\theta(\mu + 1)g + 3\mu + 2 - \theta^2(\mu + 1) \geq 0 \quad (\text{D.11a})$$

$$2\theta^3(\mu + 1)^2g - (\mu + 1)^2\theta^4 + (\mu + 1)(3\mu + 2)\theta^2 - 1 \geq 0 \quad (\text{D.11b})$$

Given that  $\theta$  is positive and  $g$  could go from zero to positive infinity, hence, the hyperstability of controller could be achieved when  $\theta$  satisfies the following inequalities:

$$3\mu + 2 - \theta^2(\mu + 1) \geq 0 \quad (\text{D.12a})$$

$$-(\mu + 1)^2\theta^4 + (\mu + 1)(3\mu + 2)\theta^2 - 1 \geq 0 \quad (\text{D.12b})$$

the first of which leads to  $\theta^2 \leq \theta_1^2 = (\mu + 1)/(3\mu + 2)$ , while the latter yields

$$\frac{3\mu + 2 - \sqrt{3\mu(3\mu + 4)}}{2(\mu + 1)} = \theta_-^2 \leq \theta^2 \leq \theta_+^2 = \frac{3\mu + 2 + \sqrt{3\mu(3\mu + 4)}}{2(\mu + 1)} \quad (\text{D.13})$$

Given that  $\theta_1^2 > \theta_+^2$  always holds for any positive  $\mu$ , therefore, the lower and upper limits of  $\theta$  are  $\theta_-$  and  $\theta_+$ , respectively. Furthermore, it is apparent that its two bounds are exactly the same as the magnitudes of poles,  $\lambda_1$  and  $\lambda_3$ , respectively, thereby proving the proposition for the case of  $n = 1$ .



# Appendix E

## Appendix related to Chapter 7

### E.1 $H_2$ Optimization of EMSD coupled with a series RLC shunt

Assuming that the external force  $F$  has a constant power spectral density  $S_f$  over the whole frequency range, we can then define a performance index  $I$  as:

$$I = \frac{E[x_1^2]}{2\pi S_f \omega_1 / k_1^2} \quad (\text{E.1})$$

where  $E[\cdot]$  denotes the mean square value. And  $E[x_1^2]$  can be evaluated by the following expression:

$$E[x_1^2] = \int_{-\infty}^{+\infty} \left| \frac{X_1}{F} \right|^2 S_f d\omega = \frac{S_f \omega_1}{k_1^2} \int_{-\infty}^{+\infty} \left| \frac{X_1}{F/k_1} \right|^2 d\lambda = \frac{S_f \omega_1}{k_1^2} \int_{-\infty}^{+\infty} G^2(\lambda) d\lambda \quad (\text{E.2})$$

The infinite integral in Eq. (E.2) can be evaluated by applying the residue theorem. An analytical form of result for this integral is also provided herein. For a rational function  $G(\lambda)$  having the form of

$$G(\lambda) = \frac{b_0 + b_1(j\lambda)^1 + b_2(j\lambda)^2 + b_3(j\lambda)^3}{a_0 + a_1(j\lambda)^1 + a_2(j\lambda)^2 + a_3(j\lambda)^3 + a_4(j\lambda)^4} \quad (\text{E.3})$$

its corresponding integral over the infinite range of frequencies can be evaluated by the following closed-form formula:

$$\int_{-\infty}^{+\infty} |G(\lambda)|^2 d\lambda = \pi \frac{\frac{b_0^2(a_2a_3 - a_1a_4)}{a_0} + a_3(b_1^2 - 2b_0b_2) + a_1(b_2^2 - 2b_1b_3) + \frac{b_3^2(a_1a_2 - a_0a_3)}{a_4}}{a_1(a_2a_3 - a_1a_4) - a_0a_3^2} \quad (\text{E.4})$$

By comparing Eqs. (7.22) and (E.3), the coefficients may be written as:

$$\begin{cases} b_0 = \phi^2 \\ b_1 = \kappa(1 + \beta) \\ b_2 = \alpha \\ b_3 = 0 \end{cases} \quad \begin{cases} a_0 = \phi^2 \\ a_1 = \kappa(1 + \beta) \\ a_2 = \alpha + \theta + \phi^2 \\ a_3 = \kappa(1 + \beta) \\ a_4 = \alpha \end{cases} \quad (\text{E.5})$$

Mathematically speaking, the global minimum of  $I(\alpha, \beta, \phi)$  is attained at points satisfying the following conditions:

$$\frac{\partial I}{\partial \alpha} = 0, \quad \frac{\partial I}{\partial \beta} = 0, \quad \frac{\partial I}{\partial \phi} = 0. \quad (\text{E.6})$$

However, the authors notice that such a global extreme of  $I(\alpha, \beta, \phi)$  does not exist. Hence, a trade-off is made and the optimization is only conducted with regard to resistance ratio  $\beta$  and frequency tuning ratio  $\phi$ , i.e.

$$\frac{\partial I}{\partial \beta} = 0, \quad \frac{\partial I}{\partial \phi} = 0. \quad (\text{E.7})$$

from which the optimal values of  $\beta$  and  $\phi$  can be obtained as a function of inductance ratio  $\alpha$ , respectively

$$\beta_{\text{opt}} = \frac{1}{\kappa} \sqrt{\alpha\theta - \frac{\theta^2}{4}} - 1, \quad \phi_{\text{opt}}^2 = \alpha - \frac{\theta}{2}. \quad (\text{E.8})$$

The non-negativity constraint on  $\phi_{\text{opt}}^2$  imposes that  $\alpha \geq \theta/2$ , and the general stability condition  $\beta > -1$  leads to  $\alpha > \theta/4$ . Therefore, the aforementioned optimal formulae (E.8) will not have physical meaning except if the inductance ratio  $\gamma$  satisfies the following constraint

$$\alpha \geq \alpha_{\text{cri,h2}} = \frac{\theta}{2} \quad (\text{E.9})$$

It is noted that this boundary value still resides in the stable region.

## E.2 Stability analysis for the resistive EMSD enhanced by series and parallel NIs

The characteristic polynomial for the electromechanical system is actually the monic form of denominator in Eq. (7.30), i.e.:

$$P(\bar{s}) = \bar{s}^4 + \delta_1 \bar{s}^3 + \delta_2 \bar{s}^2 + \delta_3 \bar{s} + \delta_4 \quad (\text{E.10})$$

whose coefficients are given by:

$$\delta_1 = \frac{\kappa(\alpha\beta + \gamma + \beta\gamma)}{\alpha\gamma}, \quad \delta_2 = \frac{\alpha\gamma + \theta\gamma + \beta\kappa^2}{\alpha\gamma}, \quad \delta_3 = \frac{\kappa(\alpha\beta + \gamma + \beta\gamma + \beta\theta)}{\alpha\gamma}, \quad \delta_4 = \frac{\beta\kappa^2}{\alpha\gamma}. \quad (\text{E.11})$$

The necessary and sufficient conditions for guaranteeing the stability are:

$$\delta_1 > 0 \quad (\text{E.12a})$$

$$\delta_3 > 0 \quad (\text{E.12b})$$

$$\delta_4 > 0 \quad (\text{E.12c})$$

$$\delta_1 \delta_2 \delta_3 > \delta_3^2 + \delta_1^2 \delta_4 \quad (\text{E.12d})$$

The combination of Eqs. (7.40) and (E.12c) yields to an inequality condition on series inductance ratio  $\alpha$  that:

$$\alpha > \alpha_{SP}^- = \frac{\theta}{2} \quad (\text{E.13})$$

Substituting Eq. (7.40) into (E.12a) leads to:

$$\gamma > \gamma_1^- = -\alpha - \frac{2\kappa^2}{2\alpha - \theta} \quad (\text{E.14})$$

Therefore, the optimal parallel inductance ratio  $\gamma$  is equal to  $\gamma_2$  and is simplified as described in Eq. (7.47). The constraint (E.12b) is assured automatically when Eq. (E.12a) is satisfied. Finally, Eq. (E.12d) associated with Eq. (7.40) results in a quadratic polynomial in  $\gamma$  as follows:

$$c_2 \lambda^2 + c_1 \lambda + c_0 > 0 \quad (\text{E.15})$$

with its coefficients expressed by

$$\begin{cases} c_2 = 2(2\alpha - \theta)^2 \\ c_1 = (2\alpha - \theta)(8\alpha^2 - 2\alpha\theta + 8\kappa^2 - \theta^2) \\ c_0 = 8\alpha^4 - 12\theta\alpha^3 + (6\theta^2 + 16\kappa^2)\alpha^2 - (\theta^2 + 4\kappa^2)\theta\alpha + 8\kappa^4 - 2\theta^2\kappa^2 \end{cases} \quad (\text{E.16})$$

which yields the allowable interval of  $\gamma$ :  $\gamma \in (-\infty, \gamma_2^-) \cup (\gamma_2^+, +\infty)$  with the two boundary values expressed as:

$$\gamma_2^- = -\alpha - \frac{2\kappa^2}{2\alpha - \theta} - \frac{\theta}{4} - \sqrt{\alpha\theta + \frac{\theta^2}{16}}, \quad \gamma_2^+ = -\alpha - \frac{2\kappa^2}{2\alpha - \theta} - \frac{\theta}{4} + \sqrt{\alpha\theta + \frac{\theta^2}{16}}. \quad (\text{E.17})$$

By comparing Eqs. (7.18), (E.14) and (E.17),  $\gamma_2^- < \gamma_1^- < \gamma_2^+ < \gamma_{SP}^+$  always holds for a small value of  $\theta$  and for series inductance ratio  $\alpha \in (0, 1)$ . Hence, the eventual allowable bound on parallel inductance ratio  $\gamma$  is defined as:  $\gamma \in (\gamma_{SP}^-, \gamma_{SP}^+)$  with its lower and upper limits formulated by:

$$\gamma_{SP}^- = \gamma_2^+ = -\alpha - \frac{2\kappa^2}{2\alpha - \theta} - \frac{\theta}{4} + \sqrt{\alpha\theta + \frac{\theta^2}{16}}, \quad \gamma_{SP}^+ = -\alpha - \theta. \quad (\text{E.18})$$

# Bibliography

- [1] Hermann Frahm. Device for damping vibrations of bodies., April 18 1911. US Patent 989,958.
- [2] J.P. Den Hartog. *Mechanical vibrations*. McGraw-Hill, New York, 4 edition, 1956.
- [3] A. Kareem, T. Kijewski, and Y. Tamura. Mitigation of motions of tall buildings with specific examples of recent applications. *Wind and Structures, An International Journal*, 2(3):201–251, 1999.
- [4] O. Nishihara and T. Asami. Closed-form solutions to the exact optimizations of dynamic vibration absorbers (minimizations of the maximum amplitude magnification factors). *Journal of Vibration and Acoustics, Transactions of the ASME*, 124(4):576–582, 2002.
- [5] G. B. Warburton. Optimum absorber parameters for various combinations of response and excitation parameters. *Earthquake Engineering & Structural Dynamics*, 10(3):381–401, 1982.
- [6] T. Asami, T. Wakasono, K. Kameoka, M. Hasegawa, and H. Sekiguchi. Optimum design of dynamic absorbers for a system subjected to random excitation. *JSME International Journal, Series 3: Vibration, Control Engineering, Engineering for Industry*, 34(2):218–226, 1991.
- [7] H. Yamaguchi. Damping of transient vibration by a dynamic absorber. *Transactions of the Japan Society of Mechanical Engineers Series C*, 54(499):561–568, 1988.
- [8] O. Nishihara and H. Matsuhisa. Design optimization of passive gyroscopic damper (stability degree maximization). *Nippon Kikai Gakkai Ronbunshu, C Hen/Transactions of the Japan Society of Mechanical Engineers, Part C*, 62(600):3090–3098, 1996.
- [9] N. D. Sims. Vibration absorbers for chatter suppression: A new analytical tuning methodology. *Journal of Sound and Vibration*, 301(3-5):592–607, 2007.

- [10] M. Zilletti, S. J. Elliott, and E. Rustighi. Optimisation of dynamic vibration absorbers to minimise kinetic energy and maximise internal power dissipation. *Journal of Sound and Vibration*, 331(18):4093–4100, 2012.
- [11] M. Z. Ren. A variant design of the dynamic vibration absorber [3]. *Journal of Sound and Vibration*, 245(4):762–770, 2001.
- [12] Y. L. Cheung and W. O. Wong. H2 optimization of a non-traditional dynamic vibration absorber for vibration control of structures under random force excitation. *Journal of Sound and Vibration*, 330(6):1039–1044, 2011.
- [13] P. Xiang and A. Nishitani. Optimum design and application of non-traditional tuned mass damper toward seismic response control with experimental test verification. *Earthquake Engineering and Structural Dynamics*, 44(13):2199–2220, 2015.
- [14] L. Dell’Elce, E. Gourc, and G. Kerschen. A robust equal-peak method for uncertain mechanical systems. *Journal of Sound and Vibration*, 414:97–109, 2018.
- [15] R. Vigi   and G. Kerschen. Nonlinear vibration absorber coupled to a nonlinear primary system: A tuning methodology. *Journal of Sound and Vibration*, 326(3-5):780–793, 2009.
- [16] G. Habib, T. Detroux, R. Vigi  , and G. Kerschen. Nonlinear generalization of den hartog’s equal-peak method. *Mechanical Systems and Signal Processing*, 52-53(1):17–28, 2015.
- [17] X. Sun, J. Xu, F. Wang, and L. Cheng. Design and experiment of nonlinear absorber for equal-peak and de-nonlinearity. *Journal of Sound and Vibration*, 449:274–299, 2019.
- [18] K. Liu and J. Liu. The damped dynamic vibration absorbers: Revisited and new result. *Journal of Sound and Vibration*, 284(3-5):1181–1189, 2005.
- [19] P. Bisegna and G. Caruso. Closed-form formulas for the optimal pole-based design of tuned mass dampers. *Journal of Sound and Vibration*, 331(10):2291–2314, 2012.
- [20] K. Xu and T. Igusa. Dynamic characteristics of multiple substructures with closely spaced frequencies. *Earthquake Engineering & Structural Dynamics*, 21(12):1059–1070, 1992.
- [21] H. Yamaguchi and N. Harnpornchai. Fundamental characteristics of multiple tuned mass dampers for suppressing harmonically forced oscillations. *Earthquake Engineering & Structural Dynamics*, 22(1):51–62, 1993.

- [22] M. Abé and Y. Fujino. Dynamic characterization of multiple tuned mass dampers and some design formulas. *Earthquake Engineering & Structural Dynamics*, 23(8):813–835, 1994.
- [23] R. S. Jangid. Optimum multiple tuned mass dampers for base-excited undamped system. *Earthquake Engineering and Structural Dynamics*, 28(9):1041–1049, 1999.
- [24] C. Li. Performance of multiple tuned mass dampers for attenuating undesirable oscillations of structures under the ground acceleration. *Earthquake Engineering and Structural Dynamics*, 29(9):1405–1421, 2000.
- [25] C. Li. Optimum multiple tuned mass dampers for structures under the ground acceleration based on ddmf and admf. *Earthquake Engineering and Structural Dynamics*, 31(4):897–919, 2002.
- [26] N. Hoang and P. Warnitchai. Design of multiple tuned mass dampers by using a numerical optimizer. *Earthquake Engineering and Structural Dynamics*, 34(2):125–144, 2005.
- [27] S. Kim and C. Lee. Optimum design of linear multiple tuned mass dampers subjected to white-noise base acceleration considering practical configurations. *Engineering Structures*, 171:516–528, 2018.
- [28] C. Li and B. Zhu. Estimating double tuned mass dampers for structures under ground acceleration using a novel optimum criterion. *Journal of Sound and Vibration*, 298(1-2):280–297, 2006.
- [29] L. Zuo. Effective and robust vibration control using series multiple tuned-mass dampers. *Journal of Vibration and Acoustics, Transactions of the ASME*, 131(3):0310031–03100311, 2009.
- [30] T. Asami. Optimal design of double-mass dynamic vibration absorbers arranged in series or in parallel. *Journal of Vibration and Acoustics, Transactions of the ASME*, 139(1), 2017.
- [31] T. Asami, Y. Mizukawa, and T. Ise. Optimal design of double-mass dynamic vibration absorbers minimizing the mobility transfer function. *Journal of Vibration and Acoustics, Transactions of the ASME*, 140(6), 2018.
- [32] Lei Zuo. *Element and system design for active and passive vibration isolation*. PhD thesis, Massachusetts Institute of Technology, 2004.
- [33] S. Jang, M. J. Brennan, E. Rustighi, and H. Jung. A simple method for choosing the parameters of a two degree-of-freedom tuned vibration absorber. *Journal of Sound and Vibration*, 331(21):4658–4667, 2012.

- [34] W. Ma, Y. Yang, and J. Yu. General routine of suppressing single vibration mode by multi-dof tuned mass damper: Application of three-dof. *Mechanical Systems and Signal Processing*, 121:77–96, 2019.
- [35] T. Dahlberg. On optimal use of the mass of a dynamic vibration absorber. *Journal of Sound and Vibration*, 132(3):518–522, 1989.
- [36] L. Zuo and S. A. Nayfeh. Minimax optimization of multi-degree-of-freedom tuned-mass dampers. *Journal of Sound and Vibration*, 272(3-5):893–908, 2004.
- [37] Y. Yang, W. Dai, and Q. Liu. Design and implementation of two-degree-of-freedom tuned mass damper in milling vibration mitigation. *Journal of Sound and Vibration*, 335:78–88, 2015.
- [38] Y. Yang, W. Dai, and Q. Liu. Design and machining application of a two-dof magnetic tuned mass damper. *International Journal of Advanced Manufacturing Technology*, 89(5-8):1635–1643, 2017.
- [39] M. C. Smith. Synthesis of mechanical networks: The inerter. *IEEE Transactions on Automatic Control*, 47(10):1648–1662, 2002.
- [40] M. C. Smith and F. U. Wang. Performance benefits in passive vehicle suspensions employing inerters. *Vehicle System Dynamics*, 42(4):235–257, 2004.
- [41] K. Ikago, K. Saito, and N. Inoue. Seismic control of single-degree-of-freedom structure using tuned viscous mass damper. *Earthquake Engineering and Structural Dynamics*, 41(3):453–474, 2012.
- [42] S. Krenk and J. Høgsberg. Tuned resonant mass or inerter-based absorbers: Unified calibration with quasi-dynamic flexibility and inertia correction. *Proceedings of the Royal Society A: Mathematical, Physical and Engineering Sciences*, 472(2185), 2016.
- [43] I. F. Lazar, S. A. Neild, and D. J. Wagg. Using an inerter-based device for structural vibration suppression. *Earthquake Engineering and Structural Dynamics*, 43(8):1129–1147, 2014.
- [44] A. Gonzalez-Buelga, L. R. Clare, S. A. Neild, J. Z. Jiang, and D. J. Inman. An electromagnetic inerter-based vibration suppression device. *Smart Materials and Structures*, 24(5), 2015.
- [45] L. Marian and A. Giaralis. Optimal design of a novel tuned mass-damper-inerter (TMDI) passive vibration control configuration for stochastically support-excited structural systems. *Probabilistic Engineering Mechanics*, 38:156–164, 2015.

- 
- [46] L. Marian and A. Giaralis. The tuned mass-damper-inerter for harmonic vibrations suppression, attached mass reduction, and energy harvesting. *Smart Structures and Systems*, 19(6):665–678, 2017.
- [47] A. Giaralis and F. Petrini. Wind-induced vibration mitigation in tall buildings using the tuned mass-damper-inerter. *Journal of Structural Engineering (United States)*, 143(9), 2017.
- [48] X. Wang, X. Liu, Y. Shan, Y. Shen, and T. He. Analysis and optimization of the novel inerter-based dynamic vibration absorbers. *IEEE Access*, 6:33169–33182, 2018.
- [49] M. Z. Q. Chen, Y. Hu, L. Huang, and G. Chen. Influence of inerter on natural frequencies of vibration systems. *Journal of Sound and Vibration*, 333(7):1874–1887, 2014.
- [50] M. Zilletti. Feedback control unit with an inerter proof-mass electrodynamic actuator. *Journal of Sound and Vibration*, 369:16–28, 2016.
- [51] Y. Hu, M. Z. Q. Chen, Z. Shu, and L. Huang. Analysis and optimisation for inerter-based isolators via fixed-point theory and algebraic solution. *Journal of Sound and Vibration*, 346(1):17–36, 2015.
- [52] Y. Hu and M. Z. Q. Chen. Performance evaluation for inerter-based dynamic vibration absorbers. *International Journal of Mechanical Sciences*, 99:297–307, 2015.
- [53] E. Barredo, A. Blanco, J. Colín, V. M. Penagos, A. Abúndez, L. G. Vela, V. Meza, R. H. Cruz, and J. Mayén. Closed-form solutions for the optimal design of inerter-based dynamic vibration absorbers. *International Journal of Mechanical Sciences*, 144:41–53, 2018.
- [54] S. Krenk and J. Høgsberg. Tuned mass absorber on a flexible structure. *Journal of Sound and Vibration*, 333(6):1577–1595, 2014.
- [55] André Preumont. *Vibration Isolation*, pages 165–197. Springer International Publishing, Cham, 2018.
- [56] David L. Platus. Negative-stiffness-mechanism vibration isolation systems. In *Proceedings of SPIE - The International Society for Optical Engineering*, volume 1619, pages 44–54, 1992.
- [57] A. Carrella, M. J. Brennan, and T. P. Waters. Static analysis of a passive vibration isolator with quasi-zero-stiffness characteristic. *Journal of Sound and Vibration*, 301(3-5):678–689, 2007.
-

- [58] G. Gatti, M. J. Brennan, and B. Tang. Some diverse examples of exploiting the beneficial effects of geometric stiffness nonlinearity. *Mechanical Systems and Signal Processing*, 125:4–20, 2019.
- [59] J. Yang, Y. P. Xiong, and J. T. Xing. Dynamics and power flow behaviour of a nonlinear vibration isolation system with a negative stiffness mechanism. *Journal of Sound and Vibration*, 332(1):167–183, 2013.
- [60] T. D. Le and K. K. Ahn. A vibration isolation system in low frequency excitation region using negative stiffness structure for vehicle seat. *Journal of Sound and Vibration*, 330(26):6311–6335, 2011.
- [61] T. D. Le and K. K. Ahn. Experimental investigation of a vibration isolation system using negative stiffness structure. *International Journal of Mechanical Sciences*, 70:99–112, 2013.
- [62] L. T. Danh and K. K. Ahn. Active pneumatic vibration isolation system using negative stiffness structures for a vehicle seat. *Journal of Sound and Vibration*, 333(5):1245–1268, 2014.
- [63] X. Wang, H. Liu, Y. Chen, and P. Gao. Beneficial stiffness design of a high-static-low-dynamic-stiffness vibration isolator based on static and dynamic analysis. *International Journal of Mechanical Sciences*, 142-143:235–244, 2018.
- [64] A. Carrella, M. J. Brennan, T. P. Waters, and K. Shin. On the design of a high-static-low-dynamic stiffness isolator using linear mechanical springs and magnets. *Journal of Sound and Vibration*, 315(3):712–720, 2008.
- [65] N. Zhou and K. Liu. A tunable high-static-low-dynamic stiffness vibration isolator. *Journal of Sound and Vibration*, 329(9):1254–1273, 2010.
- [66] X. Shi and S. Zhu. Magnetic negative stiffness dampers. *Smart Materials and Structures*, 24(7):072002, 2015.
- [67] G. Dong, X. Zhang, S. Xie, B. Yan, and Y. Luo. Simulated and experimental studies on a high-static-low-dynamic stiffness isolator using magnetic negative stiffness spring. *Mechanical Systems and Signal Processing*, 86:188–203, 2017.
- [68] W. Zheng, B. Yan, H. Ma, R. Wang, J. Jia, L. Zhang, and C. Wu. Tuning of natural frequency with electromagnetic shunt mass. *Smart Materials and Structures*, 28(2), 2019.
- [69] T. Mizuno, T. Toumiya, and M. Takasaki. Vibration isolation system using negative stiffness. *JSME International Journal, Series C: Mechanical Systems, Machine Elements and Manufacturing*, 46(3):807–812, 2003.

- 
- [70] Y. Shen, H. Peng, X. Li, and S. Yang. Analytically optimal parameters of dynamic vibration absorber with negative stiffness. *Mechanical Systems and Signal Processing*, 85:193–203, 2017.
- [71] I. A. Antoniadis, S. A. Kanarachos, K. Gryllias, and I. E. Sapountzakis. Kdamping: A stiffness based vibration absorption concept. *JVC/Journal of Vibration and Control*, 24(3):588–606, 2018.
- [72] X. Huang, Z. Su, and H. Hua. Application of a dynamic vibration absorber with negative stiffness for control of a marine shafting system. *Ocean Engineering*, 155:131–143, 2018.
- [73] H. Xiuchang, S. Zhiwei, and H. Hongxing. Optimal parameters for dynamic vibration absorber with negative stiffness in controlling force transmission to a rigid foundation. *International Journal of Mechanical Sciences*, 152:88–98, 2019.
- [74] I. H. Mualla and B. Belev. Performance of steel frames with a new friction damper device under earthquake excitation. *Engineering Structures*, 24(3):365–371, 2002.
- [75] H. A. Sodano, J. Bae, D. J. Inman, and W. Keith Belvin. Concept and model of eddy current damper for vibration suppression of a beam. *Journal of Sound and Vibration*, 288(4-5):1177–1196, 2005.
- [76] Amr M Baz. *Active and Passive Vibration Damping*. Wiley, 2019.
- [77] Y. S. Lee, G. Kerschen, A. F. Vakakis, P. Panagopoulos, L. Bergman, and D. M. McFarland. Complicated dynamics of a linear oscillator with a light, essentially nonlinear attachment. *Physica D: Nonlinear Phenomena*, 204(1-2):41–69, 2005.
- [78] Y. Chang, A. Noormohamed, and O. Mercan. Analytical and experimental investigations of modified tuned liquid dampers (mtlds). *Journal of Sound and Vibration*, 428:179–194, 2018.
- [79] S. Colwell and B. Basu. Tuned liquid column dampers in offshore wind turbines for structural control. *Engineering Structures*, 31(2):358–368, 2009.
- [80] W. Wang, X. Hua, X. Wang, Z. Chen, and G. Song. Optimum design of a novel pounding tuned mass damper under harmonic excitation. *Smart Materials and Structures*, 26(5), 2017.
- [81] Z. Lu, X. Lu, and S. F. Masri. Studies of the performance of particle dampers under dynamic loads. *Journal of Sound and Vibration*, 329(26):5415–5433, 2010.

- [82] J. Wang, N. Wierschem, B. F. Spencer, and X. Lu. Numerical and experimental study of the performance of a single-sided vibro-impact track nonlinear energy sink. *Earthquake Engineering and Structural Dynamics*, 45(4):635–652, 2016.
- [83] O. V. Gendelman and A. Alloni. Dynamics of forced system with vibro-impact energy sink. *Journal of Sound and Vibration*, 358:301–314, 2015.
- [84] R. L. Forward. Electronic damping of vibrations in optical structures. *Applied Optics*, 18(5):690–697, 1979.
- [85] N. W. Hagood and A. von Flotow. Damping of structural vibrations with piezoelectric materials and passive electrical networks. *Journal of Sound and Vibration*, 146(2):243–268, 1991.
- [86] Shu-yau Wu. Piezoelectric shunts with a parallel rl circuit for structural damping and vibration control. In *Smart Structures and Materials 1996: Passive Damping and Isolation*, volume 2720, pages 259–270. International Society for Optics and Photonics, 1996.
- [87] O. Thomas, J. Ducarne, and J. F. Deü. Performance of piezoelectric shunts for vibration reduction. *Smart Materials and Structures*, 21(1), 2012.
- [88] B. Lossouarn, M. Aucejo, J. F. Deü, and B. Multon. Design of inductors with high inductance values for resonant piezoelectric damping. *Sensors and Actuators, A: Physical*, 259:68–76, 2017.
- [89] A. J. Fleming, S. Behrens, and S. O. R. Moheimani. Reducing the inductance requirements of piezoelectric shunt damping systems. *Smart Materials and Structures*, 12(1):57–64, 2003.
- [90] G. Caruso. A critical analysis of electric shunt circuits employed in piezoelectric passive vibration damping. *Smart Materials and Structures*, 10(5):1059–1068, 2001.
- [91] P. Soltani, G. Kerschen, G. Tondreau, and A. Deraemaeker. Piezoelectric vibration damping using resonant shunt circuits: An exact solution. *Smart Materials and Structures*, 23(12), 2014.
- [92] J. J. Hollkamp. Multimodal passive vibration suppression with piezoelectric materials and resonant shunts. *Journal of Intelligent Material Systems and Structures*, 5(1):49–57, 1994.
- [93] S. Behrens, S. O. R. Moheimani, and A. J. Fleming. Multiple mode current flowing passive piezoelectric shunt controller. *Journal of Sound and Vibration*, 266(5):929–942, 2003.

- [94] D. Niederberger, A. Fleming, S. O. R. Moheimani, and M. Morari. Adaptive multi-mode resonant piezoelectric shunt damping. *Smart Materials and Structures*, 13(5):1025–1035, 2004.
- [95] J. Tang and K. W. Wang. Active-passive hybrid piezoelectric networks for vibration control: Comparisons and improvement. *Smart Materials and Structures*, 10(4):794–806, 2001.
- [96] S. Behrens, A. J. Fleming, and S. O. R. Moheimani. A broadband controller for shunt piezoelectric damping of structural vibration. *Smart Materials and Structures*, 12(1):18–28, 2003.
- [97] M. Neubauer, R. Oleskiewicz, K. Popp, and T. Krzyzynski. Optimization of damping and absorbing performance of shunted piezo elements utilizing negative capacitance. *Journal of Sound and Vibration*, 298(1-2):84–107, 2006.
- [98] M. Berardengo, O. Thomas, C. Giraud-Audine, and S. Manzoni. Improved resistive shunt by means of negative capacitance: New circuit, performances and multi-mode control. *Smart Materials and Structures*, 25(7), 2016.
- [99] M. Pohl. Increasing the performance of negative capacitance shunts by enlarging the output voltage to the requirements of piezoelectric transducers. *Journal of Intelligent Material Systems and Structures*, 28(11):1379–1390, 2017.
- [100] M. Pohl. An adaptive negative capacitance circuit for enhanced performance and robustness of piezoelectric shunt damping. *Journal of Intelligent Material Systems and Structures*, 28(19):2633–2650, 2017.
- [101] U. Yigit, E. Cigeroglu, and E. Budak. Chatter reduction in boring process by using piezoelectric shunt damping with experimental verification. *Mechanical Systems and Signal Processing*, 94:312–321, 2017.
- [102] C. Bricault, C. Pézerat, M. Collet, A. Pyskir, P. Perrard, G. Matten, and V. Romero-García. Multimodal reduction of acoustic radiation of thin plates by using a single piezoelectric patch with a negative capacitance shunt. *Applied Acoustics*, 145:320–327, 2019.
- [103] H. Sun, Z. Yang, K. Li, B. Li, J. Xie, D. Wu, and L. Zhang. Vibration suppression of a hard disk driver actuator arm using piezoelectric shunt damping with a topology-optimized pzt transducer. *Smart Materials and Structures*, 18(6), 2009.
- [104] Bilal Mokrani. *Piezoelectric shunt damping of rotationally periodic structures*. PhD thesis, Université Libre de Bruxelles, 2015.

- [105] S. Behrens, A. J. Fleming, and S. O. Reza Moheimani. Electromagnetic shunt damping. In *IEEE/ASME International Conference on Advanced Intelligent Mechatronics, AIM*, volume 2, pages 1145–1150, 2003.
- [106] S. Behrens, A. J. Fleming, and S. O. R. Moheimani. Passive vibration control via electromagnetic shunt damping. *IEEE/ASME Transactions on Mechatronics*, 10(1):118–122, 2005.
- [107] D. Niederberger, S. Behrens, A. J. Fleming, S. O. R. Moheimani, and M. Morari. Adaptive electromagnetic shunt damping. *IEEE/ASME Transactions on Mechatronics*, 11(1):103–108, 2006.
- [108] T. Cheng and I. Oh. A current-flowing electromagnetic shunt damper for multi-mode vibration control of cantilever beams. *Smart Materials and Structures*, 18(9), 2009.
- [109] T. Inoue, Y. Ishida, and M. Sumi. Vibration suppression using electromagnetic resonant shunt damper. *Journal of Vibration and Acoustics, Transactions of the ASME*, 130(4):041003, 2008.
- [110] X. Tang, Y. Liu, W. Cui, and L. Zuo. Analytical solutions to  $h_2$  and  $h_\infty$  optimizations of resonant shunted electromagnetic tuned mass damper and vibration energy harvester. *Journal of Vibration and Acoustics, Transactions of the ASME*, 138(1):011018, 2016.
- [111] H. Niu, X. Zhang, S. Xie, and P. Wang. A new electromagnetic shunt damping treatment and vibration control of beam structures. *Smart Materials and Structures*, 18(4):045009, 2009.
- [112] B. Yan, X. Zhang, and H. Niu. Design and test of a novel isolator with negative resistance electromagnetic shunt damping. *Smart Materials and Structures*, 21(3):035003, 2012.
- [113] B. Yan, X. Zhang, and H. Niu. Vibration isolation of a beam via negative resistance electromagnetic shunt dampers. *Journal of Intelligent Material Systems and Structures*, 23(6):665–673, 2012.
- [114] X. Zhang, H. Niu, and B. Yan. A novel multimode negative inductance negative resistance shunted electromagnetic damping and its application on a cantilever plate. *Journal of Sound and Vibration*, 331(10):2257–2271, 2012.
- [115] B. Yan, X. Zhang, Y. Luo, Z. Zhang, S. Xie, and Y. Zhang. Negative impedance shunted electromagnetic absorber for broadband absorbing: Experimental investigation. *Smart Materials and Structures*, 23(12):125044, 2014.

- 
- [116] A. Stabile, G. S. Aglietti, G. Richardson, and G. Smet. Design and verification of a negative resistance electromagnetic shunt damper for spacecraft micro-vibration. *Journal of Sound and Vibration*, 386:38–49, 2017.
- [117] A. Stabile, G. S. Aglietti, G. Richardson, and G. Smet. A 2-collinear-dof strut with embedded negative-resistance electromagnetic shunt dampers for spacecraft micro-vibration. *Smart Materials and Structures*, 26(4):045031, 2017.
- [118] Demetris Demetriou. *Enhancing the Practical Applicability of Smart Tuned Mass Dampers in High-Rise Civil Engineering Structures*. PhD thesis, University of Leeds, 2017.
- [119] CTBUH Journal, Issue III. Tall Buildings in Numbers. <http://global.ctbuh.org/paper/3788>, 2018.
- [120] T. Kobori, N. Koshika, K. Yamada, and Y. Ikeda. Seismic response controlled structure with active mass driver system. Part 2: Design. *Earthquake Engineering & Structural Dynamics*, 20(2):133–149, 1991.
- [121] T. Kobori, N. Koshika, K. Yamada, and Y. Ikeda. Seismic response controlled structure with active mass driver system. Part 2: Verification. *Earthquake Engineering & Structural Dynamics*, 20(2):151–166, 1991.
- [122] S. J. Dyke, B. F. Spencer Jr., P. Quast, D. C. Kaspari Jr., and M. K. Sain. Implementation of an active mass driver using acceleration feedback control. *Computer-Aided Civil and Infrastructure Engineering*, 11(5):305–323, 1996.
- [123] H. Cao, A. M. Reinhorn, and T. T. Soong. Design of an active mass damper for a tall TV tower in Nanjing, China. *Engineering Structures*, 20(3):134–143, 1998.
- [124] D. Yang, J. Shin, H. Lee, S. Kim, and M. K. Kwak. Active vibration control of structure by active mass damper and multi-modal negative acceleration feedback control algorithm. *Journal of Sound and Vibration*, 392:18–30, 2017.
- [125] I. Nishimura, T. Kobori, M. Sakamoto, N. Koshika, K. Sasaki, and S. Ohru. Active tuned mass damper. *Smart Materials and Structures*, 1(4):306–311, 1992.
- [126] Isao Nishimura. *Vibration control of building structures by active tuned mass damper*. PhD thesis, University of Tokyo, 1994.
- [127] S. Chatterjee. Optimal active absorber with internal state feedback for controlling resonant and transient vibration. *Journal of Sound and Vibration*, 329(26):5397–5414, 2010.
-

- [128] Y. L. Cheung, W. O. Wong, and L. Cheng. Design optimization of a damped hybrid vibration absorber. *Journal of Sound and Vibration*, 331(4):750–766, 2012.
- [129] M. L. Brodersen, A. Bjørke, and J. Høgsberg. Active tuned mass damper for damping of offshore wind turbine vibrations. *Wind Energy*, 20(5):783–796, 2017.
- [130] C. C. Chang and H. T. Y. Yang. Control of buildings using active tuned mass dampers. *Journal of Engineering Mechanics*, 121(3):355–366, 1995.
- [131] Y. L. Cheung, W. O. Wong, and L. Cheng. Minimization of the mean square velocity response of dynamic structures using an active-passive dynamic vibration absorber. *Journal of the Acoustical Society of America*, 132(1):197–207, 2012.
- [132] Y. L. Cheung, W. O. Wong, and L. Cheng. Optimization of a hybrid vibration absorber for vibration control of structures under random force excitation. *Journal of Sound and Vibration*, 332(3):494–509, 2013.
- [133] M. Zilletti, P. Gardonio, and S. J. Elliott. Optimisation of a velocity feedback controller to minimise kinetic energy and maximise power dissipation. *Journal of Sound and Vibration*, 333(19):4405–4414, 2014.
- [134] S. Chesné, G. Inquieté, P. Cranga, F. Legrand, and B. Petitjean. Innovative hybrid mass damper for dual-loop controller. *Mechanical Systems and Signal Processing*, 115:514–523, 2019.
- [135] C. Collette and S. Chesné. Robust hybrid mass damper. *Journal of Sound and Vibration*, 375:19–27, 2016.
- [136] S. Chesné and C. Collette. Experimental validation of fail-safe hybrid mass damper. *Journal of Vibration and Control*, 24(19):4395–4406, 2018.
- [137] T. Fujita. Application of hybrid mass damper with convertible active and passive modes using hydraulic actuator to high-rise building. In *Proceedings of 1994 American Control Conference - ACC '94*, volume 1, pages 1067–1072 vol.1, June 1994.
- [138] C. Lee and Y. Wang. Seismic structural control using an electric servomotor active mass driver system. *Earthquake Engineering and Structural Dynamics*, 33(6):737–754, 2004.
- [139] L. Dal Bo, P. Gardonio, D. E. Casagrande, and S. Saggini. Smart panel with sweeping and switching piezoelectric patch vibration absorbers: Experimental results. *Mechanical Systems and Signal Processing*, 120:308–325, 2019.

- 
- [140] C. González Díaz and P. Gardonio. Feedback control laws for proof-mass electrodynamic actuators. *Smart Materials and Structures*, 16(5):1766–1783, 2007.
- [141] Weimin Huang. *Shape memory alloys and their application to actuators for deployable structures*. PhD thesis, University of Cambridge, 1998.
- [142] S. P. Beeby, M. J. Tudor, and N. M. White. Energy harvesting vibration sources for microsystems applications. *Measurement Science and Technology*, 17(12):R175–R195, 2006.
- [143] D. Zhu, M. J. Tudor, and S. P. Beeby. Strategies for increasing the operating frequency range of vibration energy harvesters: A review. *Measurement Science and Technology*, 21(2), 2010.
- [144] R. L. Harne and K. W. Wang. A review of the recent research on vibration energy harvesting via bistable systems. *Smart Materials and Structures*, 22(2), 2013.
- [145] C. Wei and X. Jing. A comprehensive review on vibration energy harvesting: Modelling and realization. *Renewable and Sustainable Energy Reviews*, 74:1–18, 2017.
- [146] N. Tran, M. H. Ghayesh, and M. Arjomandi. Ambient vibration energy harvesters: A review on nonlinear techniques for performance enhancement. *International Journal of Engineering Science*, 127:162–185, 2018.
- [147] Y. Wang and D. J. Inman. A survey of control strategies for simultaneous vibration suppression and energy harvesting via piezoceramics. *Journal of Intelligent Material Systems and Structures*, 23(18):2021–2037, 2012.
- [148] S. F. Ali and S. Adhikari. Energy harvesting dynamic vibration absorbers. *Journal of Applied Mechanics, Transactions ASME*, 80(4), 2013.
- [149] R. L. Harne. Development and testing of a dynamic absorber with corrugated piezoelectric spring for vibration control and energy harvesting applications. *Mechanical Systems and Signal Processing*, 36(2):604–617, 2013.
- [150] Z. Yan and M. R. Hajj. Energy harvesting from an autoparametric vibration absorber. *Smart Materials and Structures*, 24(11), 2015.
- [151] T. Tan, Z. Yan, Y. Zou, and W. Zhang. Optimal dual-functional design for a piezoelectric autoparametric vibration absorber. *Mechanical Systems and Signal Processing*, 123:513–532, 2019.
- [152] K. Kecik. Assessment of energy harvesting and vibration mitigation of a pendulum dynamic absorber. *Mechanical Systems and Signal Processing*, 106:198–209, 2018.
-

- [153] D. Kremer and K. Liu. A nonlinear energy sink with an energy harvester: Transient responses. *Journal of Sound and Vibration*, 333(20):4859–4880, 2014.
- [154] D. Kremer and K. Liu. A nonlinear energy sink with an energy harvester: Harmonically forced responses. *Journal of Sound and Vibration*, 410:287–302, 2017.
- [155] G. Pennisi, B. P. Mann, N. Naclerio, C. Stephan, and G. Michon. Design and experimental study of a nonlinear energy sink coupled to an electromagnetic energy harvester. *Journal of Sound and Vibration*, 437:340–357, 2018.
- [156] A. Afsharfard. Application of nonlinear magnetic vibro-impact vibration suppressor and energy harvester. *Mechanical Systems and Signal Processing*, 98:371–381, 2018.
- [157] S. F. Masri, J. P. Caffrey, and H. Li. Transient response of mdof systems with inerters to nonstationary stochastic excitation. *Journal of Applied Mechanics, Transactions ASME*, 84(10), 2017.
- [158] A. Giaralis and F. Petrini. Wind-induced vibration mitigation in tall buildings using the tuned mass-damper-inerter. *Journal of Structural Engineering (United States)*, 143(9), 2017.
- [159] S. Zhou, C. Jean-Mistral, and S. Chesné. Optimal design of an inerter-based dynamic vibration absorber connected to ground. *Journal of Vibration and Acoustics, Transactions of the ASME*, 141(5):051017–051017–11, 2019.
- [160] S. Kim, S. Wang, and M. J. Brennan. Dynamic analysis and optimal design of a passive and an active piezo-electrical dynamic vibration absorber. *Journal of Sound and Vibration*, 330(4):603–614, 2011.
- [161] E. Arroyo, A. Badel, F. Formosa, Y. Wu, and J. Qiu. Comparison of electromagnetic and piezoelectric vibration energy harvesters: Model and experiments. *Sensors and Actuators, A: Physical*, 183:148–156, 2012.
- [162] Izrail Solomonovich Gradshteyn and Iosif Moiseevich Ryzhik. *Table of integrals, series, and products*. Academic press, 2014.



## FOLIO ADMINISTRATIF

### THESE DE L'UNIVERSITE DE LYON OPEREE AU SEIN DE L'INSA LYON

NOM : Zhou

(avec précision du nom de jeune fille, le cas échéant)

Prénoms : Shaoyi

DATE de SOUTENANCE : 23/09/2019

TITRE : Advances in Passive and Active Vibration Damping Techniques

NATURE : Doctorat

Numéro d'ordre : 2019LYSEI066

Ecole doctorale : Mécanique, Énergétique, Génie civil, Acoustique

Spécialité : GÉNIE MÉCANIQUE

#### RESUME :

Mechanical systems (e.g. flexible structures) are usually lightly damped so that they vibrate severely in response to dynamic loads. Therefore, vibration control strategies should be adopted in order to reduce the undesired vibration of mechanical systems. The objective of this thesis is to develop multiple vibration control techniques, which are either passive or active. All systems under investigation are in the mechanical and/or electrical domains, for which analytical optimization and theoretical analyses are performed.

The first part focuses on the application of inerter to enhance the vibration control performance of two existing control devices, the tuned mass damper (TMD) and the series double TMD (SDTMD). The inerter is employed to relate the tuned mass to the ground. In the case of TMD, a mechanical system under stiffness uncertainty is considered and the worst-case  $H^\infty$  optimization is addressed by means of an entirely algebraic approach. In the case of SDTMD, the vibration of a deterministic mechanical system is to be controlled and the  $H^\infty$  optimal design is carried out via an extended version of fixed points theory (FPT).

Instead of using the inerter, the second part consists in improving the control effect by incorporating a linear negative stiffness between the ground and the tuned mass. Two case studies are conducted based on the non-traditional TMD and inerter-based dynamic vibration absorber (IDVA), whose tuned mass is related to the ground by a viscous damper or an inerter-based mechanical network, respectively. Later, the exact electrical realization of non-traditional configurations with or without negative stiffness is proposed, which is based on the piezoelectric transducer enclosed by a particular shunt circuit. This electromechanical analogy enables to extend the applicability of mechanical control devices and to facilitate the precise tuning. In the last part, active and semi-active vibration control techniques are developed. The first strategy consists in enhancing the control capability of passive TMD and IDVA by feeding back the displacement signal of mechanical system to the electromagnetic actuator. The proposed controller can be regarded as one or multiple basic units arranged in series, which is featured by one pole at the origin and two coalesced zeros on the real axis. It is analytically proven that such a controller design is always stable if and only if the magnitude of introduced zeros resides within the magnitudes of the smallest and largest eigenvalues of coupled system, whose expressions are analytically formulated in both cases of TMD and IDVA. Distinguished from the previous strategy, the semi-active control technique is based on electromagnetic shunt damping (EMSD), therefore, no additional sensor is required to measure the information of mechanical system. In order to artificially increase the shunt damping performance, the employment of negative inductance (NI) in the shunt circuit is considered. Three possible layouts of NI in the EMSD are assessed in terms of the electromechanical coupling factor, which quantifies the energy conversion efficiency between mechanical and electrical domains. Finally, six types of shunt circuits are optimally tuned according to the FPT and the beneficial effect of NI and the influence of its layout can be underlined.

MOTS-CLÉS: Vibration control, shunt damping, inerter, negative stiffness, optimal design.

Laboratoire (s) de recherche : Laboratoire de Mécanique des Contacts et des Structures

Directeur de thèse: Simon Chesné

Président de jury :

Composition du jury :

Li Cheng, Professeur, Hong Kong Polytechnic University, rapporteur ;

Christophe Collette, Professeur, Université Libre de Bruxelles, rapporteur ;

Manuel Collet, Directeur de recherche CNRS, École Centrale de Lyon, examinateur ;

Guilhem Michon, Professeur, ISAE-SUPAERO, examinateur ;

Simon Chesné, Maître de conférences, INSA de Lyon, directeur de thèse ;

Claire Jean-Mistral, Maître de conférences, INSA de Lyon, co-directrice de thèse.